THE UNIVERSITY *of* EDINBURGH

Polymers at Surfaces: Nanostructures and Adhesion Studied by Atomic Force Microscopy

Jake McClements

THE UNIVERSITY *of* EDINBURGH

THESIS SUBMITTED IN PARTIAL FULFILMENT OF

THE REQUIREMENTS FOR THE DEGREE OF

DOCTOR OF PHILOSOPHY

TO THE

UNIVERSITY OF EDINBURGH

October 2018

Declaration

I declare that this thesis has been composed solely by myself and that it has not been submitted, either in whole or in part, in any previous application for a degree. Except where otherwise acknowledged, the work presented is entirely my own.

Jake McClements

October 2018

Abstract

Understanding and characterising the behaviour of polymers at surfaces is of great fundamental interest, in addition to being vitally important for many applications. Composite materials, films and coatings, functional membranes, and nanoelectronics are only a few examples of applications which rely on polymers functioning at surfaces. The interactions between polymers and surfaces are extremely influential in governing the overall bulk properties of materials and products. Despite this, the behaviour of polymers at surfaces is not fully understood and there are many unexplored areas in this field of research.

Atomic force microscopy (AFM) is a technique which can image features with a high spatial resolution down to a sub-nanometre scale. It can accurately image a variety of polymer nanostructures on surfaces such as droplets, networks, thin films, and even single chains. AFM can also be used in a mode of operation called force spectroscopy which generates information regarding the strength of adhesion between different materials with a piconewton force resolution. It can be used to measure the magnitude of interaction forces between single polymer chains and surfaces.

The primary aim of this study was to characterise the behaviour of poly(styrene-co-butadiene) random copolymers on various surfaces at the nanoscale using AFM techniques. Poly(styrene-co-butadiene) is heavily utilised within industry, particularly in the manufacturing of automotive tyres where it is mixed with carbon black to form a robust composite material. This study is the first work to provide a comprehensive report on the morphology of poly(styrene-co-butadiene) nanostructures on various surfaces, under different experimental parameters. Furthermore, it is the first time

where the specific interactions and adhesion between poly(styrene-co-butadiene) and various surfaces have been examined using AFM force spectroscopy.

A systematic study was carried out which investigated the structural behaviour of adsorbed poly(styrene-co-butadiene) random copolymers on mica and graphite surfaces using AFM imaging. A large range of concentrations and molecular weights allowed investigations and discussions of many phenomena such as thin film formation (and dewetting), networks, spherical cap nanodroplets, and single chain conformations. Polymer morphology was generally more consistent on the mica, and varied significantly on graphite. The contact angles of the nanodroplets on the mica surface were shown to be size dependent by a specific trend irrespective of molecular weight. A minimum contact angle was observed for droplets with radii ranging from 100 - 250 nm across each molecular weight. This was due to influences from line tension, changes in elastic modulus, and surface heterogeneities. On the graphite, the nanostructures exhibited distinct ordering at the nanoscale. The features reflected the crystalline symmetry of the graphite by orientating themselves at intervals of 60° due to π-π stacking interactions. The ordering was extremely precise at the lowest concentration and became less defined at higher concentrations, but remained statistically significant.

An AFM force spectroscopy study was implemented in order to investigate the adhesion and specific interactions between poly(styrene-co-butadiene) and mica, silicon, and graphite substrates. AFM tips were dip coated into polymer solutions to physically adhere polymer chains to the surface of the tips at varying molecular weights and surface coverages. Polymer chains were also adhered to AFM tips using force spectroscopy techniques. The results showed that capillary forces were increasing polymer/substrate adhesion on the more hydrophilic substrates. Single chain desorption events did occur, but had a very low probability. The experimental system was redesigned to reduce capillary effects and increase desorption events. Thin polymer films were deposited onto each substrate using dip coating and the AFM tips were left blank. The results revealed that capillary forces were eliminated using this system and the probability of single chain desorption events occurring was extremely high. It was demonstrated that the specific interactions between poly(styrene-co-butadiene) and graphite were the strongest of the three substrates due to π-π stacking interactions and van der Waals forces.

Lay Summary

The word polymer is not widely known outside of the scientific community. However, throughout the world, polymers are utilised in incredible abundance for countless applications. On any given day, someone is likely to come into contact with polymers numerous times. This includes any time that they handle a mobile phone case, laptop, water bottle, or shopping bag. Polymers are long chain-like molecules which make up all plastics. The reason why polymers are used for so many applications is due to their extremely favourable properties, such as being tough, lightweight, low cost, and malleable. However, polymers are frequently combined with filler materials to further enhance their properties. For example, strong fibres are introduced to stiff polymers (such as epoxies) to increase their strength, which makes them suitable for structural composites. Carbon particles are also added to rubbery polymers in the manufacture of automotive tyres to increase their durability and decrease wear rate.

Understanding how polymers behave at surfaces is vital for the successful development of many applications. These include composite materials such as carbon fibre reinforced polymers, nanocomposite coatings, and films used in nanoelectronic applications. The interactions between polymer molecules and different surfaces are extremely influential in determining the overall bulk properties of a material or product. For example, the strength of a carbon fibre reinforced bicycle frame is governed by the interactions between polymers and carbon fibres within the material. However, it is very challenging experimentally to investigate the behaviour of polymers on surfaces because these interactions take place at such an incredibly small length scale. This means that

currently, there is limited research within this field and still many unanswered questions.

This thesis presents an investigation into the fundamental behaviour of polymers on various surfaces at the nanoscale. Initially, analysis was carried out on the size and shape of polymer nanostructures which formed on different surfaces. The polymer nanostructures were imaged using a technique known as atomic force microscopy (AFM). AFM is an extremely powerful imaging technique which can accurately provide high resolution images of individual polymer molecules on a surface. These experiments showed that the behaviour of the polymer nanostructures varied significantly on different surfaces. The strength of interactions between individual polymer chains and various surfaces were then directly measured by AFM whilst using a different mode of operation. These experiments provided valuable information regarding the nature of interaction forces at the molecular scale which are dominant in these systems. This thesis provides a comprehensive report on the behaviour of polymers on surfaces at the nanoscale. It presents novel findings which broaden the scope of knowledge within the field and are useful to many applications where polymers are used.

Acknowledgments

There are many people who have helped me extensively over the course of my PhD. Firstly I would like to thank my principal supervisor, Professor Vasileios Koutsos. He has provided me with incredible support throughout both the highs and lows of the project. His patience, encouragement, and insightful input have been invaluable. A big thanks to my second supervisor, Professor Michael Shaver for the many useful discussions and feedback on my work.

I would also like to thank the SOFI CDT which gave me the opportunity to pursue a PhD and provided me with a wealth of incredible experiences. I thank Michelin and Marc Couty for providing support, resources, and discussions throughout the project. Marc Couty, who is based at Michelin in Clermont-Ferrand, provided the styrene-butadiene samples and carried out the GPC, DSC, and NMR measurements which are presented in the thesis.

I have had the opportunity to work with many fantastic people throughout my PhD. I would like to thank everyone from SOFI Cohort 1. You made the beginning of my PhD and my time in Durham so much more enjoyable and fun. I would also like to thank all of the past and current members of the Green Materials Laboratory and the Koutsos group, in addition to, all of the office mates I have had throughout my time in Edinburgh. There are too many to name each of you, but thank you for everything. A special thanks to Fergus Cuthill and Tamas Parkanyi for helping me and patiently answering all my questions when I first arrived in Edinburgh.

I would also like to thank everyone who I have worked with on collaborative projects throughout my PhD. Special thanks to Elsa Lasseuguette, Cosimo Buffone, Adeel Shafi, and Dimitrios Mamalis. Thank you to the undergraduate project students I have worked with, in particular Chris Acheson for massively helping with data analysis.

Thank you to all my amazing friends who have made my time in Edinburgh some of the best years of my life, and have consistently shown me that work is not everything. The members of TS5, Ross, Emily, and Stefan, you guys have been incredible and filled my time in Edinburgh with excitement, fun, and laughter. I hope we can share many more adventures and good times together. Murv, Yaz, Gerry, Ben, Maguire, Sally, Fern, Beven, Christian, Lewis, Josh, Becky, Dan, Lauren, Jenny and anyone else I may have forgotten, thank you all so much for all of the good times.

I am incredibly grateful to my family. My amazing grandparents, who have always been there to provide tons of love and support throughout the years. My sister Chelsea for all of the support, as well as, showing me what it was possible for someone from Rye Hills to achieve. I would also like to thank Sharon and Simon who are always so unbelievably generous, supportive, and welcoming. To Mam and Dad, I am so incredibly lucky to have you guys for parents. You have provided me unwavering love and support, and encouraged me to pursue whatever makes me happy in life. I really could not have done it without you, and you make me really proud. I love so both so much.

Finally, I would like to thank you Kim-Sue. You have always provided me with unimaginable love and support. You have been there to guide me through the low points, but also to celebrate and share in the successes. Your kindness, caring, unshakable positivity, and general lust for life have been a true inspiration and a constant source of comfort. I would like to thank you so much for making the daunting move to Edinburgh, it has made these last couple of years some of the happiest of my life. I would also like to thank you for all of the hours spent proof reading my papers and thesis, this has really been incredibly helpful. We have had some amazing adventures together and both achieved so much throughout the last few years. Now this chapter is over, I cannot wait to see what is around the corner. Thank you for everything, I love you.

Contents

List of Tables

Chapter Three

Chapter Five

Chapter Six

Chapter Seven

List of Figures

Chapter Two

Chapter Three

Chapter Four

Chapter Five

Chapter Six

Chapter Seven

List of Acronyms

AFM	Atomic force microscopy
CNT	Carbon nanotube
DSC	Differential scanning calorimetry
FFT	Fast Fourier transform
FJC	Freely jointed chain
GPC	Gel permeation chromatography
HOPG	Highly ordered pyrolytic graphite
InvOLS	Inverse optical laser sensitivity
LB	Langmuir-Blodgett
MWCNT	Multi-walled carbon nanotube
NMR	Nuclear magnetic resonance
PG1	First-generation dendronised polymer
PG5	Fifth-generation dendronised polymer
SEM	Scanning electron microscopy
SMFS	Single-molecule force spectroscopy
SPM	Scanning probe microscopy

STM	Scanning tunnelling microscopy
TEM	Transmission electron microscopy
TMV	Tobacco mosaic virus
WLC	Worm-like chain
ZYA	Graphite substrate with a mosaic spread of 0.4 - 0.7˚

List of Symbols

a_l	Length of the major axis of a polymer aggregate (nm)
A	Hamaker constant (J)
b	Kuhn segment length (nm)
b_l	Length of the minor axis of a polymer aggregate (nm)
c^*	Overlap concentration
D	Diameter of a dewetted hole (nm)
E_f	Adhesive energy across force plateaus and steps (kJ/mol)
E_s	Adhesive energy per Kuhn segment (kJ/mol)
F	Adhesive force between an AFM tip and substrate (nN)
F_{Step}	Magnitude of force step (pN)
h	Height of a polymer aggregate (nm)
h_f	Polymer film thickness (nm)
H	Maximum height of a dewetted hole's rim (nm)
k	Spring constant of an AFM cantilever (nN/nm)
l	Evaluation length used in surface roughness measurements (nm)
L	Length of a fully stretched polymer chain (nm)
L_l	Length of force plateaus and steps (nm)
M_0	Molar mass of a Kuhn segment (kg/mol)

M_e	Entanglement molecular weight (kg/mol)
M_n	Number average molecular weight (kg/mol)
N	Degree of polymerisation
N_A	Avogadro's number (mol^{-1})
r	Radius of a polymer coil (nm)
r_r	Real contact radius of a polymer aggregate (nm)
R_a	Arithmetic surface roughness (nm)
R_g	Radius of gyration (nm)
R_t	Radius of an AFM tip (nm)
S	Spreading Coefficient (mJ/m^2)
τ	Line Tension (N)
T_g	Glass transition temperature (˚C)
V_a	Apparent volume of a polymer aggregate (nm^3)
V_p	Pervaded volume (nm^3)
V_r	Real volume of a polymer aggregate (nm^3)
W_a	Apparent contact width of an elongated polymer aggregate (nm)
W_{cap}	Real contact width of a polymer aggregate (nm)
W_{el}	Real contact width of an elongated polymer aggregate (nm)
x	Deflection of an AFM cantilever (nm)
γ	Surface energy/Interfacial energy (mJ/m^2)
ε	Eccentricity
θ	Contact angle (˚)
κ	Characteristic decay length of a dewetted hole's rim (nm)
ρ	Density (g/cm^3)
Đ	Dispersity

1 Introduction

1.1 Overview

Since their initial development, synthetic polymers have been used for countless applications due to their low cost, versatility, and extremely favourable properties. For over a century, research in the field of polymer science has focused on improving the properties of polymers, and understanding their behaviour. Much of this research has focused on investigating the properties and behaviour of polymers in the bulk state. However, many applications rely on polymers functioning at surfaces, and therefore the interfacial behaviour of polymers is incredibly important. It is well established that the behaviour and properties of polymers can be significantly different in the bulk compared to at an interface. However, precisely how and why the behaviour changes is not fully understood. Consequently, research which investigates the behaviour of polymers at an interface is important to fundamental polymer science, as well as, the successful development of many applications, such as carbon fibre-reinforced polymers and automotive tyres.

Accurately investigating the behaviour of polymers at an interface can be very difficult experimentally. This is because the polymers must be examined at incredibly small length scales so that there is not a significant influence from bulk behaviour. Atomic force microscopy (AFM) is one of the few techniques which can accurately investigate many aspects of polymer behaviour at surfaces. It can be used to image polymers at the nanoscale and investigate a range of phenomena, from thin films and dewetting to single chain conformations. Furthermore, AFM can be also be utilised to investigate the specific interactions and adhesion between polymers and different surfaces. This can provide detailed quantitative information regarding the intermolecular and surface forces which govern interfacial polymer behaviour.

Previous AFM experiments have highlighted the complex behaviour of polymers at surfaces. However, there are still many aspects of this area which are not understood. Furthermore, many polymer/surface systems which are extensively utilised within industry have not been investigated. Consequently, there is a huge potential for research within this area, which could be of great benefit to fundamental polymer science and many applications.

1.2 PhD aims and scope

The primary objective of this study was to investigate the fundamental behaviour of adsorbed poly(styrene-co-butadiene) random copolymers on various substrates at the nanoscale. Poly(styrene-co-butadiene) is extensively utilised within industry, most commonly in the manufacturing of automotive tyres where it is combined with carbon black to make a robust composite material. If a better understanding of the interfacial behaviour of poly(styrene-co-butadiene) was achieved, this could benefit in the intelligent design and manufacturing of tyres, as well as, numerous other materials and applications. AFM imaging was utilised to investigate the morphology of poly(styrene-co-butadiene) nanostructures on mica and graphite substrates at various concentrations and molecular weights. Whilst AFM force spectroscopy was used to investigate the specific interactions and adhesion between poly(styrene-co-butadiene) and mica, silicon, and graphite substrates.

1.3 Thesis structure

This thesis contains eight chapters. Chapter 2 is a literature review which focuses on the topic of polymers at surfaces. The applications which rely on polymers functioning at surfaces were explored, as well as, the techniques which can be utilised to investigate this topic. However, the primary focus of the chapter was to outline the common areas of research and developments that have taken place in the field of polymers at surfaces using AFM imaging and force spectroscopy.

Chapter 3 describes the experimental methods and apparatus which have been used for each experiment within the thesis. A discussion is presented regarding the polymers and substrates used in the experiments, as well as, a detailed outline of the sample preparation methods and substrate deposition techniques. Each aspect of AFM imaging and force spectroscopy is discussed in detail including basic principles, the machines used, experimental procedures, and analysis of results.

Chapter 4 presents an AFM imaging investigation of the morphology of poly(styrene-co-butadiene) random copolymers physically adsorbed on mica substrates using spin coating. Detailed analysis is presented of how the morphology of the adsorbed polymer

nanostructures varied with both solution concentration and molecular weight. Furthermore, the relationship between droplet contact angle and radius is investigated at the nanoscale and the macroscale. Large aspects of this chapter have previously been presented in the following article:

McClements, J.; Buffone, C.; Shaver, M. P.; Khellil, S.; Koutsos, V. Poly(styrene-co-Butadiene) Random Copolymer Thin Films and Nanostructures on a Mica Surface: Morphology and Contact Angles of Nanodroplets. *Soft Matter* **2017**, *13*, 6152–6166.

Chapter 5 presents an AFM imaging investigation of the adsorbed morphology of poly(styrene-co-butadiene) random copolymers on a graphite substrate. The materials and methods were identical to those used in Chapter 4, except the mica substrate was replaced with graphite. This allowed for direct comparison between the two chapters. The morphology of the polymer nanostructures was investigated at many concentrations and molecular weights. Furthermore, the specific ordering of poly(styrene-co-butadiene), polystyrene, and polybutadiene was investigated on the graphite surface. Large aspects of this chapter have previously been presented in the following article:

McClements, J.; Shaver, M. P.; Sefiane, K.; Koutsos, V. Morphology of Poly(Styrene-Co-Butadiene) Random Copolymer Thin Films and Nanostructures on a Graphite Surface. *Langmuir* **2018**, *34*, 7784–7796.

Chapter 6 presents an AFM force spectroscopy study which investigates the adhesion between poly(styrene-co-butadiene)-coated AFM tips and mica, silicon, and graphite substrates. Polymer chains were physically adsorbed to AFM tips using dip coating and force spectroscopy techniques, and were then used to interact with the surface of each substrate. The coated-tip/substrate adhesion was investigated for each substrate, and the advantages and limitations of the techniques were thoroughly examined. Furthermore, the impact that the tip history and tip/substrate contact time had on the measured adhesion was also examined.

Chapter 7 presents an AFM force spectroscopy study which investigates the specific interactions and desorption forces between poly(styrene-co-butadiene) and mica,

silicon, and graphite substrates. Blank AFM tips were used to pick up polymer chains from thin films on each substrate, which had been prepared by dip coating. The specific interactions and desorption forces between the polymer and each substrate/AFM tip are presented, as well as, an examination of the forces associated with the globule-extended coil conformational transition and chain pull-out from the thin films. Furthermore, a detailed examination of polymer bridging between the tips and each substrate is presented.

Chapter 8 presents conclusions for the investigations outlined above, as well as, describing the potential areas for future work.

2 Literature review

Summary

This chapter begins with a brief historical overview of the polymer industry and a discussion regarding the favourable properties of polymers. The chapter then focuses on the topic of polymers at surfaces. This includes a detailed discussion of applications which rely on polymers functioning at surfaces, as well as, outlining techniques which are utilised to investigate polymers at surfaces. Finally, a comprehensive discussion is presented of the main research areas of polymers at surfaces, which have been investigated using AFM imaging and force spectroscopy.

2.1 Polymers

2.1.1 History of the polymer industry

Polymers have existed since life began. They occur in a natural form and are vitally important for plant and animal life.[1] DNA, RNA, polysaccharides, and proteins are biopolymers which are so fundamental to life on earth that they are collectively known as the molecules of life. Each of the four biopolymers are vitally important for every organism on Earth.[2] Polymers are not only essential to the biology of humans, they have also been utilised as materials for thousands of years. For example, spiders silk has been used to manufacture clothing and decorations since ancient times due to its extremely favourable properties.[3] However, during these times, humans did not understand that they were dealing with polymers.[4] The birth of the modern polymer industry did not occur until the 19th century, when significant discoveries were made which involved modifying natural polymers to improve their physical properties.[1]

In 1839, Charles Goodyear made a major discovery when he noted that the properties of rubber were vastly improved when heated with sulphur.[1,5] This discovery was revolutionary, as natural rubber used in applications at the time became tacky and soft in the heat, whilst being stiff and inelastic in the cold. Goodyear's process, called vulcanisation, eliminated these issues and even further enhanced the properties of rubber.[5] Other major breakthroughs came later in the 19th century, where cellulose nitrate was plasticised to create tough and flexible materials, which were commercially known as Parkesine and Celluloid.[1] However, the first truly synthetic polymer to be produced and commercialised was known as Bakelite resin. This was a densely cross-linked thermoset which was synthesised by Leo Baekeland in 1907. Bakelite was revolutionary, not only as it was the first synthetic polymer, but also due to its favourable properties which meant it was heavily utilised within the automotive and electrical industries.[6]

In the early 20th century, the polymer industry was established and chemists were synthesising polymers for commercial use. However, production was low (less than one million tonnes per annum), which was partly due to a lack of understanding of polymer science.[1,7] At this point, the concept of macromolecules was not understood and chemists

believed that the materials in question were in fact aggregations of small molecules.[4] This meant that there was a lack of intelligent design in polymer synthesis, which limited both the production rates and quality of the manufactured polymers. The composition of polymers was not understood until 1920, when Hermann Staudinger established his macromolecular hypothesis. This hypothesis stated that polymers are made of up many small units which are covalently bonded to one another to form what Staudinger called macromolecules.[8] The word polymer was initially introduced many years previously by Jöns Jakob Berzelius, who used it to describe molecules with the same chemical composition, but different properties. The word is derived from Greek where *polys* means 'many' and *meros* means 'part'. However, Berzelius did not have high molecular weight macromolecules in mind when he coined the term.[8,9] It was only later in time when the words macromolecule and polymer became interchangeable. Staudinger's hypothesis provided the understanding and knowledge which facilitated rapid progress in the field of polymer science in the following years. At this time, it was stated that humans had entered into the 'plastic age'.[6]

In the years after Staudinger's hypothesis, there were many significant advances in the field of polymer science, which occurred in relatively quick successions. Notable scientists such as Flory, Kuhn, De Gennes, Rouse, and Zimm carried out extensive, pioneering research in the field of polymer science.[4] The production of polymers also drastically increased and many polymers were synthesised for commercial applications for the first time including polystyrene, nylon 6.6, and poly(styrene-co-butadiene).[1] In this time period, polymers became one of the most commonly used materials on earth.

2.1.2 The polymer industry in the modern day

The production of synthetic polymers has rapidly increased since their initial development in the early 20th century. Currently, around 300 million tonnes of synthetic polymers are produced worldwide every year.[7] Due to this, polymers are commonplace in modern society and a human can expect to come into contact with polymer-based products many times within a single day. The polymer industry has been incredibly beneficial in many fields, and facilitated huge advancements in areas such as transportation, personal devices, and medical applications.[7] Furthermore, polymer

research is at the forefront of materials science and is heavily involved in the development of innovative products such as composite materials, nanotechnological devices, and smart materials.[10–12] However, there are still many aspects of polymer science which are not fully understood and research is ongoing.

2.1.3 Polymer properties

The reason why polymers have been produced in such enormous quantities since their initial development is due to their extremely favourable properties. They are strong, lightweight, malleable, corrosion resistant, durable, and good insulators.[7] Furthermore, polymers are incredible versatile, as well as, being low-cost and easy to manufacture.[13] Polymers are generally separated into three classifications; thermoplastics, elastomers, and thermosets.[1] Thermoplastics are linear or branched polymers with no crosslinks. They become liquid upon heating, which means they can be repeatedly moulded into almost any shape.[14] Techniques such as liquid injection moulding and extrusion are utilised to create an enormous range of thermoplastic products.[15,16] Thermoplastics can either by semi-crystalline or amorphous, which also impacts their material properties.[1] Common examples of thermoplastics include polyethylene, nylon, and polyvinyl chloride.

Elastomers are composed of polymer chains which are crosslinked to one another. The crosslink density is fairly low which means that elastomers have a low Young's modulus and high elasticity. When elastomers are stretched, their chain conformations become extended in the direction of the applied force. However, the crosslinks between chains prevent permanent deformation and upon release of the force, entropy drives the chains to return to their original, more random conformations.[1] Elastomers are generally described as rubbery, and are well above their glass transition temperatures ($T_g's$) at room temperature.[17] The main application for elastomers is in the manufacture of automotive tyres, and common examples include polyisoprene, polybutadiene, and poly(styrene-co-butadiene).[18]

Thermosets are polymers with a very high crosslink density. They are extremely rigid and stiff, with a high degree of chemical and heat resistance.[1] To allow thermosets to be

utilised for specific applications, they are often purchased in a liquid form which is then cured by the user to induce crosslinking and harden the polymer. Curing is generally implemented using heat or some other external stimuli.[19] Thermosets are frequently used as a polymer matrix for composite materials such as carbon fibre reinforced polymers.[20] Typical examples of thermosets include epoxy, polyester, and polyurethane.[21]

2.1.4 Poly(styrene-co-butadiene)

Poly(styrene-co-butadiene) is an elastomeric copolymer composed of styrene and butadiene monomer units. For commercial applications, the polymer units are generally arranged in a random configuration and the styrene-butadiene ratio is approximately 25:75.[22] Poly(styrene-co-butadiene) was first developed for commercial applications in Germany in 1937, where it was named Buna S. This was to counteract the shortage of natural rubber which was expected to occur during the Second World War. During the following decades, major advancements took place regarding the polymerisation of poly(styrene-co-butadiene). This significantly improved its properties which meant that it became the most commonly utilised rubber.[23]

Poly(styrene-co-butadiene) is used for many applications, such as the manufacture of adhesives, shoe products, sealants, and O-rings. However, the primary use for poly(styrene-co-butadiene) is in the manufacture of automotive tyres.[22] On its own, poly(styrene-co-butadiene) does not have the adequate strength and wear resistance to be suitable for a modern day tyre. Therefore, filler materials such as carbon black or silica are utilised to reinforce the tyres. This creates a composite material with significantly increased strength, stiffness, abrasion resistance, and tear strength.[24,25]

2.2 Polymers at surfaces

Understanding the behaviour and properties of polymers in their bulk state is incredibly important to polymer science and has been an area of widespread research. However, studying polymers in their bulk state does not adequately represent the full spectrum of

polymer use and applications. This is because a huge amount of applications rely on polymers functioning at surfaces. Consequently, the interfaces between polymers and different materials, which are not accounted for in the research of bulk polymers, are very important. The behaviour of polymers at an interface is extremely influential in governing the overall bulk properties of a material.[26] Furthermore, it is well established that polymer behaviour at an interface can differ greatly from behaviour in the bulk.[27] For example, studies have demonstrated that the elastic modulus and T_g of polymers can change substantially at an interface.[28,29] However, a comprehensive understanding of polymers at surfaces, including the drivers responsible for these behavioural changes has not being achieved. There is even speculation surrounding the exact characterisation of the interfacial region, such as how far from the surface do polymers need to be for their properties to be governed by bulk parameters, and what external factors does this distance depend on.[26] If a greater understanding of the behaviour of polymers at interfaces was achieved, this would be incredibly beneficial to fundamental polymer science, as well as, many applications.

2.3 Applications of polymers at surfaces

Polymers functioning at surfaces are vital for many applications. These applications are extremely diverse and span across many areas of industry; from structural composites to emerging nanotechnology applications, such as nanoelectronics.

2.3.1 Nanopatterning

Nanopatterning is the process of patterning a surface at the nanoscale. It is often implemented to create ordered patterns of polymeric material on substrates. The most commonly utilised technique to create polymer nanopatterns is photolithography.[30] The process of photolithography involves using a mask to expose certain areas of a polymer film to photoirradiation (see Figure 2.1).[31] The photoirradiation can induce a number of reactions in the polymers such as decomposition, photopolymerisation, and photocrosslinking. Desired areas of the polymer film can also be removed by dissolving

them with solvents. Photolithography can create polymer structures with a pattern resolution of less than 100 nm.[31,32]

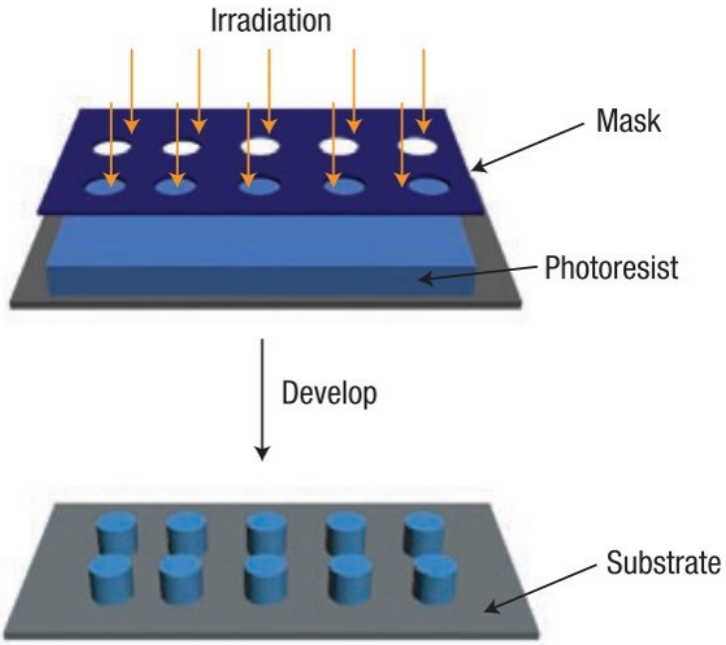

Figure 2.1: Illustration outlining the optical photolithography method which can be utilised to create polymer nanopatterns.[31]

Polymer nanopatterns are utilised for many applications. Nanoelectronics rely on nanopatterning to create high quality electronic components.[33] For example, developing plastic electronics by patterning semiconducting polymers onto substrates.[34] Polymer nanopatterning is also utilised within the medical industry to manufacture scaffolds for tissue engineering.[31,35] These applications rely on understanding how polymers interact with various surfaces at the nanoscale. In nanoelectronics, the stability and wetting properties of the polymer structures are extremely important. Whereas in medical applications, how the polymers interact with human tissue in vivo is vital; not only for the success of the scaffolds, but also for the health of the patient.[31,35]

2.3.2 Biofouling

Biofouling is the accumulation of organisms on surfaces which occurs when the surface is exposed to water or high humidity conditions. It is an extremely prevalent and serious problem which impacts many areas of industry. For example, extensive biofouling occurs on the submerged hulls of ships which increases surface roughness, and therefore leads to increased fuel consumption and a decrease in top speed.[36] Another example of where biofouling is a serious problem is implanted medical devices such as catheters. Accumulations of bacteria commonly occur inside catheter tubes which can cause serious infections for patients.[37]

Polymer coatings are often utilised to reduce biofouling. A small number of synthetic polymers possess the specific properties which prevent the adsorption of organic material to their surfaces. Furthermore, the polymers are also biocompatible and non-toxic. These properties make the polymers suitable for numerous non-biofouling applications.[38] Due to this, there is extensive research in creating polymer films and coatings which can be used to prevent biofouling in various areas of industry. This field of research is directly focused on the interfacial properties of polymers. How polymers interact with organisms to prevent biofouling, but also the interface between the polymers and the substrate surface, such as a ship's hull or catheter tube.[36–38]

2.3.3 Composite materials

A composite material is when two or more materials are combined to create a new material with properties which the original component materials did not possess. Humans have been utilising composite materials since ancient times. For example, mortars for building structures were made from combinations of clay, mud, and straw.[39] However, it is only in more recent years when polymers became a key component in the manufacture of composite materials. Polymer composites generally consist of a polymer matrix combined with filler materials, such as glass fibres or various carbon products. Polymer composites can have extremely favourable properties such as high strength and stiffness, whilst being very lightweight. This makes them suitable for many structural

applications such as high-cost components for aircrafts and vehicles, as well as, more personal items including sporting equipment.[40,41]

The use of carbon filler materials in polymer composites is of particular interest to many industries. This is due to the excellent electrical and mechanical properties of polymer/carbon composites.[42] Examples of polymer/carbon composites which are heavily utilised within industry are carbon fibre reinforced epoxies and carbon black reinforced poly(styrene-co-butadiene).[43] Furthermore, the relatively recent development of carbon 'super' materials, graphene and carbon nanotubes (CNTs), has created the potential for a new class of nanocomposites with even greater properties.[44,45] The polymer/carbon interface is extremely influential in governing the overall properties of the composite material. Therefore, there has been substantial amounts of research which has focused on the interfacial behaviour of polymers at carbon surfaces. Investigations which examine the interactions between polymers and carbon nanomaterials, such as graphene and CNTs are particularly prominent (see Figure 2.2).[46,47] However, this area of research is still relatively new and there are many unanswered questions.

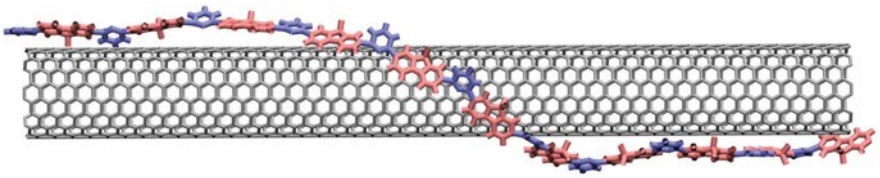

Figure 2.2: Illustration showing the interactions between a single copolymer chain and a carbon nanotube.[46]

2.4 Techniques for investigating polymers at surfaces

There are many techniques which can be utilised to investigate polymers at surfaces. Some examples include ellipsometry, Raman spectroscopy, x-ray and neutron reflectivity, dynamic secondary ion mass spectroscopy, and nuclear reaction analysis.[26,48] However, the following section will focus mainly on imaging and force spectroscopy techniques, which are commonly utilised to investigate polymers at surfaces. Imaging techniques generally examine the morphology and properties of polymer thin films and

nanostructures on substrates.[49] Force spectroscopy techniques investigate the mechanical properties of polymer chains at the nanoscale, or the specific interactions between polymers and different surfaces.[50] These techniques are generally very precise as the length scales and forces involved in the investigations are incredibly small.[26]

2.4.1 Electron microscopy

Scanning electron microscopy (SEM) is an imaging technique which involves scanning a focused electron beam across a sample. The electrons interact with the sample and produce signals which can generate an accurate image at the nanoscale. The first commercial SEM was developed in 1965, although research of electron microscopy techniques began many years earlier.[51] SEM has many advantages as an imaging technique. It can image samples with a high resolution, down to 1 nm in some circumstances. Furthermore, SEM machines are easy to operate and imaging is time efficient.[51] SEM can be utilised to image (coated) polymer structures such as microbeads, interacting with different materials and surfaces.[52]

There are some distinct disadvantages of imaging polymers using SEM. Polymers are generally not electrically conductive, which leads to a build-up of negative charge when imaging. This causes a significant reduction in the image resolution.[53,54] Polymer samples can be coated in thin layers of conductive materials such as gold, which increases conductivity and alleviates this problem. However, conductive coatings can lead to ambiguity in the images, particularly when investigating extremely small polymer nanostructures. Another problem with imaging polymers using SEM is that the electron beam can irreversibly damage the polymer samples.[53] Accurate imaging of polymer nanostructures at surfaces using SEM can be difficult, and there are a number of limitations to consider.

Transmission electron microscopy (TEM) is also an imaging technique which can be utilised to investigate polymer nanostructures and thin films. The experimental setup and procedures are similar to SEM. However, electrons are not scanned across the sample's surface, instead they are transmitted through the sample and collected on a detector which creates an image. Areas in the images appear light or dark depending on the amount of electrons which have been transmitted through the sample in that specific

area. TEM can be utilised to image polymer morphology, but it can also examine the composition of materials, investigate defects, grain boundaries and dislocations, and examine crystal structure.[55] TEM has a greater image resolution and magnification than SEM.[56] Although, there are some distinct disadvantages with the technique when investigating polymers. For example, in order for successful imaging to be carried out, the samples need to be extremely thin so that they are electron transparent. However, creating thin polymer films which are suitable for TEM can be very difficult experimentally. Furthermore, the contrast when imaging is often very low due to polymers generally containing the same light elements, which do not strongly interact with the electron beam. Similarly to SEM, the electron beam irradiation can also damage the polymer samples.[56]

2.4.2 Magnetic tweezers

Magnetic tweezers are a force spectroscopy technique which can be utilised to investigate the mechanical properties of single polymer molecules. Magnetic tweezers operate by fixing one end of a single molecule to a substrate, and the other end to a magnetic particle. A magnetic field is then generated by magnets positioned above the particle. This creates an upward force on the particle, and therefore extends the polymer molecule. Additionally, the magnets can rotate, which causes the molecule to twist under torsional force.[50,57] Figure 2.3 shows the experimental apparatus used for magnetic tweezer experiments. The extension of the molecule is calculated by tracking the position of the magnetic particle, and the force applied can be calculated from the magnitude of the magnetic field. Magnetic tweezers can exert extremely small forces on molecules, down to 0.01 pN.[50]

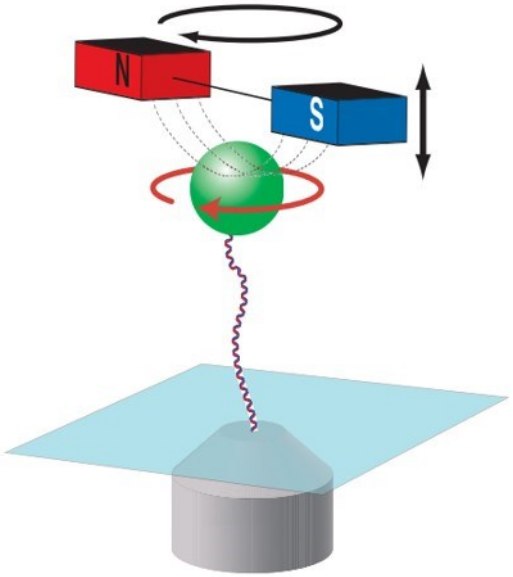

Figure 2.3: Illustration showing the experimental apparatus for magnetic tweezers. A single DNA molecule experiences torsional strain due to the rotation of the magnetic particle.[50]

The most common experiments using magnetic tweezers focus on examining the mechanical properties of single DNA molecules.[58] In the experiments, DNA molecules are extended and twisted which builds up torsional strain. At a critical point of torsional strain, the extension suddenly reduces as the molecule buckles and forms a plectoneme.[59] This research can provide detailed information regarding the supercoiling of DNA, which is useful for understanding DNA interactions and structural transitions.[58] Although magnetic tweezers have a high force sensitivity and the ability to apply torsional strain to molecules, there are some significant drawbacks with the technique. In particular, there is a lack of versatility when using magnetic tweezers, especially when compared to similar techniques. Other than applying a torsional strain to the molecules, there are very few additional investigations which can be performed without the need for complex experimental procedures and apparatus.[50]

2.4.3 Optical tweezers

Optical tweezers are a force spectroscopy technique which can be utilised to investigate the mechanical properties of polymer chains. The experimental setup and procedures

used for optical tweezers are similar to those used for magnetic tweezers. However, there are some distinct differences between the two techniques. Primarily, that optical tweezers create an optical trap by focusing a laser through a microscope objective at a diffraction limited area. The focused beam then attracts any particles in close proximity, which have a higher refractive index than the surrounding medium. The particles become trapped at the beam focus due to a three-dimensional restoring force. External forces which are applied to the particle are measured from the change in position of the particle in the optical trap, or by investigating the deflection of the focused beam. The technique can exert forces ranging from approximately 0.1 pN to 100 pN on trapped particles of various sizes, and can measure the displacement of the particles with a very high degree of accuracy (sub-nm).[50,60] Optical tweezers are generally utilised to investigate the mechanical properties of polymers by attaching a particle at the end of a polymer chain. The other end of the chain is permanently fixed to a substrate in close proximity to the focus beam. The polymer chain is then stretched by moving the substrate using a piezo-driven stage and the resulting force can be measured.[61] An alternative experimental procedure is called the dumbbell assay, which uses two focused beams to trap polymer chains with particles at each end. One of the beams is then moved which causes the chain to stretch.[50,60]

A common area of investigation using optical tweezers is to stretch and measure the force response of DNA and RNA molecules.[60,62,63] The molecules can be stretched in different aqueous mediums which produces force-extension curves. The curves can then be fitted to the WLC model which allows values such as persistence length to be calculated in different environmental conditions.[60,61] Optical tweezers have many advantages, such as being very versatile with an extremely high force resolution. However, there are also some limitations associated with the technique. For example, any dielectric particles which are in close proximity to the focused beam will be trapped. Therefore, many particles can be trapped in the beam simultaneously, which can make it difficult to achieve accurate results regarding the mechanics of single chains. Local heating due to the intensity of the laser beam can also impact results in optical tweezer experiments. For example, heating can affect the properties of the molecules being stretched or can alter the viscosity of the aqueous solutions in close proximity to the beam.[50]

2.4.4 Contact angle goniometry

Contact angle goniometry is a technique which can be utilised to measure the wettability of liquids on substrates. The technique generally involves depositing a sessile liquid droplet onto a substrate and using a high-resolution camera to record the droplet. Drop shape analysis is then carried out on the software which provides a value of the tangent angle of the droplet at the three phase contact point.[64] The experiments are mostly performed using macroscopic droplets, which generally have a size limitation close to 1 mm.[65] The most common investigations of polymers at surfaces using contact angle goniometry involve measuring the wettability of different liquids on polymer films. This can provide information regarding the polymer/liquid interface, and also the hydrophobicity of the polymers.[66] Furthermore, some studies have examined how the wettability of polymer thin films changes when film thickness is reduced down to less than 50 nm.[67] Contact angle goniometry is time efficient, uncomplicated, and can provide meaningful data regarding polymers at surfaces. However, the technique does have some distinct limitations. For example, it cannot obtain quantitative information regarding specific polymer/substrate interactions.

2.4.5 Atomic force microscopy - imaging

Atomic force microscopy (AFM) is an imaging technique which is classified as a form of scanning probe microscopy (SPM). Before the invention of AFM, the first SPM technique was developed in 1981 by Binnig and Rohrer at IBM's research laboratory. The technique was called scanning tunnelling microscopy (STM), and it laid the foundation for future techniques, such as AFM.[68] The process of STM involves bringing a sharp metal tip into extremely close proximity with a sample. A voltage is applied, which creates tunnelling between the tip and the sample. The resulting current intensity in the tip is dependent on the distance between the tip and sample's surface. As the tip scans across the varying topography of the surface, the current is kept constant by altering the voltage applied to the piezo. The changes to the voltage allow for a topographical image to be created at the atomic scale. This was the first technique with the capabilities to image with an atomic resolution.[68,69] STM can also be used to move and position single atoms on a surface, and

was famously utilised by Eigler and Schweizer to create the IBM logo on a nickel surface using xenon atoms (see Figure 2.4).[70] The development of STM was revolutionary to the field of materials science and physics, and was the first technique of its kind. However, there are some significant disadvantages of STM. Most notably that it relies on tunnelling, which means that it can only image conducting or semi-conducting surfaces. Therefore, materials such as non-conducting polymers and biological samples cannot be investigated using STM.[71]

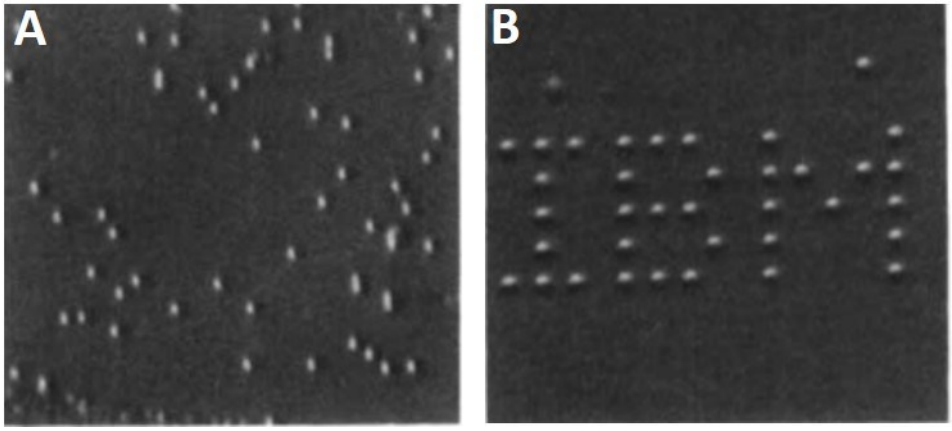

Figure 2.4: STM images of xenon atoms on a nickel surface. (A) Immediately after xenon dosing where the xenon atoms are arranged at random. (B) The xenon atoms are arranged into the IBM logo using STM techniques.[70]

The STM was revolutionary but it had distinct limitations. Therefore, in 1985, the same team at IBM developed the AFM. The major advantage of AFM was that it had the ability to image non-conducting surfaces.[71] AFM does not rely on tunnelling but instead it operates in a similar way to a record player. An extremely sharp tip, which is attached to a cantilever, is scanned across a surface. A feedback loop is utilised to control the height of the piezo tube, and therefore the distance between the tip and the sample. The changes in the piezo height due to surface topography can be used to generate an image of the sample's surface with a resolution in the sub-nm scale. The most common mode of AFM imaging is called tapping mode, where the cantilever oscillates causing the tip to have intermittent contact with the surface.[72] AFM imaging can also be used to generate information regarding the viscoelastic and adhesion properties of a sample's surface.[73] As AFM can image non-conductive materials, it was a revolutionary development in the

research of polymers and biological sciences.[71] Detailed explanations of AFM apparatus and experimental procedure are included in Chapter 3.

AFM is an extremely versatile imaging technique which has an incredibly high resolution and does not damage the sample during operation. Even preliminary results with the first AFM machine presented a lateral and vertical resolution of 3 nm and 0.1 nm, respectively.[71] Since this initial development, the improvements in AFM techniques have been significant. AFM can accurately image macromolecules, such as single polymer chains and DNA molecules, in air and liquid.[74,75] Furthermore, in 2009, Gross et al.[76] used a modified AFM system, with a tip which was terminated by a carbon monoxide molecule, to image the chemical structure of a single pentacene molecule (see Figure 2.5). In the images, the five benzene rings which make up the molecule were clearly observed. In more recent years, a combination of AFM and STM was utilised by Pavliček et al.[77] to synthesise and image a triangulene molecule (see Figure 2.6). Triangulene was first hypothesised 1953, but it had never been successfully synthesised due its extreme reactivity. This pioneering experiment by Pavliček et al. allowed a previously elusive molecule to be synthesised and characterised using AFM/STM.[77]

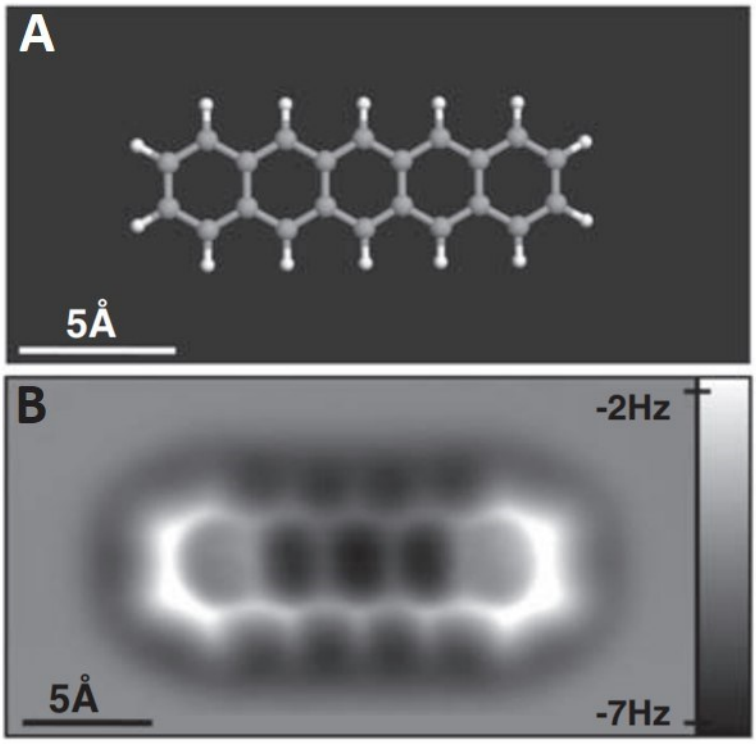

Figure 2.5: (A) Model of a single pentacene molecule. (B) AFM image of a single pentacene molecule on a copper substrate.[76]

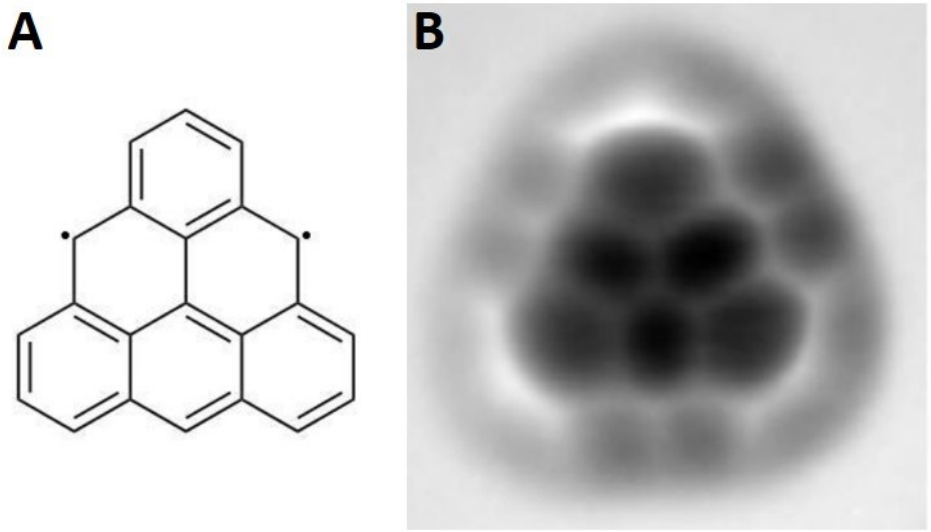

Figure 2.6: (A) Schematic of a triangulene molecule. (B) AFM image of a triangulene molecule on a copper substrate.[77]

Since its relatively recent development, AFM imaging has been extensively utilised within the field of multidisciplinary materials science. Investigations which study the behaviour of synthetic polymers at surfaces are particularly common. These experiments examine many aspects of polymer behaviour, including thin film formation, dewetting, and single chain conformations.[49,75] AFM is an extremely useful technique for imaging a wide variety of polymer nanostructures on surfaces. However, it still has some drawbacks and limitations. For example, the z-range of the piezo movement is very small, so only samples with a very low surface roughness can be accurately imaged. Convolution errors are also inevitable when imaging, which cause the lateral size of features to appear larger than in reality. This is due to the finite size of the AFM tip, and means that deconvolution methods must be implemented.[78] Furthermore, AFM can be very time consuming as the scan rate is generally low, and extensive user experience is required to achieve consistent results.

2.4.6 Atomic force microscopy - force spectroscopy

In addition to imaging surfaces, AFM can also be used in a mode of operation known as force spectroscopy. Force spectroscopy is utilised to provide quantitative information regarding the strength of interactions between different materials at the nanoscale. Furthermore, it can also be used to investigate the mechanical properties of different materials. The general process of AFM force spectroscopy involves using a sharp tip to come into contact, and then retract from a sample's surface. When the tip retracts, it experiences an adhesive force which causes the cantilever to deflect. This deflection can be converted into a value of adhesive force experienced between the tip and the sample. AFM force spectroscopy is extremely sensitive with a force resolution of approximately 10 pN. This allows the technique to investigate a large range of intermolecular interactions from stronger covalent bonds, down to much weaker van der Waals forces.[50] Chapter 3 includes a comprehensive review of the apparatus and experimental procedures used for AFM force spectroscopy investigations.

The first AFM force spectroscopy experiments were carried out only a few years after the initial development of AFM as an imaging technique. In 1989, Burnham et al.[79] and Weisenhorn et al.[80] utilised AFM force spectroscopy to produce force-distance curves

which investigated the interactions between AFM tips and different substrates. In the following years, force spectroscopy experiments became more advanced and single-molecule force spectroscopy (SMFS) was developed. SMFS investigates the behaviour and forces associated with single molecules. It can provide information regarding the specific intermolecular and surface forces which govern polymer behaviour at an interface.[81] SMFS experiments often involve covalently bonding a polymer chain to the surface of an AFM tip, and measuring the interactions between the single polymer chains and various substrates (see Figure 2.7).[82] However, there are a number of alternative experimental procedures which are also utilised. The development of SMFS has provided a huge amount of information regarding the interfacial behaviour of polymers at various surfaces.

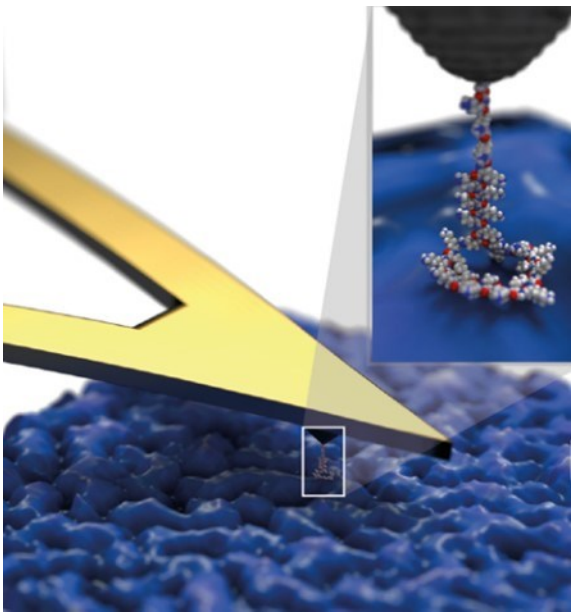

Figure 2.7: Illustration of a single polymer molecule, which is covalently bonded to an AFM tip, interacting with a thin polyelectrolyte film.[82]

There are many AFM force spectroscopy experiments which have investigated the behaviour of polymers at surfaces. This research often focuses on measuring the desorption forces of polymer chains on various substrates.[81] Furthermore, individual chains can be stretched, which provides information regarding the elasticity and force

response of single polymer molecules.[83,84] Certain experiments alter parameters such as solvent conditions, polymer architecture, and the functionalisation of polymers to observe how this impacts desorption forces and chain stretching.[85–87] AFM force spectroscopy is an incredibly useful technique for investigating the forces associated with polymers at surfaces, as it is extremely versatile with a large force range. However, experimental procedures can often be complex, particularly in SMFS experiments. Furthermore, experiments can be very time consuming due to having a low probability of observing meaningful data regarding specific interactions.

2.5 AFM investigations of polymers at surfaces

The following section details some of the main research areas of polymers at surfaces using both AFM imaging and force spectroscopy.

2.5.1 AFM imaging

2.5.1.1 Thin film formation and dewetting

Polymer thin films are a key component in many applications such as anti-fouling coatings, thin film transistors, solar cells, and microelectronic devices.[88–90] However, thin film formation and dewetting has proven to be very complex. Many studies have demonstrated that the behaviour of polymer thin films differs greatly from behaviour in the bulk. Therefore, investigating and characterising the behaviour of polymer thin films is essential for the successful development of many applications. Consequently, there has been widespread research within this area using AFM imaging.[91]

The process of creating a polymer thin film generally involves depositing a small amount of polymer solution onto a substrate. A coating technique is then utilised to create an extremely thin, homogenous film of polymeric material on the substrate's surface. These techniques commonly include spin coating, dip coating, spray coating, and drop casting.[90] The thickness of polymer films created using these techniques are generally less than 100 nm. After initial formation, the polymer film can either remain stable and completely

wet the substrate, or it can become unstable and experience dewetting. The spreading coefficient (S) can be utilised to indicate whether a polymer film will dewet a substrate or remain stable. The spreading coefficient is governed by the imbalance of interfacial tensions in the three phase system and is defined by the following equation:[92]

$$S = \gamma_{SG} - \gamma_{SL} - \gamma_{LG} \tag{2.1}$$

Where γ_{SG}, γ_{SL}, and γ_{LG} represent the interfacial tensions of the solid-gas, solid-liquid, and liquid-gas phases. If $S > 0$ then the polymer film will completely wet the surface, whereas if $S < 0$ only partial wetting occurs.[93] Similarly, the Hamaker constant of the three phase system can also be calculated to indicate whether the polymer films will be stable or unstable at a substrate. The Hamaker constant represents the magnitude of van der Waals forces acting across a system and can be expressed using the following mixing rule:[94]

$$A_{Substrate/Film/Air} = A_{Film/Film} - \sqrt{A_{Film/Film}A_{Substrate/Substrate}} \tag{2.2}$$

Where $A_{i/j}$ is the Hamaker constant of the materials *i* and *j* interacting across a vacuum. When $A > 0$, the polymer film should be unstable and when $A < 0$, the film should be stable.[94] The spreading coefficient and Hamaker constant provide a good indication as to whether a polymer film will wet or partially wet a substrate's surface. In reality, many polymer thin films are not stable and they experience dewetting when they are forced to cover a substrate. Dewetting is the formation of holes in the thin films which can be caused by various factors, such as nucleation due to impurities or spinodal decomposition. The dewetted holes can grow and change their morphology over time.[95–97] A great deal of research has been carried out which investigates the dewetting behaviour of holes in polymer thin films.

The dewetting of polystyrene thin films has been extensively examined within the literature.[49,91,98,99] Polystyrene has a T_g which is far greater than ambient room temperatures. This means that polystyrene thin films are glassy at room temperature, and capillary forces are not always strong enough to drive dewetting, even on non-

wettable substrates. However, if annealing is performed to temperatures marginally greater than the T_g, the polymer becomes visco-elastic, and significant amounts of dewetting are experienced in the films. Reiter et al.[49,91,100] thoroughly examined the dewetting of polystyrene thin films on highly non-wettable polydimethylsiloxane-coated substrates. They demonstrated that after a short duration of annealing, many cylindrical holes formed in the film. At this stage of dewetting, the polymeric material from the dewetted holes was uniformly distributed across the whole film. Therefore, the overall film thickness between the holes increased. As annealing time was increased, the rate of hole growth decreased and frictional forces at the substrate-film interface caused the formation of asymmetrical raised rims around the circumference of the holes. The rims had a steep inside edge and a curved outside edge which could be fitted to an exponential decay (see Figure 2.8).[49,91] There was a linear relationship between the height of the raised rims and the diameter of the dewetted holes. This trend, alongside the asymmetric shape of the rims, strongly suggested that the films were being plastically deformed, and that viscous flow was not responsible for the dewetting behaviour. Reiter et al. also observed that molecular weight did not seem to significantly impact the dewetting behaviour of the films. This suggested that the viscosity of the polymer film did not influence the rate of hole growth. This series of investigations was pioneering in understanding the dewetting behaviour of confined polymer thin films.[49,91,100]

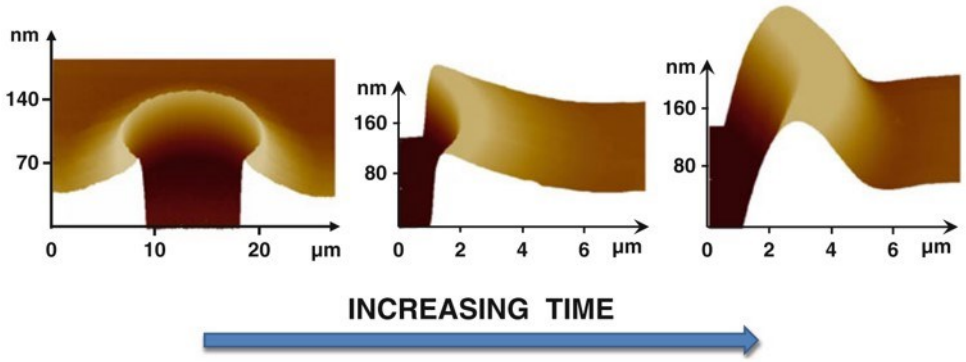

Figure 2.8: AFM images showing the evolution of a dewetted hole with increasing annealing time for a polystyrene thin film on a non-wettable polydimethylsiloxane-coated silicon substrate.[91]

Many studies have also focused on how different aspects, such as the type of solvent and substrate topography, can influence dewetting behaviour. Akhrass et al.[95] carried out experiments which examined the dewetting of polystyrene thin films on a nanopatterned substrate after annealing (see Figure 2.9). Many studies of dewetting use completely flat and defect free substrates. However, this is not always realistic for applications. Furthermore, the dewetting of thin films on patterned substrates could create ordered polymer nanopatterns which would be useful for many applications.[33] The results of Akhrass et al. study demonstrated that the dewetted morphology on the patterned surface was highly dependent on film thickness, and therefore could be controlled by altering experimental parameters. It was observed that the dewetted films formed either cylindrical holes, spherical cap nanodroplets, or toroids depending on film thickness. It was presented that the width of the rim around the circumference of the dewetted holes was crucial in determining this dewetting behaviour.

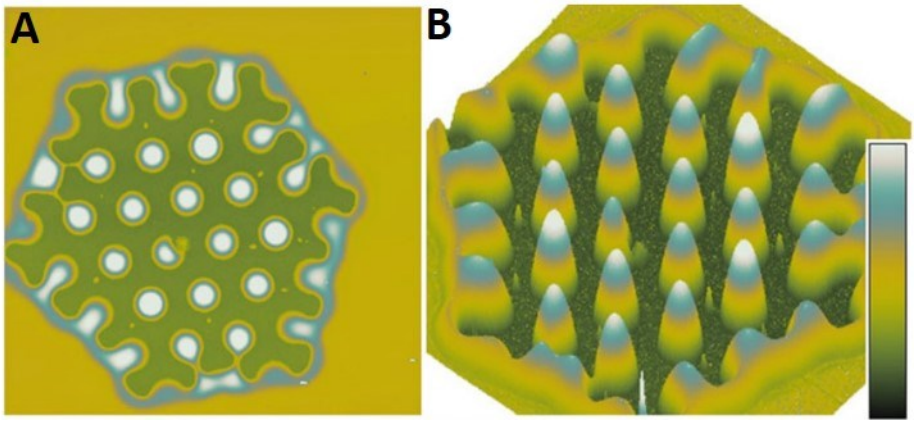

Figure 2.9: AFM images of the dewetted structures in a polystyrene thin film on a patterned substrate after annealing. (A) 2D AFM height image, (B) 3D AFM height image.[95]

Spangler et al.[101] demonstrated that the morphology of spin coated polystyrene thin films was influenced by the type of solvent used in the film preparation. In toluene (very good solvent conditions), the polymer formed thin films which had fairly smooth and flat surfaces. However, for ethyl acetate (fair solvent conditions), the polymer films were much rougher and had a less uniform morphology. This demonstrated how the specific conformations of polymer chains due to variations in solvent quality could influence thin film formation.[101] Reiter et al.[102] expanded on this work and demonstrated that residual

stresses within polystyrene thin films could impact dewetting behaviour. The residual stresses were created during film preparation by the rapid evaporation of dilute polymer solutions on the substrate surface after spin coating. This created individual chains which had 'frozen-in' non-equilibrium conformations on the substrate. The study demonstrated that polystyrene thin films, which were aged for approximately one year at room temperature before annealing, exhibited different dewetting behaviour to films which were annealed immediately after spin coating. The films which had been aged for approximately one year formed significantly fewer dewetted holes upon annealing. Furthermore, the raised rims at the circumference of the dewetted holes were considerably smaller compared to the samples which had experienced no ageing at room temperature. This demonstrated that ageing the samples, even in a glassy state, allowed the chains to form conformations which were closer to their equilibrium structures. Therefore, this reduced the residual stresses in the films which influenced the dewetting behaviour.[102] Many studies have demonstrated that thin film behaviour is very different to behaviour in the bulk. However, it is not fully understood how interface and confinement effects influence the wide array of observed dewetting behaviours in polymer thin films. Therefore, research in this field remains a popular area of investigation.

2.5.1.2 Single chain conformations

Studying the behaviour of single polymer chains at surfaces using AFM is vital for fundamental polymer science. This is because individual polymer chains have no influence from the bulk, and therefore interfacial and confinement effects can be thoroughly investgated.[103] Furthermore, the conformations and structures of polymer chains with varying molecular weights and architectures can be directly observed and characterised.[104–106] There are also many applications where understanding and controlling the behaviour of single polymer chains is vital. Examples of these include nanoelectronics, biotechnological applications, and photovoltaics. In biology, there are many highly complex macromolecules which function as nanomachines. However, this level of technology has not yet been achieved using synthetic polymers. Consequently,

there is extensive ongoing research which is focused on utilising synthetic macromolecules as nanodevices.[104]

Studying single polymer chains using AFM can be complex experimentally. This is because it can be difficult to isolate single chains on a substrate as they generally have a tendency to create aggregates. Experiments are often carried out which use polymers with very high molecular weights or bulky architectures. This makes the single chains easier to identify and image on the substrate surface. Spin coating using very dilute solutions can be utilised to adsorb single chains on surfaces.[105] However, there are a number of disadvantages associated with this preparation technique. For example, spin coating often creates very sparse arrangements of chains on a surface, and subsequently it can be very time consuming to locate single chains using AFM. Furthermore, if there are very few chains on the surface, it limits the potential for detailed statistical analysis.[105] Therefore, many investigations use Langmuir-Blodgett (LB) troughs to spread a very dilute polymer solution on the surface of water, and then transfer the solution to the desired substrate. This method allows for more control of the distribution of single polymer chains on the substrate's surface.[75]

Numerous studies have examined the conformations of single diblock copolymers on surfaces, in particular high molecular weight polystyrene-*block*-poly(methyl methacrylate) on mica.[107,108] Polystyrene is a hydrophobic polymer, and therefore in the presence of water, it collapses to form a globule. Poly(methyl methacrylate) is more hydrophilic and it spreads as a monolayer in the presence of water. In the studies, the polymer was prepared using the LB trough method and exposed to high humidity conditions where a water layer formed on the hydrophilic mica surface. AFM imaging revealed that on the mica surface, the poly(methyl methacrylate) block adsorbed in a monolayer conformation (nanoribbons) with a thickness of 0.2 - 0.5 nm. Whereas, the polystyrene block formed globules on top of the poly(methyl methacrylate) monolayer with lengths and heights of approximately 11 - 15 nm and 2.5 nm, respectively (see Figure 2.10). This research observed and analysed the distinct morphology of single block copolymer chains on surfaces in high humidity conditions, where each block had a different hydrophobicity.[107,108]

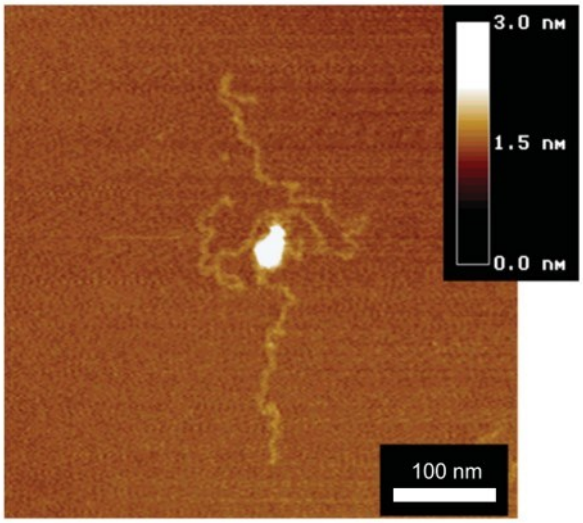

Figure 2.10: AFM height image showing polystyrene-*block*-poly(methyl methacrylate) on a mica surface after exposure to high humidity conditions for 27 hours. The poly(methyl methacrylate) blocks are more hydrophilic and form monolayer structures on the mica. The hydrophobic polystyrene blocks form globular particles on top of the poly(methyl methacrylate) monolayer.[108]

Studies have also examined the behaviour of single homopolymer chains on surfaces. Roiter and Minko[109] demonstrated that the conformations of single poly(2-vinylpyridine) protonated cationic polyelectrolyte chains on a mica surface varied significantly when pH was increased. AFM imaging was carried out in aqueous mediums with different pH values. It was demonstrated that at a pH of 3.89, the polymers had a more extended conformation on the mica surface with larger radii of gyration and end-to-end distances. Furthermore, there was a much lower fraction of loop conformations in the adsorbed chains. When pH was increased to 4.24, the polymers formed much more globular conformations with smaller radii of gyration and end-to-end distances, whilst the fraction of loops in the chains dramatically increased. This change in polymer conformation was due to the decreasing degree of ionisation in the chains with increasing pH of the aqueous medium.[109] Investigations into the movements of homopolymer chains on surfaces have also been carried out. Kumaki et al.[103] demonstrated that isotactic poly(methyl methacrylate) chains move across a mica substrate in high humidity conditions. Chains which were not permanently fixed to the mica, moved along their own lengths across the surface in a monolayer conformation. The degree of movement in the chains increased with increasing humidity due to the presence of a more established condensed water layer on the mica, which allowed the

chains to adsorb and desorb from the substrate. At lower humidity conditions, the water layer was less established and the chain movements were more subtle.[103,108] These investigations demonstrated the complex conformational behaviour of adsorbed homopolymer chains under different environmental conditions.

Many investigations characterise the behaviour and morphology of single polymer molecules with varying architectures. For example, a study by Schappacher and Deffieux analysed the morphology of polymers with complex figure-of-eight and trefoil knot architectures.[105] By grafting many well-defined oligomers on the backbone of the polymers with complex architectures, it effectively increased the size of the polymer chains and made them much easier to identify using AFM imaging. This process was described as a form of magnification and allowed the conformation, morphology, and architecture of the complex polymer structures to be directly investigated. A study by Zhang et al.[106] examined the morphology of dendronised polymers with varying architectures. This work attempted to create well-controlled, extremely large molecules similar to those found in biology, such as the tobacco mosaic virus (TMV). First-generation (PG1) to fifth-generation (PG5) dendronised polymers were synthesised and imaged using AFM. The PG5 polymers were the largest well-controlled covalent macromolecules to ever be synthesised with an estimated molecular weight of 200,000 kg/mol. AFM imaging was carried out which investigated the morphology of each polymer type on a mica surface. The height of the adsorbed PG1 polymer was approximately 0.4 nm, which is characteristic of the height of a single chain fully adsorbed to a surface. Whereas the height of the adsorbed PG5 polymer was approximately 6.2 nm, which demonstrated that the larger molecule did not flatten out and adsorb as strongly to the mica. This research characterised the morphology of extremely large single polymer molecules and could compare this morphology directly to that of the TMV using AFM imaging.[106] Figure 2.11 shows AFM images of single polymer molecules with different architectures from various studies within the literature.

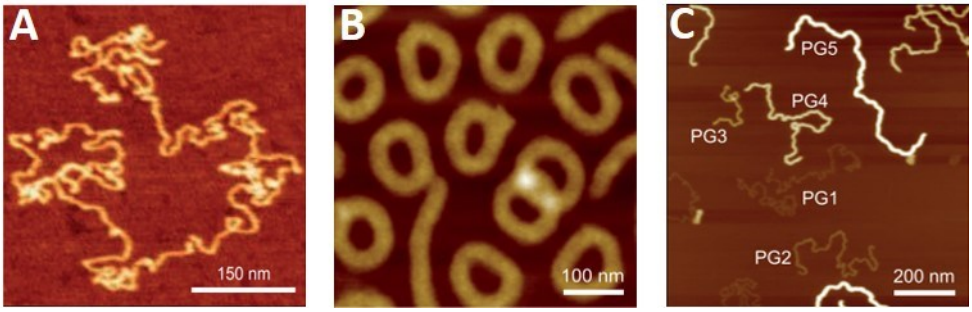

Figure 2.11: AFM images of single polymer molecules with various architectures. (A) Linear polyelectrolytes. (B) Graft copolymer chains with some figure-of-eight conformations. (C) Dendronised polymer chains where the PG1 - PG5 labels represent the number of generations of side dendrons on each chain.[104]

2.5.1.3 Ordered polymer nanostructures

Creating ordered polymer nanostructures can be extremely useful in nanopatterning applications, such as nanoelectronics and tissue engineering.[31,33] As previously mentioned, the most common preparation methods utilised to create ordered polymer nanostructures are lithography techniques.[30] However, there have also been many investigations which focus on creating ordered polymer nanostructures using different techniques such as spin coating, and characterising the nanostructure morphology using AFM.[110] This research is particularly interesting as the specific polymer/substrate interactions are utilised to create the ordering within the system. This research has provided an alternative means for creating ordered polymer nanostructures using relatively simple and low-cost preparation techniques.

Many investigations have focused on creating ordered polymer nanostructures on graphite substrates using crystalline polymers, such as polyethylene. The first study to investigate this system was in 1970, where Tuinstra and Baer observed the epitaxial growth of polyethylene on graphite, which created ordered polymer structures with orientations at 60° intervals.[111] This research took place before the development of AFM, therefore the polymer structures were observed on micrographs and the characterisation was limited. However, this provided the initial observations which would be a basis for future AFM investigations. The epitaxial ordering of polyethylene on graphite occurs due to the very similar size of the a-axis of the graphite until cell (2.46 Å) and the c-axis of the polyethylene crystal cell (2.55 Å). Therefore, epitaxial nucleation

occurs on the graphite surface which creates an ordered polymer morphology.[112,113] AFM investigations of polyethylene on graphite have demonstrated this epitaxial ordering in much greater detail and provided further analysis of the system. For example, studies by Tracz et al.[114] and Prokhorov et al.[112] demonstrated that polyethylene could form ordered rectangular structures (see Figure 2.12) arranged at 60° on a graphite substrate. It was stated that these rectangular structures are probably the centres of epitaxial nucleation.

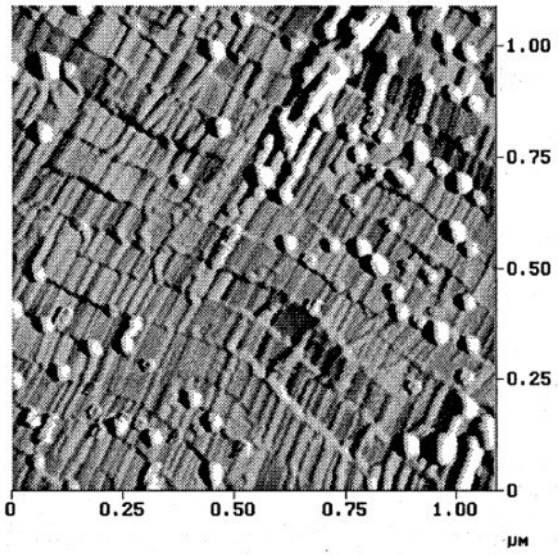

Figure 2.12: AFM image of polyethylene crystallised on graphite. The image clearly shows the formation of ordered rectangular polymer nanostructures.[114]

Distinct ordering of amorphous polymers with alkyl side chains has also been observed on graphite substrates. In these instances, ordered nanopatterns are formed due to the distance of the 1,3 methylene group (2.51 Å) in trans alkyl chains being very similar to the a-axis of the graphite until cell.[115,116] An investigation by Prokhorova et al.[117] examined the ordering of polystyrene with bulky dendronised side groups on a graphite substrate. The polymer formed a monolayer conformation on the graphite with distinct ordering (see Figure 2.13). It was demonstrated that if the density of branching was very high in the polymer molecules, steric hindrance between the alkyl side chains was increased and the degree of ordering was reduced. For molecules with lower branching densities, a higher degree of ordering was observed.[117] A small number of studies have also investigated the specific ordering of amorphous linear polymers on graphite using

AFM. Although, this area of research is still relatively unexplored and could prove to be extremely useful for nanopatterning applications. Chen et al.[110] observed that specific ordering occurred in poly(4-vinylpyridine) on graphite substrates. The poly(4-vinylpyridine) strongly adsorbed to the graphite and created films with varying degrees of dewetting. When the film had a monolayer thickness, highly ordered anisotropic nanotrenches formed on the surface. As film thickness increased, the degree of ordering decreased. At a film thickness of 4.0 nm, the dewetted structures were isotropic and no specific ordering was observed. Chen et al. cited this ordering to the pyridine group distribution in the polymer matching the lattice of the graphite, and the potential for nucleation along mosaic block boundaries.[110]

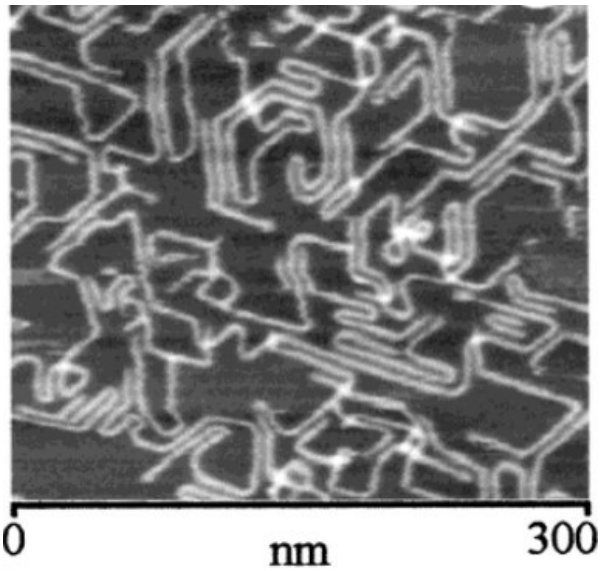

Figure 2.13: AFM image showing the distinct ordering of polystyrene with bulky dendronised side chains on a graphite substrate.[117]

Investigations which focus on creating ordered polymer nanopatterns using relatively simple preparation techniques, such as spin coating, could become very important in nanopatterning applications. However, there are still many polymers which have not yet been investigated, and therefore there is a huge potential for future work.

2.5.1.4 Polymer nanodroplets and nanoislands

The formation of polymer nanodroplets is generally observed when polymer chains are deposited onto a weakly adsorbing substrate, and self-assemble to reduce interfacial contact. The morphology of polymer nanodroplets can often be characterised by a distinct spherical cap shape. However, on more strongly adsorbing substrates, polymers tend to form less uniform aggregates with more asymmetrical shapes and lower height values. These aggregates are known as polymer nanoislands.[118] Investigating polymer nanodroplets and nanoislands has the potential to be useful for many applications such as nanopatterning, adhesion, and drug delivery.[28] There are many aspects of nanodroplet/nanoisland formation and morphology which have been investigated within the literature using AFM techniques.

Many studies have investigated the wetting and spreading behaviour of polymer nanodroplets on different substrates using AFM imaging. An investigation by Lau et al.[119] demonstrated that the wetting behaviour of latex nanodroplets on silicon was not only governed by surface tension and line tension (as is the case with a liquid drop), but also the elastic modulus of the droplets. This work was developed upon by Evangelopoulos et al.[28] who demonstrated that as the volume of polybutadiene nanodroplets on mica decreased below a critical value, the elastic modulus of the droplets exponentially increased due to surface and confinement effects. This increase in elastic modulus led to increased dewetting of the polymer nanodroplets. Many investigations have focused on examining the impact that line tension has on the dewetting of polymer nanodroplets on various surfaces. When examining the wetting behaviour of macroscopic droplets on flat substrates, Young's equation can be used to provide a value of the droplet contact angle (θ_Y):[120]

$$\cos\theta_Y = \frac{\gamma_{SG} - \gamma_{SL}}{\gamma_{LG}} \tag{2.3}$$

However, for nanodroplets, line tension and surface curvature can significantly influence dewetting behaviour and the contact angles of the nanodroplets can be very different from the values predicted by Young's equation. Therefore, the modified Young's equation

was developed to provide an accurate value of nanodroplet contact angle by taking into account line tension and droplet size:[120]

$$\cos\theta = \cos\theta_Y - \frac{\tau}{\gamma_{LG} r} \tag{2.4}$$

Where τ is the line tension value for the system, and r is the contact radius of the nanodroplet. Line tension is defined as the excess free energy per unit length at a contact line where three phases exist. It is similar to surface tension as it changes the shape of the nanodroplet in order to minimise free energy in the system. For a positive line tension value, the length of the contact line will decrease which increases the contact angle of the droplet, and therefore minimises free energy.[121] The influence from line tension can lead to a distinct drop size dependence on the contact angle of the nanodroplets which is not accounted for in Young's original equation. Although line tension is a defined thermodynamic quantity, there are many conflicting reports on its magnitude and whether it has a significant influence on the dewetting behaviour of polymer nanodroplets.[122] For example, Seeman et al.[92] investigated the wetting behaviour of polystyrene nanodroplets on a silicon oxide surface. They calculated that the value of line tension was negative for the polystyrene nanodroplets at approximately -10^{-11} N. In comparison, Milchev et al.[123] simulation experiments regarding polymer nanodroplets on a weakly adsorbing surface suggested that a positive line tension value caused an increase in the contact angle of polymer nanodroplets as their radius decreased. Currently, the calculated values of line tension range in many orders of magnitude (approximately $10^{-11} - 10^{-4}$ N) with both positive and negative values.[124] It is likely that a greater understanding of this phenomenon will be achieved using a combination of AFM experiments and simulations.

The formation and morphology of asymmetrical nanoislands has also been the focus of many investigations within the literature. For example, Glynos et al.[118] examined the morphology of polybutadiene star-like polymers when the number of arms per molecule was increased from 18 to 59. AFM imaging revealed that polymer nanoislands mostly formed on the mica surface, but the morphology varied depending on the functionality of the polymer molecules. The polymers with 18 arms formed much flatter nanoislands, whereas the polymers with 59 arms formed a shape more similar to a soft colloid. This

result was explained due to an increased intermolecular crowding effect which was experienced by the polymer with high functionality. Subsequently, there was a decrease in the degree of adsorption of the polymer. Glynos et al.[125] also investigated the formation of amphiphilic poly(isoprene-b-ethylene oxide) block copolymer micelles on a mica surface over time. Initially after deposition, the polymer formed asymmetrical nanoislands on the mica. However, over time the mica surface became less hydrophilic which reduced the amount of water on its surface. Consequently, the polymer nanoislands changed their morphology due to the variations in surface hydrophilicity. Nanoislands which were initially large, formed spherical cap shapes with larger height values (see Figure 2.14). Whereas, the smaller nanoislands became flatter and more asymmetrical. Regardless of the size of the nanoislands, the polymer always formed a surface micelle structure due to the hydrophilic nature of the poly(ethylene oxide) block, and the flexibility of the hydrophobic polyisoprene block.[125]

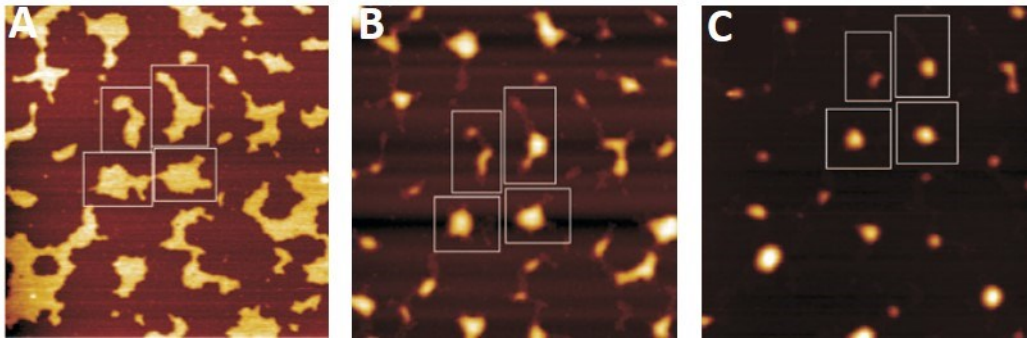

Figure 2.14: AFM images showing the evolution of poly(isoprene-b-ethylene oxide) nanoislands on a mica surface over time. (A) 89 minutes, (B) 745 minutes, (C) 2740 minutes.[125]

There have been extensive AFM investigations focused on the formation and behaviour of polymer nanodroplets and nanoislands, on various surfaces. However, research in this area often produces conflicting results, and much of the interfacial behaviour of polymer nanodroplets and nanoislands is still not fully understood. For example, line tension does not influence macroscopic polymer behaviour. However, it may play a significant role in influencing polymer behaviour at the nanoscale but the magnitude of this effect is currently unknown. Consequently, there are still many potential avenues for future work

within this area which could be useful to numerous applications such as nanopatterning, adhesion, and drug delivery.[28]

2.5.2 AFM force spectroscopy

2.5.2.1 Investigating polymer/substrate interactions

Intermolecular and surface forces generally govern the behaviour of polymers at surfaces. Understanding and characterising these forces is extremely beneficial for many applications, and also to fundamental polymer science.[50,126] Therefore, AFM force spectroscopy has been extensively utilised in order to investigate the specific interactions between polymers and different substrates. This often involves pulling adsorbed polymer chains from a substrate's surface and measuring the magnitude of the desorption forces. Although, these experiments are conceptually simple, it can be fairly difficult to achieve reliable results due to the experiments taking place on such an incredibly small length scale. Therefore, there are a number of different experimental procedures which are utilised to investigation specific polymers/substrate interactions. Some studies rely on physically adsorbing polymer chains to AFM tips or substrates. Whilst this method is generally simple and time efficient, ambiguity can arise in the results due to desorption from both the AFM tip and substrate.[127] Another common experimental procedure is to covalently attach polymer chains to the surface of AFM tips. This method ensures desorption is only observed from the substrate's surface, which increases the accuracy of the results. However, the tip preparation procedure can be time consuming and experimentally complex.[81,82,127] There appears to be a number of obvious advantages and disadvantages for many of the experimental procedures used to investigate polymer/substrate interactions with AFM force spectroscopy.

The interactions between numerous linear polymers and substrates have been investigated using AFM force spectroscopy. For example, a number of investigations have focused on measuring the interactions between poly(ethylene oxide) and various substrates in aqueous mediums.[127–129] The first experiment of this nature was carried out by Braithwaite et al.[128] in 1996. In the experiment, a glass particle was adhered to a tipless cantilever and used to interact with a glass substrate in a poly(ethylene oxide)

solution. It was demonstrated that when the glass substrate was incubated in the polymer solution for 30 mins, attractive polymer/substrate interactions were measured due to bridging effects when the tip was in close proximity to the surface (~50 nm). It was also demonstrated that the polymer interactions were more significant when the approach speed of the tip was reduced. In 2017, Zhang et al.[127] examined the desorption forces of poly(ethylene oxide) on a hydroxyl-group modified quartz substrate. The experiments were carried using two different experimental procedures, and the resulting desorption forces were directly compared. In the first experiment, polymer chains were chemically adsorbed to the surface of an AFM tip, whilst in the second, the chains were physically adsorbed to the substrate's surface. Histograms showing the distribution of desorption forces for each experimental procedure were presented (see Figure 2.15). The histogram for the experiments where the chains were chemically adsorbed to the AFM tip showed a symmetrical distribution with a distinct peak at 1092 pN. Whereas, the histogram for the experiments where the chains where physically adsorbed to the substrate was more asymmetrical with a long tail. Furthermore, the peak force was lower, with a value of 695 pN. It was suggested that this difference in peak desorption force was related to the geometry of the AFM tip. When the chains were chemically adsorbed to the tip, they interacted with a flat substrate which allowed for a higher degree of adsorption with a lot of anchor points. However, when the tip interacted with the chains on the substrate, there were less anchor points on the AFM tip which led to lower desorption forces. Furthermore, desorption from the AFM tip may have influenced the adhesion results. Despite the difference in the results, the desorption forces for both experimental procedures were still relatively large due to the interactions between the polymer chains and the hydroxyl groups which took place in each experiment.

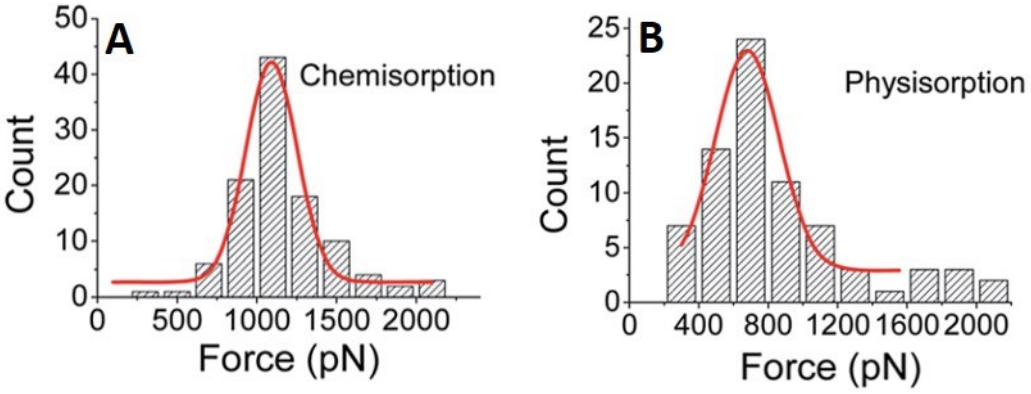

Figure 2.15: Histograms showing the distributions of desorption forces for poly(ethylene oxide) on a hydroxyl-group modified quartz substrate. (A) Polymer chains were chemically adsorbed to the surface of the AFM tips. (B) Polymers were physically adsorbed to the substrate surface.[127]

Many experiments have also investigated the interactions between various other polymers and surfaces. For example, Balzer et al.[82] investigated the desorption forces of polystyrene, poly(allylamine), and poly-L-lysine hydrobromide from a polyelectrolyte thin film on a silicon substrate. Each polymer was covalently bonded to the AFM tip and polyelectrolyte films were prepared with varying thicknesses. The results demonstrated that when the thickness of the films was very low, the peak adhesive force was largest. This was because the adhesion of the polymers was governed by the surface potential of the silicon substrate. When the films had larger thicknesses, the peak adhesive force was lower as the adhesion properties of the polymers began to become more influenced by polymer/polymer interactions. Hugel et al.[83] investigated the desorption forces of polyvinylamine on a silicon oxide substrate in aqueous solutions. The desorption force was analysed under different salt concentrations and polymer charge densities. It was demonstrated that as the charge density of the polymer was increased, the peak desorption force increased. Furthermore, when charge density remained constant and salt concentration was increased, then so did the peak desorption force. Some studies have also investigated the pulling angle dependence on the desorption force of polymers at substrates. If polymers are immobile on a surface, then it has been demonstrated that an increased pulling angle of the polymer chains by the AFM tip can lead to smaller desorption forces.[130,131]

A study by Kienle et al.[86] investigated the desorption forces of polymer chains with various architectures from a hydrophobic, hydrogenated diamond substrate in water. The main experiment compared the desorption forces and force-separation graphs of linear polyisoprene, and polyisoprene with polystyrene side chains of different molecular weights. Histograms demonstrated that the peak desorption force was similar for each experiment, but the distributions were widest for the experiments using the graft copolymer. This was due to the variations in desorption forces for the styrene and isoprene segments, as well as, the higher probability of the simultaneous desorption of many segments for the graft copolymer. It was also observed that when the polystyrene side chains had the largest molecular weight, the resulting force-separation graphs had the highest probability of exhibiting chain stretching. This was due to the decreased mobility of the graft copolymer with longer side chains on the substrate's surface.[86]

AFM force spectroscopy experiments have been carried out which investigate polymer/substrate interactions for many systems. This has included investigating how desorption forces vary for polymers with different properties and architectures. However, there are still many systems where specific polymer/substrate interactions have not been investigated, despite their widespread use within industry for many applications. Consequently, there is still a large potential for future work within this area.

2.5.2.2 Pull-out/peel experiments

AFM force spectroscopy can also be utilised to investigate the interfacial energy between CNTs and different polymers. These experiments involve attaching a nanotube to the end of an AFM tip, and generally performing pull-out or peel tests on various polymers.[132–135] This is an important area of research as nanocomposites such as CNT/polymer materials have a huge potential to be utilised for many applications, and therefore it is vital to carry out extensive characterisation of their interfacial properties. It can be experimentally difficult to attach a single nanotube to the end of an AFM tip, and therefore the process is often carried out inside an SEM. This allows for the AFM tip and nanotubes to be directly observed in high-resolution (see Figure 2.16). There are a number of specific techniques which are utilised to attach nanotubes to AFM tips. For example, a nano-manipulator can be used to pick up nanotubes dispersed on carbon tape with an AFM tip.

The nanotubes can then be attached to the tip using amorphous carbon deposition.[134] Some other techniques rely on positioning nanotubes at the edge of a sharp metal surface inside an SEM using an AC current. An AFM tip can then be brought into contact with the nanotubes, and a DC bias voltage is applied between the tip and CNTs. As both the CNTs and AFM tip are conductive, this creates an electrostatic attraction which allows a single nanotube to be positioned at the end of the AFM tip. Amorphous carbon deposition is then used to adhere the nanotube to the tip.[136] In pull-out experiments, the nanotube-AFM tip is generally pushed into a molten polymer surface. The AFM tip then remains immobile while the polymer cools and solidifies. The nanotube is then retracted from the polymer, and the interfacial energy can be examined from the resulting force-distance curves. In peel experiments, the AFM tip approaches the substrate so that the nanotube makes lateral contact with the polymer surface. The AFM tip is then retracted which causes the nanotube to peel from the surface and the resulting nanotube/polymer interactions can be investigated from the force-distance curves.[137,138]

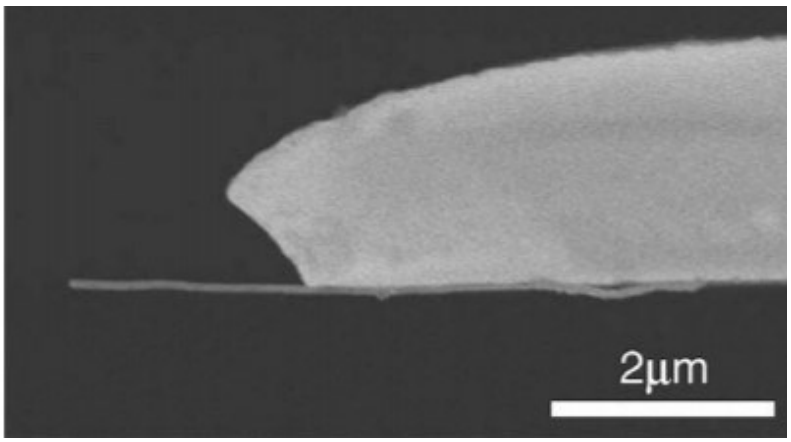

Figure 2.16: SEM image showing a single carbon nanotube attached to the end of an AFM tip. The nanotube-tip was used for peel experiments on various surfaces.[135]

Many pull-out experiments have investigated the interfacial shear strength between CNTs and various polymer surfaces. However, the results often exhibit large variations in the measured values. This appears to be due to the difficulty in controlling each aspect of the experiments at such a small length scale. For example, the nanotubes can bend, break, or separate from their layers which impacts the measured shear strengths. Cooper

et al.[139] examined the adhesion of CNTs to an epoxy matrix using AFM in conjunction with SEM. It was demonstrated that the shear strength of the multi-walled carbon nanotube (MWCNT)/epoxy interface ranged from 35 MPa to 376 MPa. The shear strength was calculated by dividing the maximum pull-out force by the interfacial area of the embedded nanotube. Barber et al.[132,134] demonstrated that the interfacial shear strength between MWCNTs and polyethylene–butane ranged from 10 MPa to 90 MPa. The results confirmed that the polymer matrix around the nanotubes was able to withstand significantly greater amounts of stress compared to the bulk polymer. Tsuda et al.[133] calculated the interfacial shear strength between MWCNTs and poly(ether ether ketone), which ranged from 6 MPa to 14 MPa. The results demonstrated that the interfacial shear strengths varied considerably depending on the type of polymer used in each experiment.

It is much more common for experiments to investigate CNT/polymer interactions by performing pull-out tests rather than peel tests. However, despite this, Strus et al.[135] examined the interfacial energy between CNTs and polyimide, graphite, and epoxy substrates by performing peel experiments. In each experiment, the force-distance curves exhibited three distinct stages. The first occurred at lower peeling point displacements and was called line-contact. Line-contact was characterised by an S-shape in the force-distance curves, and represented the force associated with the length of the nanotube peeling from the substrate's surface. The second stage was point-contact which exhibited an arc shape in the curves. Point-contact represented the force associated with desorbing the final part of the nanotube, which remained in contact with the substrate after the initial peeling. The final stage was no-contact where the nanotube had completely desorbed from the substrate. The results demonstrated that the interfacial energy between the CNT and epoxy was largest of the three substrates. Whilst the interfacial energy between the CNT and polyimide was the smallest of the three substrates. The study by Strus et al. was significant as it demonstrated that the interfacial energy between nanotubes and different substrates could be accurately investigated using peel experiments.

2.5.2.3 Investigating polymer/polymer interactions

Some AFM force spectroscopy studies have also focused on investigating polymer/polymer interactions. This can involve measuring the interactions between different polymer chains, or measuring the force associated with conformational transitions of single polymer chains adhered to surfaces. Although this topic is not widely examined within the literature, it is still important for many applications which rely on polymers functioning at surfaces. This is because the behaviour of polymers at surfaces is generally influenced by polymer/polymer interactions, as well as, polymer/substrate interactions.

In poor solvent conditions, polymer chains will adsorb to surfaces in collapsed globular conformations. When an elongation force is applied to the chain, a transition takes place where the globule becomes an extended coil. AFM force spectroscopy can be utilised to extend single collapsed polymer chains and measure the interaction forces associated with this conformational transition. Koutsos et al.[140] investigated the polymer-extended coil transition of polydimethylsiloxane chains on a silicon substrate in air. The resulting force-separation graphs exhibited force plateaus and steps, which appeared to represent the extension of polymer chains from their globular conformations. The force associated with the globule-extended coil transition was estimated at 25 ± 10 pN, which was in good agreement with theoretical predictions. Haupt et al.[141] carried out force-spectroscopy experiments on single poly(N-isopropylacrylamide) and poly(ethylene oxide) chains adsorbed onto silicon nitride substrates in both poor and good solvent conditions. When the experiments were carried out in good solvent conditions, the force-separation graphs exhibited saw-tooth patterns, which are typical of the stretching of extended single polymer chains. However, when the experiments were carried out in a poor solvent, the force-separation graphs exhibited force plateaus and steps, which represented the pulling of polymer chains from their globular conformations. The peak step force associated with the globule-extended coil transition had a value of 12 - 18 pN. The investigations by Koutsos et al. and Haupt et al. were the first to experimentally investigate and characterise the force associated with the polymer globule-extended coil transition. Previously, this conformational transition had only been theoretically predicted.[140,141]

Some studies have also focused on examining the interactions between different polymer chains. For example, Liu et al.[129] measured the force required to desorb poly(ethylene oxide) chains from a single crystal on a silicon substrate. In the experiments, single crystals of poly(ethylene oxide), which were end-terminated with thiol particles, were deposited onto silicon substrates. A gold-coated AFM tip was then used to interact with the crystals where the thiol terminals could become attached to the AFM tip. The tip was then retracted, which allowed for the force required to extract a single poly(ethylene oxide) chain from the crystal on the silicon substrate to be directly measured. The results demonstrated that the peak force associated with extracting a single poly(ethylene oxide) chain from a crystal was approximately 40 pN, which was typical of non-covalent bonds. Another investigation by Cui et al.[142] examined the desorption force of polystyrene segments from a polystyrene substrate in water. It was demonstrated that the desorption force per polystyrene monomer unit was in the range of 1.3 - 2.1 pN. The interactions appeared to be primarily due to short-range hydrophobic interactions between the two hydrophobic polystyrene surfaces.

2.5.2.4 Stretching polymer chains

Many AFM force spectroscopy studies have investigated the stretching of single polymer chains which are adsorbed to a substrate in a solvent (poor - good). These investigations provide information regarding the behaviour of single chains under extensional force. At lower chain extensions, entropic forces are dominant as the polymer chains experience a loss of conformational entropy due to the reduction in the possible chain conformations. As the extension of the chains increases, the bonds in the polymer backbone become stressed and deform, which leads to an influence from both enthalpic elasticity and entropic forces.[81] There are many experimental procedures which can be carried out to investigate the stretching of single polymer chains. The most simple involves physically adsorbing polymer chains to a substrate using dip coating or spin coating. A blank AFM tip is then used to pick up and stretch the polymer chains. Although this method is time efficient and simple, there can be a very low probability of observing chain stretching.[85] Therefore, in many experiments, polymer chains are chemically attached to the AFM tip and/or substrate to increase the probability of observing chain

stretching.[81,143] The stretching of polymer chains is represented by a spiked curve in force-separation graphs. If many chains are picked up and stretched by the tip simultaneously, this can lead to a saw-tooth pattern of multiple spiked curves. These graphs can provide information regarding the elasticity and force response of single chains. The curved spikes can be fitted to statistical models such as the worm-like chain (WLC) and freely jointed chain models (FJC). This can allow for calculations of physical quantities such as polymer Kuhn length to be carried out.[81,85]

Numerous studies have focused on examining the stretching of commonly utilised linear polymers. For example, in 1997, Kikuchi et al.[144] investigated the stretching of polystyrene on a silicon substrate in toluene. The polystyrene was end terminated with carboxyl groups, whilst the silicon substrate and AFM tip were treated with H_2O_2 to form hydroxyl groups. Therefore, the carboxyl group on each end of the polystyrene chains formed covalent bonds with the hydroxyl groups on the silicon tip and substrate, which allowed for the observation of chain stretching. The results for the experiments were not in good agreement with theoretical predictions, and it appeared that the elastic constant of the chain segments was much smaller than the spring constant for the steric structural change of a polystyrene backbone. It was speculated that each chain consisted of a number of random coil segments divided into blobs. When the chain was stretched, the blobs went from spherical shaped to elliptical, and therefore the small elastic constant of the chain segments could be due to the elasticity of the blob deformation. Radiom et al.[85] also investigated the stretching of polystyrene chains. However, in this study, the stretching of polystyrene in various solvents and on various substrates was examined. It was demonstrated that the spiked curves in the force-separation graphs were the same regardless of what substrate was used. Therefore, the spiked-curves represented only polymer stretching. The experiments were repeated for a number of solvents ranging from poor solvent quality to good solvent quality. The resulting spiked curves in the force-separation graphs were fitted to the FJC model. It was demonstrated that the elasticity constant of the polymer remained constant with solvent quality, but the Kuhn length varied considerably with solvent quality. The Kuhn length of the polymer was 0.42 nm when the experiments were carried out in toluene (good solvent). Whereas, the polymer Kuhn length was 0.27 nm when the solvent was ethanol (poor solvent). The results demonstrated that there was an approximately negative linear relationship between the polymer Kuhn length and the Flory-Huggins interaction parameter for the

polymer in each solvent (see Figure 2.17) This was the first experiment to demonstrate experimentally that the Kuhn length of polymers systematically changed with solvent quality.[85]

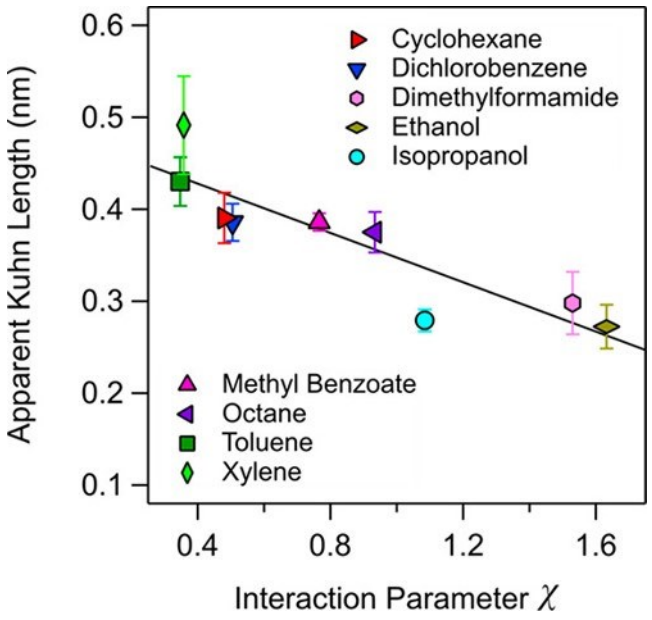

Figure 2.17: Graph showing the relationship between the Kuhn length of polystyrene obtained using AFM force spectroscopy and the Flory-Huggins interaction parameter for the polymer in each solvent.[85]

Ortiz et al.[145] investigated the stretching of poly(methacrylic acid) using AFM force spectroscopy. The polymer was covalently attached to a gold substrate via gold-thiolate bonds and was physically adsorbed to the AFM tip upon contact. The spiked curves in the force-distance graphs were fitted to the FJC and WLC models, and the persistence length of the polymer was calculated to be approximately 0.3 nm. This was roughly the same length of a poly(methacrylic acid) monomer which suggested that the polymer chains were fairly flexible. Hugel et al.[83] investigated the elasticity of polyelectrolyte chains with varying charge densities in different salt concentrations using AFM force spectroscopy. Chains were covalently attached to both the AFM tip and silicon substrate to increase the probability of observing chain stretching. The force-distance curves were fitted to the WLC model, and it was demonstrated that the persistence length and segment elasticity constant were the largest when the chain had the highest degree of charge density. This demonstrated that the elasticity of the polyelectrolyte chains

decreased as the distance between electrical charges along the polymer chains increased. Furthermore, for each polymer investigated, the persistence length and segment elasticity constant increased with increasing salt concentration. This demonstrated that an increased salt concentration increased the screening of electrical charges on the polymer chains which also led to a decrease in the chain flexibility. Investigations of polymer chain stretching using AFM force spectroscopy is fairly limited for synthetic polymers. It is much more common for investigations to focus on examining the elasticity of biopolymers, such as DNA and proteins. Therefore, the elasticity and force responses of many synthetic polymers have not yet been experimentally examined using AFM force spectroscopy.

2.6 Conclusions

Understanding and characterising the behaviour of polymers at surfaces is extremely important to fundamental polymer science, as well as, many applications. Numerous experiments have highlighted that polymer behaviour at an interface can greatly deviate from behaviour in the bulk. However, there is a distinct lack of understanding regarding the drivers for these behavioural changes. Atomic force microscopy is one of the few experimental techniques which can accurately investigate the fundamental behaviour of polymers at surfaces. AFM imaging can be used to investigate the morphology of polymer thin films, nanostructures, and single chains on various substrates. Whereas AFM force spectroscopy can be utilised to investigate the strength of interactions between polymers and substrates. In addition, AFM force spectroscopy also has the capabilities to investigate polymer/polymer interactions, and the stretching and elasticity of single polymer chains. Despite extensive examinations within the literature, there are still many aspects of the interfacial behaviour of polymers which are not fully understood or have not yet been investigated. The content of this thesis aims to use AFM imaging and force spectroscopy to broaden the understanding of the interfacial behaviour of polymers.

3 Experimental techniques

Summary

This chapter presents the experimental techniques and methods implemented in order to systematically study the behaviour of polymers at surfaces. It outlines in detail both spin coating and dip coating techniques, which were used to deposit polymeric material onto various substrates. Furthermore, it demonstrates how AFM experiments were carried out using both tapping mode imaging and force spectroscopy. Details of the techniques used to analyse the AFM images and force-distance curves are also included.

3.1 Introduction

Understanding the fundamental behaviour of polymers at surfaces is vital for many applications.[31,47,146] However, accurately investigating polymers at surfaces can prove to be very difficult experimentally. This is because the research involves trying to characterise the behaviour of macromolecules at the nanoscale. This requires well controlled sample preparation and the utilisation of extremely precise experimental methods which can accurately provide information at an incredibly small length scale. For these reasons, there are only a limited number of experimental techniques which are suitable for this field of research.

AFM is an imaging technique which has the capabilities to provide high resolution images of polymers at surfaces down to the sub-nanometer scale.[147] It is extremely common in studies of polymers at surfaces, and has been heavily utilised in the field since its development in 1986.[71] It has the capability to accurately analyse the morphology of single polymer chains adsorbed to a surface.[103,107,148] It can also generate information regarding the viscoelastic properties of polymers using phase imaging mode.[73,149]

AFM can also be used to provide information regarding the strengths of interactions between polymers and different substrates with a force resolution of approximately 10 pN.[50] This mode of operation is known as AFM force spectroscopy. Force spectroscopy is commonly utilised to provide information regarding the types of polymer/substrate interactions which dominate at the nanoscale. These commonly include van der Waals forces, hydrophobic forces, π-π stacking interactions, hydrogen bonding, and electrostatic interactions.[87,150] Polymer chains are often chemically or physically adhered to AFM tips in order to measure the strength of interactions with various substrates under different experimental conditions.[82,85,142]

Both spin coating and dip coating are commonly utilised to deposit polymers on surfaces, which are then characterised using AFM. These AFM experiments often involve investigating the dewetting of common homopolymers such as polystyrene,[49,98,102] or studying the morphology of block copolymers at surfaces.[73,108,125] However, studies which characterise random copolymers such as poly(styrene-co-butadiene) random copolymers are very limited. A comprehensive investigation which extensively characterises the fundamental behaviour of poly(styrene-co-butadiene) random

copolymers at different surfaces does not exist, despite the fact that the polymer is important for many applications, such as car tyres, sealants, and O-rings.

The following chapter details the experimental methods and techniques used throughout the course of the PhD. This primarily involves characterising poly(styrene-co-butadiene) on different surfaces at the nanoscale using AFM techniques. Polymer solutions were prepared in toluene at various molecular weights and concentrations. The polymers were deposited onto different substrates using both spin coating and dip coating techniques. All imaging of the polymer features was carried out using tapping mode AFM in air, whilst the strength of interactions between polymers and surfaces was investigated using AFM force spectroscopy in air. Additional experiments examining the behaviour of polymers on surfaces were carried out at the macroscale including viscosity measurements and contact angle goniometry.

3.2 Materials

3.2.1 Polymer samples

For each experiment, the polymers which were primarily investigated were poly(styrene-co-butadiene) random copolymer samples. Poly(styrene-co-butadiene) is a linear amorphous copolymer made up of individual styrene and butadiene monomer units. It is commonly referred to as styrene-butadiene rubber. Figure 3.1 shows the structure of styrene and butadiene monomers. The polymers were random copolymers, which means that the styrene and butadiene monomer units were arranged in a random configuration along the chain length. 1H NMR was conducted by Michelin to examine the monomer distribution in the random polymer chains. The results demonstrated that in the chains there was a >95% probability that the styrene blocks had lengths of 1 - 3 monomer units. Due to their random configurations, random copolymers have similar properties to that of homopolymers and can often have the desirable properties of each of the molecules making up the chain.[1] Figure 3.2 is an illustration outlining the monomer configuration in a random copolymer chain. Three poly(styrene-co-butadiene) samples were provided by Michelin as this polymer is utilised extensively in the manufacture of tyres. Gel permeation chromatography (GPC) conducted by the provider showed that the

molecular weights (M_n) of each of the samples were 46 kg/mol, 86 kg/mol, and 355 kg/mol. The molecular weights of the polymers were all considerably above the entanglement molecular weights (M_e) of polystyrene (17 kg/mol) and polybutadiene (1.9 kg/mol) (values taken from the literature where small-angle neutron scattering was implemented).[151,152] Therefore, this means that the copolymers used in the experiments were able to readily entangle with one another.[4] GPC also showed that the polymers were monodisperse with polydispersity (Đ) values of 1.03, 1.01, and 1.02 for the 46 kg/mol, 86 kg/mol, and 355 kg/mol samples, respectively. Using monodisperse polymers improved the consistency and repeatability of results. Differential scanning calorimetry (DSC) conducted by the provider showed very similar glass transition temperatures (T_g) of -36.4˚C, -35.1˚C, and -35.4˚C for the three copolymers. The T_g values were considerably lower than ambient room temperatures meaning that in all experiments, the polymer samples were well above (by ~55˚C) their T_g's, and therefore they behaved as viscoelastic polymer melts. The polymers had styrene-butadiene ratios of 25.9:74.1, 26.3:73.7, and 25.9:74.1 for the 46 kg/mol, 86 kg/mol, and 355 kg/mol samples, respectively. Table 3.1 presents the properties of each poly(styrene-co-butadiene) sample.

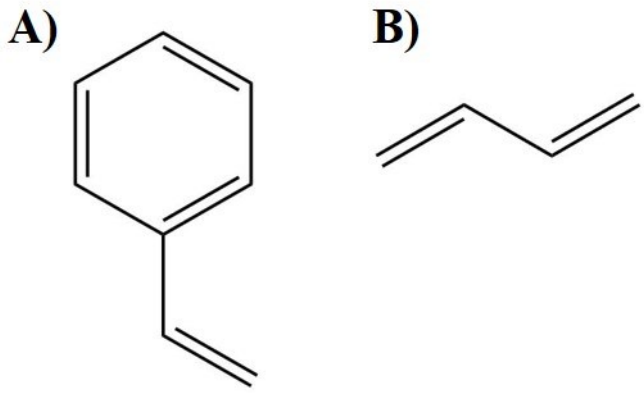

Figure 3.1: The structure of (A) styrene and (B) butadiene.

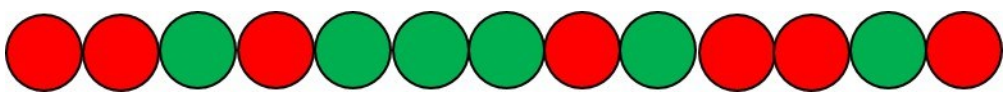

Figure 3.2: Illustration showing the random configuration of monomer units within a random copolymer chain.

Table 3.1: Properties of the poly(styrene-co-butadiene) samples used in each experimental chapter.

Polymer	M_n (kg/mol)	T_g (°C)	Đ	Styrene-butadiene ratio
Poly(styrene-co-butadiene)	46	-36.4	1.03	25.9:74.1
Poly(styrene-co-butadiene)	86	-35.1	1.01	26.3:73.1
Poly(styrene-co-butadiene)	355	-35.4	1.02	25.9:74.1

Polystyrene homopolymers were used in complimentary experiments in Chapter 5. Two polystyrene samples were purchased from Sigma-Aldrich, with molecular weights of 150 kg/mol and 560 kg/mol. The polystyrene samples were monodisperse with Đ's of 1.02 and 1.04 for the 150 kg/mol and 560 kg/mol samples, respectively. Additionally, a polybutadiene homopolymer was also used in complementary experiments in Chapter 5 and was purchased from Sigma-Aldrich. The polybutadiene had a molecular weight of approximately 200 kg/mol and it was assumed that the sample was fairly polydisperse, but Đ was not directly measured. The molecular weights of both the polystyrene and polybutadiene homopolymers were significantly larger than the respective entanglement molecular weights. As the polystyrene and polybutadiene homopolymers only had limited use in complimentary experiments, extensive characterisation of the polymers was not necessary.

3.2.2 Substrates

Three substrates were used throughout the experiments. Ruby muscovite mica was purchased from Agar Scientific. Muscovite mica [$(K\,Al_2(OH)_2\,AlSi_3O_{10}]$) is a mineral with a layered crystal structure which is shown in Figure 3.3A. It is composed of two tetrahedral honeycomb sheets of SiO_4 and AlO_4 which have a 4:1 ratio, respectively. In the middle of the tetrahedral sheets is an octahedral layer of AlO_6 and OH groups. The

tetrahedral and octahedral layers are connected due to shared oxygen atoms which creates a 1 nm thick 2:1 layer. The individual 2:1 layers are connected to one another due to the presence of K^+ ions on the outside of each tetrahedral sheet which creates a stacked crystal structure.[153] Within the 2:1 tetrahedral and octahedral layers, there are a large number of strong covalent bonds. However, the ionic bonds between the 2:1 layers and the K^+ ions are significantly weaker. This means that under force, the mica will consistently break at the K^+ layer. Consequently, the exposed surface is a perfectly flat (001) basal plane of the negatively charged tetrahedral honeycomb sheet (see Figure 3.3B).[154] The monoclinic unit cell of the top surface has parameters of a=0.519 nm, b=0.901 nm, and c=2.00 nm.[155] The process of exposing the basal plane is known as cleaving and can be very easily carried out using scotch tape. Each mica substrate can be cleaved many times as the process only removes an extremely thin layer of material from the surface. Not only does the process of cleaving create a perfectly flat surface, it is also extremely clean as the new surface has had no previous exposure to any atmospheric conditions since the crystal was originally created millions of years ago.[156]

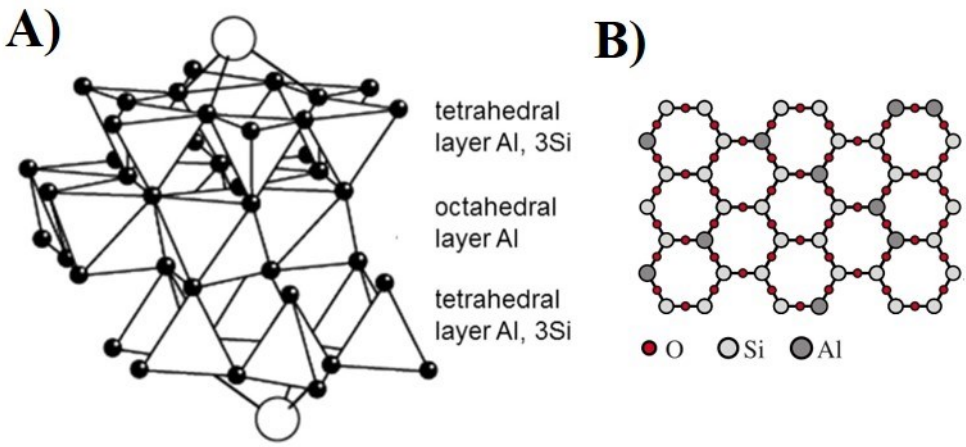

Figure 3.3: (A) Chemical structure of muscovite mica showing the two tetrahedral layers on either side of the octahedral layer and K^+ ions at each end.[153] (B) (001) basal plane of a cleaved mica surface.[154]

Mica is the most common substrate used in AFM experiments. This is due to its perfect cleavage which exposes an atomically flat and truly fresh surface. Furthermore, it has a low cost and is widely available.[156] The surface facilitates the accurate imaging of single molecules at a sub-nanometer scale without any topographical influence from the mica

substrate. Freshly cleaved mica is extremely hydrophilic with a water contact angle of <5°.[157,158] The hydrophilic nature of mica is a disadvantage in AFM force spectroscopy experiments as it is favourable for water to condense at the surface. This can create significant capillary forces in the system which can impact results.[159] Chapter 4 presents a comprehensive investigation into the morphology of poly(styrene-co-butadiene) on a mica surface.

ZYA highly ordered pyrolytic graphite (HOPG) substrates were purchased from Scanwel Ltd. Graphite is an allotrope of carbon which is composed of stacks of 2-dimensional single planes, known as graphene. Each graphene plane is made up of carbon atoms which are arranged in repeating hexagonal crystal cells.[45] In order to improve the quality of graphite and remove defects, pyrolysis procedures were carried out by the provider. This involved annealing the graphite at extremely high temperatures and pressures for long periods of time. The process creates HOPG, which has very few defects and a low mosaic spread angle (<1°).[160] The mosaic spread angle is the degree of how aligned each plane is to one another and is measured using x-ray diffraction.[161] This is important for AFM studies, as only HOPG with a low mosaic spread angle is suitable as a substrate. ZYA HOPG is the highest quality graphite available and the substrates had a very low mosaic spread of 0.4° - 0.7°. This ensured that the graphite surface would cleave well and would be mostly defect free.

Figure 3.4 shows the chemical structure of graphite. In a single plane, each carbon atom is covalently bonded to three other carbon atoms. These bonds are strong and the next nearest neighbour distance is 0.142 nm. However, the strength of the bonds between the individual planes are much weaker. This is because the distances between the atoms in each plane (0.335 nm) are considerably larger than the next nearest neighbour distance.[162] This means that the graphite acts in a similar way to mica and cleaving the surface with scotch tape breaks the bonds holding the hexagonal graphene sheets together, which exposes a mostly smooth and clean top surface. Unlike mica, graphite frequently does not cleave perfectly and the surface can exhibit atomic steps which expose different graphene layers (see Figure 3.5). These steps are created either internally during crystal growth, or externally by the cleaving process.[163] The presence of steps on the graphite surface did not impact results such as orientation analysis. This

was because the quality of graphite used was the highest available with a very low mosaic spread angle.

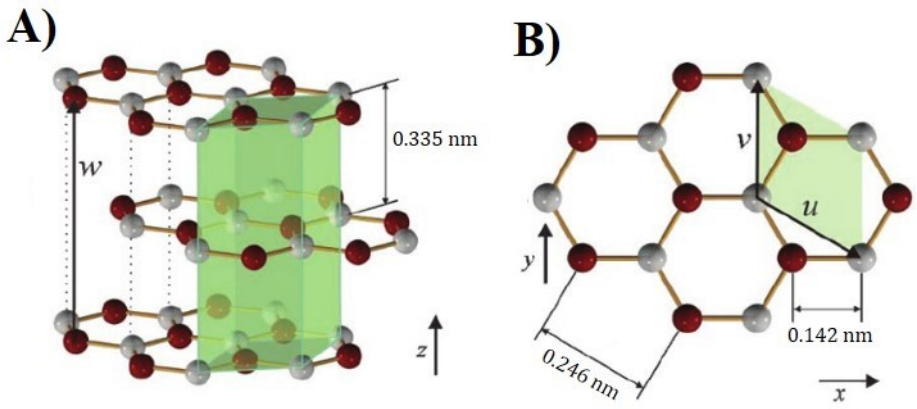

Figure 3.4: Illustrations showing the chemical structure of graphite. The unit cell is represented by the green box. (A) Shows the layered crystal structure of graphite where the distance between atoms in each plane is 0.335 nm. (B) Shows the top view of a graphite surface. The lattice constant is 0.246 nm, and the next nearest neighbour distance is 0.142 nm.[162]

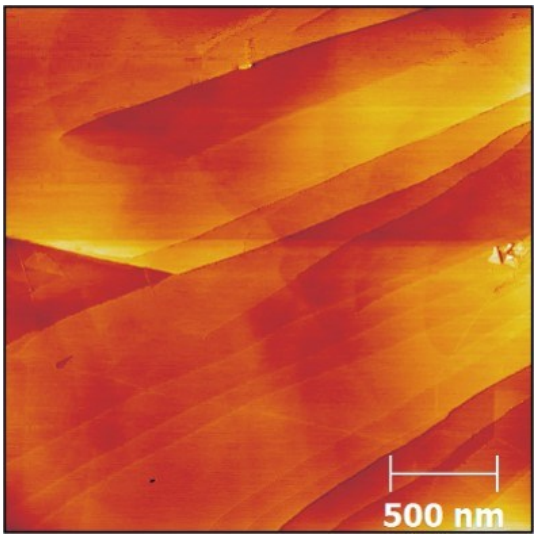

Figure 3.5: AFM height image showing the surface of a freshly cleaved ZYA HOPG substrate. Distinct steps can clearly be observed in the image.

Graphite has a water contact angle ranging from 84° - 86°.[164–166] This means that less water condenses at the graphite surface, which reduces any impact from capillary forces

in AFM force spectroscopy experiments. Numerous AFM investigations use graphite as a substrate to study polymer/carbon interactions.[110,112,167] This is essential in order to better understand the bulk behaviour of composite materials, which is often governed by the fundamental interactions between polymers and various carbon components such as carbon black, carbon fibre, carbon nanotubes, and graphene.[168] In Chapter 5, the morphology of poly(styrene-co-butadiene) was investigated on a graphite surface. The preparation of polymer samples and AFM methodology are the same in both Chapter 4 and 5, but the mica substrates are replaced with graphite.

Silicon substrates were purchased from Agar Scientific. They were cut into wafers (5 mm^2) by the provider with a thickness of approximately 0.5 mm. Silicon substrates are composed of crystalline silicon which has a diamond crystal structure. This means that there are 8 silicon atoms per unit cell arranged in a FCC structure with 4 atoms within the cell itself (see Figure 3.6).[169,170] The silicon atoms are covalently bonded to one another and there is a lattice constant of 0.543 nm.[171] The silicon had a crystallographic orientation of (111), which means its crystal plane is triangular shaped with 2 atoms within the plane.[172] Silicon is a material which is extensively utilised in many electronic applications due to its semi-conducting properties. This makes it a suitable material for the manufacture of many components such as transistors.[173]

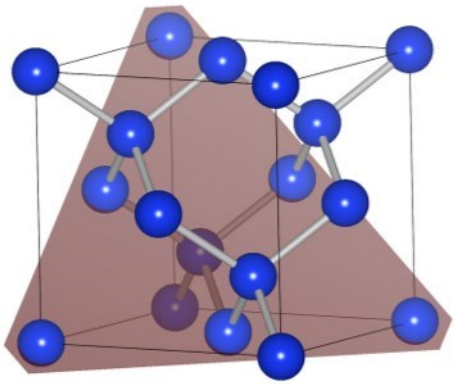

Figure 3.6: Illustration showing the diamond lattice structure of a silicon unit cell. The shaded triangle represents the (111) plane.[170]

The surface of silicon cannot be easily cleaved like mica and graphite. Therefore, the surfaces were cleaned and extensively polished by the provider to give a surface

roughness of <1 nm and a top layer with no oxide coating. However, with exposure to atmospheric conditions over time, it was inevitable that an extremely thin native oxide layer would grow on the substrate surfaces. The native oxide layer can change the properties of a silicon surface such as its hydrophilicity.[174] However, this appears to be highly dependent on the thickness of the layer and it has been demonstrated that the rate of oxide growth under ambient conditions is fairly slow.[175] The cleaning process of the silicon substrates also impacts the hydrophilicity of the surface. The substrates in the current study were cleaned with acetone and ethanol immediately before use and did not undergo extensive chemical cleaning. Therefore, it was expected that the surfaces would not be extremely hydrophilic. This was confirmed from goniometry experiments which produced an average water contact angle for the silicon substrates of 45.8°. This meant that capillary forces may impact results when carrying out force spectroscopy experiments. However, the magnitude of the capillary forces should be substantially less than those experienced on the extremely hydrophilic mica substrates.

Silicon wafers are most commonly used in electronic applications. However, they are also frequently utilised as substrates in AFM studies.[176–178] This is due to their many favourable properties, such as an extremely low surface roughness, low cost, and the relative ease at which the wafers can be cut into small pieces suitable for AFM substrates. Furthermore, silicon substrates can be advantageous in force spectroscopy experiments, where an approximately symmetrical system can be created between the silicon tip and substrate.[179] Silicon substrates were used in the force spectroscopy experiments in Chapter 6 and 7.

3.3 Solution preparation

Solutions of poly(styrene-co-butadiene) were prepared in toluene at varying concentrations. Toluene was used as the samples are readily soluble in this apolar solvent. Toluene is classed as a good solvent for poly(styrene-co-butadiene), which means the polymer interacts favourably with the solvent creating expanded chains within the solution.[4] The polymer solutions were stirred using a magnetic stirrer at 750 rpm for at least 4 hours to ensure the solutions were homogenous. The solutions were

made according to the polymer's overlap concentrations, *c**. This is the concentration in which polymer chains in solution will begin to overlap with one another.[180] The overlap concentrations were calculated theoretically for each sample by first calculating the pervaded volume (V_p) of the chains using the following equation:[4]

$$V_p \approx R^3 \tag{3.1}$$

Where R is the size of the polymer chain which was calculated using the scaling parameter for a chain in good solvent conditions, which is valid for poly(styrene-co-butadiene) in toluene. The overlap concentration could then be found using the following equation:[4]

$$c^* = \frac{M_n}{V_p N_A} \tag{3.2}$$

Where M_n is molecular weight and N_A is Avogadro's number. The solutions were prepared at 3c*, 1c*, 0.1c*, 0.01c*, and 0.001c*. The solutions ranged from far below the overlap concentration (dilute regime) to above the overlap concentration (semi-dilute regime). Utilising a wide range of concentrations allowed for the investigation of many polymer nanostructures on the substrates from thin films, networks, and spherical caps down to single chain conformations. Figure 3.7 is an illustration showing polymer density for solutions that are well below, equal to, and well above the overlap concentration. Calculating the overlap concentration for each polymer was very useful as it demonstrates which concentration regimes are realistic.[181] Table 3.2 shows conversions to concentration-by-weight for each polymer sample.

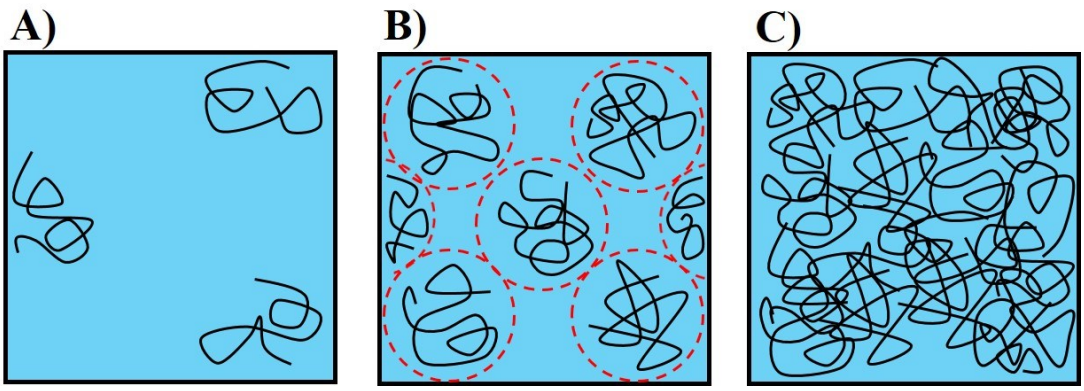

Figure 3.7 Illustrations showing polymer density at different solution concentrations. (A) Well below the overlap concentration (dilute). (B) At the overlap concentration. (C) Well above the overlap concentration (semi-dilute).

Table 3.2: Conversions from c^* to mg/ml

	46 kg/mol sample (mg/ml)	86 kg/mol sample (mg/ml)	355 kg/mol sample (mg/ml)
3c*	17.34	11.13	4.17
1c*	5.81	3.71	1.39
0.1c*	0.581	0.371	0.139
0.01c*	0.0581	0.0371	0.0139
0.001c*	0.0058	0.0037	0.0014

3.4 Polymer deposition

3.4.1 Spin coating

Spin coating is an experimental technique which facilitates the production of thin films, ultrathin films, and nanostructures upon substrates. It is widely utilised throughout many fields of research, but it is particularly common in experiments involving polymers on surfaces.[182,183] Spin coating has many advantages compared to other deposition techniques such as the ability to create homogenous structures across fairly large surface areas, and a high degree of control and reproducibility. For instance, an ultrathin polymer film with an (almost) fixed thickness can be repeatedly produced using spin coating if all parameters are kept constant. Spin coated polymer films have many applications such as microelectronics, membranes, and protective coatings.[176]

The process of spin coating involves depositing a small amount of polymer solution onto a stationary substrate. The substrate then begins to rotate and quickly accelerates to a very high angular velocity. The substrate itself is held under vacuum, but the centrifugal force created by the rotation causes the solution to spread across the substrate and much

of the solution is expelled from the surface altogether. A very thin layer of polymer solution is left on the substrate and rapid evaporation of the solvent leaves behind a homogenous thin film of polymeric material. In many cases, such as where the polymer behaves as a liquid due to having a low T_g, dewetting occurs creating nanostructures, such as spherical caps or networks. An illustration outlining the process of creating polymer thin films/nanostructures using spin coating is presented in Figure 3.8.

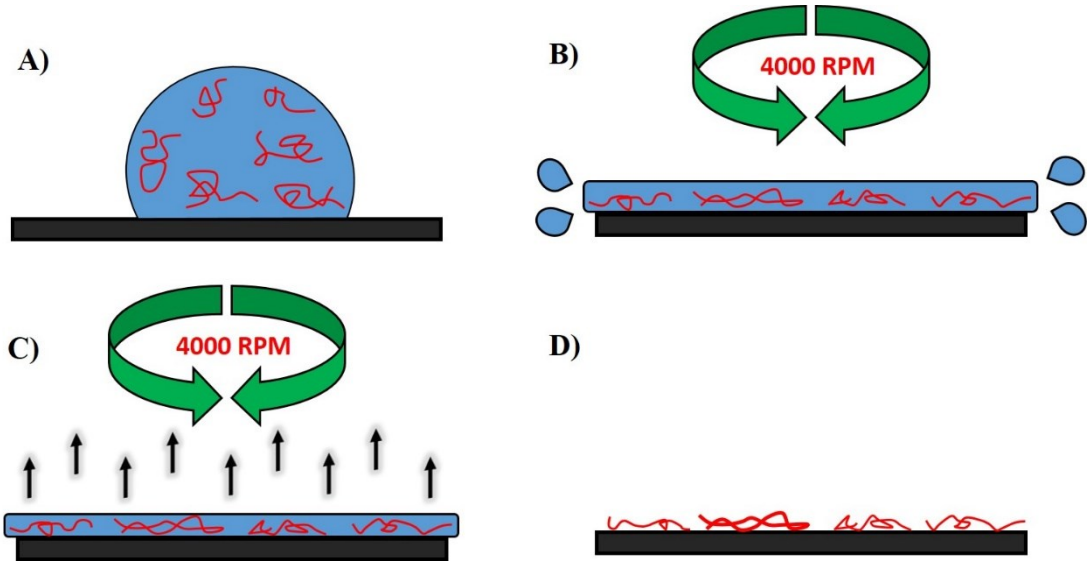

Figure 3.8: Illustration outlining the process of creating polymer thin films/nanostructures on a substrate using spin coating. (A) Polymer solution is deposited onto a substrate. (B) The substrate is rotated at a high angular velocity leaving a thin layer of the solution on the substrate. (C) Solvent evaporation takes place. (D) A polymer thin film/nanostructure is left on the substrate.

Polymer morphology can be controlled during spin coating by altering many experimental parameters. These include type of solvent, molecular weight, glass transition temperature, solution concentration, and substrate type.[176] Furthermore, the spin coating parameters themselves can be controlled in order to change polymer morphology. The controllable parameters on most spin coaters are time, acceleration, and angular velocity. If time is increased, generally more polymer solution will be expelled from the surface which creates a film with a lower thickness. Likewise, if acceleration and angular velocity are increased, generally film thickness will reduce. Figure 3.9 clearly shows this relationship between film thickness and angular velocity.[176]

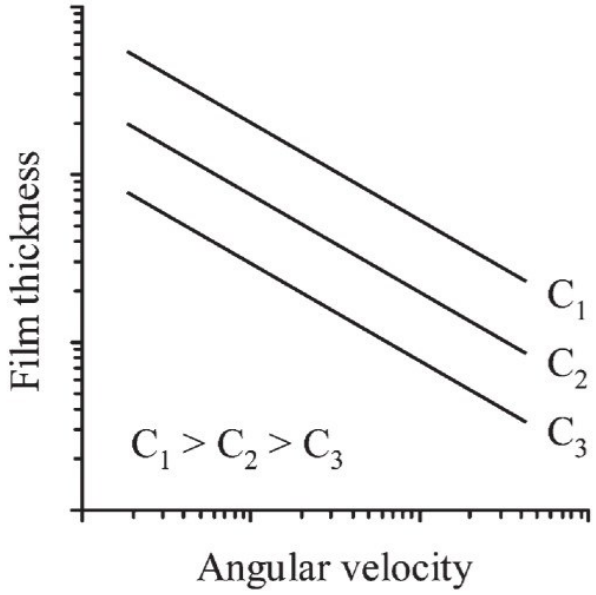

Figure 3.9: Graph showing the relationship between polymer film thickness and the angular velocity of spin coating for three concentrations of polymer solution. For each concentration, the polymer film thickness decreases with increasing angular velocity. Furthermore, the graph shows that an increase in solution concentration also leads to larger film thicknesses.[176]

Spin coating was used to create all thin films and nanostructures examined in the experiments in Chapters 4 and 5. A SPIN150 Wafer Spinner was used in all experiments (see Figure 3.10). Initially the mica and graphite substrates were cleaved with scotch tape in order to remove the top surface of material and expose a completely clean layer. For each molecular weight, solutions were prepared at five different concentrations. The solutions were deposited onto the substrates, and the spin coating was then carried out for 90 seconds with an acceleration of 2000 rpm/second and an angular velocity of 4000 rpm. The parameters were fixed for every experiment to ensure consistency in the results. The spin coating parameters were set to a relatively large angular velocity and time period. This meant that much of the polymer solution was expelled from the surface, creating films and nanostructures with extremely low thicknesses. This is vital for studying the fundamental behaviour of polymers at surfaces. After spin coating, all the samples were thoroughly dried with a gentle nitrogen stream for five minutes and left in a fume hood for 16 - 72 hours to ensure the samples were dry before imaging. By using a large range of solution concentrations, films with varying initial thickness values were

formed on the substrates. More dewetting took place in the films with lower thickness values. Therefore, this led to a range of polymer morphologies on the surface. Furthermore, toluene is a rapidly evaporating solvent which promoted dewetting and the production of polymer nanostructures.

Figure 3.10: Photograph showing the SPIN 150 Wafer Coating model spin coater used to make all thin films and nanostructures in Chapters 4 and 5

Spin coating can create homogenous films and nanostructures across relatively large surface areas. However, as the nanostructures investigated in Chapters 4 and 5 were extremely small (down to single chains), minor changes in morphology across the substrate may have had a significant impact on statistical analysis. Therefore, a preliminary experiment was designed in order to analyse the homogeneity of the polymer nanostructures across different areas of the substrate. A polymer solution of the 46 kg/mol sample was prepared at a concentration of 0.1c* and spin coated onto a mica surface. AFM imaging was carried out at three areas on the surface which were called the centre, outer centre, and outer edge. Figure 3.11 is an illustration showing the location of where each AFM scan took place.

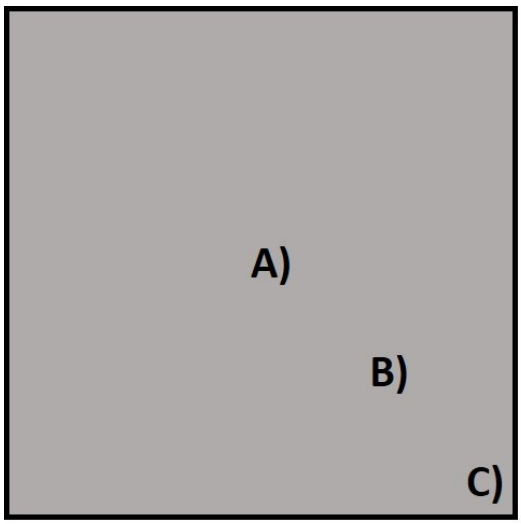

Figure 3.11: Illustration showing the positions of each AFM scan on the mica substrate in order to examine any changes in polymer morphology across the surface. (A) Centre of the substrate. (B) Outer centre of the substrate. (C) Outer edge of the substrate.

Figure 3.12 shows typical AFM images of polymer morphology at each area on the substrate. Detailed analysis revealed that polymer morphology varied at the different areas of the substrate. Table 3.3 shows the average height and radius values of the nanodroplets at each area on the mica substrate, as well as, the average number of aggregates in each image. At the centre of the substrate, there were the largest number of aggregates, but they had the smallest average size. The aggregates at the outer centre had larger heights and fewer aggregates compared to the centre, but a very similar average radius value. At the outer edge of the substrate, there were the smallest number of aggregates, but they had the largest heights and radii. This demonstrated that the position of the AFM scan on the substrate could impact the analysis of polymer morphology. Therefore, to improve the consistency of results, all imaging of the spin coated structures was carried out in close proximity to the centre of the substrates.

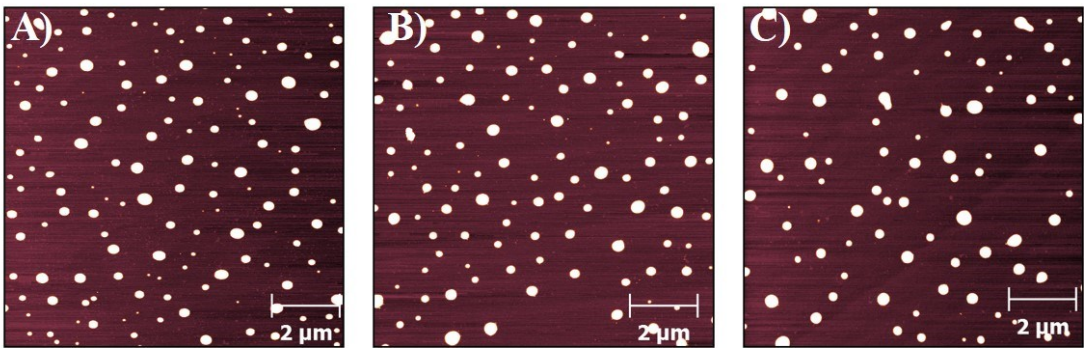

Figure 3.12: Typical AFM images of the 46 kg/mol sample spin coated onto mica at a concentration of 0.1c*. (A) Centre of the substrate, (B) outer centre of the substrate, (C) outer edge of the substrate.

Table 3.3: Average height, radius, and number of nanodroplets at each area on the substrate.

	Average Height (nm)	Average Radius (nm)	Average Number of Nanodroplets
Centre	10.3	117.0	154
Outer Centre	11.8	118.2	133
Outer Edge	11.9	148.4	103

3.4.2 Dip coating

Dip coating is another method commonly used to deposit thin films and nanostructures onto substrates. Dip coating is the oldest commercially applied coating process and it is frequency used to deposit polymers onto surfaces.[184] Dip coating has many advantages; it is experimentally simple and does not require any expensive machinery, as well as, allowing the rapid coating of fairly large surfaces areas. However, the major disadvantages of dip coating are the difficultly in controlling the thickness of films and reproducing results accurately. Furthermore, films may lack homogeneity across a surface and extremely small features, such as monolayers, are difficult to achieve.[185]

The process of dip coating involves immersing a substrate into a polymer solution for a fixed amount of time. The polymer chains will then adhere to the substrate in the solution. The substrate is then removed from the solution leaving a thin layer of residual

polymer solution upon the substrate. Evaporation takes place leaving behind a thin film of polymeric material on the surface. Figure 3.13 illustrates the process of dip coating in a polymer solution. There are many ways in which polymer morphology can be varied using dip coating methods. These include the speed at which the substrate is immersed and removed from the solution, the immersion time, solution concentration, and molecular weight.[176] Although these parameters influence polymer morphology, there is not the same level of control compared to spin coating.

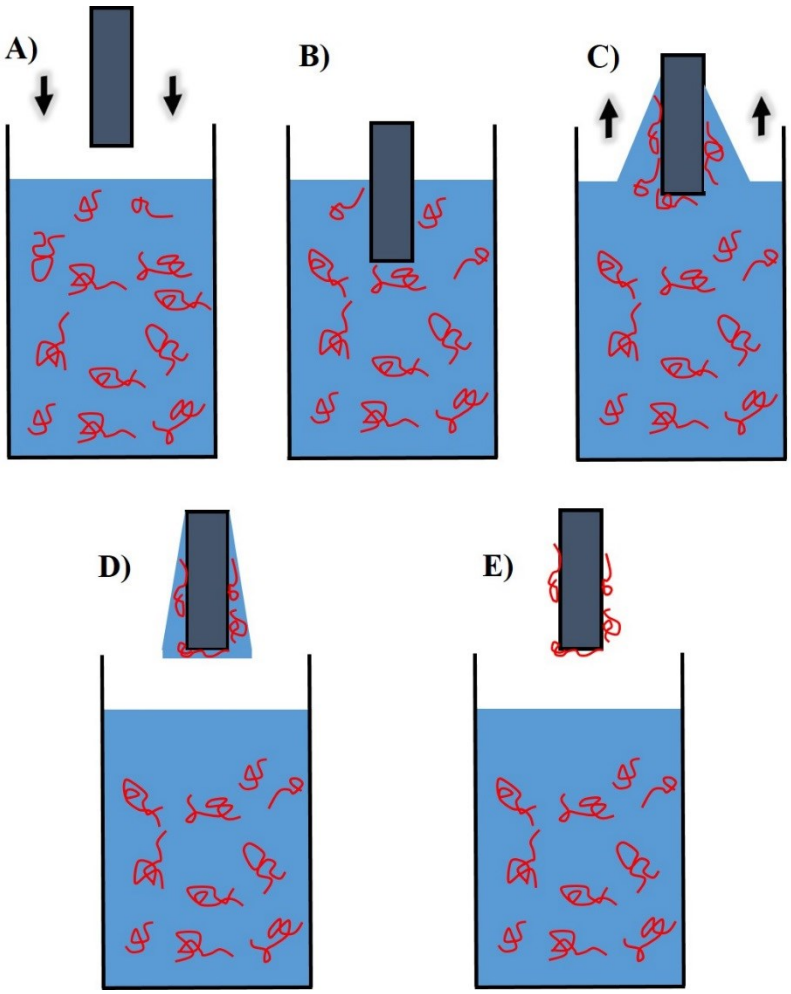

Figure 3.13: An illustration outlining the process of dip coating into a polymer solution. (A) A substrate is immersed into a polymer solution. (B) Chains begin to adhere to the surface. (C) The substrate is removed from the solution, although a thin layer of residual polymer solution remains on the substrate. (D) Solvent evaporation takes place. (E) A thin polymer film remains on the substrate.

In Chapter 6, dip coating was implemented in order to physically adhere poly(styrene-co-butadiene) chains to an AFM tip. This allowed the adhesion between poly(styrene-co-butadiene) and various substrates to be directly measured at the nanoscale. AFM tips are extremely small and fragile, and any slight impact to them will cause severe damage. Due to this, many coating techniques such as spin coating, were not suitable as they would damage the tips. Therefore, dip coating was implemented as it is a technique with a low risk of damaging the tips during coating. Polymer solutions of the 46 kg/mol and 355 kg/mol samples were prepared at 1c* and 5c*. Concentrations equal to the overlap concentration or above were used to ensure significant polymer adhesion to the surface of the tips. The solutions were prepared in a glass petri dish and the AFM tip was carefully placed in the bottom of the petri dish where it was completely submerged. A glass lid was then put on the petri dish in order to reduce solvent evaporation. The tips were immersed for 10 - 60 minutes to ensure a high degree of polymer coating. When the tips were removed from the solution, they were dried with a gentle stream of nitrogen for two minutes before being left overnight. If a tip with a low polymer surface coverage was required, then the tip was rinsed thoroughly with toluene immediately after removal from the polymer solution.

In Chapter 7, dip coating was also used to create thin films on various substrates. This was in order to measure the interaction forces between polymer thin films on different substrates and a blank AFM tip. To allow for comparison with the previous experiments using coated AFM tips in Chapter 6, the substrates were prepared using the same experimental methods. Solutions of the 355 kg/mol samples were prepared at a concentration of 5c* in a glass petri dish. The mica and graphite substrates were cleaved with scotch tape immediately before immersion into the solution. However, as silicon cannot be cleaved, a new substrate was used for every experiment which had been cleaned with acetone and ethanol. To ensure the formation of thin films, the immersion time was 60 minutes for the experiments. The samples were then dried with a gentle stream of nitrogen for two minutes before being left in a fume hood overnight.

3.5 Tapping mode AFM

Tapping mode AFM was used to image all polymer thin films and nanostructures formed on each substrate. AFM is an extremely useful tool for imaging polymer thin films and nanostructures as it can obtain high resolution images at the nanoscale.[147] Furthermore, it does not damage the polymer surface, and does not depend on electron transfer so it can image non-conductive surfaces without having to apply a coating to the sample. This leads to an increased accuracy when imaging very small features.[54]

An AFM system usually consists of an extremely sharp tip which is mounted to a cantilever, a piezoelectric scanner, a laser diode, a feedback control centre, and a position sensitive photodetector.[186] The process of AFM imaging in tapping mode involves mounting the tip and cantilever into the piezo actuator which applies a force to the base of the cantilever. This causes the cantilever to oscillate at a frequency close to its natural resonant frequency. A laser is positioned to reflect off the back side of the cantilever, it is then reflected off a mirror before hitting the position sensitive photodetector. The amplitude of cantilever oscillation can be measured from the position of the laser on the photodetector and is kept constant via the feedback loop.[72] When the tip approaches a surface, it begins to intermittently come into contact with the surface or "tap" it. When the tip encounters a rise in surface topography the oscillation of the cantilever decreases. When the tip encounters a depression in the surface, the oscillation of the cantilever increases. The change in oscillation of the cantilever alters the reflection of the laser and changes the position of where it hits the photodetector. Measurements are made of laser intensity on the two parts (upper and lower) of the photodetector and sent to the feedback control centre. This allows the change in oscillation amplitude to be measured and a signal is sent to the piezo which adjusts the tip-sample separation in order to keep the amplitude oscillation fixed.[187] The changes in piezo height are recorded in order to build a topographical image of the sample's surface on the software.

Tapping mode has many advantages over other AFM imaging modes. It avoids problems, such as friction and adhesion in the system which occur when using contact mode. Tapping mode is particularly beneficial when imaging polymers as the tip only briefly comes into contact with the surface, meaning there is less chance of 'picking up' polymer

chains.[147] This increases image quality and reduces the chances of artefacts occurring. Figure 3.14 is an illustration outlining the components in a typical AFM system.

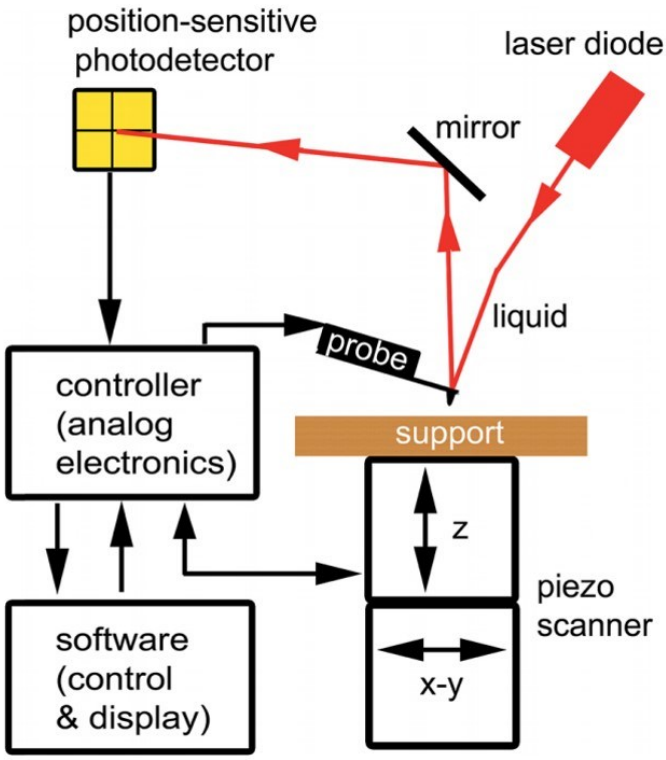

Figure 3.14: A schematic diagram outlining the experimental components in a typical AFM system.[186]

In the experiments, all AFM images were obtained using a Bruker Multimode/Nanoscope IIIa (Bruker, Santa Barbara, Ca, USA). Figure 3.15 is a photograph showing the Bruker AFM used for all imaging. Throughout the experiments, two scanners were used with different x-y ranges. For larger images, a J-scanner was used, which had an x-y range of ~160 µm. For smaller images, an E-scanner was used which provided higher image resolution over smaller length scales. The E-scanner had an x-y range of ~15 µm. The scans varied in size depending on the sample from 2 μm^2 to 150 μm^2. All imaging was carried out in air under ambient lab conditions.

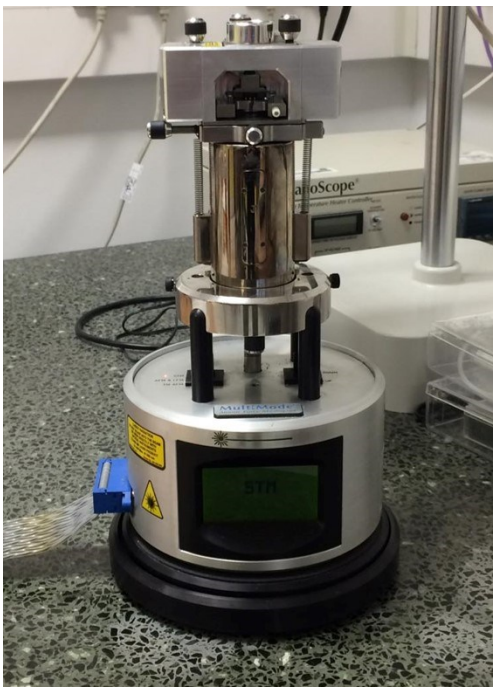

Figure 3.15: Photograph of the Bruker Multimode/Nanoscope IIIa AFM used in all experiments.

The process of carrying out AFM tapping mode imaging first involved fixing the underside of a substrate to a metallic AFM specimen disk using double sided adhesive. The disk was then mounted onto the piezo tube. Next, a probe was loaded into the AFM piezo actuator. The tip and cantilever are attached to a larger silicon mount which means the tip can be loaded into the AFM with relative ease using tweezers. The position of the laser and mirror were then adjusted in order to ensure the laser beam reflected from the backside of the cantilever to the photodetector. The position of the photodetector was then adjusted so that the reflected laser hit directly into its centre. The Nanoscope software could then be used to 'tune' the cantilever which ensured it would oscillate close to its resonant frequency during imaging. Finally, the substrate was brought into very close proximity to the surface by moving the position of the piezo tube. This was carried out using a hand lens to avoid hitting the substrate into the tip and causing damage. The tip is then engaged and scanning begins. During scanning, the amplitude set point was kept at approximately 0.6 for all of the imaging. The scans were carried out at a low frequency of approximately 0.25 Hz. This ensured an optimal image quality.

3.5.1 Tapping mode tips

An AFM tip is an extremely sharp micro-fabricated tip mounted to a cantilever.[156] The cantilever is then fixed to a silicon mount to provide ease of handling. The collective term for the tip, cantilever, and mount is often referred to as an AFM probe.

For all imaging, AFM probes were purchased from Bruker. RTESPA model probes were used due to their suitability for high sensitivity tapping mode imaging in air (see Figure 3.16). The cantilevers were rectangular with a nominal thickness of 3.75 µm and had a reflective aluminium coating on the backside to increase laser signal at the photodetector. The cantilevers had a nominal resonant frequency of 300 kHz and a nominal spring constant of 40 N/m. The tips were made of silicon and had a rotated shape, which reduced artefacts associated with asymmetry in larger features. The height of the tips were 15 - 20 µm which is considerably larger than the height of any features imaged. The tips were extremely sharp with a nominal tip radius of 8 nm, which ensured high image resolution.

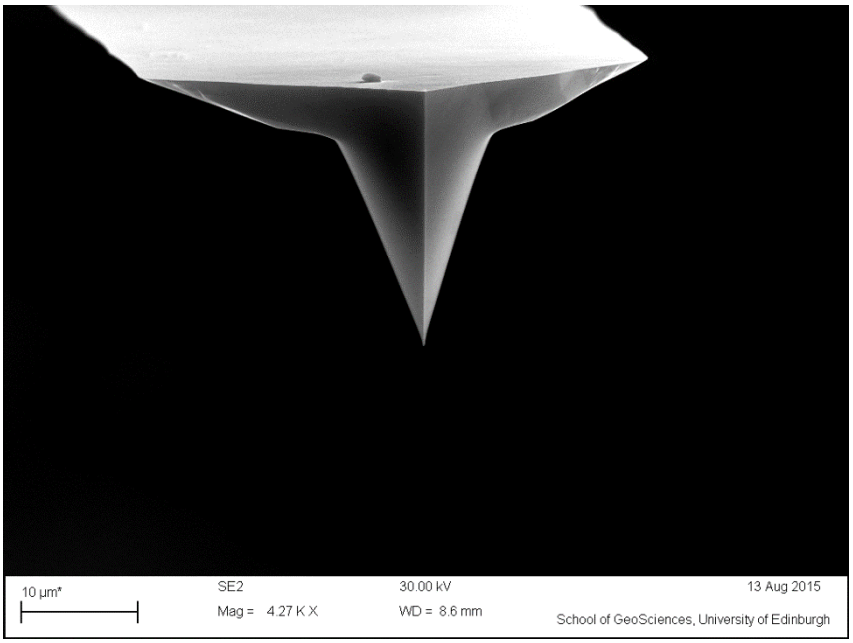

Figure 3.16: An SEM image of a Bruker RTESPA tip. This model of probes was used for all imaging in the experiments in each chapter.

3.5.2 Types of imaging

AFM tapping mode generates three types of images which all provide different information about the sample's surface. These are height images, amplitude images, and phase images. Height images show the surface topography of a sample and any contrast relates only to differences in the heights of the features.[156] Amplitude images clearly display edges and shapes within the sample and can often be used to help with qualitative analysis when contrast is poor in height images. However, the z-scale on amplitude images is meaningless, which means quantitative analysis cannot be implemented. Phase images use contrast to show the phase angle shift between the driving signal of the cantilever and the output signal. Therefore, the contrast in phase images can show differences in viscoelastic and adhesion properties of materials in an image. For example, if the material is softer, the cantilever will experience dampening at the surface, and consequently the phase angle shift will be larger. However, phase images can be somewhat ambiguous as contrast can also be affected by surface topography. Despite this, there is a strong contribution from the mechanical properties of materials in an image and clear differences in contrast often relate to different materials being present at a surface.[73,149] In all experiments, height images were primarily investigated which allowed for detailed analysis of polymer morphology to be carried out. Phase images were occasionally analysed in experiments when contrast in height images were poor, such as investigating extremely small polymer features like single polymer chains. Furthermore, phase images were used to confirm that the dewetted holes in thin films actually exposed the substrate surface. This information was necessary in order to measure film thickness using AFM techniques. Amplitude images were not used for any analysis in the experiments.

3.5.3 Image analysis

Analysis of the images was carried out using the free software Gwyddion (http://gwyddion.net/).[188] The software was used to correct the images for presentation via data processing functions such as plane levelling and removing horizontal scars. Detailed statistical analysis of the images was also implemented using Gwyddion. Size parameters of the features such as values of radius, height, and volume were obtained

using thresholding techniques. Furthermore, values for the number of features in an image and the total surface coverage were also generated.

In Chapters 4, 6, and 7, polymer morphology was mostly in the form of spherical cap nanodroplets and thin films. Therefore, analysis could be effectively carried out using thresholding techniques. However, in Chapter 5, the polymer morphology on a graphite surface was much more variable. At concentrations of 1c* and 0.1c*, the polymers consistently formed continuous networks on the graphite. In order to measure the peak-to-peak distances of these networks, fast Fourier transform (FFT) analysis was implemented using Gwyddion. Line scans were taken across the centre of the transform images to give profile plots with distinctive peaks. These peaks provided the frequencies of separation of the nanostructures in reciprocal space. A Lorentzian function was then fitted to the profile plot to obtain an exact peak position. From this, the peak-to-peak distance of the polymer network was calculated. Figure 3.17 outlines each step in the FFT analysis.

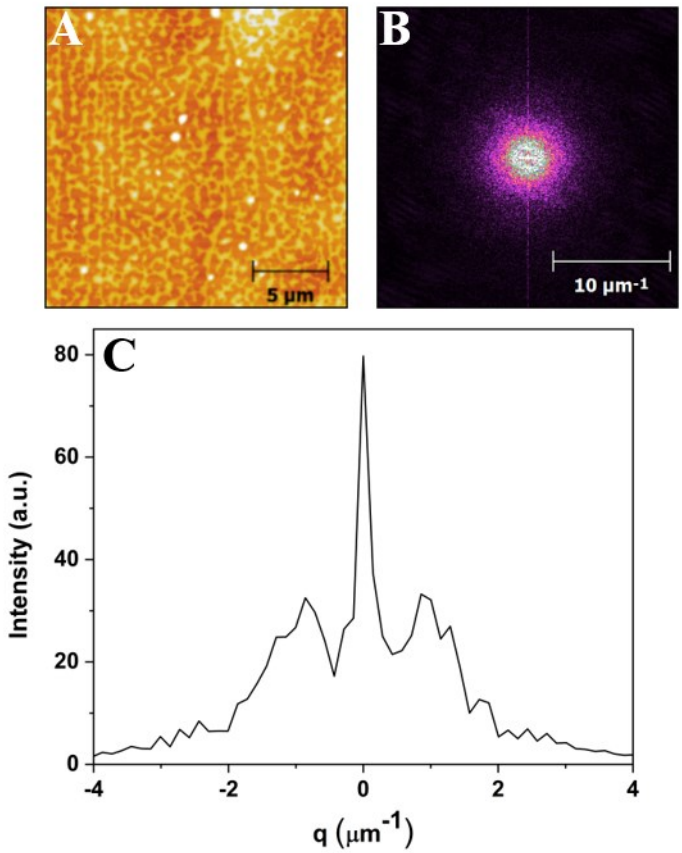

Figure 3.17: Images outlining the steps used to calculate the peak-to-peak distances of the polymer networks. (A) AFM height image of a polymer network formed on the graphite surface for the 355 kg/mol sample at 1c*. (B) An FFT image of the polymer network. (C) A profile plot of a line scan taken across the FFT, where q shows the separation of the peaks in reciprocal space.

3.5.4 Deconvolution

Convolution is the apparent increase in the width of objects when imaged using AFM. It is unavoidable and is caused by the finite size of the cantilever tip.[78] The convolution effect caused analysis of the polymer aggregates to be inaccurate, as the width of the aggregates appeared larger than in reality. This also impacted measurements that required a known width such as volume, number of chains per aggregate, and contact angle. Figure 3.18 illustrates the convolution effect during AFM imaging. For all of the experiments, deconvolution had to be implemented in order to achieve a more accurate value of the lateral size of the polymer aggregates imaged by AFM.

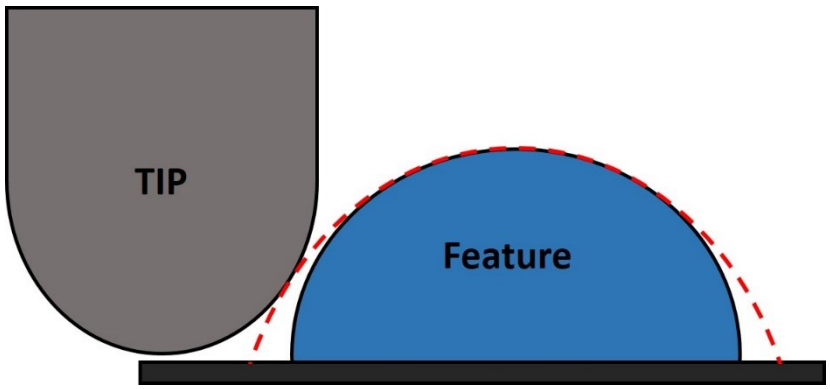

Figure 3.18: Illustration outlining how convolution arises when carrying out imaging using AFM techniques.

In Chapter 4, the polymers generally formed spherical cap shaped aggregates on the mica surface. The 'real' or deconvoluted volume of the aggregates was determined using a method developed by Glynos et al. [118] Where V_r is the real volume of the aggregate after deconvolution, V_a is the apparent volume of the aggregate, h is the height of the aggregate which is unaffected by convolution, and R_t is the radius of the AFM tip:

$$V_r = V_a - \pi h^2 R_t \tag{3.3}$$

Once the 'real' volume, V_r, was known for the aggregates then this was substituted into the equation for the volume of a spherical cap and thus, rearranging gave a value for the 'real' contact radius, r_r:

$$r_r = \sqrt{\frac{2V_r - \frac{1}{3}\pi h^3}{\pi h}} \tag{3.4}$$

The number of chains in each aggregate was then found by calculating the volume of a single chain by its number average molecular weight M_n, and its density, ρ:

$$V_c = \frac{\left(\frac{M_n}{N_A}\right)}{\rho} \tag{3.5}$$

Where N_A is Avogadro's number, and V_c is the volume of a single polymer chain. The density of the poly(styrene-co-butadiene) copolymers was assumed to be equal to their bulk values (~0.95 g/cm^3).[4] The total 'real' volume, V_r was then divided by the volume of a single polymer chain to provide a value of how many chains made up each aggregate.

In Chapter 5, polymer morphology was far more variable on the graphite surface. Therefore, multiple deconvolution methods were adopted to account for each type of polymer feature. Also, the polymer feature widths were measured rather than radii. At some concentrations, the polymer formed more elongated structures on the surface, such as ribbons or networks. Cross-sections were taken of these structures to measure their apparent widths, W_a. In order to measure the real width, W_{el}, of these elongated structures, a method was adopted from Fung et al.[189] who developed a technique of deconvolution for oligopeptides on a surface:

$$W_{el} = W_a - 2\sqrt{h(2R_t - h)} \tag{3.6}$$

Where h is the height of the structures. This method was adopted as the oligopeptides in Fung et al. study had similar morphologies to the polymer nanoribbons or networks formed on the graphite surface. Therefore, giving a good estimation of the real lateral size of the polymer structures.

Individual polymer aggregates (nanoislands) also formed on the graphite. However, they were not uniform in shape as some were spherical cap shaped and others were more elongated. In order to determine which deconvolution method was appropriate for the

individual aggregates, their eccentricity ε, was measured to identify how circular or elliptical an aggregate was. The eccentricity was defined as:

$$\varepsilon = \sqrt{1 - \frac{{b_l}^2}{{a_l}^2}} \tag{3.7}$$

Where b_l is length of the minor axis (width), and a_l is the length of the major axis (length). When ε ranged from 0.6 – 1, the features had a more elongated shape and Equation 3.6 was used to calculate the width of the features. When ε ranged from 0 – 0.6, the droplet could be considered a spherical cap and the following equation was used to give the real width, W_{cap}, of the spherical cap shaped aggregates:

$$W_{cap} = 2\sqrt{\frac{2V_r - \frac{1}{3}\pi h^3}{\pi h}} \tag{3.8}$$

3.5.5 Contact angles of nanostructures

In Chapter 4, contact angle measurements were carried out on polymer nanodroplets that formed on the mica surface. The contact angles of the aggregates were calculated geometrically using the aggregates 'real' contact radius, r_r, and the aggregates height, h:

$$\frac{\theta}{2} = \tan^{-1}\left(\frac{h}{r_r}\right) \tag{3.9}$$

This method gives reliable results when the shape of the aggregate is a spherical cap and the aggregates are small enough to not be affected by gravity. This was the case with the nanodroplets in this study.[64]

In Chapter 5, polymer morphology on the graphite surface was variable. Some aggregates were more spherical cap shaped and this meant that Equation 3.9 could be used to calculate contact angle values. However, many of the aggregates were less uniform in shape. Therefore, in order to achieve reasonable contact angle values for the less

uniformly shaped aggregates, such as network features or asymmetrical nanoislands, multiple line scans were taken along the profile of each aggregate. Individually, the line scans across the features appeared as 2D cap shaped and thus, the contact angle along that profile was measured using Equation 3.9. Therefore, the average contact angles of the multiple line scans were calculated to give an overall value for each aggregate. Figure 3.19 shows profile plots of polymer features at each concentration (networks, asymmetrical nanoislands, and nanoribbons) fitted to spherical caps.

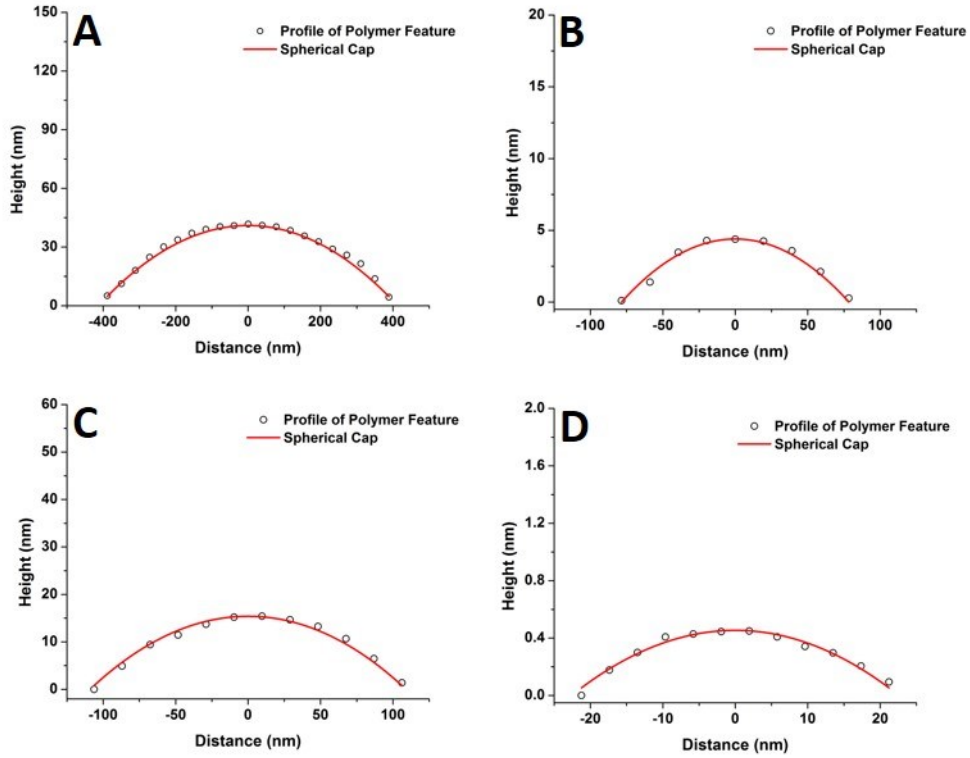

Figure 3.19: Cross-sectional profile plots of typical polymer features formed at each concentration on the graphite surface. The cross-sections were fitted to spherical caps. (A) 1c* for the M_n = 86 kg/mol sample. (B) 0.1c* for the M_n = 46 kg/mol sample. (C) 0.01c* for the M_n = 86 kg/mol sample. (D) 0.001c* for the 46 kg/mol sample.

3.6 AFM force spectroscopy

AFM can also be used to obtain quantitative data regarding the strength of interaction forces between different materials. This mode of operation is known as force spectroscopy. The setup of the AFM is the same for both force spectroscopy and imaging.

The process of AFM force spectroscopy involves bringing a tip into contact with a substrate's surface. The substrate is then pushed against the tip to induce concave deflection in the cantilever up to a fixed amount of force. Piezo movement then begins to separate the tip and the substrate surface. However, adhesion forces between the tip and the substrate mean that the tip is held in contact with the substrate. This causes the cantilever to deflect in a convex orientation, whilst the tip remains at the substrate. Consequently, the changes in cantilever deflection cause the laser position on the photodiode to change. The variations in laser position on the photodiode are measured and a value of the cantilever deflection is generated. As the tip-sample separation is increased further, the tip is released from the substrate. The interaction forces between the sample and the tip, *F*, can be calculated using Hooke's law:

$$F = kx \tag{3.10}$$

Where k is the spring constant of the AFM cantilever and x is the deflection of the cantilever expressed as a distance.

All force spectroscopy experiments were also carried out using the Bruker Multimode/Nanoscope IIIa (see Figure 3.15). The J-scanner was used in all experiments. The approach/retract cycles were either carried out at a fixed point on the surface, or in an array where the horizontal and vertical steps were 500 nm. The delay time (time before each approach) was set at 1 second for all experiments. The contact time (contact time between tip and substrate before retracting) was also kept at 1 second for all experiments unless explicitly stated otherwise. All experiments were carried out in air under ambient lab conditions.

The process of the force spectroscopy experiments is similar to the process outlined for AFM imaging in Section 1.5. However, there are some fundamental differences. First, calibration of the AFM cantilever must be carried out. This involves loading a hard, clean substrate onto the piezo tube. To achieve consistent results, the calibration substrate must be the same in all experiments. For the experiments presented in Chapters 6 and 7, freshly cleaved mica was always used as the calibration substrate. The probe was then loaded into the AFM and the laser was aligned to reflect off the cantilever and hit the photodetector at its centre. As the cantilever did not oscillate during the experiments, no tuning was required. The tip-sample separation was reduced manually and the tip was

then engaged with the surface. Parameters such as delay time, contact time, z-range, and cantilever spring constant were then set. A single approach/retract cycle was carried out on the substrate which produced a standard force-distance curve showing short range adhesion forces. From the force-distance curve, calibration was carried out using the software which determined the sensitivity of the system. This measures how the deflection of the cantilever in nanometres related to the laser movement on the photodetector in volts. An inverse optical laser sensitivity (InvOLS) value was generated, which allowed the system to convert the movement of the laser on the photodetector into deflection of the cantilever. Once calibration was completed, the mica substrate was replaced with the substrate required for the current experimentation. Care was taken not to change the laser alignment at this point, as this would mean recalibration was required.

3.6.1 Force spectroscopy tips

For all force spectroscopy experiments, MSNL-10 model tips were used which were purchased from Bruker. The cantilevers were made of silicon nitride and had a nominal thickness of 0.55 μm. The cantilevers had a triangular geometry and a low nominal spring constant of 0.01 N/m. Soft cantilevers were required to improve the lowest detectable force value in the system, and therefore improve the force resolution. The MSNL-10 cantilevers are extremely sensitive as 10 pN of force resulted in a deflection of 1 nm. The cantilevers had a reflective gold coating on the backside to increase the intensity of the laser signal at the photodetector. The tips were made from silicon and had a rotated geometry. The tip height is 2.5 - 8.0 μm, which is far greater than any features investigated. The tips are extremely sharp with a nominal radius of 2 nm.

3.6.2 Force-distance curve analysis

The force spectroscopy experiments generated force-distance curves. Force-distance curves were analysed to extrapolate information regarding the strength and type of interactions between the polymers and substrates. Initially, the force-distance curves were converted into text documents using the free software Nanoscope Analysis. From

this, graphs were generated using the software Origin. In cases where clear polymer/substrate interactions were observed, such as single chain desorption events, graphs representing force against tip-sample separation were more appropriate. It was calculated that any error associated with InvOLS was minor and would not affect the overall results. The total adhesive force for each graph was found using the minimum force value in the data. The total adhesive energy was calculated by integrating the complete area above each curve in the fourth quadrant of the force-separation graphs using Origin. Individual events were analysed using an Origin plugin which allowed the distance between two points to be measured. This meant the distance between events, force of events, and tip-sample separation at events could be accurately measured. The adhesive energy per segment (E_s) was calculated by first integrating the area above the curves in the fourth quadrant where only force plateaus and steps occurred. This gave the total adhesive energy across the force plateaus and steps, E_f, which could be used to calculate adhesive energy per segment with the following equation:

$$E_s = \frac{E_f b}{L_l} \tag{3.11}$$

Where b is Kuhn length, and L_l is the length of the force plateaus and steps.

Thermal noise is present in all curves generated by force spectroscopy.[190] This is due to the constant fluctuations in air caused by factors, such as Brownian motion.[50] As the tips are extremely soft (low spring constant), they are affected by these thermal fluctuations. This creates noise in force-distance curves which reduces the force resolution in the system. However, the magnitude of the noise was small and could only be observed when a small part of a curve was zoomed into. Figure 3.20 shows a full force-separation curve and a zoomed area of the same curve. Noise is only visible in the zoomed curve in Figure 3.20B. From this curve, it is clear that the fluctuations due to noise had a significantly smaller magnitude than any desorption events. Analysis was carried out on multiple curves in order to measure the magnitude of the noise in the experiments. The magnitude of the thermal noise was calculated to be 3.2 pN. This is over a factor of ten times smaller than the average force of desorption events on each substrate. This shows that any effects from thermal noise were negligible, as desorption events can clearly be identified and measured on the curves.

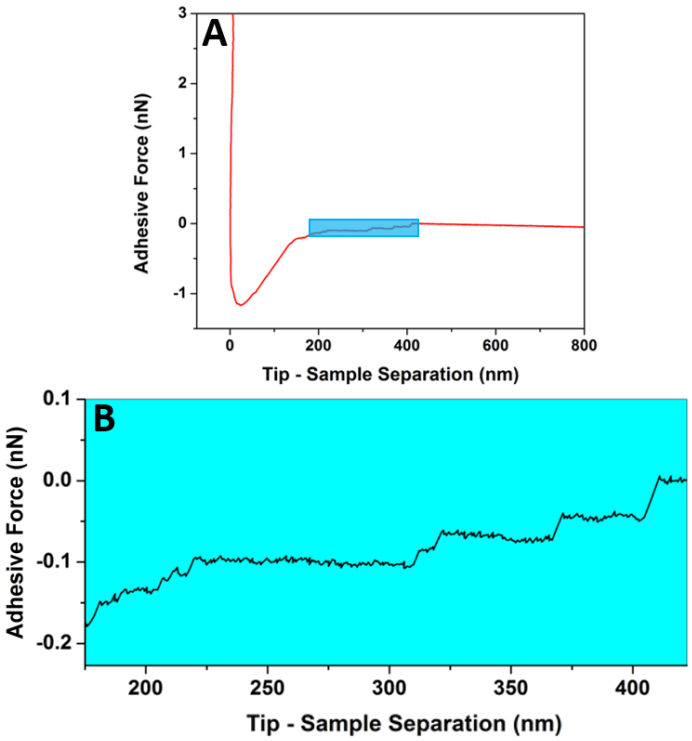

Figure 3.20: A typical force-separation curve for a blank AFM tip interacting with a poly(styrene-co-butadiene) thin film on a silicon substrate. (A) The complete curve with no observable noise. (B) A zoomed in section of the curve, which is represented by the blue box in graph (A).

3.7 Macroscopic contact angle measurements

Macroscopic droplets were prepared by depositing small pieces of bulk polymer samples onto the mica surface, followed by thermal equilibration of the samples in an oven at 40˚C. This resulted in polymer droplets forming on the mica surface (see Figure 3.21). These droplets had radii ranging from approximately 1 – 5 mm, and volumes from 0.2 – 50 mm^3. The 46 kg/mol samples required 24 hours to reach equilibrium, whilst the 86 kg/mol samples required seven days. After over eight weeks in the oven, the polymer with a molecular weight of 355 kg/mol did not form droplets on the surface. Therefore, no macroscopic contact angle measurements were possible for this sample. Macroscopic contact angle measurements were carried out using a KRÜSS Drop Shape Analyser DSA30S at ambient temperatures. Measurements were taken after the samples had been left for one week at ambient temperatures. Macroscopic contact angle measurements of

polymer droplets on graphite surfaces were also carried out. However, due to difficulties in optimising experimental parameters, only a small amount of data was obtained (see Appendix). Therefore, the results were only preliminary and this area remained an avenue for future work.

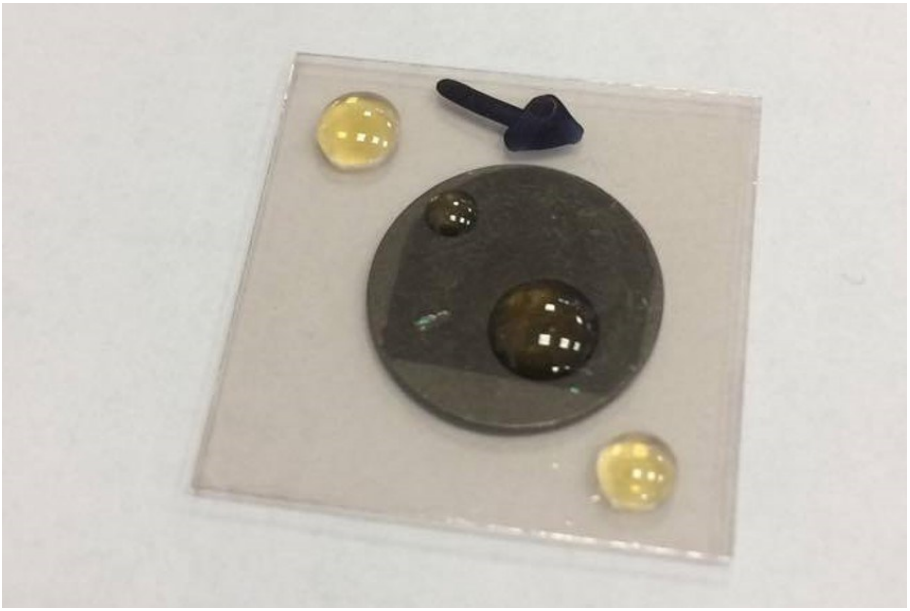

Figure 3.21: Photograph showing macroscopic droplets of the 86 kg/mol poly(styrene-co-butadiene) on a mica surface.

3.8 Viscosity measurements

The viscosity of polymer solutions were measured for the 46 kg/mol, 86 kg/mol and 355 kg/mol samples at a concentration of 1c*. Furthermore, the viscosity of toluene was also measured. All measurements were carried out on a Thermo Scientific HAAKEMARS Rheometer. Parallel plate geometry was used for each measurement, and the temperature was set at 20˚C. The shear rate range for the experiments was set at 0 to 50 s^{-1}.

3.9 Conclusions

The behaviour of polymers on various substrates at the nanoscale has been comprehensively investigated using AFM techniques. Three molecular weights of poly(styrene-co-butadiene) random copolymers were prepared in toluene solutions according to the individual polymer's overlap concentration values. Additionally, polystyrene and polybutadiene homopolymers were prepared using identical methods. The polymer solutions were deposited onto mica, graphite, and silicon substrates, and the formation of thin films and nanostructures was observed. The deposition methods used in the experiments were spin coating and dip coating. The polymers were spin coated onto freshly cleaved mica and graphite substrates, at various concentrations and molecular weights. The polymers exhibited various morphologies on each substrate including thin films, spherical cap nanodroplets, continuous networks, asymmetrical nanoislands, and nanoribbons. All imaging of the spin coated films took place in close proximity to the centre of the substrates to improve consistency of results. Dip coating was implemented in order to coat AFM tips and each substrate with polymer chains in a non-destructive way.

Tapping mode AFM imaging was used to analyse the polymer morphology on each substrate at the nanoscale. All imaging was carried out in air, under ambient conditions. Complete analysis of the polymer morphology was carried out using the freeware Gwyddion. This included FFT analysis to provide peak-to-peak distances of polymer networks. Deconvolution methods are presented for polymer features of varying morphologies, which allowed for an accurate measurement of the lateral size of the features to be achieved. Furthermore, a method for calculating the contact angle of various polymer features using AFM is presented.

AFM force spectroscopy was utilised to measure the fundamental interactions between polymers and various substrates. All force spectroscopy experiments were carried out in air, under ambient laboratory conditions. A soft cantilever with a low spring constant was used in order to achieve a high force resolution. Comprehensive analysis of the force-distance curves was carried out which provided information regarding the total adhesive force, total adhesive energy, and specific interactions. Thermal noise was present in the curves, but its magnitude was small and therefore did not affect analysis.

Complementary experiments were carried out on macroscopic polymer samples/solutions. Viscosity measurements were taken of polymer solutions with different molecular weights at a fixed concentration. Contact angle goniometry was used to study the effect that polymer droplet size has on contact angle, at the macroscale.

4 Polymer morphology on a mica surface

Summary

This chapter presents an AFM investigation of the morphology of adsorbed poly(styrene-co-butadiene) random copolymers on a mica surface. Polymer solutions with varying molecular weights and concentrations were deposited onto mica surfaces using spin coating. Differences in morphology, depending on concentration and molecular weight, have been observed directly in real space. Furthermore, it was demonstrated that the contact angles of the nanodroplets were size dependent and exhibited a specific trend regardless of molecular weight.

4.1 Introduction

Many applications depend on polymers functioning at surfaces. These include, functional membranes,[146] nanoelectronics,[33] biofouling,[86] and composite materials.[47] However, the understanding of how these polymers interact with surfaces at the nanoscale is incomplete. It is well documented that polymers behave differently in the bulk compared to at an interface,[191–193] although the drivers for these behavioural changes remains under investigation. A greater understanding of how polymers behave in the vicinity of a surface at a fundamental level is essential to promote the intelligent design of composite materials and polymers at interfaces.

Comprehensive studies have been carried out investigating the morphology of many different types of polymers on surfaces using AFM. These include end-grafted polymers where pinned micelles form on a surface,[194,195] polymer blends and their phase separation on surfaces,[191,196,197] and diblock copolymers where terraced or layered structures are formed.[73,108,198] Some research has been carried out investigating the morphology of crystalline homopolymers on surfaces, where crystalline nanolamellae can form.[112,114] However, research on amorphous homopolymers is much less common, especially in the area of physisorbed homopolymers or random copolymers. This is somewhat surprising, as these important polymers dominate commercial applications in both the polymer industry and composite materials.

Contact angle studies are also an area of intensive research investigating the wetting properties of liquids on different surfaces. While the wetting phenomena of various liquids at the macroscale are well understood, the study of contact angles at the nanoscale is much less common. [64] It is hypothesised that specific factors that may have very little influence at the macroscale can have a much larger impact at the nanoscale. These factors include surface heterogeneities, as topographical changes over very small length scales have minimal impact on the contact angle of macroscopic droplets. However, at the nanoscale, these topographical changes have a much larger effect on a droplet's contact angle.[122,199] Line tension is another factor that may affect the contact angle of nanodroplets. In the nanoscale, Young's equation must be altered to include line tension to allow for the influence of surface curvature and the specific free energy of the three-phase contact line. However, the magnitude of the effect of line tension is not

currently known, nor is the sign of line tension and this is what affects the size dependence of the contact angles.[92,122,124] Another proposal suggests that below a critical value, polymer nanodroplets exhibit an increased elastic modulus which increases dewetting.[28,200]

This chapter elucidates several fundamental aspects of polymer behaviour on surfaces for a random copolymer system on a weakly adsorbing mica substrate. This proves the complex interplay of many factors in the formation of polymer nanostructures, despite the simplicity of the system. The random monomer composition in the polymer chains results in a copolymer that effectively behaves as an amorphous homopolymer. Three different poly(styrene-co-butadiene) molecular weights were spin coated onto cleaved mica surfaces. A large range of concentrations was investigated, which allowed an examination into phenomena from thin film formation and dewetting to nanoscopic droplets and single polymer chains. Experiments were carried out at three distinctly different molecular weights and results showed that molecular weight had a significant impact on the morphology of the polymer nanostructures. Finally, a detailed exploration of the contact angles of the polymer droplets both at the nanoscale and macroscale is presented.

4.2 Materials and methods

All experiments were carried out using three molecular weights of poly(styrene-co-butadiene) random copolymers (46 kg/mol, 86 kg/mol, and 355 kg/mol). The samples were monodisperse and had styrene-butadiene ratios of approximately 25:75. The samples were well below their T_g's at room temperature and their molecular weights were well above their entanglement molecular weights. The polymers were prepared in toluene at five different solution concentrations (3c*, 1c*, 0.1c*, 0.01c*, and 0.001c*). The polymers were deposited onto freshly cleaved mica using spin coating with fixed parameters.

All imaging of the samples was carried out using tapping mode AFM in air at room temperature. The AFM model was a Bruker Multimode/Nanoscope IIIa, and RTESPA probes were used for all imaging. The sizes of the scans varied from 2 - 150 μm^2. All

analysis of polymer morphology was carried out on the software Gwyddion. Deconvolution was implemented (see Chapter 3 for details) to provide accurate measurements of the lateral size of nanostructures. AFM techniques were used to measure the contact angles of the cap shaped nanodroplets. Additional techniques used throughout the experiments included viscosity measurements on a HAAKE MARS Rheometer and contact angle goniometry using a KRÜSS Drop Shape Analyser DSA30S.

4.3 Results and discussion

4.3.1 AFM images and profile plots

AFM height images were obtained from five different polymer solution concentrations varying from very dilute to above the overlap concentration. Figures 4.1 - 4.3 show representative images for each molecular weight (46 kg/mol, 86 kg/mol, and 355 kg/mol) of the poly(styrene-co-butadiene) samples. Additionally, typical profile plots are presented for each image, whereby each plot was taken as a complete horizontal line across the image. These profile plots provide a greater insight into the surface morphology of the samples.

4.3.1.1 M_n = 46 kg/mol

Figures 4.1A and 4.1B show that a mostly continuous thin film formed on the surface at 3c*, only broken by several circular holes with depths ranging from 2.4 nm to 26 nm. Numerous aggregates were also present on the surface with heights ranging from 16 nm to 36 nm. At lower concentrations (1c* - 0.001c*), the polymer formed spherical cap shaped aggregates on the mica surface. The sizes of the aggregates varied dramatically with solution concentration. Figures 4.1C and 4.1D show that at 1c*, the aggregates were polydisperse with radii and heights ranging from 10 nm to 910 nm, and 5.6 nm to 241 nm, respectively. Figures 4.1E and 4.1F show that at 0.1c*, the aggregates had a much narrower range of radius and height values than at 1c*, ranging from 14 nm to 361 nm, and 3.9 nm to 21 nm, respectively. Some droplet coalescence was observed which created longer, thinner aggregates. Figures 4.1G and 4.1H show that at 0.01c*, the

aggregates radii and heights ranged from 8.4 nm to 78 nm, and 1.5 nm to 11 nm, respectively. Figures 4.1I and 4.1J show that at 0.001c*, there was very little polymer present on the mica surface. Very small nanodroplets formed with radii and heights ranging from 5.1 nm to 44 nm, and 2.3 nm to 7.7 nm, respectively. The range of radii and heights were smallest at this concentration.

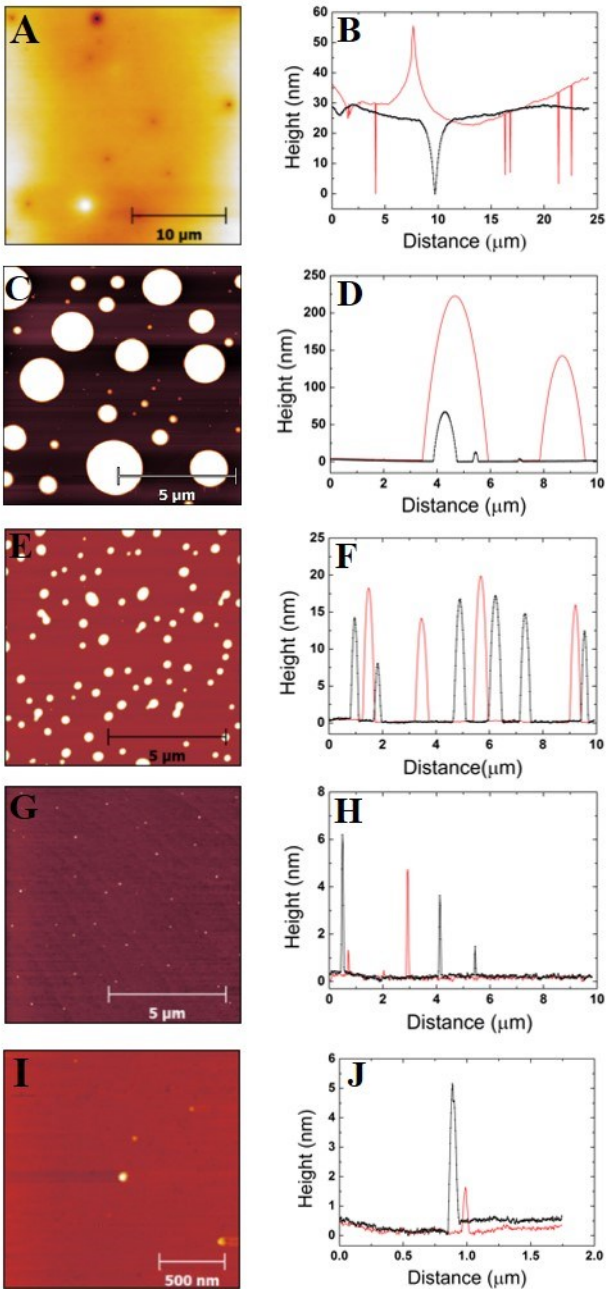

Figure 4.1: A series of AFM height images and profile plots for the 46 kg/mol sample at varying concentrations on a mica surface. The profile plots correspond with horizontal line scans taken from the AFM image. (A) 3c* = 17.43 mg/ml, (B) profile plot at 3c*, (C) 1c* = 5.81 mg/ml, (D) profile plot at 1c*, (E) 0.1c* = 0.581 mg/ml, (F) profile plot at 0.1c*, (G) 0.01c* = 0.0581 mg/ml, (H) profile plot at 0.01c*, (I) 0.001c* = 0.0058 mg/ml, (J) profile plot at 0.001c*.

4.3.1.2 M_n = 86 kg/mol

Figures 4.2A and 4.2B show the polymer morphology at 3c* where a mostly continuous polymeric thin film formed on the surface. However, some dewetting was observed, characterised by the large circular aggregates with holes around them. The depth of these holes ranged from 2.2 nm to 17 nm, and the height of the aggregates ranged from 9.2 nm to 634 nm. Once again, spherical cap shaped aggregates formed at all lower concentrations. Figures 4.2C and 4.2D show that at 1c*, the aggregates had the largest ranges of radii and heights from 16 nm to 1.1 μm, and 2.1 nm to 411 nm, respectively. Figures 4.2E and 4.2F show that at 0.1c*, the aggregates radii and heights ranged from 4.7 nm to 383 nm, and 3.4 nm to 46 nm, respectively. Figures 4.2G and 4.2H show that at 0.01c*, the range of aggregates radii and heights were lower than 1c* and 0.1c* with values from 6.2 nm to 92 nm, and 1.3 nm to 12 nm, respectively. Figures 4.2I and 4.2J show at 0.001c*, very small aggregates were observed with radii and heights ranging from 3.7 nm to 35 nm, and 1.4 nm to 6.7 nm, respectively. As with the 46 kg/mol sample, the average range of radii and heights of the aggregates were lowest at this concentration.

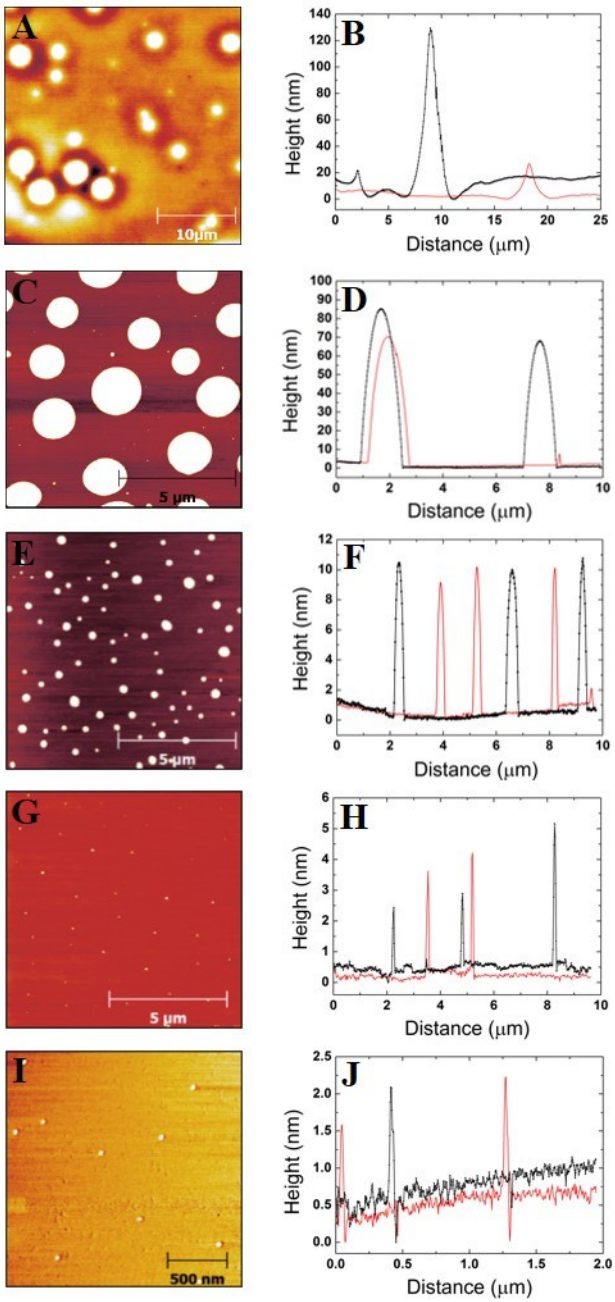

Figure 4.2: A series of AFM height images and profile plots for the 86 kg/mol sample at varying concentrations on a mica surface. The profile plots correspond with horizontal line scans taken from the AFM image. (A) 3c* = 11.13 mg/ml, (B) profile plot at 3c*, (C) 1c* = 3.71 mg/ml, (D) profile plot at 1c*, (E) 0.1c* = 0.371 mg/ml, (F) profile plot at 0.1c*, (G) 0.01c* = 0.0371 mg/ml, (H) profile plot at 0.01c*, (I) 0.001c* = 0.0037 mg/ml, (J) profile plot at 0.001c*.

4.3.1.3 Mn = 355 kg/mol

Figures 4.3A and 4.3B show that at 3c*, a mostly continuous thin film formed on the surface. Dewetting was observed in the film, and there were a number of large holes with depths ranging from 2.9 nm to 32 nm which exhibited raised outer rims. Aggregates were observed on the film with heights ranging from 8.7 nm to 342 nm. At 3c*, there was a larger degree of dewetting for this sample compared to the two lower molecular weights. Similarly to the previous molecular weights, spherical cap shaped aggregates were observed at all other concentrations. Figures 4.3C and 4.3D show that at 1c*, aggregate radii and heights ranged from 95 nm to 1.1 μm, and 26 nm to 211 nm, respectively. Figures 4.3E and 4.3F show that at 0.1c*, fairly uniform aggregates were formed with a narrower range of radii (16 nm to 324 nm) and heights (2.9 nm to 191 nm) compared to the 1c* sample. Figures 4.3G and 4.3H show that at 0.01c*, uniform aggregates were formed with radii and heights ranging from 6.8 nm to 72 nm, and 2.2 nm to 29 nm, respectively. Figures 4.3I and 4.3J show that at 0.001c*, very small aggregates formed with aggregate radii and heights ranging from 7.9 nm to 63 nm, and 1.1 nm to 10 nm, respectively.

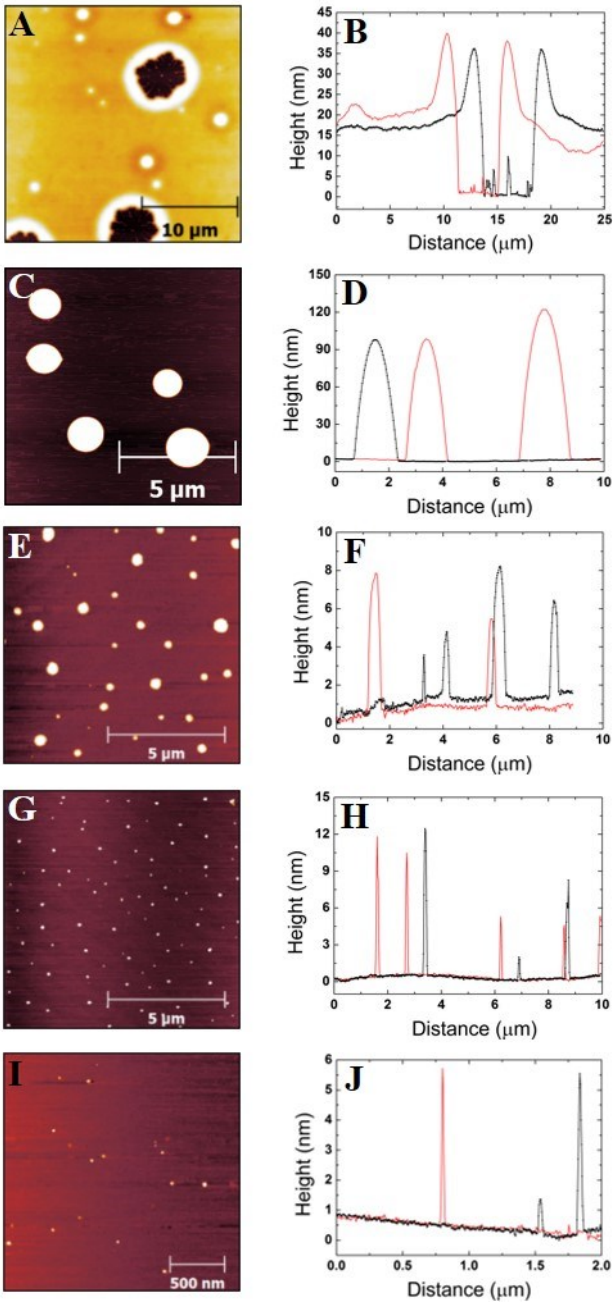

Figure 4.3: A series of AFM height images and profile plots for the 355 kg/mol sample at varying concentrations on a mica surface. The profile plots correspond with horizontal line scans taken from the AFM image. (A) 3c* = 4.17 mg/ml, (B) profile plot at 3c*, (C) 1c* = 1.39 mg/ml, (D) profile plot at 1c*, (E) 0.1c* = 0.139 mg/ml, (F) profile plot at 0.1c*, (G) 0.01c* = 0.0139 mg/ml, (H) profile plot at 0.01c*, (I) 0.001c* = 0.0014 mg/ml, (J) profile plot at 0.001c*.

4.3.1.4 Spherical cap shape of nanodroplets

In order to confirm that the nanodroplets were spherical cap shaped, cross-sectional profile plots of individual droplets were fitted to spherical caps. The equation used to fit the spherical cap profile was:

$$Z = h - r_r + \sqrt{r_r^2 - x^2} \tag{4.1}$$

Where Z is the vertical coordinate, h is the height of the nanodroplet, r_r is the contact radius of the spherical cap, and x is the horizontal coordinate. Figure 4.4 shows an example of a typical cross-sectional profile plot of a nanodroplet fitted to a spherical cap. From the results, it is clear that the profiles of the nanodroplets were fitted well with the 2D equation, confirming that the droplets themselves were spherical caps.

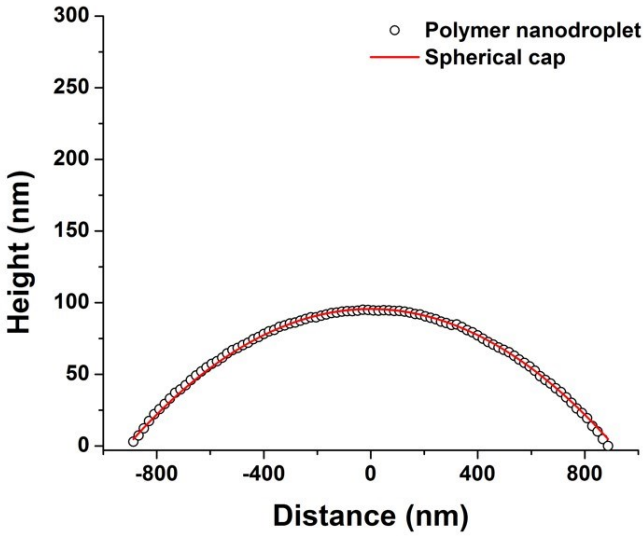

Figure 4.4: A typical cross-sectional profile plot of a poly(styrene-co-butadiene) random copolymer nanodroplet fitted to a spherical cap.

4.3.1.5 Data analysis

In the graphs which exhibit individual points with vertical bars, each point on the graphs represents an average value of either height, radius, number of chains per aggregate, number of aggregates, or contact angle at a given concentration or molecular weight. These average values of aggregate morphology were taken from a large array of individual aggregates. The bars on the plots are not error bars; they represent the overall range of aggregate values by showing the maximum and minimum values for each array. The reason for this was to examine the distributions of aggregate size at each concentration or molecular weight and observe the level of polydispersity in the aggregate dimensions for each of these parameters. In Figure 4.5, typical histograms for each measured parameter at 0.01c* are presented for the 46 kg/mol sample. The typical histograms show both asymmetrical and symmetrical distributions, and it is clear that bars representing standard deviation were not appropriate for many of the data points as they did not have a normal distribution. The error in the z-direction for AFM measurements was in the sub-nanometer scale, which is at the size of the symbols used (or smaller). Furthermore, deconvolution was implemented (see Chapter 3) which meant the error in the x-direction was also extremely small. Error in both x and z directions was estimated to be less than 1%.

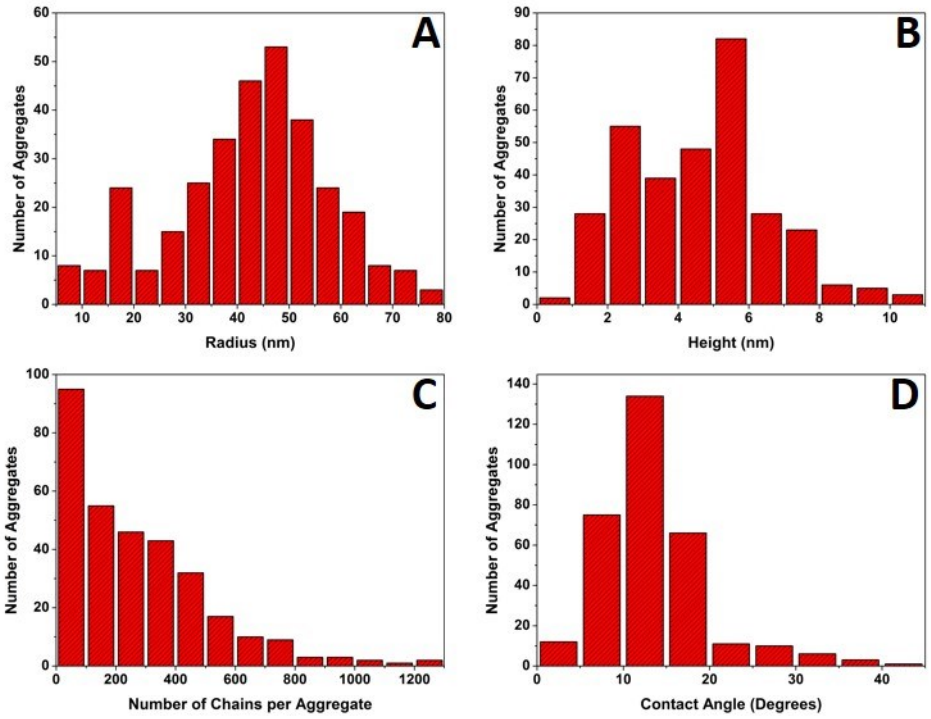

Figure 4.5: Typical histograms showing the distribution of aggregates for each parameter for the 46 kg/mol sample at a concentration of 0.01c*. (A) Radius, (B) height, (C) number of chains per aggregate, (D) contact angle.

4.3.2 Concentration effects

4.3.2.1 Size distributions of aggregates

Figure 4.6 shows how the radius of the aggregates varied with concentration at each molecular weight. The aggregate radius increased non-linearly with increasing concentration; the range of aggregate radii was largest at 1c* and it decreased with decreasing concentration across all molecular weights. The aggregates formed at 1c* were polydisperse, but at the lowest concentrations the aggregates were more monodisperse with consistently small radii. The radius of the aggregates varied considerably, but their spherical cap shape was independent of individual aggregate size. Polymers on non-wetting surfaces in a poor solvent (in this case air), form aggregates of spherical cap shapes to minimise free energy.[201]

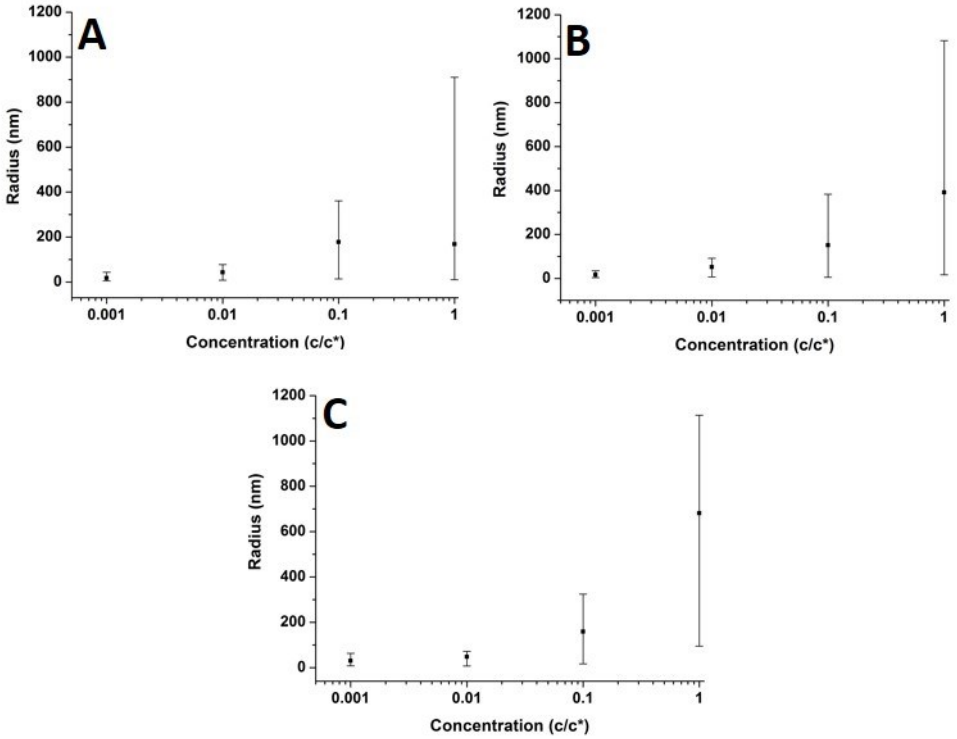

Figure 4.6: Graphs showing the relationship between the radius of the polymer aggregates and concentration on the mica surface at varying molecular weights. Each graph presents the average values and has bars which indicate the range of values. (A) M_n= 46 kg/mol, (B) M_n= 86 kg/mol, (C) M_n= 355 kg/mol.

Figure 4.7 shows that the height of the aggregates increased with increasing concentration for each of the three molecular weights. This trend was similar to the relationship between aggregate radius and concentration, as the overall height and the range of heights were largest at the higher concentrations. At higher concentrations, there were many polymer chains present at the surface during the solvent evaporation and drying processes. This allowed (via entanglements) the creation of some aggregates with larger sizes. Conversely, at lower concentrations, there were simply not enough chains at the surface for large aggregates to form, leading to a much smaller range of aggregate sizes.

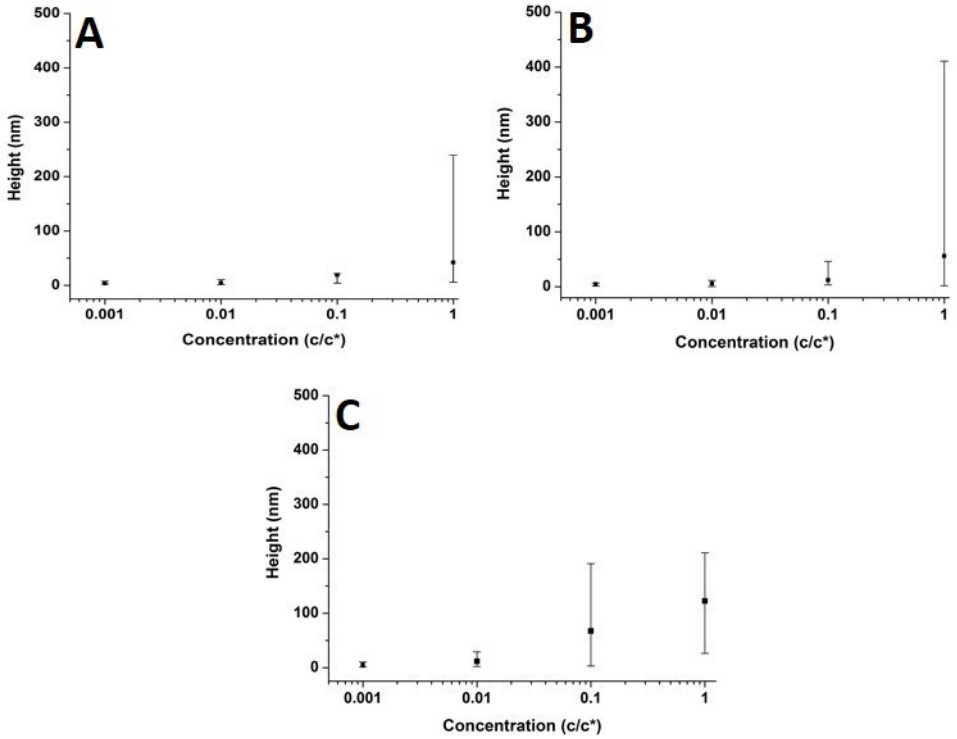

Figure 4.7: Graphs showing the relationship between the heights of the polymer aggregates and concentration on the mica surface at varying molecular weights. Each graph presents the average values and has bars which indicate the range of values. (A) M_n= 46 kg/mol, (B) M_n= 86 kg/mol, (C) M_n= 355 kg/mol.

4.3.2.2 Number of chains per aggregate and single chain nanodroplets

Figure 4.8 shows that the number of chains per aggregate increased with concentration. At higher concentrations, the aggregate size was generally larger, and therefore the individual aggregates were made up of more polymer chains. Similarly with aggregate radius and height, the range of number of chains per aggregate was much larger at higher concentrations. At the lowest concentration (0.001c*), the average number of chains per aggregate at each molecular weight was consistently small (14 - 41), showing that aggregates formed which contained very few polymer chains. Although, single chains were observed most frequently at 0.001c*, some single chains were also present at higher concentrations. For the 46 kg/mol sample in Figure 4.8A, the average height of the single chains was 2.5 nm and the average radius was 4.4 nm. For the 86 kg/mol sample in Figure 4.8B, the average height of the chains was 3.3 nm and the average radius

was 5.2 nm. For the 355 kg/mol sample in Figure 4.8C, the average height of the chains was 3.1 nm and the average radius was 6.5 nm. As a polymer chain adsorbed flat on a surface has a characteristic height and width of ~0.4 nm,[109,125] these results showed that single chains on mica do not lie flat at the interface. A single hydrophobic polymer chain will instead create a globule, folding on itself to dewet the hydrophilic mica surface. This behaviour reduces surface contact, which is very similar to the behaviour of the larger aggregates.

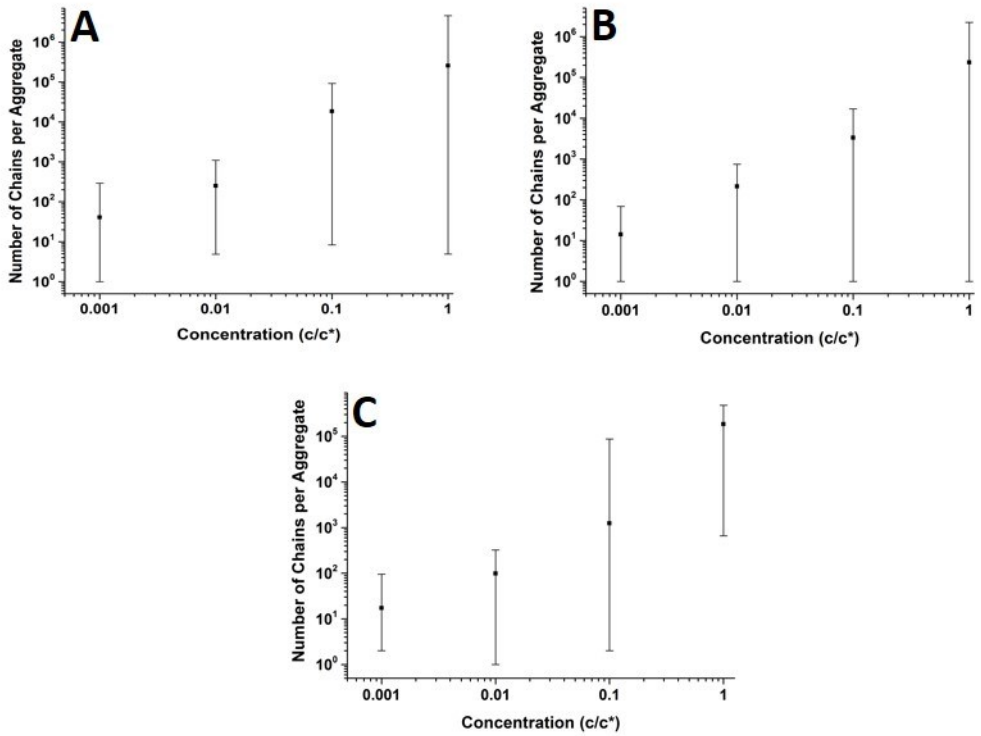

Figure 4.8: Graphs showing the relationship between the number of chains per aggregate and concentration on the mica surface at varying molecular weights. Each graph presents the average values and has bars which indicate the range of values. (A) M_n= 46 kg/mol, (B) M_n= 86 kg/mol, (C) M_n= 355 kg/mol.

4.3.2.3 Thin film morphology

At 3c*, across all molecular weights, the polymers formed mostly continuous thin films on the mica surface and not spherical cap shaped aggregates. Often polymer thin films are not homogenous and flat, but are unstable. For instance, when polystyrene thin films are annealed above their T_g, they become unstable and dewetting occurs,[98,202] while

stability and smoothness is maintained below the T_g in the spin-coated films. For each molecular weight, the poly(styrene-co-butadiene) films, which were well above their T_g values, experienced partial dewetting on the mica surface. This dewetting phenomenon can generally be separated into three stages. First, many small cylindrical holes are formed in the film, this is often thought to occur due to unstable rapid nucleation caused by small imperfections and impurities on the substrate (or the film itself) or to spinodal dewetting caused by thermal fluctuations.[95–97] This is exemplified in Figure 4.1A which shows a mostly continuous film with some small cylindrical holes which is typical of the early stages of dewetting. The second stage of dewetting is characterised by larger holes which have asymmetrical raised rims and viscous fingering patterns. It is thought that after nucleation, capillary forces generally drive the dewetting process and force the polymer chains to accumulate around the circumference of the hole to form a raised rim.[49] This stage of dewetting is observed in the typical height and phase images of the 355 kg/mol sample at 3c* in Figure 4.9, which clearly show dewetted holes with raised rims and viscous fingering patterns. The final stage of dewetting is when the holes are large enough to coalesce, with Plateau-Rayleigh instability causing droplets to form on the surface. The droplets on the surface have reached equilibrium and this signifies the end of the dewetting process.[95] This final stage of dewetting was not reached for the films at 3c*, which suggested that the thin films were in a state of metastable equilibrium.

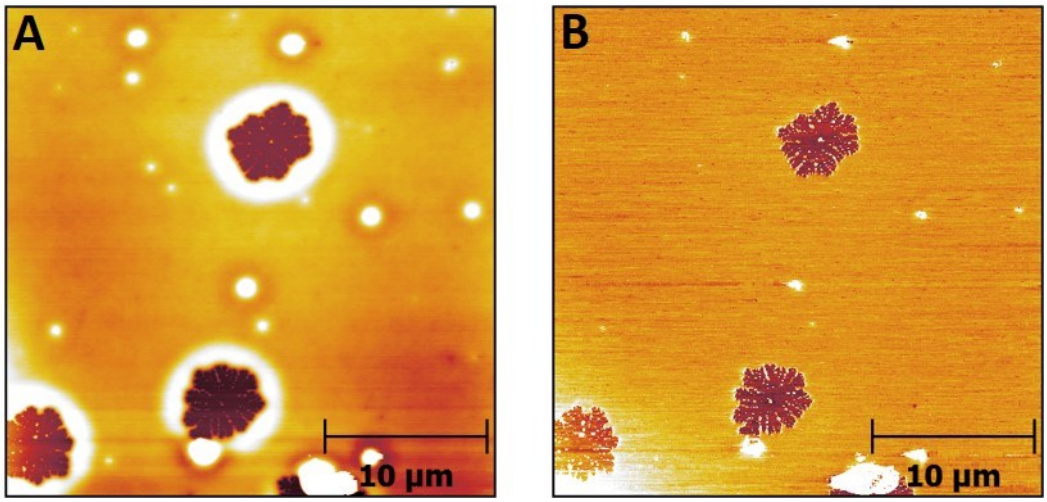

Figure 4.9: AFM images of the 355 kg/mol sample at a concentration of 3c*. (A) Height image which shows raised rims at the circumferences of the dewetted holes. (B) Corresponding phase image where viscous fingering patterns are clearly observed.

The heights of the raised rims increased linearly with the diameter of the dewetted holes for the 355 kg/mol sample (see Figure 4.10). The same trend has previously been observed by G. Reiter when studying the dewetting phenomena of 'almost glassy' polystyrene thin films close to their T_g.[49] Reiter presented the following equation:

$$D^2 \pi h_f \propto 2\pi D H \kappa \tag{4.2}$$

Where D is the hole diameter, h_f is the film thickness, H is the maximum height of the rim, and κ is the characteristic decay length of the rear side of the rim which can be fitted to an exponential decay. For each individual hole, h remained constant, and κ did not change with time. Therefore, Reiter showed that the height of the rim (H) must grow at the same rate as the diameter of the hole (D). Reiter explained that this relationship meant the polymer was not flowing like a liquid, and capillary forces were plastically deforming the highly elastic polymer films. Interestingly, the same linear relationship was observed between hole diameter and rim height for the viscoelastic poly(styrene-co-butadiene) in the current study which was well above its T_g at room temperature. In contrast to Reiter, the dewetted holes on mica also exhibited viscous fingering patterns (see Figure 4.9B). These occur when frictional forces acting at the interface between the polymer and the substrate oppose the hole growth which induces rim instability. This rim instability leads to the formation of viscous fingering patterns, which are characteristic of polymer films above their T_g.[203] Thus, for the poly(styrene-co-butadiene) thin films, viscous fingering patterns were observed in the holes, as well as, a linear relationship between rim height and hole diameter. This suggests that the polymers did not behave as a simple fluid, but exhibited aspects of both viscous dewetting and plastic deformation.

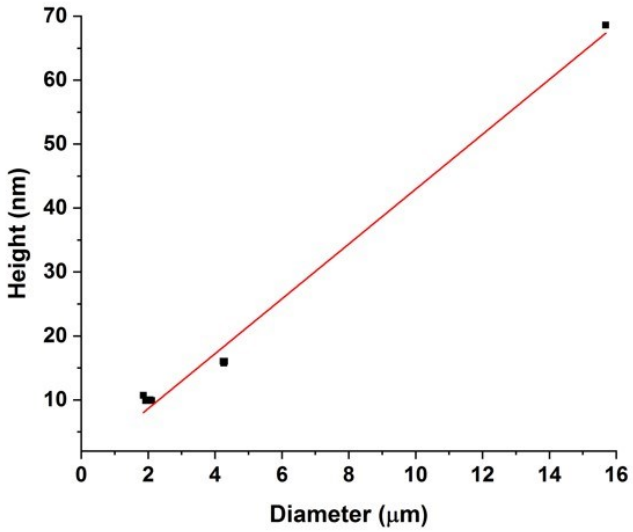

Figure 4.10: Graph showing the linear relationship between rim height and hole diameter for dewetted holes. The measurements were carried out on 9 holes in the polymer films formed at 3c* for the 355 kg/mol sample.

The widths of the dewetted holes ranged from 1.9 μm to 15.7 μm. The rims were asymmetrically shaped and their widths fluctuated due to instabilities. However, after measuring the average rim width by taking numerous measurements along the circumference, a trend was identified which showed that rim width also scaled linearly with hole diameter. Figure 4.11 shows the linear relationship between rim width and hole diameter for the dewetted holes at 3c* for the 355 kg/mol sample. The investigations into dewetted hole morphology showed that on average both rim height and rim width increased linearly with increasing hole diameter. This is an interesting result, although not completely unexpected as it is logical that rim height and rim width will be closely linked.

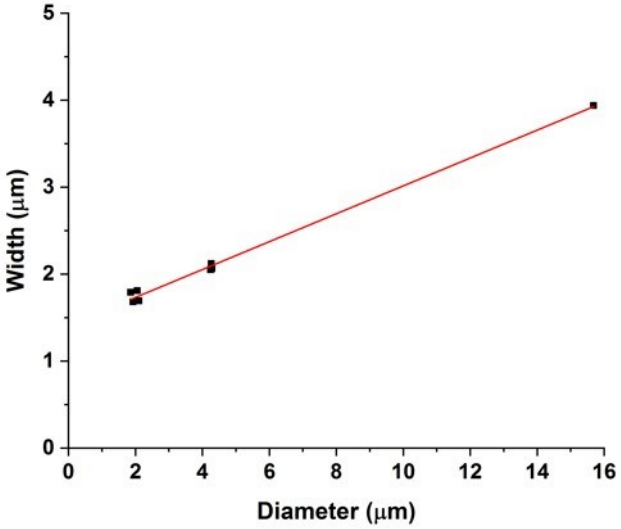

Figure 4.11: Graph showing the linear relationship between average rim width and hole diameter for the dewetted holes present in the films at 3c* for the 355 kg/mol sample.

The thickness of the polymer films at 3c* were approximately 6.6 nm, 8.4 nm, and 19.0 nm for 46 kg/mol, 86 kg/mol, and 355 kg/mol samples, respectively. The film thickness values were obtained by using AFM techniques. Firstly, phase images were analysed to confirm that the dewetted holes in the films at 3c* exposed the mica substrate. Figure 4.9B shows a typical phase image for the 355 kg/mol sample at 3c*. Distinct colour contrast is observed between the inside of the dewetted holes and the polymer film. This confirms that the holes exposed the mica surface below, and therefore could be used to measure film thickness. Cross-sectional profile plots were then taken across the holes in the film's surface. The distance between the exposed mica surface and the surface of the polymer film was measured to provide a value for film thickness. In order to achieve a more accurate value, the measurements were taken from a flat area of the polymer surface and not close to the hole's circumference where a raised rim may be present. Figure 4.12 shows a typical cross sectional-profile plot across a dewetted hole with horizontal lines denoting the film thickness.

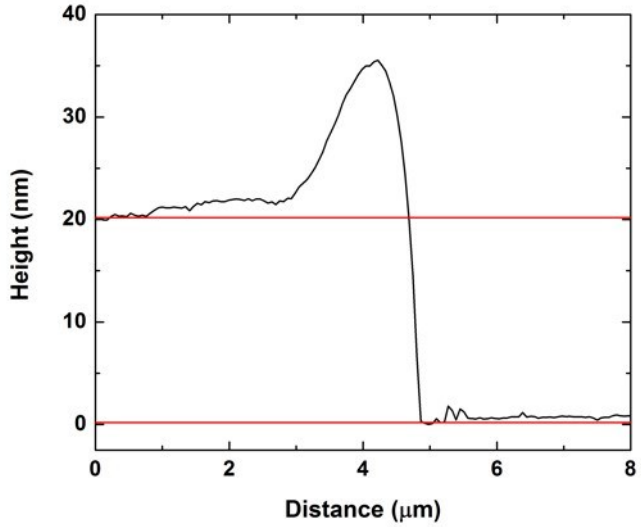

Figure 4.12: An example of a typical cross-sectional profile plot used to measure the thickness of the polymer films. This example is taken from a hole in the film of the 355 kg/mol sample at a concentration of 3c*.

For the thin films which formed at 3c*, larger molecular weights correlated to a larger film thickness and increased dewetting (see Figure 4.1A, 4.2A, and 4.3A). It has been reported that the dewetting phenomena of polymer films can be highly dependent on film thickness. This is because, factors that affect dewetting such as the magnitude of the van der Waals force acting on the film are heavily influenced by film thickness.[95] When films are thicker, dewetting takes place at a faster rate and larger holes with raised rims and viscous fingering patterns are often observed. Also, it is reported that for films with a low thickness, there is a greater number of holes in the film but less dewetting overall.[49] In polystyrene samples, it was reported that increasing polymer molecular weight caused an increase in the thickness of thin films spin coated onto a surface at a fixed concentration.[101] This agrees with the presented results; increasing the molecular weight of the polymers resulted in a greater thickness of the thin films, and therefore more dewetting was observed. Regardless of molecular weight, the polymer films formed at 3c* always experienced some degree of dewetting and total wetting was never observed. This was likely due to the polymer's very low T_g's which meant that at ambient conditions, the observation of a distinct wetting/dewetting transition line did not occur.[204]

Many factors can affect dewetting behaviour in thin polymer films including solvent evaporation, film thickness, annealing time, and chemical composition.[96] A very common study of dewetting is carried out with polystyrene films on silicon substrates, which involves annealing films above the T_g to allow dewetting.[49,205,206] The samples are then quenched back to room temperature to "freeze" the polymer surface and lock the dewetted structures in place. For these polystyrene films, the amount of dewetting increases with annealing time until droplets are formed on the silicon and the system reaches equilibrium; after this point, more annealing has no effect. Several hours of annealing at temperatures generally ranging from 5 - 50°C above the T_g of polystyrene are required to form droplets. Interestingly, different results are observed with the poly(styrene-co-butadiene) on mica. Despite the polymers being approximately 55°C above their T_g's throughout the experiments (16 - 72 hours), equilibrium structures were not formed at 3c* where total dewetting would be expected. Dewetting occurred very slowly in this system, potentially due to a change in the polymer's T_g in the vicinity of a surface, as interfaces and confinement can impact these temperatures.[192,207] Importantly, it has been demonstrated that the poly(styrene-co-butadiene) thin films on mica appeared to be in metastable equilibrium and dewet the mica surface very slowly.

To further investigate the dewetting mechanisms of the polymer on the mica surface, AFM imaging was carried out 15 minutes after the spin coating process. This meant that the early stages of dewetting could be examined at varying experimental parameters, and compared to the polymer formation after 16 - 72 hours of drying. Figure 4.13 shows typical AFM images comparing the polymer formation of the 46 kg/mol sample after approximately 15 minutes of drying and after 16 - 72 hours of drying. For the 46 kg/mol sample at a concentration of 1c*, a mostly continuous thin film was observed on the mica surface after 15 minutes of drying. The film had many small holes, as well as, some circular aggregates. The thickness of the film was approximately 3.3 nm. In contrast, when the 1c* sample was left for 16 - 72 hours, spherical cap shaped aggregates were observed on the surface. This showed that at the overlap concentration, dewetting did not occur immediately after polymer deposition during the solvent evaporation or initial drying processes. Instead, most of the dewetting occurred during the 16 - 72 hours the samples were left to dry in the fume hood.

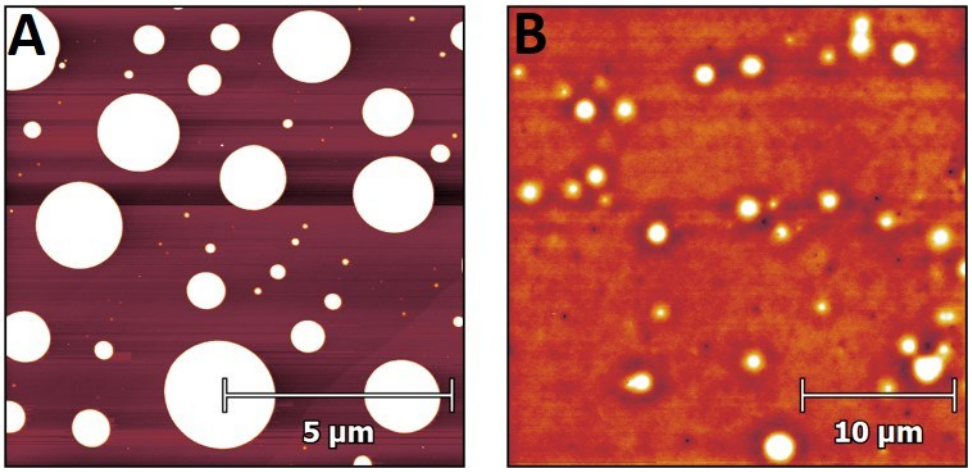

Figure 4.13: AFM images for the 46 kg/mol sample at a concentration of 1c*, showing the polymer formation on the mica surface after: (A) 16 - 72 hours of drying, and (B) 15 minutes of drying.

At a concentration of 0.1c* (Figure 4.14), similar results were observed after both 15 minutes of drying and 16 - 72 hours of drying, whereby spherical cap shaped nanodroplets formed on the mica surface. This showed that at lower concentrations, the majority of dewetting occurred soon after polymer deposition during solvent evaporation or initial drying. Interestingly, the average radii and heights of the polymer aggregates after 15 minutes of drying were 14% and 36% larger than the aggregates that were left for 16 - 72 hours. This is likely because after 15 minutes, the polymer aggregates were not completely dry, and therefore the chains were slightly swollen, which created larger droplets. These results show that the time it takes for dewetting to occur is influenced by solution concentration. At lower concentrations, droplet formation happened quickly, whilst at higher concentrations, it occurred over a larger time scale. When the concentration was increased up to 3c*, only partial dewetting was observed and the thin films entered a state of metastable equilibrium.

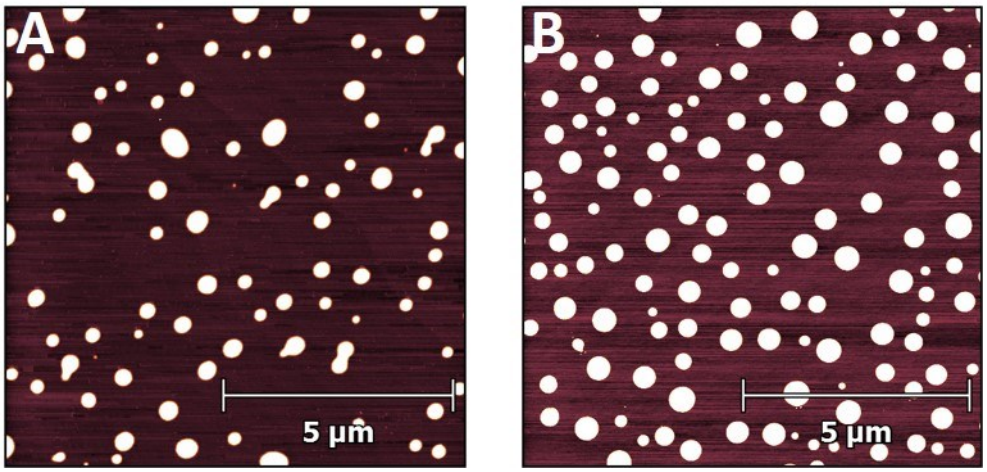

Figure 4.14: AFM images for the 46 kg/mol sample at a concentration of 0.1c*, showing the polymer formation on the mica surface after: (A) 16 - 72 hours of drying, and (B) 15 minutes of drying.

In a previous study, Liu and Wang[208] observed that after spin coating from toluene solutions, polyisoprene thin films ($M_n > M_e$) with a thickness of 50 nm did not experience any dewetting, even after a month's exposure to air at room temperature. This demonstrated that the polyisoprene films were stable over large time scales. In the current study, the thin films which formed at 3c* (thickness ranging from 6.6 nm - 19.0 nm) were in a state of metastable equilibrium, as only partial dewetting was observed after 16 – 72 hours. This suggests that the stability of (thicker) films in air is directly related to film thickness. Therefore, additional experiments were carried out to test this hypothesis. Figure 4.15 shows an AFM image of a thin film formed at a concentration of 7c* for the 355 kg/mol sample, after 24 hours in air. The image shows that as concentration (and presumably film thickness) increased further, a negligible amount of dewetting was observed in the film. This showed that a significant increase in film thickness corresponded to an increase in film stability.

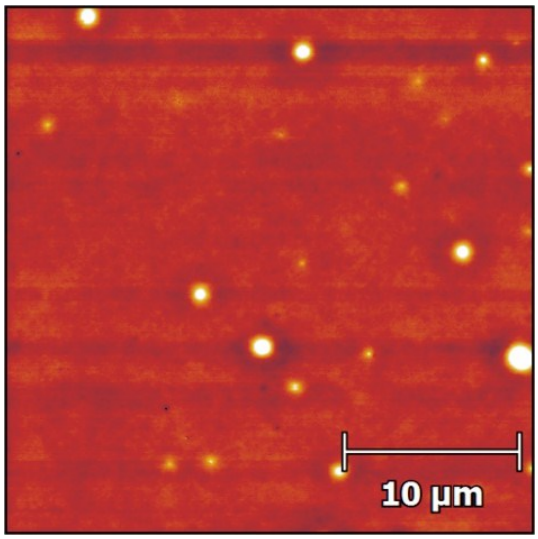

Figure 4.15: AFM image of a thin film formed at 7c* (9.73 mg/ml) for the 355 kg/mol sample after 24 hours.

4.3.3 Molecular weight effects

4.3.3.1 Size distribution of aggregates

Figures 4.16 - 4.18 show the relationship between molecular weight and aggregate radius, height, and number of chains per aggregate at varying concentrations.

Figure 4.16 shows that at a concentration of 1c* and 0.001c*, the overall radius of the aggregates increased with increasing molecular weight. However, for the other concentrations, the radius remained nearly constant with increasing molecular weight. The range of radius values were large and similar across the molecular weight range.

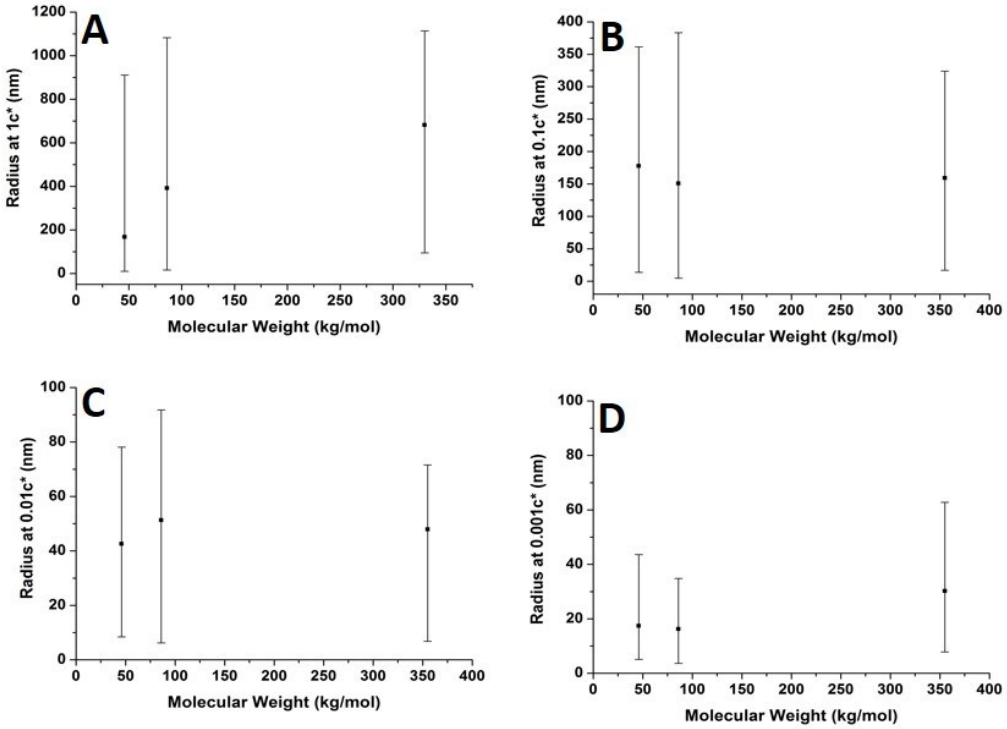

Figure 4.16: Graphs showing the relationship between aggregate radius and molecular weight on the mica surface at varying concentrations. Each graph presents the average values and has bars which indicate the range of values. (A) 1c*, (B) 0.1c*, (C) 0.01c*, (D) 0.001c*.

Figure 4.17 shows aggregate height against molecular weight at varying concentrations. The overall height of the aggregates increased with increasing molecular weight, however this is not a strong trend at 0.001c*. The range of heights was generally largest for the highest molecular weight sample, and the 46 kg/mol and 86 kg/mol samples had smaller ranges. However, this was not the case at 1c* where the highest molecular weight sample had the smallest range of values. The results showed that generally aggregate height increased with increasing molecular weight; both higher solution viscosities and greater degrees of entanglement at higher molecular weights appeared to play a role in shaping this behaviour (*vide infra*).

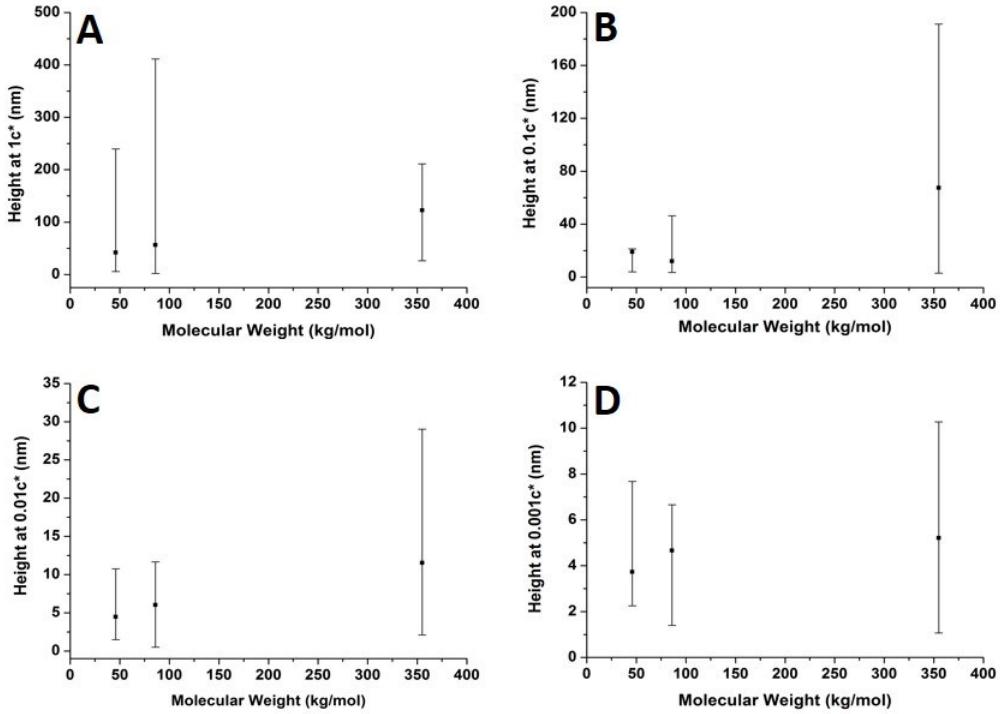

Figure 4.17: Graphs showing the relationship between the height of the polymer aggregates and molecular weight on the mica surface at varying concentrations. Each graph presents the average values and has bars which indicate the range of values. (A) 1c*, (B) 0.1c*, (C) 0.01c*, (D) 0.001c*.

Figure 4.18 shows the number of chains per aggregate against molecular weight at varying concentrations. As the molecular weight increased, the number of chains per aggregate decreased. Although, there is only a weak trend for the 1c* and 0.1c* samples. Generally, the average heights of the aggregates increased with increasing molecular weight. Additionally, the individual polymer chains are longer at higher molecular weights. Therefore, fewer chains were required to make larger aggregates. For the 46 kg/mol sample, the range of number of chains per aggregates was largest at the two lower concentrations and also fairly large at the two higher concentrations. This is because there were a greater number of shorter chains in the solution which encouraged a larger range of chains per aggregate.

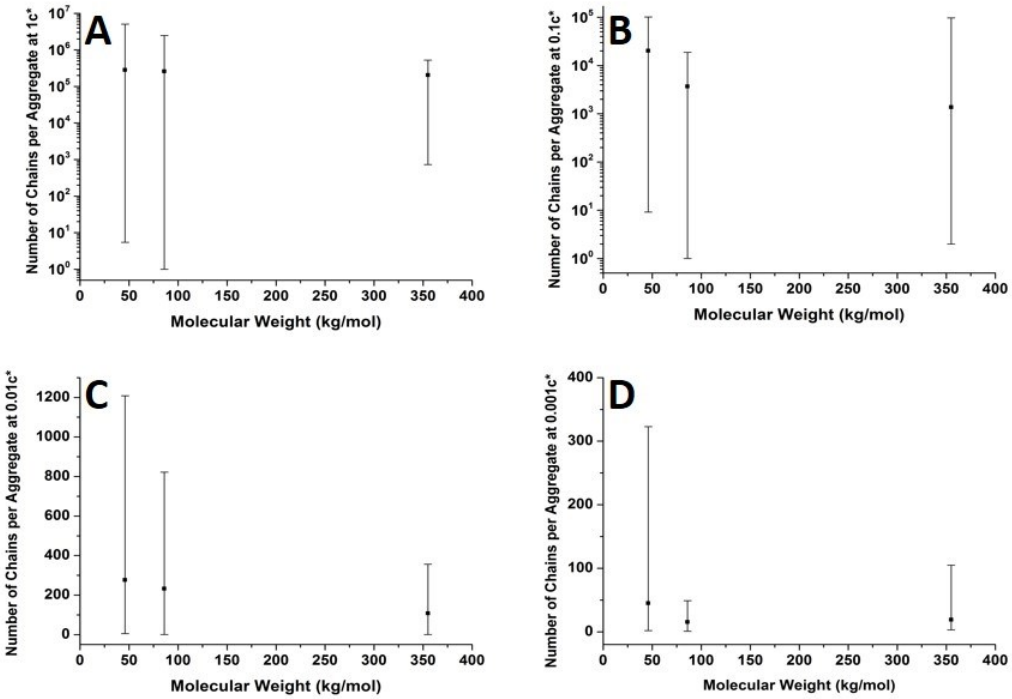

Figure 4.18: Graphs showing the relationship between the number of chains per aggregate and molecular weight on the mica surface at varying concentrations. Each graph presents the average values and has bars which indicate the range of values. (A) 1c*, (B) 0.1c*, (C) 0.01c*, (D) 0.001c*.

Figures 4.16 - 4.18 demonstrate that the aggregates were generally larger in size at higher molecular weights. The increase in aggregate size at higher molecular weights is likely influenced by the viscosity of a sample, which will generally increase with increasing molecular weight.[101] If viscosity was larger at higher molecular weights, there may have been less polymeric material expelled from the surface during spin coating, leaving behind larger aggregates and thicker films. Remember that the polymer solutions in this chapter were prepared relative to the individual polymer's overlap concentration. This means that as the molecular weight of the polymer was increased, the total mass of polymer in solution was decreased. As the concentration by weight of a polymer solution decreased, then so will the viscosity.[209] These two factors thus work in opposing ways. To further investigate this, the viscosities of 1c* solutions at each molecular weight were measured. The measured dynamic viscosity of toluene at 20°C was 0.59 mPa·s, which was consistent with previous reports.[210] The dynamic viscosities of the 1c* polymer solutions were 0.80, 0.81, and 0.85 mPa·s for the 46, 86, and 355 kg/mol samples,

respectively. The relative viscosities were therefore 1.36, 1.37, and 1.44 for the three samples. This confirmed that the viscosity of the solutions did increase with increasing molecular weight, under these conditions. As the solution viscosity increased, larger aggregates and thicker films formed, providing a significant reason for the change in aggregate size with molecular weight.

The change in viscosity is not the only factor which created larger aggregates at higher molecular weights as chain entanglements were also significant. Figure 4.19 shows the average number of aggregates on a specific area of the mica surface against molecular weight at varying concentrations. As molecular weight increased, the number of aggregates present on the surface generally decreased and the range of values was predominantly lowest at 355 kg/mol. However, the number of aggregates remained constant at a concentration of 0.01c*. It has been established that as molecular weight increased, there were fewer but larger polymer aggregates present on the mica surface. As the solutions were prepared according to the overlap concentration, polymers with larger molecular weights had fewer but larger chains present in the solution. The polymer chains were in the same proximity to each other in the solution at a given concentration, regardless of molecular weight. Consequently, polymer chains with higher molecular weights experienced more entanglements than chains with lower molecular weights. Therefore, at higher molecular weights, the smaller quantity of larger chains will entangle to a greater degree compared to the lower molecular weight chains; hence creating fewer but larger aggregates on the mica surface. Subsequently, increased chain entanglements also contributed to the changes in polymer morphology on the mica surface.

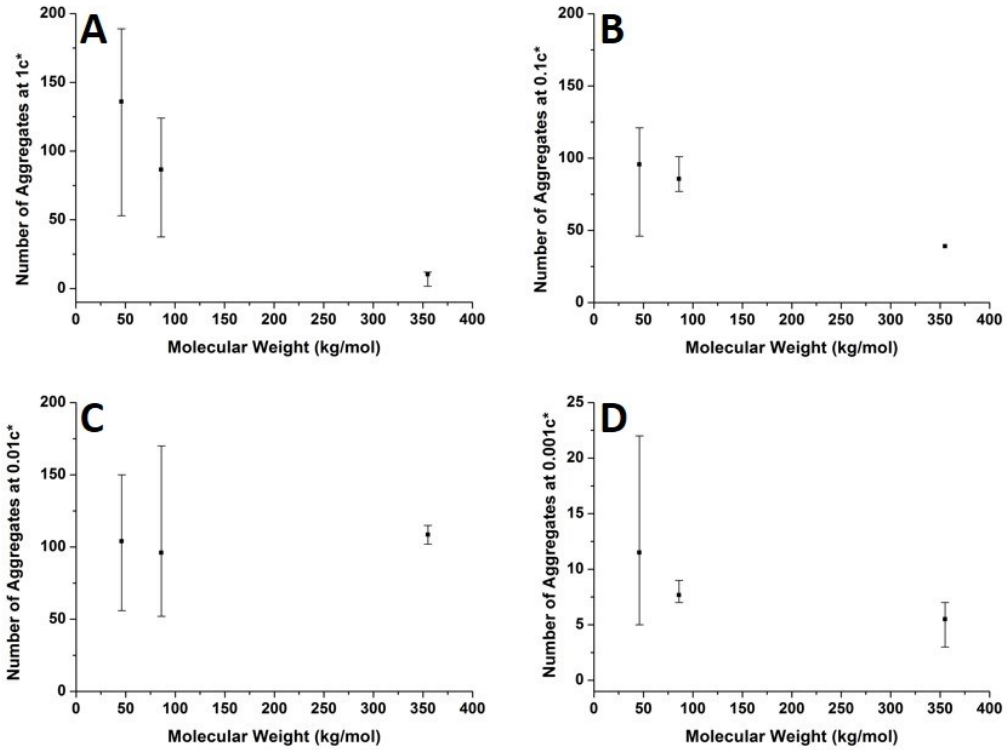

Figure 4.19: Graphs showing the relationship between the number of polymer aggregates on a specific surface area of mica and molecular weight at varying concentrations. Each graph presents the average values and has bars which indicate the range of values. (A) 1c*, (B) 0.1c*, (C) 0.01c*, (D) 0.001c*.

4.3.4 Contact angle effects

4.3.4.1 Nanoscale behaviour

Figure 4.20 compares the contact angle of the polymer droplets against concentration at varying molecular weights, on the mica surface. Generally, it was observed that at 1c* and 0.001c*, the average contact angle of the droplets was largest, and the minimum values were at 0.01c* or 0.1c*. The range of values were largest at 1c* for the 46 kg/mol and 86 kg/mol samples. However, for the 355 kg/mol sample, the range of values were largest at 0.001c*. These results suggest that the contact angles of the droplets were size dependent, and that the contact angle appeared to be larger for both the very small and much larger droplets. However, as explained previously, there were many small droplets present at higher concentrations which could affect this conclusion.

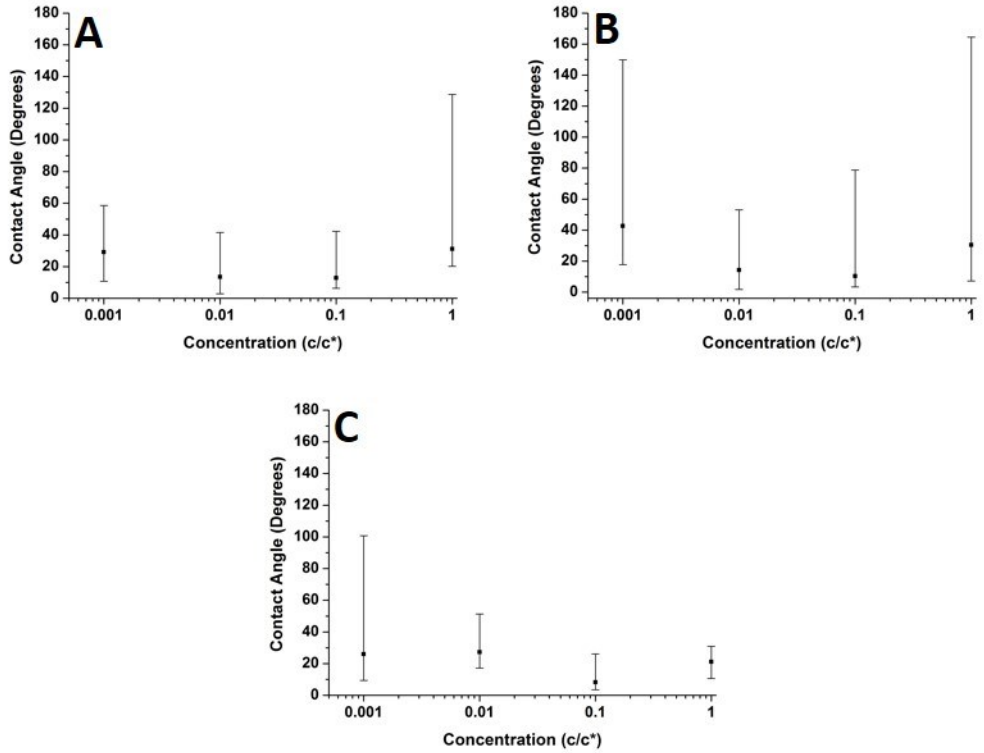

Figure 4.20: Graphs showing the relationship between the average contact angle of polymer aggregates and concentration on the mica surface at varying molecular weights. Each graph presents the average values and has bars which indicate the range of values. (A) M_n= 46 kg/mol, (B) M_n= 86 kg/mol, (C) M_n= 355 kg/mol.

Figure 4.21 shows the relationship between contact angle and nanodroplet radius across varying concentrations at each molecular weight. These plots corrected the previous ambiguity and confirmed that there was a systematic droplet size dependence on contact angle. The overall trend was independent of the molecular weight; the contact angle values were greatest for both the smaller and larger droplets, and a minimum was present at 100 – 250 nm.

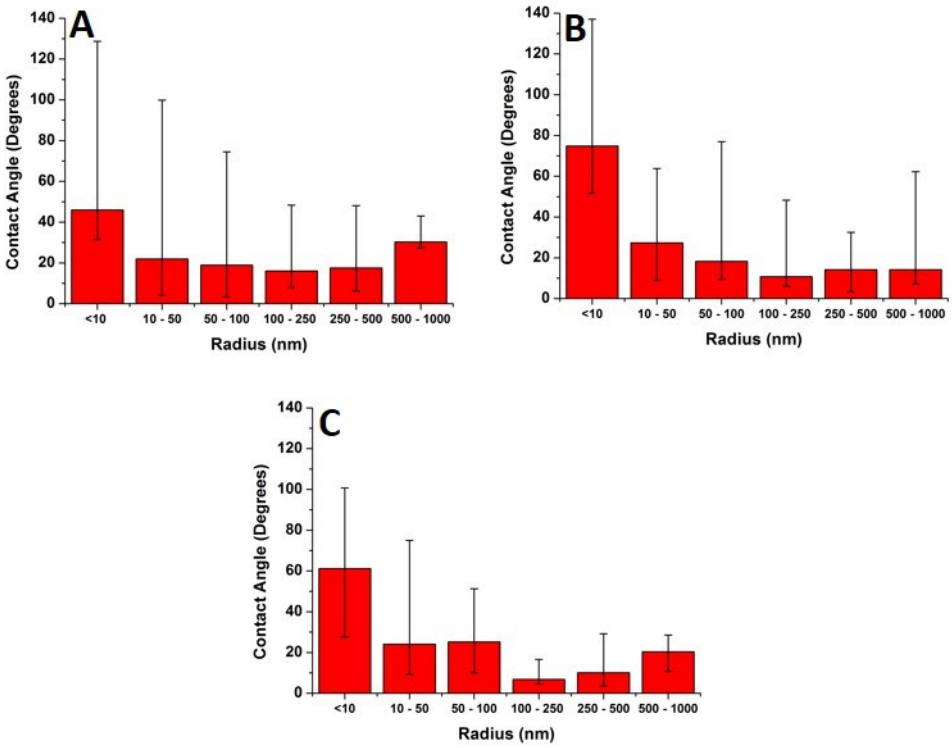

Figure 4.21: Graphs showing contact angle against radius for the nanodroplets on a mica surface at varying molecular weights. Each graph presents the average values and has bars which indicate the range of values. (A) M_n= 46 kg/mol, (B) M_n= 86 kg/mol, (C) M_n= 355 kg/mol.

Figure 4.22 shows typical profile plots fitted to spherical caps for nanodroplets with radii ranging from 100 - 250 nm at each molecular weight. The plots show that despite their low contact angles, the nanodroplets in this size range maintained a spherical cap shape. This is a significant result, as it shows that the uniform shape of the droplets was maintained despite dramatic differences in contact angle values.

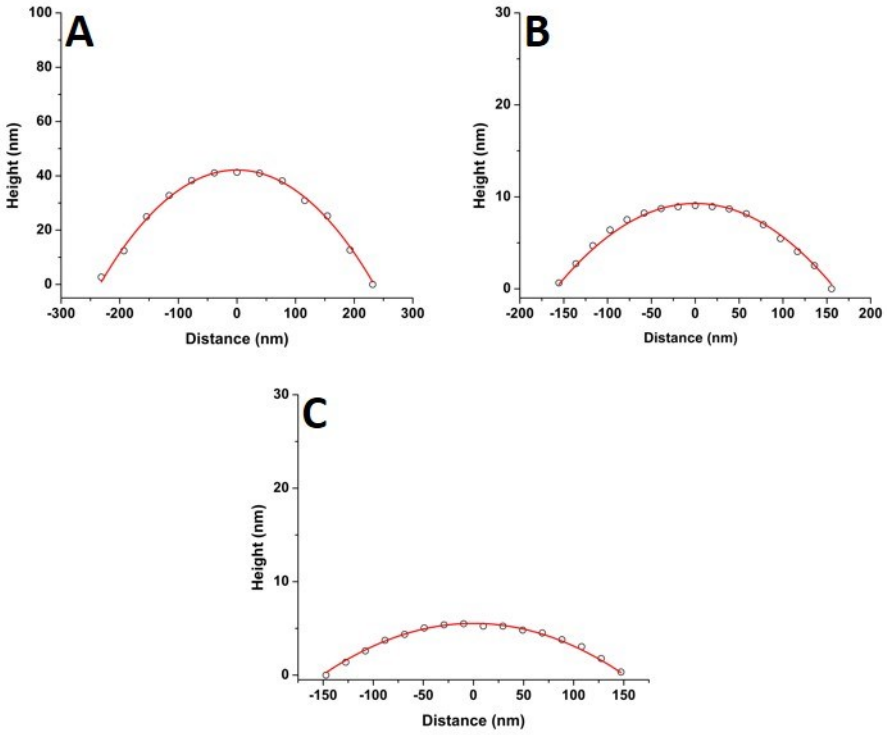

Figure 4.22: Cross-sectional profile plots of typical poly(styrene-co-butadiene) nanodroplets with radii in the range of 100 – 250 nm at each molecular weight. The cross-sections are fitted to spherical caps. (A) M_n = 46 kg/mol, (B) M_n = 86 kg/mol, (C) M_n = 355 kg/mol.

When the radii of the droplets were smaller than 100 – 250 nm, a sharp rise in contact angle was observed. The contact angle was at a maximum when the droplet radius was <10 nm across each molecular weight. At this range of radii, the droplets were predominantly made up of aggregates containing very few chains and the average contact angles were 46˚, 75˚, and 61˚ for the 46 kg/mol, 86 kg/mol, and 355 kg/mol samples, respectively. These contact angle values were large and indicated that very small aggregates did not lie flat on the mica, but strongly dewetted the surface. Evangelopoulos et al.[28] observed that as the size of polybutadiene droplets were reduced to the nanoscale on a mica surface, the dewetting of the nanodroplets increased. They showed that surface and line tension effects could not explain the observed behaviour and attributed it to an increased elastic modulus. After a certain critical value of size (at the nanoscale), the elastic modulus of the polymer droplets began to exponentially increase which increased dewetting, and thus contact angle. This was due to the effect of interactions and confinement which occur when a polymer is in the proximity of a

surface, and can have an entropic origin.[211–215] This phenomenon has also been reported with polymer nanofibers.[200,216,217] The materials and methods used in Evangelopoulos et al.[28] study are similar to the ones used in the current experiments, and their results agree with the presented observations. Both the linear polybutadiene used in Evangelopoulos et al. study and the poly(styrene-co-butadiene) in this chapter are viscoelastic. However, it is important to remember that the polymers can also exhibit elastic properties. Examples of where viscoelastic polymers can experience elasticity are from entanglements or via pinning/physical bonding to the surface that creates anchor points (effective crosslinks). Therefore, viscoelastic polymers will only experience flow over large time scales which suggests they are in metastable equilibrium. Both the polybutadiene and poly(styrene-co-butadiene) had high molecular weights ($M_n > M_e$), which meant that elastic behaviour could occur. Therefore, this explanation of the droplet size dependence on the contact angle is plausible for the current system.

However, a simulation study carried out by Milchev et al.[123] also showed very similar results to the current study, but instead attributed this behaviour to line tension. In the nanoscale, Young's equation must be altered to include line tension to allow for the influence of surface curvature and the specific free energy of the three-phase contact line.[122,124] They found that when a polymer droplet was subjected to long-range van der Waals forces on a flat substrate with weak polymer/substrate adhesion, there was a distinct size dependence on the contact angle of the nanodroplets. The droplets underwent a sharp increase in contact angle as droplet size was reduced in the nanoscale, and this was attributed to the existence of a positive line tension influencing droplet morphology. These results also agree with the current observations as there is weak adhesion between the polymer nanodroplets and the mica surface. However, the study of line tension is a controversial subject and neither the magnitude nor the sign of the line tension value is currently established.[122,124] For example, Seeman et al.[92] calculated the line tension of polystyrene nanodroplets on a silicon dioxide substrate to have a negative value. These opposing results regarding line tension at the nanoscale are not uncommon. However in this case, they could possibly be attributed to the differences in polymer/substrate adhesion. Two studies are presented with results that agree with the current experimental data regarding the size dependence on the contact angle of polymer nanodroplets. Currently, whilst neither theory can be decisively confirmed with the quantitative results presented in the chapter; it appears that both are plausible. It is

worthwhile noting that for polymer nanodroplets on surfaces, positive line tension and an increased elastic modulus may be intrinsically linked creating the observed changes in nanodroplet contact angle.

The relationship between droplet height and contact angle was also investigated at the nanoscale. Figure 4.23 shows average contact angle against nanodroplet height for each molecular weight. There was not a specific dependence between nanodroplet height and contact angle. This is unlike the results examining radius against contact angle which showed a distinct size dependence. For the 46 kg/mol sample (A), there was a local minimum at 15 – 30 nm in an overall increasing trend. For the 86 kg/mol sample (B), there was a local minimum at 10 – 15 nm in a more fluctuating trend, and for the 355 kg/mol sample (C), there was a local maximum at 15 – 30 nm in an otherwise fairly flat trend.

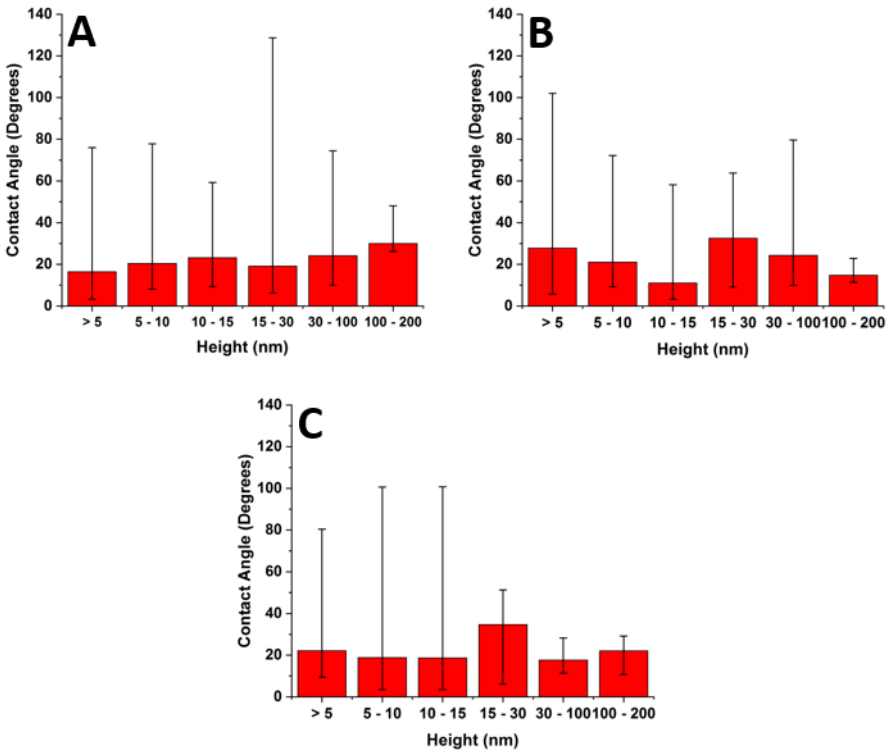

Figure 4.23: Graphs showing contact angle against height for the nanodroplets formed at each molecular weight. Each graph presents the average values and has bars which indicate the range of values. (A) M_n = 46 kg/mol, (B) M_n = 86 kg/mol, (C) M_n = 355 kg/mol.

The relationship between contact angle and height normalised by radius of gyration was also investigated. Generally, the polymer chains will take on a random coil conformation on the mica surface. If the height of the nanodroplets was similar to the value of radius of gyration, this may mean that the polymer conformation could be perturbed from a random coil. Consequently, this may have impacted the contact angles of the nanodroplets. This theory was investigated by calculating the radius of gyration, R_g, of each of the polymers. First, the number of Kuhn monomers, *N,* was calculated for each polymer sample using the following equation:

$$N = \frac{M_n}{M_0} \tag{4.3}$$

Where M_n is the molar mass of the polymer samples and M_0 is the molar mass of its Kuhn monomers. The radius of gyration of the samples could then be found using the following equation for linear chains:

$$R_g^2 = \frac{b^2 N}{6} \tag{4.4}$$

Where b is the polymer's Kuhn length. Values of M_0 and b for polystyrene and polybutadiene were taken from Polymer Physics by Rubinstein and Colby.[4] Radius of gyration values were calculated as 6.5 nm, 8.9 nm, and 18.0 nm for the 46 kg/mol, 86 kg/mol, and 355 kg/mol samples, respectively. Many of the nanodroplets had height values which were similar or lower than the polymer's radius of gyration. Figure 4.24 shows the average contact angle of the nanodroplets against height normalised by radius of gyration for each molecular weight. There was no specific trend in nanodroplet contact angle when h/R_g was in the order of 1. In ranges containing the value h/R_g = 1, the average contact angle was at a midpoint for the 46 kg/mol sample (A), at a midpoint for the 86 kg/mol sample (B), and at a maximum for the 355 kg/mol sample (C). These results show that there is not a clear relationship between h/R_g and contact angle, and there is no distinct dewetting behaviour independent of molecular weight when h/R_g is close to 1.

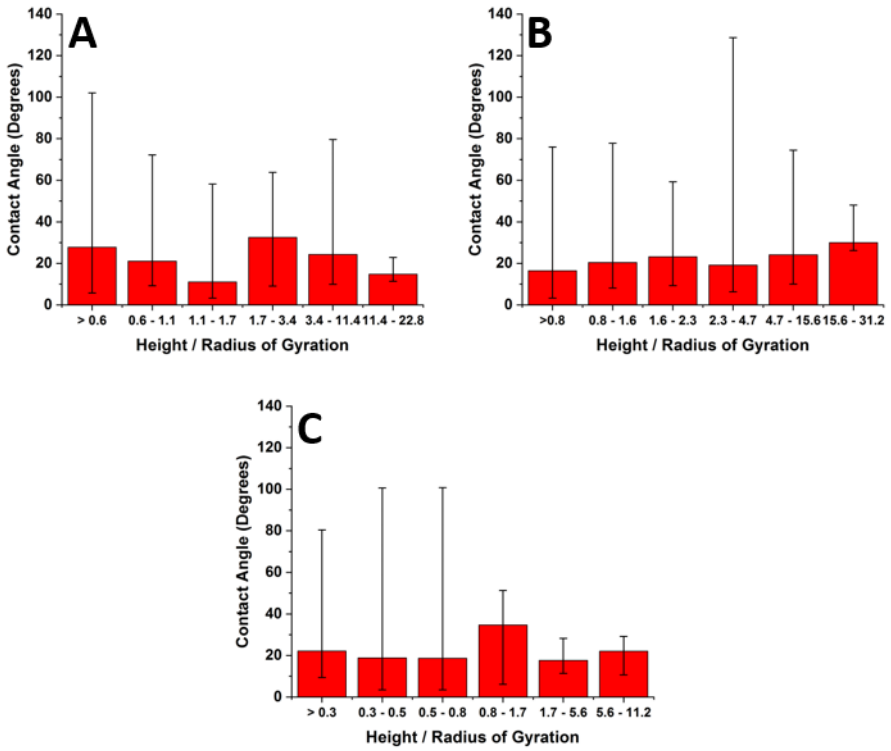

Figure 4.24: Graphs showing contact angle against height normalised by radius of gyration for the nanodroplets formed at each molecular weight. Each graph presents the average values and has bars which indicate the range of values. (A) M_n = 46 kg/mol, (B) M_n = 86 kg/mol, (C) M_n = 355 kg/mol.

4.3.4.2 Macroscale behaviour

Figure 4.21 shows that when the droplet radii was larger than 100 - 250 nm, the contact angle of the polymer droplets also increased. This increase in contact angle continued up to the largest polymer droplets which were examined using AFM. In order to investigate the relationship between droplet radius and contact angle further, the experiments were repeated at the macroscale. The contact angle of polymer droplets with radii ranging from approximately 1 - 5 mm were measured using contact angle goniometry. Figure 4.25 is an annotated photograph showing a typical macroscopic polymer droplet on the mica surface.

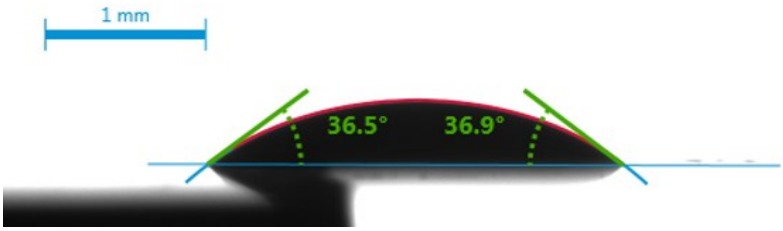

Figure 4.25: Photograph showing an example of a typical macroscopic poly(styrene-co-butadiene) droplet (M_n = 46 kg/mol) on a mica surface, annotated with contact angle values.

After annealing, the contact angles of the samples were measured at varying intervals over the course of 1 week (168 hours). Figure 4.26 shows how the contact angles of the macroscopic droplets varied with time after annealing. The 355 kg/mol polymer samples did not form equilibrium droplets on the surface, even after very prolonged periods (> 8 weeks) of annealing. This meant results could not be obtained for this molecular weight. The graphs show that the contact angles of the droplets remained mostly constant over the course of 168 hours. This suggested that the droplets had formed equilibrium structures on the mica surface after annealing. The slight fluctuations in contact angle values were accounted for by experimental error.

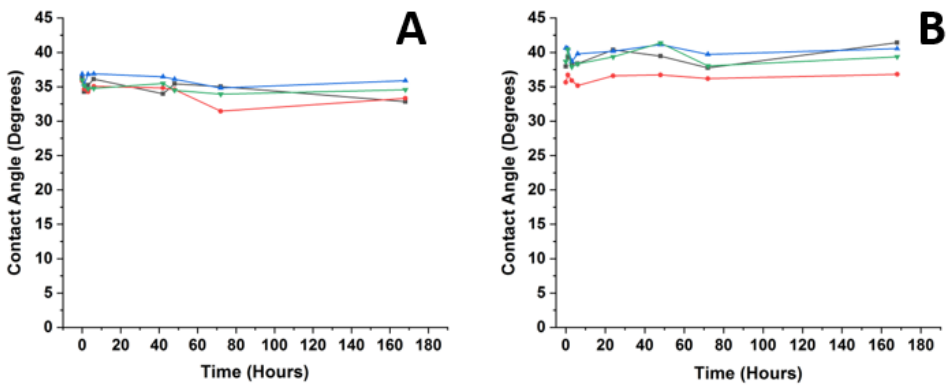

Figure 4.26: Graphs showing how the contact angles of the macroscopic polymer droplets varied with time after annealing. (A) M_n = 46 kg/mol, (B) M_n = 86 kg/mol.

After confirmation that the contact angles of the droplets remained mostly constant with time, the size dependence of the contact angle values were investigated. All measurements took place 1 week after annealing. Figure 4.27 shows the relationship

between contact angle and radius for the 46 kg/mol and 86 kg/mol polymer droplets at the macroscale. The macroscopic angles were larger than the minimum in Figure 4.21, with values ranging from 30˚ to 36˚ for the 46 kg/mol sample, and values ranging from 34˚ to 41˚ for the 86 kg/mol sample. However, unlike the nanoscale, there was no apparent droplet size dependence on contact angle. The contact angle of the droplets appeared to be fairly independent of droplet radius at the macroscale. The combination of nanoscopic and macroscopic measurements showed that when the radius of the droplets were larger than 100 - 250 nm, the contact angle increased with droplet radius until it reached a plateau for the macroscopic contact angle values. Checco et al.[199] observed that the contact angle of alkane droplets increased with increasing droplet radius from approximately 200 nm to macroscopic levels. They concluded that line tension could not explain this behaviour and instead cited surface heterogeneities as the cause. The droplets will form on the most wettable parts of the surface and the existence of surface heterogeneities make this more probable for smaller droplets. On the contrary, larger droplets will not be able to avoid heterogeneities and thus will have larger contact angles; the same can apply for the current system. Freshly cleaved mica is hydrophilic but becomes less hydrophilic rather rapidly creating surface heterogeneities.[218] The size of heterogeneities are in the sub-micrometer range,[125] fitting with the minimum of contact angle in the region of 100 - 250 nm.

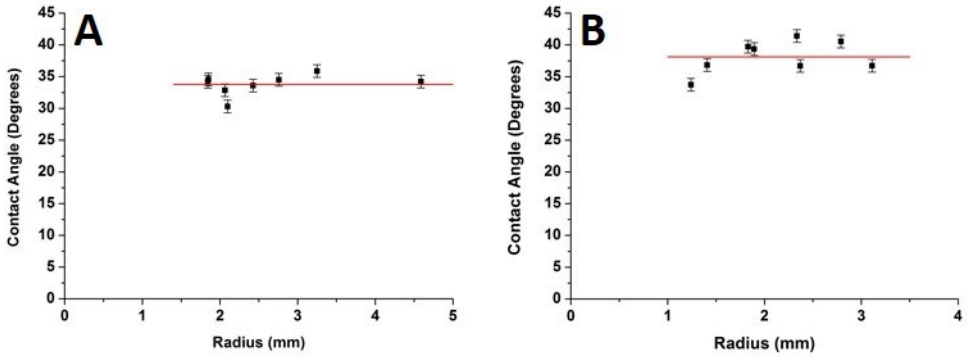

Figure 4.27: Graphs showing contact angle against droplet radius for the macroscopic poly(styrene-co-butadiene) droplets at varying molecular weights on a mica surface. Measurements were taken 1 week after the samples were removed from the oven. Each horizontal line represents the overall average value of the measurements. The bars on the graphs represent the experimental error. (A) M_n = 46 kg/mol, (B) M_n = 86 kg/mol.

A distinct range of radii where the nanodroplet's contact angle was at a minimum for each molecular weight has been presented. It appeared that the observed phenomenon was due to a substrate surface effect. As the droplet size was increased, the contact angle increased until it plateaued to its macroscopic value. As the droplet radius decreased from the minimum, a sharp increase in contact angle was observed owing to the increase of elastic modulus and possible influence from line tension. It appears that this is the first observation of such contact angle behaviour, and may prove useful in controlling the wetting properties of polymer droplets from the nanoscale to macroscale.

4.4 Conclusions

Varying solution concentration and molecular weight had a significant impact on polymer morphology on a mica surface. At the highest concentration, mostly continuous thin films formed on the mica surface with the higher molecular weight samples having a greater thickness. Only partial dewetting was observed in the films despite the polymer's low T_g, which meant that the polymers were in a state of metastable equilibrium. Additionally, the polymers did not behave like a simple fluid but exhibited both viscous dewetting and plastic deformation. This was demonstrated by the observation of both a linear relationship between rim height and hole diameter of the dewetted holes which is characteristic of plastic behaviour, as well as, fingering patterns which are characteristic of viscous behaviour. This chapter has provided an insight into the relatively unexplored field studying the dewetting mechanisms of polymer films above their T_g at room temperature, and has shown that the polymers were in metastable equilibrium.

At lower concentrations, total dewetting occurred over a small time scale and spherical cap shaped nanodroplets formed on the mica surface during the solvent evaporation and initial drying processes. Although, at the overlap concentration, nanodroplets formed over a larger time scale (<16 hours) due to more polymeric material being present on the surface. The size of the nanodroplets varied from single chains to aggregates containing millions of chains. Single polymer chains will dewet the mica surface and form spherical cap shaped nanodroplets. At higher concentrations, the average size of the aggregates were larger, although the nanodroplet distribution was polydisperse. At

lower concentrations, the aggregates were much smaller on average, but their size distribution was more monodisperse.

Changing molecular weight also affected the formation of the spherical cap shaped nanodroplets; as molecular weight was increased, there were fewer but larger aggregates present on the surface. This was due to more polymer entanglements and an increased solution viscosity which occurred at higher molecular weights. Altering molecular weight and solution concentration did not only affect the size of the nanodroplets formed on the mica surface. There was also a significant impact on the number of droplets present on the surface and the size distributions of nanodroplets. This result provided further insight into polymer behaviour at an interface and suggested how the morphology of polymer aggregates could be controlled by altering basic parameters.

A specific size dependence on the contact angle of the droplets at the nanoscale was observed. A distinct minimum in the contact angle was observed for droplets with radii ranging from 100 – 250 nm across each molecular weight. When the droplet size was lower than this minimum, a sharp increase in contact angle was observed. This appeared to be due to an exponential increase in elastic modulus that occurred below a critical value in the nano-regime (<100 nm) or a positive line tension value due to weak polymer/substrate adhesion. Additionally, line tension and elastic modulus may be intrinsically linked creating this dewetting behaviour. If the droplet size was larger than the minimum, then an increase in contact angle was observed which appeared to plateau at the macroscale. This effect has been observed in alkanes, and it is thought to be due to surface heterogeneities causing preferential wetting. The results show that the contact angle behaviour in the nanoscale is the result of two opposing factors: the elastic modulus increase/line tension at <100 nm and the existence of heterogeneities at the substrate surface which affected aggregates with radii larger than 250 nm. This systematic trend is previously unexplored and may prove valuable in understanding and controlling the wetting properties of polymer nanodroplets at an interface. Additionally, there is a distinct difference in the contact angle behaviour of polymer droplets at the nanoscale compared to the macroscale. This highlights that one cannot adopt the same assumptions for polymer behaviour at an interface across large length scales. This is

because factors such as elastic modulus and line tension which are negligible in the macroscale can have significant impact at the nanoscale.

5 Polymer morphology on a graphite surface

Summary

This chapter presents a comprehensive examination of the morphology of spin coated poly(styrene-co-butadiene) random copolymers on a strongly adsorbing graphite substrate using AFM. Polymer morphology varied dramatically, and was highly dependent on concentration and molecular weight. Specific ordering of the nanostructures on the surface was observed at many concentrations. The contact angles of the nanostructures remained constant with varying feature width.

5.1 Introduction

Polymers are often used as a component in high performance composite materials due to their high toughness and low manufacturing cost.[181] This has led to polymer based composites frequently replacing traditional materials in many applications, such as components for cars and aircrafts.[219,220] The interface between the polymer matrix and filler components within composite materials is extremely influential in determining the materials bulk physicochemical properties.[221] Despite this, the interactions between polymers and filler materials are often poorly understood at a fundamental level. The underlying physicochemical origins for the deviations in behaviour of polymers at surfaces are often unknown or simply unexplored. If the behaviour of polymers at surfaces were more thoroughly understood at a fundamental level, then this would aid in both the design and manufacture of polymer coatings, thin films, and composite materials with enhanced properties.

Composite materials that utilise the polymer/carbon interface have been used in numerous applications for many years.[222] Carbon black particles are used to reinforce elastomeric rubbers in the manufacture of car tyres, which significantly increases properties such as the tensile strength, stiffness, and abrasion resistance of the tyres.[24] Carbon fibres are woven together and embedded into epoxy resins to create a lightweight composite material with very high strength properties which can be used for many structural applications.[223,224] In more recent years, the discovery of carbon 'super materials' such as carbon nanotubes (CNTs) and graphene have led to further advancements in polymer/carbon nanocomposites.[44,45,47,225,226] The understanding of the carbon/polymer interface is vital for improving the physicochemical properties of composite materials. However, there are still many open questions regarding the fundamental behaviour of polymers at carbon surfaces.[227,228]

Studying the polymer/carbon interface is an area of extensive research. This research commonly includes investigating the electrical properties of polymer/carbon composites,[42,229] studying the interactions between carbon nanotubes and polymers,[132,133] and studying the self-assembly of polymers on graphene for nanolithography applications.[230–233] AFM can also be used as an imaging technique to

study the behaviour of many different organic molecules including polymers, on graphite surfaces at the nanoscale. [234,235] Many AFM studies have focused on characterising the distinct ordering of polymers on graphite. This behaviour is commonly observed in crystalline polymers, such as polyethylene. In these instances, the dimension of the c-axis of the polyethylene crystal cell is very similar to the graphite lattice constant (a-axis). This encourages epitaxial interactions, which create a distinctly ordered polymer morphology. A similar effect is also reported for polymers with alkyl chains. The distance of the 1,3-methylene group in trans alkyl chains is very similar to the graphite lattice constant (a-axis), which also creates an ordered polymer morphology.[115,117,236] Investigations into the distinct ordering of amorphous linear polymers on graphite is a mostly unexplored area, and could prove useful for various nanopatterning applications. It appears that there are no studies which comprehensively characterise polymer thin films, networks, nanoislands, and nanoribbons on graphite, across a wide range of concentrations and molecular weights. Furthermore, investigations into the behaviour of linear amorphous copolymers, such as poly(styrene-co-butadiene) on graphite are limited. It appears that there are no studies investigating the specific ordering of poly(styrene-co-butadiene) on graphite. This is surprising as these polymers are extensively utilised within industry for polymer/carbon composite applications and would serve as a model system of graphitised carbon black.

This chapter investigates the simple system of poly(styrene-co-butadiene) random copolymers on a strongly absorbing graphite substrate. The chapter demonstrates that despite the simplicity of the system, there is a great deal of complexity in polymer morphology created through specific interactions and by altering experimental parameters. Polymer morphology varied significantly with solution concentration and the formation of thin films, continuous networks, asymmetrical nanoislands, and nanoribbons were observed on the surface. The polymer formed ordered nanopatterns on the graphite due to π-π stacking interactions. At the lowest concentration, this ordering was very pronounced. At higher concentrations, it was less defined but still statistically significant. The contact angles of the polymer nanostructures remained mostly constant with size, which is due to the strong polymer/graphite adhesion dominating over line tension and entropic effects.

5.2 Materials and methods

The same poly(styrene-co-butadiene) random copolymers samples were used in both the current chapter and in the experiments in Chapter 4. Furthermore, the polymer/toluene solutions were prepared at identical concentrations. The solutions were then spin coated onto freshly cleaved ZYA graphite using the same fixed parameters as Chapter 4. Polystyrene and polybutadiene homopolymers were also used with molecular weights of 150 kg/mol and 200 kg/mol, respectively. The molecular weights of the homopolymers were well above their entanglement molecular weights. At room temperature, the polybutadiene was well above its T_g, but the polystyrene was well below its T_g. The homopolymers were prepared in toluene according to their individual overlap concentrations and spin coated onto freshly cleaved ZYA graphite using the same fixed parameters as the other experiments.

Imaging of the graphite samples was carried out using tapping mode AFM in air at room temperature. The AFM machine, probes, and experimental methodology were identical to those used in Chapter 4. Likewise, all image analysis was also carried out using Gwyddion. Multiple deconvolution methods were implemented in order to account for the varying polymer morphology on the graphite surface (see Chapter 3 for details). The contact angles of the various nanostructures were calculated using AFM methods.

5.3 Results and discussion

5.3.1 AFM images and profiles

In Chapter 4, a systematic investigation of the formation of poly(styrene-co-butadiene) random copolymers on a mica surface was presented. The preparation of polymer samples and AFM methodology are the same in both studies, but the mica substrates are replaced with graphite.

Figures 5.1 – 5.3 show representative AFM height images of the poly(styrene-co-butadiene) samples on graphite, at each concentration and molecular weight. Line scan

plots showing the surface profiles of the images are also included. Generally, the line scans were taken as a full horizontal line across an image. The black lines on the profile plots relate to a scan which was taken across the upper part of the image, whilst the red lines relate to a scan across the lower part of the image. At some lower concentrations, bars in the AFM images represent the area where the line scan took place.

5.3.1.1 M_n = 46 kg/mol

Figures 5.1A and 5.1B show that at 3c*, the polymer formed a mostly continuous thin film. Some dewetting occurred, creating circular holes in the film with depths ranging from 2.4 nm to 20 nm. Circular aggregates were also observed on the film with heights ranging from 37 nm to 41 nm. Figures 5.1C and 5.1D show that at 1c*, a very coarse polymer network was formed on the graphite. The peak-to-peak distances of the network features ranged from 867 nm to 7.4 μm, while their heights ranged from 16 nm to 79 nm. Figures 5.1E and 5.1F show a very fine continuous network at 0.1c*, with peak-to-peak distances and heights of 199 nm to 805 nm and 2.4 nm to 9.7 nm, respectively. The range of values were much smaller than the coarser network formed at 1c*. Figures 5.1G and 5.1H show that at 0.01c*, asymmetrical polymer nanoislands formed with widths and heights ranging from 16 nm to 561 nm and 0.5 nm to 18 nm, respectively. Figures 5.1I and 5.1J show that at 0.001c*, polymer nanoribbons formed at the surface. Nanoribbons are extremely small polymer features, which contain very few chains. They have an elongated shape and very low height values due to the strongly adsorbing graphite surface. The nanoribbons had widths and heights ranging from 5.3 nm to 80 nm and 0.3 nm to 0.7 nm, respectively.

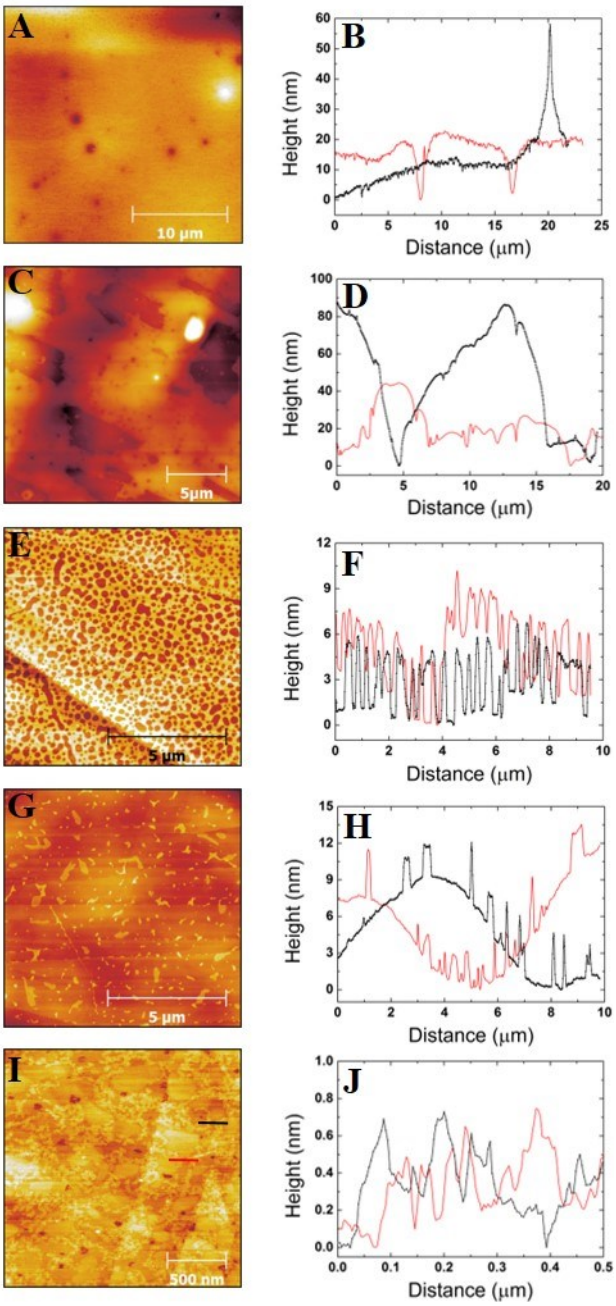

Figure 5.1: AFM height images and profile plots for the 46 kg/mol poly(styrene-co-butadiene) sample at varying concentrations on a graphite surface. The profile plots represent a horizontal line scan across the images, unless a bar is present, which corresponds to where the profile plot has taken place. (A) 3c* = 17.43 mg/ml, thin film (B) profile plot at 3c*, (C) 1c* = 5.81 mg/ml, network (D) profile plot at 1c*, (E) 0.1c* = 0.581 mg/ml, network (F) profile plot at 0.1c*, (G) 0.01c* = 0.0581 mg/ml, nanoislands (H) profile plot at 0.01c*, (I) 0.001c* = 0.0058 mg/ml, nanoribbons (J) profile plot at 0.001c*.

5.3.1.2 M_n = 86 kg/mol

Figures 5.2A and 5.2B show that at 3c*, a mostly continuous thin film formed with a few small holes with depths ranging from 1.3 nm to 9 nm. There were several aggregates present with heights ranging from 20 nm to 42 nm. Figures 5.2C and 5.2D show that at 1c*, a coarse continuous network was formed with peak-to-peak distances and heights ranging from 1.0 μm to 2.1 μm and 11 nm to 78 nm, respectively. Figures 5.2E and 5.2F show that at 0.1c*, a finer continuous network was formed with peak-to-peak distances and heights of 125 nm to 301 nm and 0.9 nm to 3.6 nm, respectively. Figures 5.2G and 5.2H show that at 0.01c*, irregular nanoislands formed with widths and heights ranging from 2.8 nm to 839 nm and 1.6 nm to 53 nm, respectively. Figures 5.2I and 5.2J show that at 0.001c*, nanoribbons formed with widths and heights ranging from 23 nm to 107 nm and 0.2 nm to 0.8 nm, respectively.

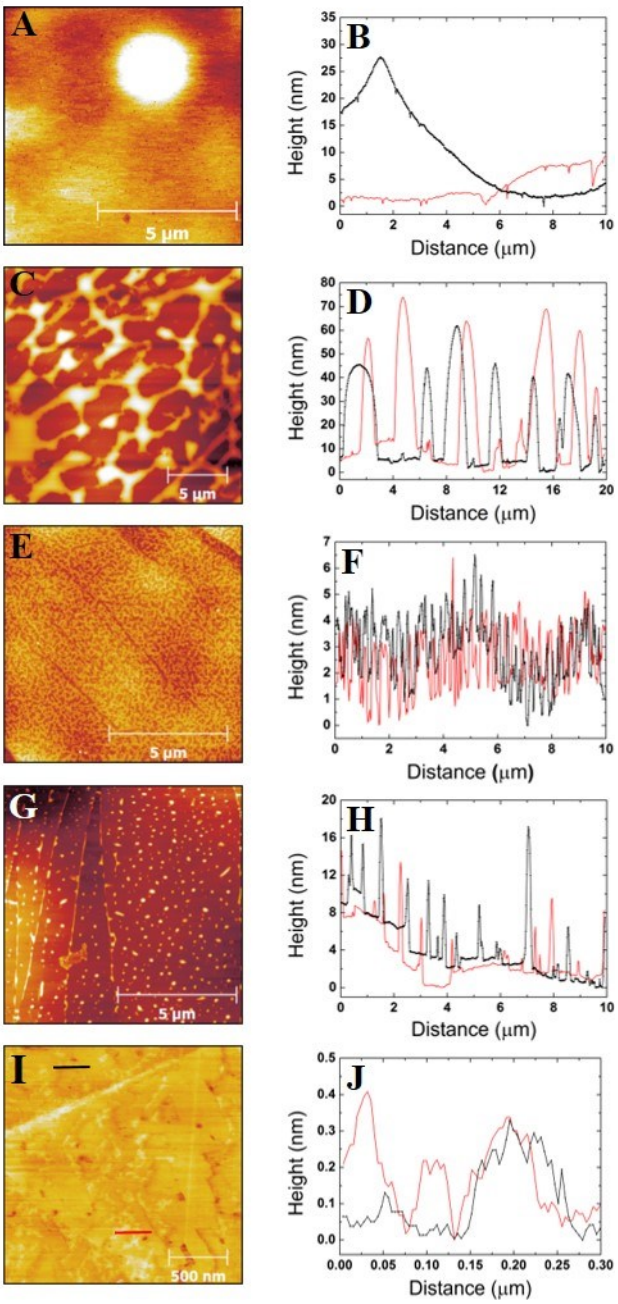

Figure 5.2: AFM height images and profile plots for the 86 kg/mol poly(styrene-co-butadiene) sample at varying concentrations on a graphite surface. The profile plots represent a horizontal line scan across the images, unless a bar is present, which corresponds to where the profile plot has taken place. (A) 3c* = 11.13 mg/ml, thin film (B) profile plot at 3c*, (C) 1c* = 3.71 mg/ml, network (D) profile plot at 1c*, (E) 0.1c* = 0.371 mg/ml, network (F) profile plot at 0.1c*, (G) 0.01c* = 0.0371 mg/ml, nanoislands (H) profile plot at 0.01c*, (I) 0.001c* = 0.0037 mg/ml, nanoribbons (J) profile plot at 0.001c*.

5.3.1.3 M_n = 355 kg/mol

Figures 5.3A and 5.3B show that at 3c*, a thin film formed with some significant amounts of dewetting characterised by holes with raised rims around their circumference. The depths of these holes ranged from 2.0 nm to 32 nm. There were numerous circular aggregates on the film with heights ranging from 6.5 nm to 225 nm. Figures 5.3C and 5.3D show that at 1c*, a coarse network was formed with peak-to-peak distances and heights ranging from 485 nm to 728 nm and 6.3 nm to 22 nm, respectively. Figures 5.3E and 5.3F show a finer continuous network at 0.1c*, with peak-to-peak distances and heights ranging from 275 nm to 441 nm and 1.1 nm to 3.3 nm, respectively. Figures 5.3G and 5.3H show that at 0.01c*, nanoislands formed with widths and heights ranging from 27 nm to 353 nm and 2.1 nm to 5.3 nm, respectively. Figures 5.3I and 5.3J show that at 0.001c*, the features were much less defined than the nanoribbons that formed at lower molecular weights. The features widths and heights ranged from 8.3 nm to 46 nm and 0.2 nm to 2.0 nm, respectively.

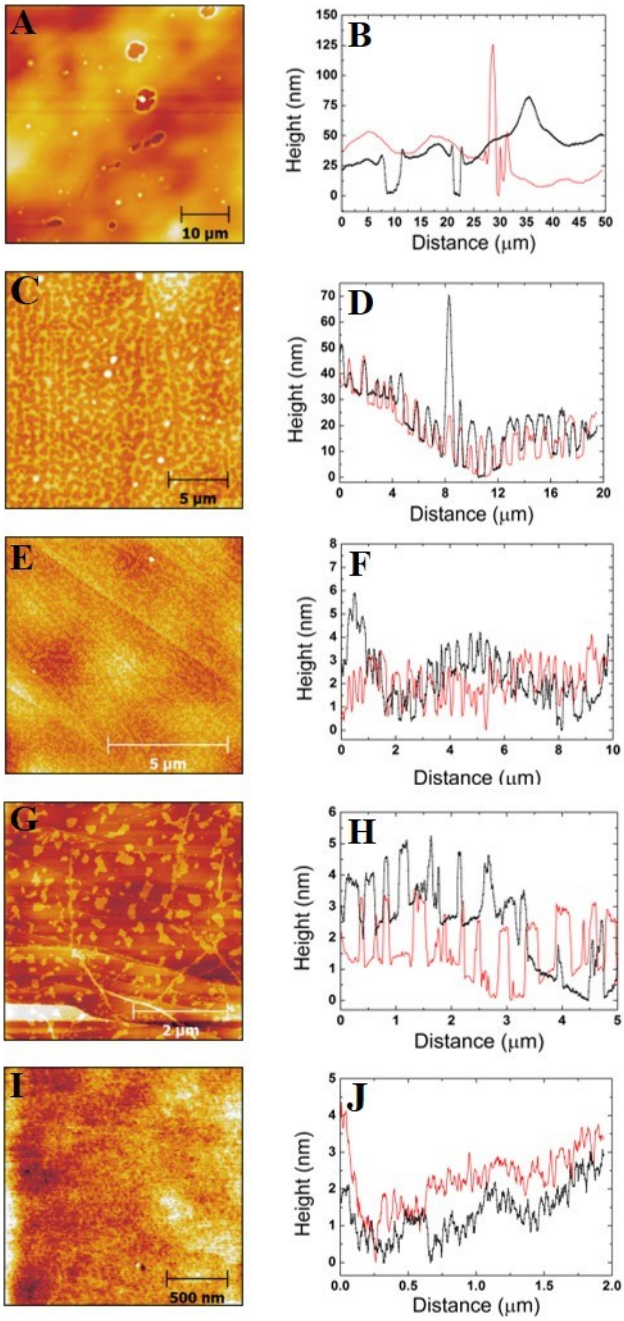

Figure 5.3: AFM height images and profile plots for the 355 kg/mol poly(styrene-co-butadiene) sample at varying concentrations on a graphite surface. The profile plots represent a horizontal line scan across the images. (A) 3c* = 4.17 mg/ml, thin film (B) profile plot at 3c*, (C) 1c* = 1.39 mg/ml, network (D) profile plot at 1c*, (E) 0.1c* = 0.139 mg/ml, network (F) profile plot at 0.1c*, (G) 0.01c* = 0.0139 mg/ml, nanoislands (H) profile plot at 0.01c*, (I) 0.001c* = 0.0014 mg/ml, nanoribbons (J) profile plot at 0.001c*.

5.3.1.4 Data analysis

The analysis methods and presentation of data were similar to those utilised within Chapter 4. In each AFM image, there were many individual polymer features that formed on the graphite. Therefore, in the graphs which have bars, each point represents an average value of feature width, height, contact angle, or number of chains per aggregate. As many of the images did not exhibit normal distributions of polymer morphology (see Figure 5.4 for typical examples of distributions). The bars on the graphs show the maximum and minimum value from the data set examined at a given parameter. From the histograms, it was clear that adding bars to the graphs which represented standard deviation was not appropriate for the data sets. As with Chapter 4, error bars associated with the error using AFM were omitted as they were at the size or smaller than the symbols used. The graphite substrates had distinct topographies. The surfaces had terraced structures with steps of low height values. Over larger length scales, the surfaces also exhibited some undulations. These can clearly be observed in the AFM images and profile plots in Figures 5.1 - 5.3. Accurate analysis of the polymer features could still be carried out, despite the varying topography. For the most part, polymer morphology was not impacted by the surface topography. However, at a concentration of 0.01c*, it was observed that polymeric material could accumulate at the steps on the surface. Figure 5.5 shows two AFM images of the 86 kg/mol sample at 0.01c*. Accumulation of polymeric material at the steps is clearly observed. Analysis of these features was not included in the results.

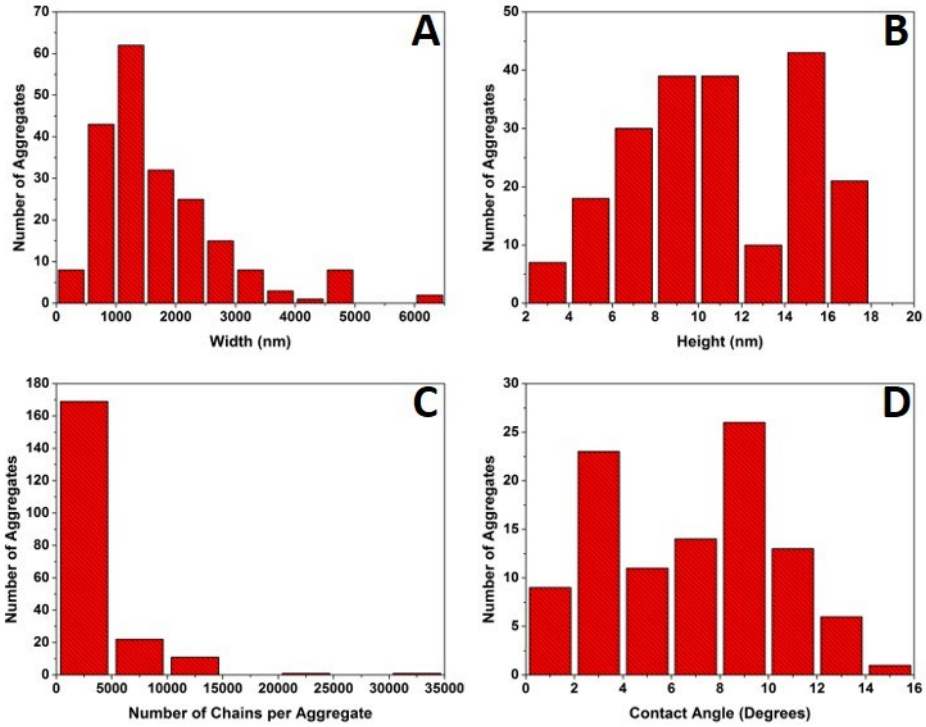

Figure 5.4: Typical histograms showing the distributions of polymer feature morphology for the 46 kg/mol sample at a concentration of 0.01c* on the graphite surface. (A) Width, (B) height, (C) number of chains per aggregate, (D) contact angle.

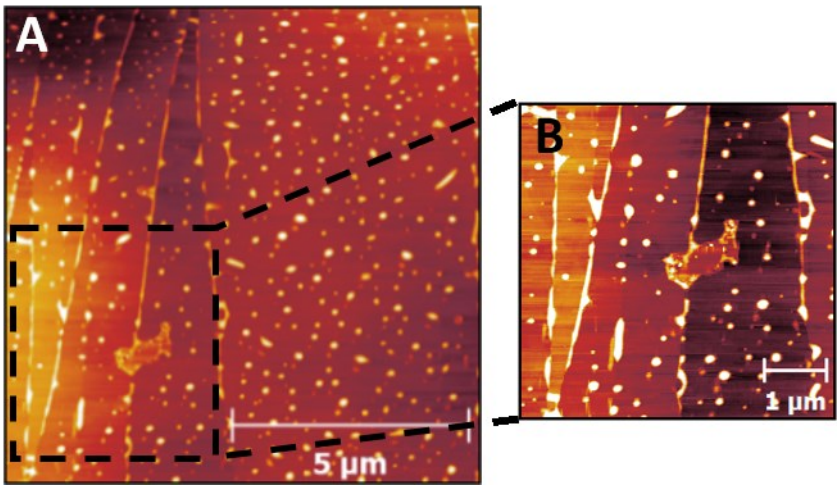

Figure 5.5: Typical AFM height image of the 86 kg/mol sample at a concentration of 0.01c* on graphite. (A) 10 μm^2 image, (B) 5 μm^2 zoomed image.

5.3.2 Concentration effects

5.3.2.1 Size distribution of polymer features

Figure 5.6 shows how the width of the polymer features varied with concentration for each molecular weight. The average width of the polymer features increased in small increments between 0.001c* and 0.1c*. The nanoribbons that formed at 0.001c* always had average width values less than 50 nm. Whereas, the networks that formed at 0.1c* all had average width values greater than 170 nm. There was a consistent abrupt increase in feature width between 0.1c* and 1c* for all molecular weights investigated. At 1c*, the polymer morphology changed from a fine continuous network to a much coarser one, and the average width values varied from approximately 600 nm to 3000 nm. Furthermore, the range of values for the coarse networks at 1c* were considerably larger than the three lower concentrations. The coarse networks had a polydisperse width distribution, whereas at 0.001c*, the width distribution was much more monodisperse. For the 86 kg/mol sample, the nanoislands that formed at 0.01c*, also had a more polydisperse width distribution.

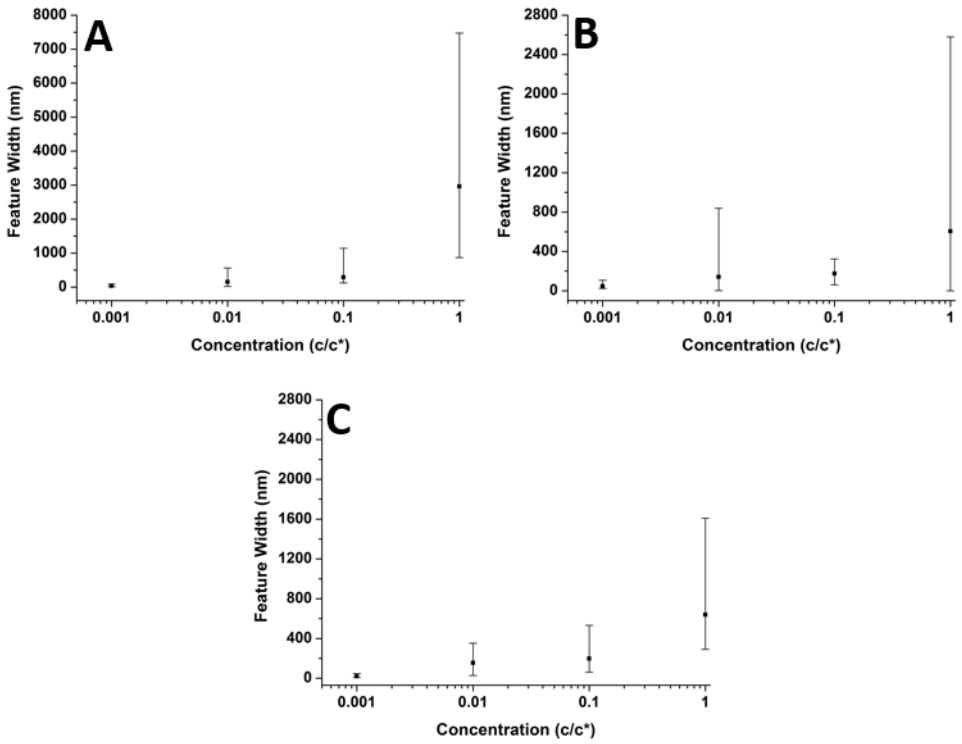

Figure 5.6: Graphs showing the relationship between polymer feature width and solution concentration at varying molecular weights. Each graph presents the average values and has bars which indicate the range of values. (A) M_n= 46 kg/mol, (B) M_n= 86 kg/mol, (C) M_n= 355 kg/mol.

Figure 5.7 shows the relationship between feature height and concentration at each molecular weight. At 0.001c*, the nanoribbons had small average height values (<1nm) and a monodisperse height distribution. At 1c*, the average height values were significantly larger than the three other concentrations, and the distribution was more polydisperse. However, the average height of the polymer features did not increase consistently with concentration. This is demonstrated at 0.01c*, where the asymmetrical nanoislands had larger average height values than the continuous networks that formed at 0.1c*. Furthermore, the range of values at 0.01c* were always larger than at 0.001c* and 0.1c*. At each concentration, the polymer features had much greater width values than height values. This was expected as the polymer strongly adsorbed onto the graphite surface.

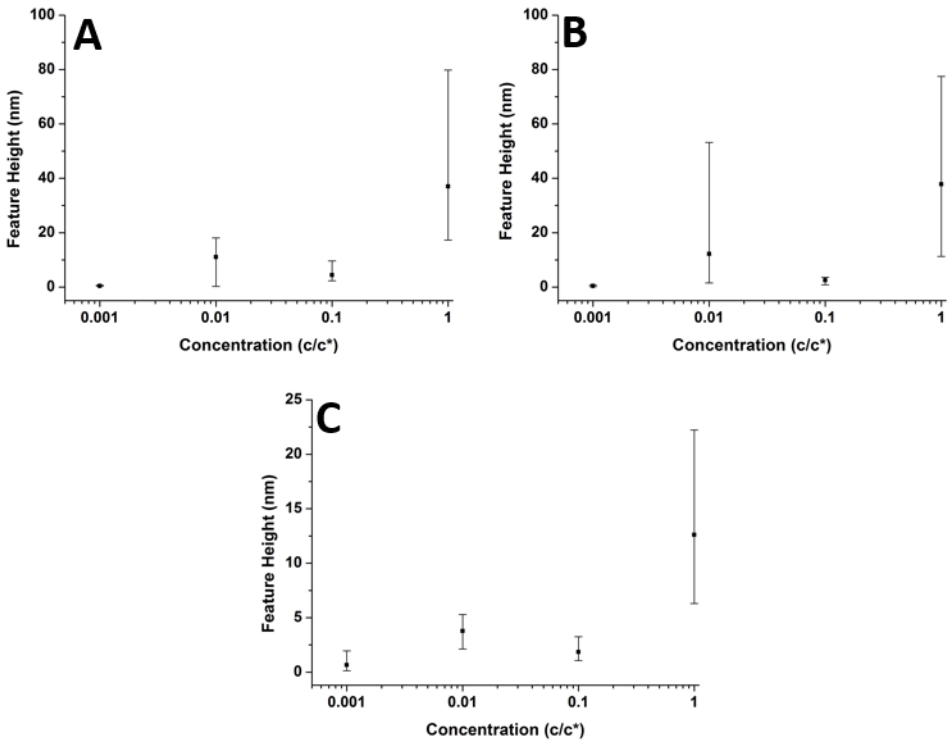

Figure 5.7: Graphs showing the relationship between polymer feature height and solution concentration at varying molecular weights. Each graph presents the average values and has bars which indicate the range of values. (A) M_n= 46 kg/mol, (B) M_n= 86 kg/mol, (C) M_n= 355 kg/mol.

The nanoribbons that formed at 0.001c* are of particular interest due to their extremely small average height values of 0.44 nm, 0.42 nm, and 0.65 nm for the 46 kg/mol, 86 kg/mol, and 355 kg/mol samples, respectively. These values are comparable to the characteristic height of a single polymer chain adhered to a surface (~0.4 nm).[109,125] This suggests that at this concentration, many of the polymers were adsorbed onto the graphite surface in a monolayer. However, the average widths of the nanoribbons were 38 nm, 48 nm, and 22 nm for the 46 kg/mol, 86 kg/mol, and 355 kg/mol samples, respectively. These values are far greater than the width of a single polymer chain. This suggests that at the graphite surface, the polymer chains either fold against themselves, or many chains aggregate side by side to create a nanoribbon with monolayer thickness.

5.3.2.2 Thin film morphology

At the highest concentration (3c*), mostly continuous thin films were formed on the graphite at each molecular weight. Film thickness values were determined using the AFM techniques outlined in Chapter 4. Using phase images to confirm that the holes in the films exposed the graphite surface is particularly important in a system where the polymer is deposited onto a strongly absorbing substrate. This is because it is possible that the surface of the holes could be covered by a thin layer of polymer and not actually expose the graphite surface. However, Figure 5.8 shows clear contrast between the holes and the polymer film which indicates that the holes fully exposed the graphite surface. The film thickness values could then be calculated using cross-sectional profile plots (see Figure 5.9). The film thickness values were 20 nm and 32 nm for the 46 kg/mol and 355 kg/mol samples, respectively. An accurate measurement of film thickness could not be obtained for the 86 kg/mol sample as the dewetted holes imaged were small. Consequently, it was not certain that the holes exposed the graphite surface. However, it can be concluded that the films had a thickness of ≥ 9 nm.

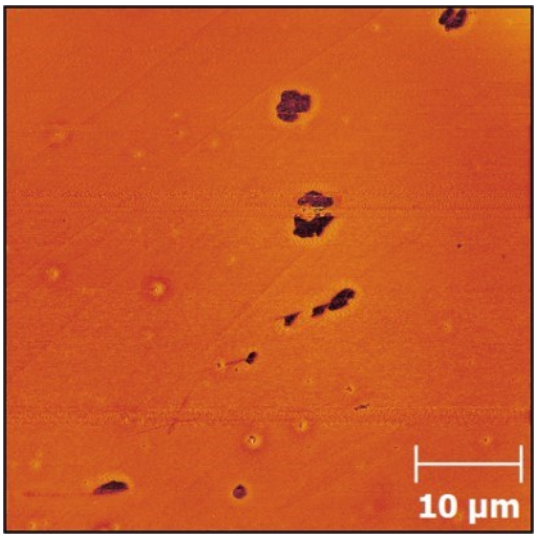

Figure 5.8: Typical AFM phase image showing dewetted holes in the polymer film of the 355 kg/mol sample at a concentration of 3c*.

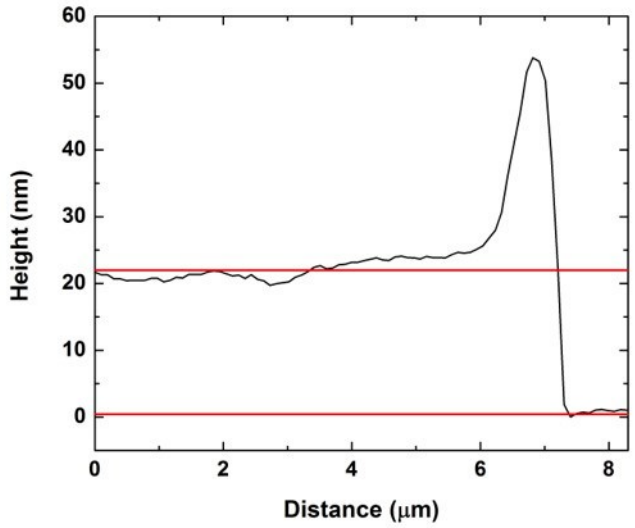

Figure 5.9: An example of a typical cross-sectional profile plot used to calculate the thickness of polymer films which formed at 3c*. The plot is taken from the 355 kg/mol sample.

In order to investigate the stability of the polymer films that formed at 3c*, the radius of gyration (R_g) values for each of the copolymers used in the study were compared to the thickness of the polymer films. As discussed in Chapter 4, the R_g values were 6.5 nm, 8.9 nm, and 18.0 nm for the 46 kg/mol, 86 kg/mol, and 355 kg/mol samples, respectively. It has been reported that the dewetting of polymer films on a wettable substrate is highly dependent on film thickness.[237] If film thickness is smaller than the polymer's R_g, then the films experienced dewetting. Whereas, if the film thickness was larger than the polymer's R_g, then no dewetting was observed. For each molecular weight in the current study, the thin films that formed on the graphite had greater thickness values than the polymer's R_g. Therefore, it was expected that the films would not experience dewetting on the strongly adsorbing graphite surface. To further investigate film stability, the effective Hamaker constant for the system was calculated using Equation 2.2. Values for the Hamaker constant of polystyrene range from 6.1 - 7.9 x 10^{-20} J, and the value for polybutadiene is reported as 8.2 x 10^{-20} J.[94,150] The Hamaker constant for graphite is reported as 47 x 10^{-20} J.[150] Therefore, the effective Hamaker constant for the current system was calculated (using the styrene-butadiene ratio of 25:75) to be approximately -1.1 x 10^{-19} J. As the calculated effective Hamaker constant is negative, the films should

have been stable and dewetting was not expected. From the analysis regarding the stability of the thin films (Hamaker constant, R_g), it was expected that the polymer films would be continuous and no dewetting would be observed on the surface. However, this was not the case as holes formed in the films created by dewetting through rapid nucleation caused by impurities, thermal fluctuations, or spinodal decompositon.[96,97] The holes in the films were either small (Figure 5.1A), or larger with raised rims around their circumference (Figure 5.3A). After 16 – 72 hours at ~ 55˚C above their T_g, the polymers did not form equilibrium structures on the graphite. This shows that the films were in a state of metastable equilibrium. This metastable state could be caused by interface effects and surface confinement.[192,207]

To further probe the dewetting behaviour of the thin films, the relationship between the diameter of the dewetted holes and the height of the rims around the circumference of the holes was investigated. A linear relationship between hole diameter and rim height was observed by G. Reiter using almost glassy polystyrene thin films on a highly nonwettable substrate annealed close to their T_g.[49] Reiter explained that this linear trend, alongside the asymmetric shape of the rim, strongly suggested that the polymer did not flow like a viscous liquid. Instead, driving capillary forces were responsible for plastically deforming the film, creating dewetting. Furthermore, under these experimental conditions, the reptation time of the polymer was over a year, which means viscous flow could not occur in the experimental time scale.

Figure 5.10 shows the relationship between rim height and hole diameter at 3c* for the 355 kg/mol sample. The graph shows that there is a linear relationship between hole diameter and rim height for the poly(styrene-co-butadiene) thin film at 355 kg/mol, despite the polymer being deposited onto a strongly adsorbing substrate. Furthermore, the shape of the rims were asymmetric, with sloped rear sides and steep insides (see Figure 5.9). This behaviour was only observed for the 355 kg/mol sample, as the films were in a more advanced state of dewetting due to an increased film thickness. This led to larger holes and the formation of raised rims. The slope of the graph in Figure 5.10 relates to the material properties of the system including film thickness, viscosity in the film, and the coefficient of friction at the interface.[93] This is an interesting result as the 355 kg/mol polymer was considerably above its T_g at room temperature, which can

account for the viscous fingering observed in the films (Figure 5.3A), but cannot account for the above observations which are usually attributed to plastic deformation.[49] Although, it cannot be conclusively stated that the film had experienced plastic deformation, the observed dewetting behaviour does indicate this. Therefore, the polymer films may have exhibited both viscous dewetting and plastic deformation. This could have been influenced by an increase in the effective T_g of the adsorbed polymers due to confinement effects at the interface.[29]

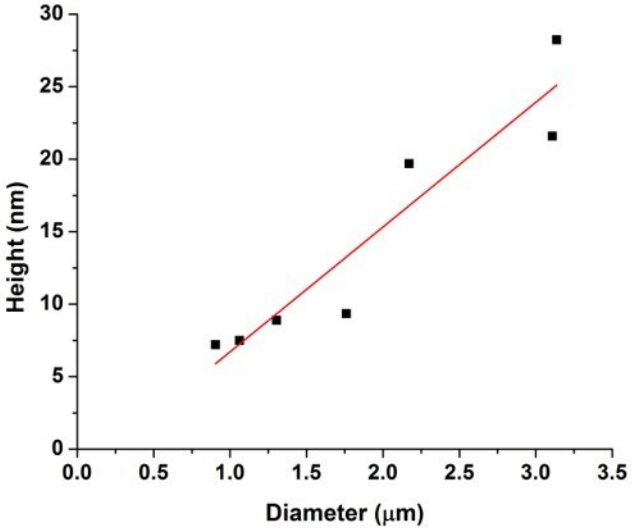

Figure 5.10: Graph showing the relationship between the height of the raised rims around the circumference of the holes and diameter of the dewetted holes at 3c*. The results are taken from the 355 kg/mol sample.

Figure 5.11 shows that the relationship between the average width of the rims and the hole diameters was also linear. This result supplies further evidence of plastic deformation in the films. In Chapter 4, the thin films on the mica surface also exhibited both viscous dewetting and plastic deformation. This demonstrates that the general mechanisms of the dewetted hole formation were similar for the polymer on both weak (mica) and strong (graphite) adsorbing substrates. However, there are also some significant differences in the dewetting behaviour of the thin films on each substrate. On

the mica surface, the dewetted holes were large with maximum diameters of ~ 15 μm. Whereas, under the same experimental conditions on the graphite surface, the dewetted holes were smaller with diameters up to only ~ 3 μm. This led to the average heights and widths of the rims on the mica surface (2.1 μm and 18.6 nm, respectively) being significantly larger than those on the graphite surface (0.8 μm and 14.6 nm, respectively). Additionally, on the mica substrate, the thin films had much larger viscous fingering patterns. This suggests that strong adsorption of the polymers to the graphite surface caused a decrease in the rate of hole growth by preventing movement of the chains. Therefore, the holes in the films on the graphite were in the earlier stages of dewetting. Consequently, there was a reduced accumulation of polymeric material around their circumferences which led to limited viscous fingering patterns.

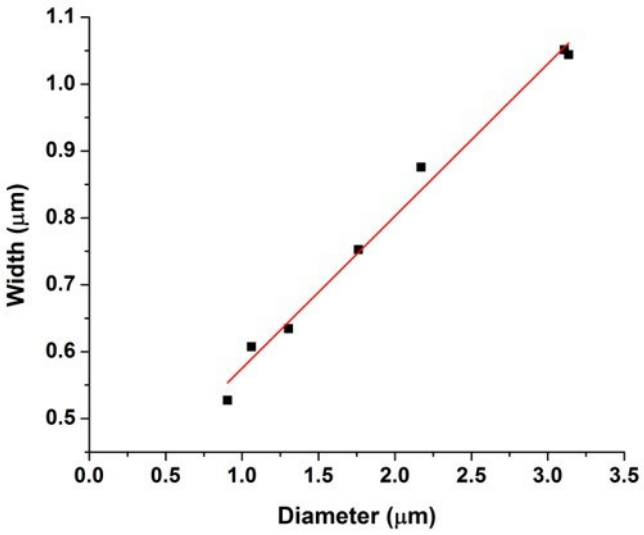

Figure 5.11: Graph showing the relationship between the average width of the raised rims around the circumference of the holes and the hole diameter at 3c*. The results were taken from the 355 kg/mol sample.

5.3.2.3 Distinct ordering of polymer nanostructures

Figure 5.12A shows an AFM phase image for the 86 kg/mol polymer at 0.001c*. The image shows a series of nanostructures on the surface created through self-assembly of the polymer, with specific ordering at intervals of 60˚. This is further demonstrated in the histogram in Figure 5.12B, which exhibits distinct peaks at intervals of 60˚. This shows that the polymer chains orientated themselves to reflect the crystalline symmetry of graphite, creating an ordered nanopattern.[158] This behaviour has been previously observed with crystalline polymers, such as polyethylene. Whilst graphite has a hexagonal crystalline structure and polyethylene has an orthorhombic crystal structure;[112,113] the distance of the a-axis of the graphite unit cell (2.46Å) is similar to the length of the c-axis in a polyethylene crystal cell (2.55Å).[111] This encourages epitaxial nucleation on the graphite surface resulting in an ordered polymer morphology. The effect has also been observed on graphite using polymers with pendant alkyl chains. In these instances, the 1,3-methylene group distance (2.51Å) in trans alkyl chains matches the distance of the a-axis of the graphite unit cell, with adsorption of the alkyl chains onto the graphite surface driving the distinct ordering.[115,117,236]

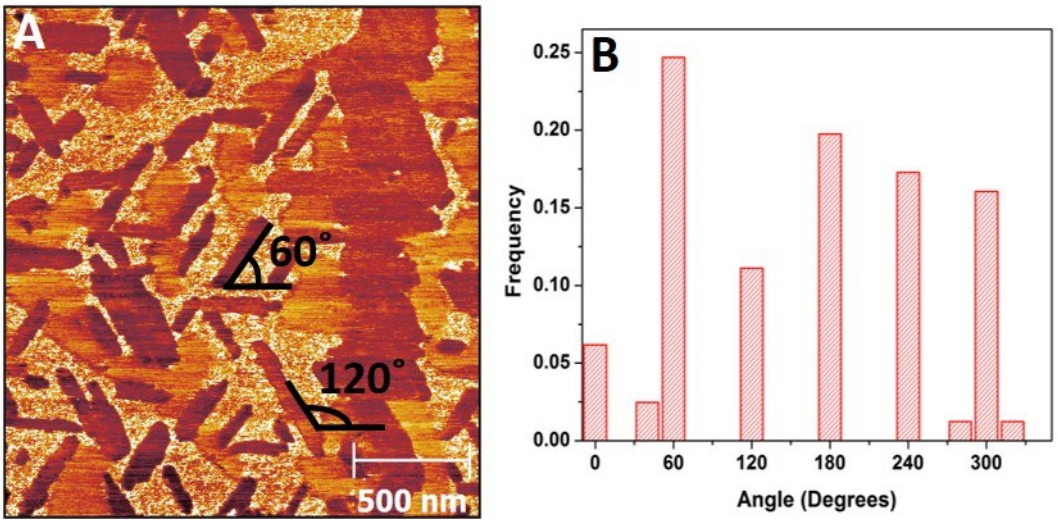

Figure 5.12: (A) AFM phase image of the 86 kg/mol sample at 0.001c*. Annotations show examples of the specific ordering of the nanostructures. (B) Histogram showing the angle (relative) frequency distribution of the nanostructures which formed at 0.001c* for the 86 kg/mol sample.

Previous research has demonstrated that observing distinct ordering on graphite is uncommon when using a linear amorphous polymer. Chen et al.[110] observed specific ordering with the amorphous homopolymer poly(4-vinylpyridine) on graphite. Chen et al. study demonstrated that this epitaxy-like orientation in dewetted thin films of poly(4-vinylpyridine) occurred only when the height of the nanostructures was less than 4 nm. For structures with heights of 4 nm, no evidence of ordering was observed. Chen et al. cited this epitaxy-like behaviour to the pyridine-group distribution matching the graphite lattice and nucleation at mosaic-block boundaries.[110] To our knowledge, the investigation by Chen et al. is the only study to observe the distinct ordering of a linear amorphous homopolymer on graphite. Specific ordering on graphite has never been observed with a linear amorphous copolymer.

Figures 5.12B and 5.13 show typical examples of the angle (relative) frequency distributions for polymer features that form at 0.001c* to 1c*. Below the overlap concentration (0.001c* to 0.1c*), clear peaks are present in the histograms at intervals of 60˚. At the overlap concentration (1c*), there are still some peaks at 60˚ intervals but they are not so distinct. At the lowest concentration (0.001c*), the ordering was very precise and 96% of the features measured were arranged at intervals of 60˚. At 0.01c* and 0.1c*, 69% and 68% of the features measured were arranged at angles of 60˚, respectively. At 1c*, the average height of the features was 38 nm, and 48% of the features measured were arranged at 60˚ intervals. This ordering may be due to π-π stacking interactions between the poly(styrene-co-butadiene) and the graphite surface. π-π stacking is the electrostatic, non-covalent attraction which occurs between π-bonds within molecules.[238] π-bonds are formed at double or triple covalent bonds when two p-orbitals overlap with one another, creating an electrostatic dipole.[239] π-π stacking is strongest between aromatic rings, a phenomenon which is sometimes referred to as aromatic stacking.[240] It is likely that π-π stacking occurs between the aromatic ring in the polystyrene molecule and the hexagonal lattice structure of the graphite surface. Therefore, this leads to features which are aligned at intervals of 60°. This intermolecular interaction appears to also drive ordering in samples at higher concentrations, as some ordering is observed for nanostructures with height values much greater than previously reported with amorphous polymers.[110]

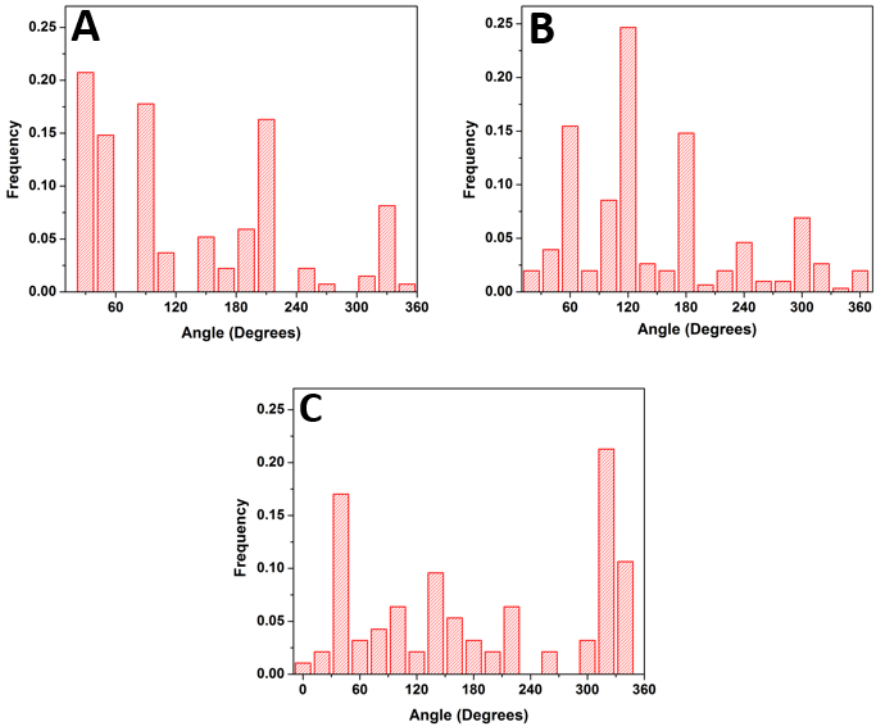

Figure 5.13: Typical histograms showing the angle (relative) frequency distributions for the polymer nanostructures at varying concentrations. (A) 355 kg/mol sample at 0.01c*, (B) 355 kg/mol sample at 0.1c*, (C) 86 kg/mol sample at 1c*.

The π-π stacking interactions may be more favourable between polystyrene and graphite compared to polybutadiene and graphite, due to the aromatic ring in the styrene unit. Thus, the nanopatterning may be driven by the ~25% styrene units in the random poly(styrene-co-butadiene) copolymers. Therefore, the morphology of polystyrene and polybutadiene homopolymers on graphite was studied to investigate the influence of aromatic rings in creating this ordering in polymers at the nanoscale. The homopolymers had similar molecular weights to the poly(styrene-co-butadiene) samples and were deposited onto graphite using the same experimental methods. Table 5.1 shows the heights and percentage of features orientated at 60° intervals for each sample investigated.

Table 5.1: Showing the ordering and average heights of poly(styrene-co-butadiene) (SBR), polystyrene (PS), and polybutadiene (PB) nanostructures on graphite at various concentrations.

Polymer	Concentration (c/c*)	Average height (nm)	Ordering at 60° intervals (%)
SBR	0.001	0.4	96
SBR	0.01	3.8	69
SBR	0.1	1.9	68
SBR	1	38	48
PS	0.01	1.5	42
PS	0.1	1.9	42
Annealed PS	0.1	2.5	37
PB	0.1	3.5	42
PB	1	2.5	41

Figures 5.14 and 5.15 show typical AFM height images and angle (relative) frequency distributions for the polystyrene homopolymers at each concentration investigated. The polystyrene formed a continuous network and asymmetrical nanoislands on the surface. The average height of the network was 1.3 nm, and 42% of the features measured were orientated at 60° intervals. The average height of the asymmetrical nanoislands was 1.5 nm, and 42% of the features measured were orientated at 60° intervals. For nanostructures with similar height values, there was significantly more ordering for poly(styrene-co-butadiene) than polystyrene. This is somewhat surprising, as polystyrene contains a greater number of aromatic rings and therefore has the potential for increased π-π stacking. Yang et al.[241] demonstrated that chain flexibility can affect the interactions between polymers and CNTs. In the current study, the poly(styrene-co-butadiene) chains are more flexible than polystyrene, and the aromatic rings are arranged randomly along the chain. NMR conducted by Michelin demonstrated that there was a >95% probability that the styrene blocks in the chains had lengths of 1 - 3 monomer units. This shows that the random copolymers did not contain large blocks of styrene monomer units. Therefore, the random distribution of the styrene units may have prevented *in-chain* π-π stacking interactions, and gave the chain enough flexibility to allow the rings to align on the surface and maximise π-π stacking with the graphite. In

polystyrene, the aromatic rings are adjacent to each other, and the chain is less flexible. This prevents free movement of the rings and means that collectively, they cannot align to maximise π-π stacking with the surface.

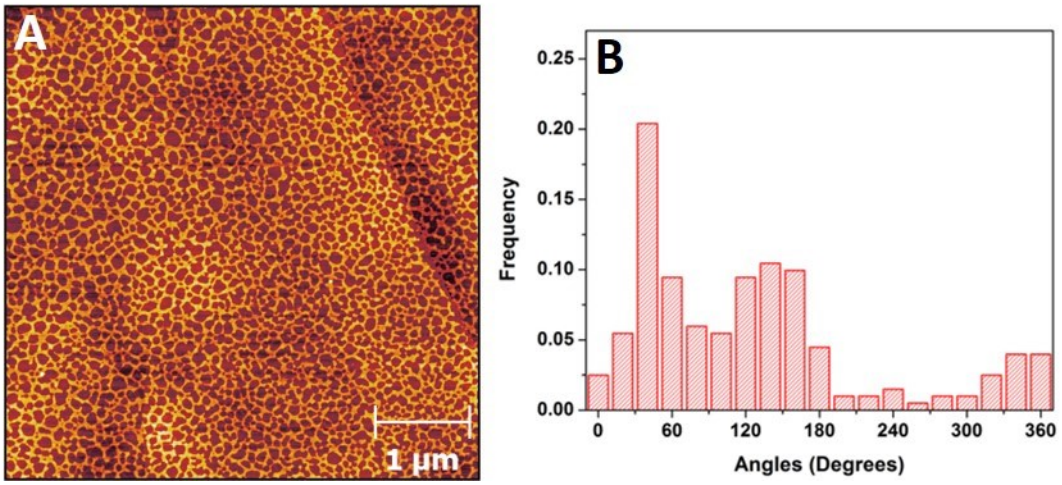

Figure 5.14: (A) Typical AFM height image of the 150 kg/mol polystyrene nanostructures formed on the graphite surface at a concentration of 0.1c*. (B) Accompanying angle (relative) frequency distribution histogram for the polystyrene at 0.1c*.

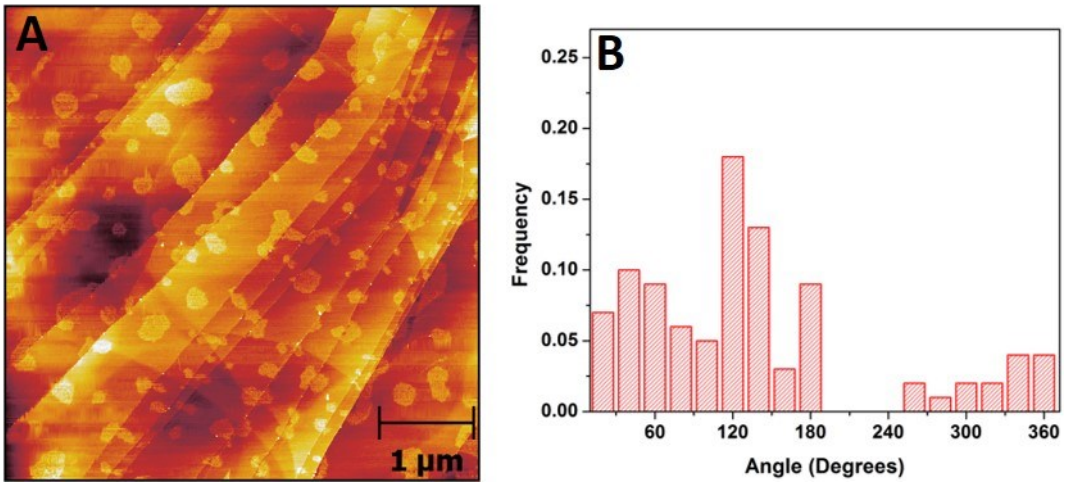

Figure 5.15: (A) Typical AFM height image of the 150 kg/mol polystyrene nanostructures formed on the graphite surface at a concentration of 0.01c*. (B) Accompanying angle (relative) frequency distribution histogram for the polystyrene at 0.01c*.

Additional experiments investigating ordering were carried out on the polystyrene homopolymers after they had undergone annealing. This is because all experiments were carried out at room temperature, which is significantly lower than the T_g of polystyrene (~100˚C).[242] Therefore, the polystyrene was glassy during the experiments and may not have been able to form equilibrium structures on the graphite surface. This could have impacted the degree of ordering of the polymer. The poly(styrene-co-butadiene) and polybutadiene samples had very low T_g values (approximately -35˚C and -100˚C, respectively).[243] This means that throughout the experiments, the polymers were well above their respective T_g's. Therefore, they behaved as viscoelastic liquids and could form equilibrium or metastable equilibrium polymer structures on the surface. In order to create a more accurate comparison between samples, annealing was carried out on the polystyrene samples at a temperature above the T_g value. This allowed for the formation of equilibrium or metastable equilibrium structures. The polystyrene samples were annealed at 120˚C (~20˚C above T_g) for 2 hours. All AFM imaging was carried out shortly after the samples had reached room temperature.

Figure 5.16 shows a typical AFM image and the angle (relative) frequency distribution for the polystyrene sample at a concentration of 0.1c*, after 2 hours of annealing at 120˚C. Figures 5.14 and 5.16 were prepared using identical experimental methods, with the only difference being that the sample in Figure 5.16 had experienced annealing. The results show that the process of annealing significantly impacted polymer morphology. The polymer formed a continuous network before annealing, and asymmetrical nanoislands after annealing. Therefore, this suggests that before annealing, the polystyrene did not form equilibrium or metastable equilibrium structures on the graphite. The average height of the nanoislands was 2.5 nm which is greater than the height of network before annealing. After annealing, 37% of the features are orientated at 60˚ intervals, which is slightly less than the degree of ordering in Figure 5.14. However, there was not a significant difference between the two values. These results show that although annealing impacted polymer morphology, the degree of ordering of the polymer nanostructures on the surface actually decreased. This demonstrated that π-π stacking interactions do not significantly depend on whether the polymer is in a glassy or liquid state.

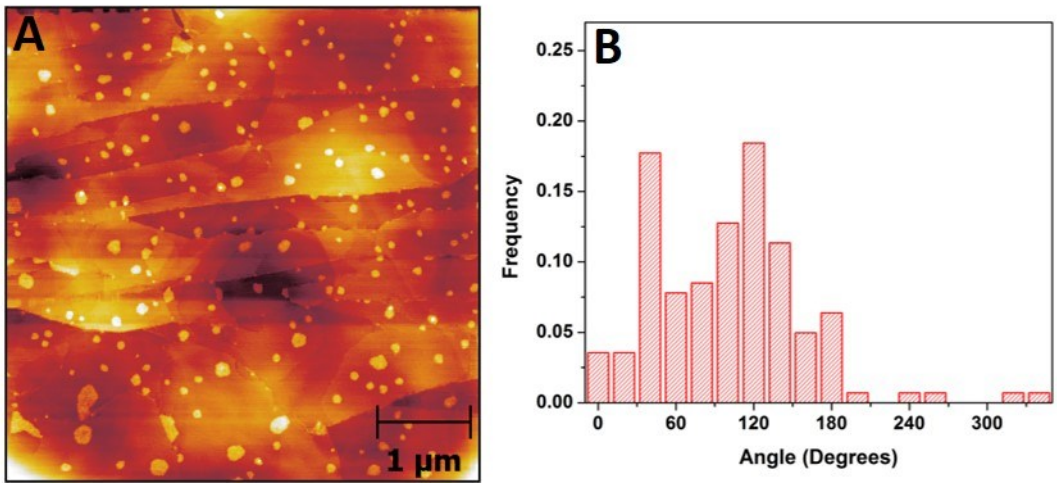

Figure 5.16: (A) Typical AFM height image of the 150 kg/mol polystyrene nanostructures formed on the graphite surface at a concentration of 0.1c*, after annealing at 120˚C for 2 hours. (B) Accompanying angle (relative) frequency distribution histogram for the annealed polystyrene at 0.1c*.

A polybutadiene homopolymer was also deposited onto the graphite surface using the same methods as the previous experiments. This allowed further comparisons between ordering and polymer structure to be carried out. Figures 5.17 and 5.18 show typical AFM height images and angle (relative) frequency distributions for the polystyrene homopolymers at each concentration investigated. The polybutadiene homopolymer formed a semi-continuous film and asymmetrical nanoislands at the concentrations investigated. The average height of the semi-continuous film was 2.5 nm, and 42% of the features measured were orientated at intervals of 60˚. The average height of the asymmetrical nanoislands was 3.5 nm, and 41% of the features measured were orientated at 60˚ intervals. The heights of the polybutadiene structures were very similar to that of the poly(styrene-co-butadiene) networks and nanoislands. The poly(styrene-co-butadiene) experienced a significantly greater degree of ordering on the surface. This demonstrates that although polybutadiene is flexible, the lack of aromatic rings prevents a high degree of ordering due to limited π-π stacking. These results suggest that the ordering of amorphous polymers on a carbon surface is heavily influenced by both chain flexibility and the proportion of aromatic rings in a chain. This ordering effect at a carbon surface could prove useful in nanopatterning applications.

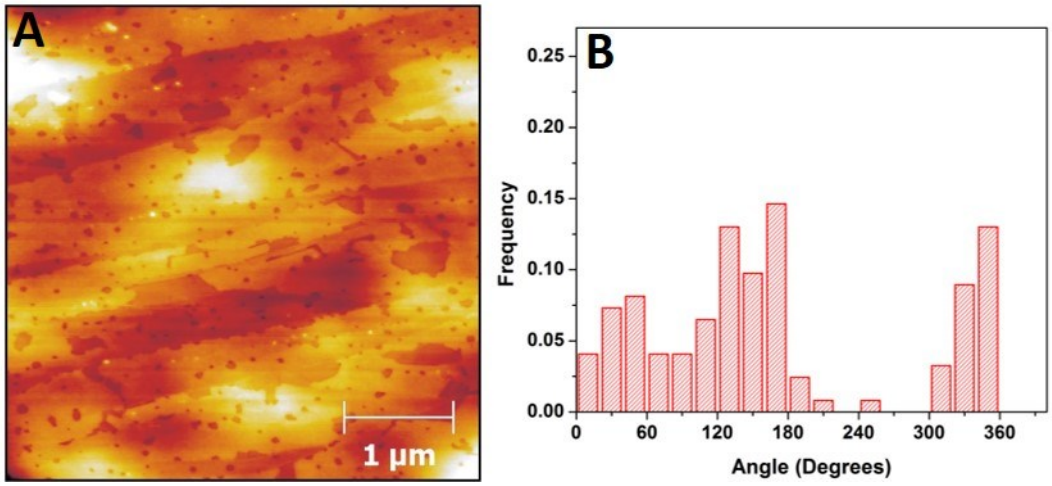

Figure 5.17: (A) Typical AFM height image of the 200 kg/mol polybutadiene nanostructures formed on the graphite surface at a concentration of 1c*. (B) Accompanying angle (relative) frequency distribution histogram for the polybutadiene at 1c*.

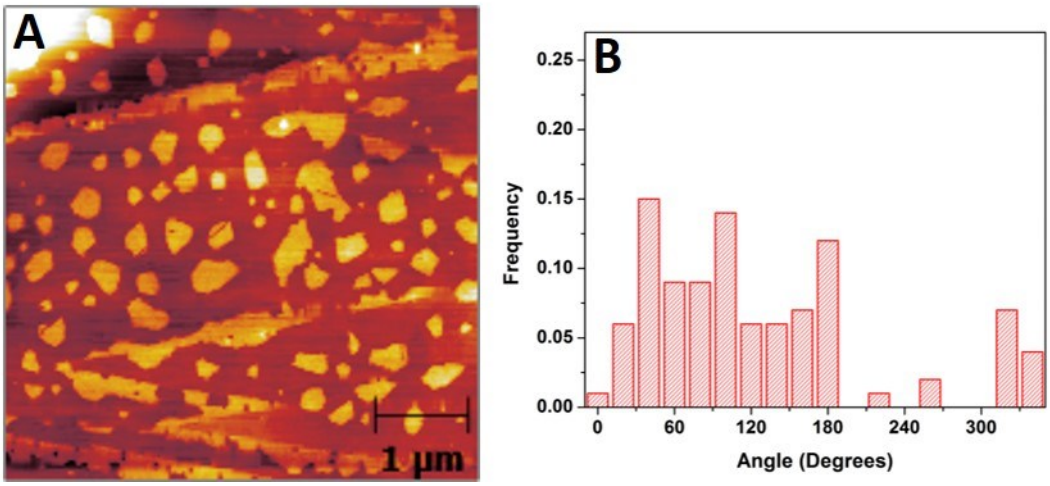

Figure 5.18: (A) Typical AFM height image of the 200 kg/mol polybutadiene nanostructures formed on the graphite surface at a concentration of 0.1c*. (B) Accompanying angle (relative) frequency distribution histogram for the polybutadiene at 0.1c*.

5.3.3 Molecular weight effects

5.3.3.1 Size distribution of polymer features

Figures 5.19 and 5.20 compare molecular weight against feature width and height at varying concentrations on the graphite surface. Figure 11 shows the average number of chains per aggregate against molecular weight at 0.01c*. The number of chains per aggregate could only be examined at 0.01c* as this was the only concentration where individual nanoislands formed.

Figures 5.19A and 5.19B show how the width of the network features that formed at 1c* and 0.1c* varied with molecular weight. The two graphs show similar trends as the average width values of the networks consistently decreased between 46 kg/mol and 86 kg/mol, and then stayed at similar values for the 355 kg/mol sample. Therefore, the networks had the largest width values when the polymer chains were the shortest. Additionally, the width distributions were largest for the 46 kg/mol sample at both 1c* and 0.1c*. Figure 5.19C shows that at a concentration of 0.01c*, where individual nanoislands formed, feature width remained fairly constant with increasing molecular weight. The average width value of the nanoislands only varied by 14 nm across all three molecular weights, although the range of values was lowest for the 355 kg/mol sample. Figure 5.19D shows that the average width of the polymer nanoribbons formed at 0.001c* was lowest at 355 kg/mol, whilst the 46 kg/mol and 86 kg/mol samples had similar values of 39 nm and 48 nm, respectively. The 355 kg/mol sample also had the smallest range of values, whereas the two lower molecular weights had similar width distributions.

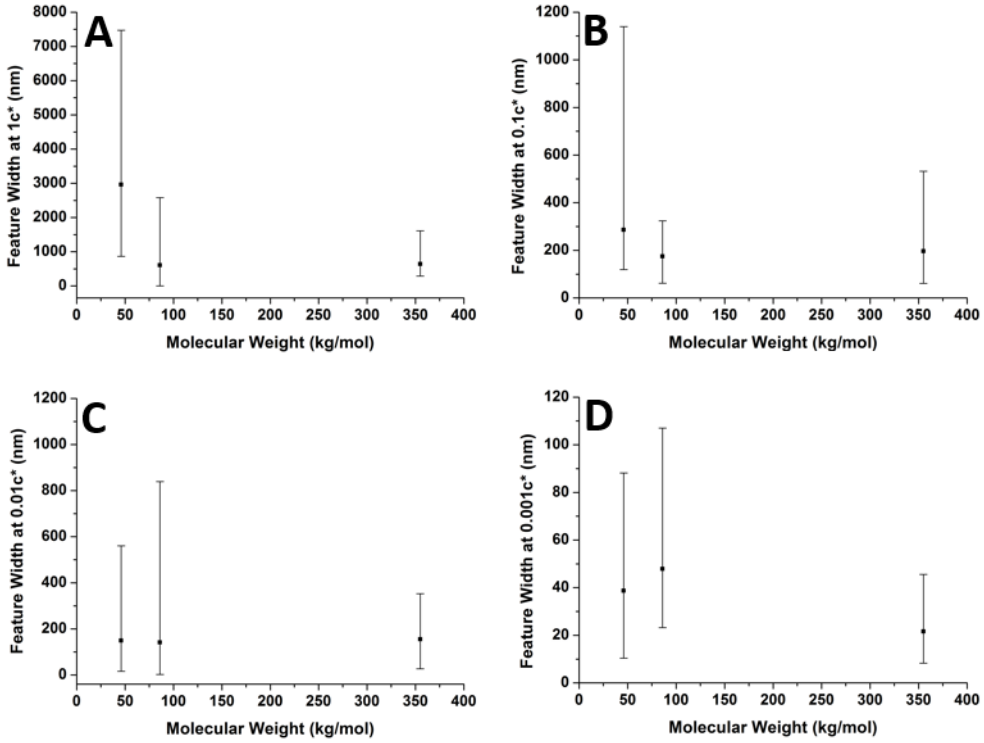

Figure 5.19: Graphs showing the relationship between polymer feature width and molecular weight at varying concentrations. Each graph presents the average values and has bars which indicate the range of values. (A) 1c*, (B) 0.1c*, (C) 0.01c*, (D) 0.001c*.

The graphs in Figures 5.20A and 5.20B show similar trends as feature height decreased with increasing molecular weight for the networks formed at both 1c* and 0.1c*. Furthermore, the height distribution was lowest at 355 kg/mol at both concentrations. Figure 5.20C shows that at 0.01c*, the height values of the nanoislands generally remained constant as molecular weight was increased. The average height value only varied by 9 nm across all three molecular weights. However, the 355 kg/mol sample had a considerably smaller height distribution than the two lower molecular weight samples. Figure 5.20D shows that the heights of the nanoribbons that formed at 0.001c* were very similar for the 46 kg/mol and 86 kg/mol samples which had average values of 0.44 nm and 0.42 nm, respectively. The 355 kg/mol sample had a marginally larger average height value (0.65 nm) and the largest height distribution.

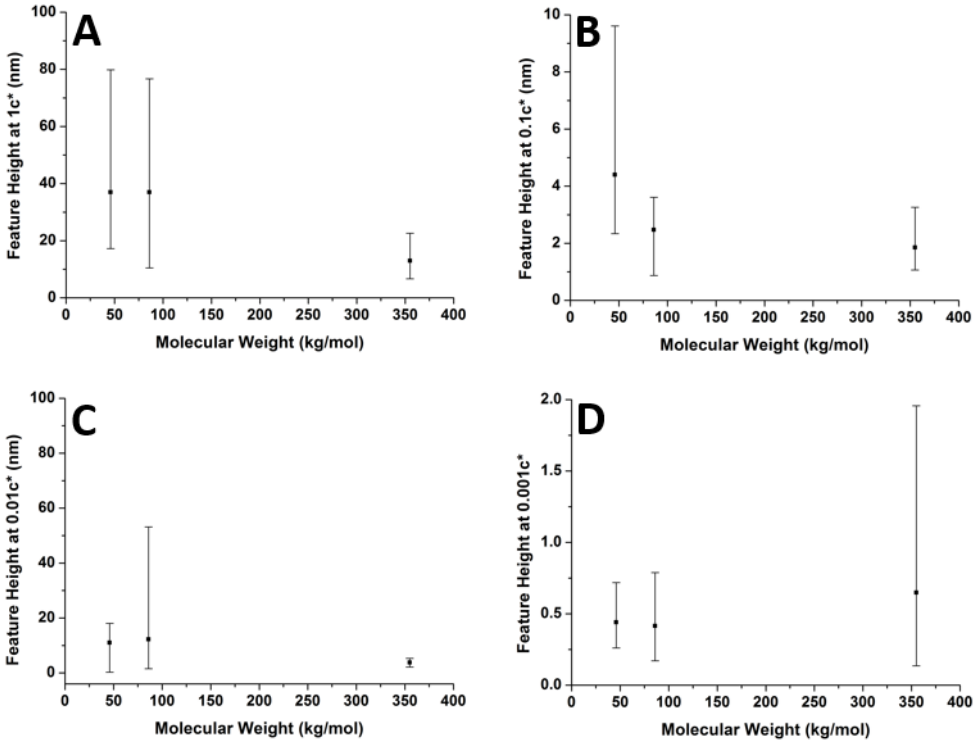

Figure 5.20: Graphs showing the relationship between polymer feature height and molecular weight at varying concentrations. Each graph presents the average values and has bars which indicate the range of values. (A) 1c*, (B) 0.1c*, (C) 0.01c*, (D) 0.001c*.

Figure 5.21 shows that the average number of chains per aggregate decreased with increasing molecular weight for the nanoislands formed at 0.01c*. This is a fairly linear relationship and the range of values are all large. This was expected behaviour, as Figures 5.19 and 5.20 show that the heights and widths of the nanoislands remained mostly constant with variations in molecular weight. Therefore, as molecular weight increased and the polymer chains became longer, it took fewer chains to assemble into aggregates of the same size.

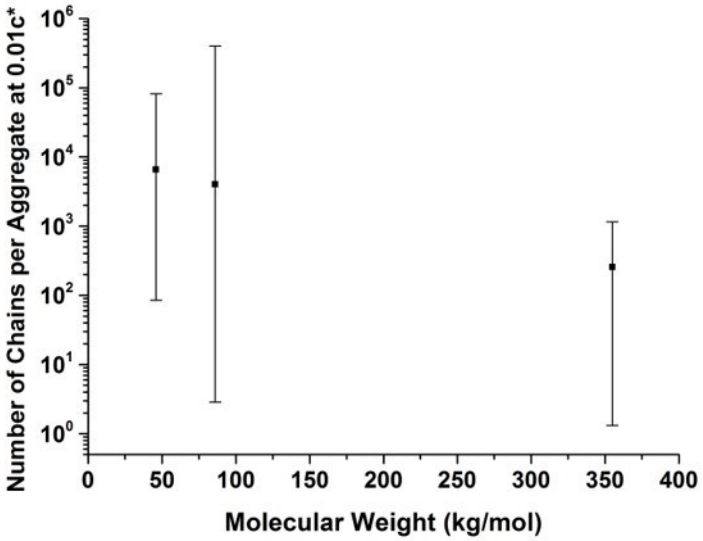

Figure 5.21: Graph showing the relationship between the number of chains per aggregate and molecular weight at 0.01c*. The graph presents the average values and has bars which indicate the range of values.

For the networks that formed at 1c* and 0.1c*, generally the average size of the polymer features decreased with increasing molecular weight. However, for the nanoislands and nanoribbons that formed at 0.01c* and 0.001c*, the size of the features remained similar when molecular weight increased. The reason for this varying relationship between molecular weight and nanostructure size is due to adsorption effects. Chains with higher molecular weights tend to maximise their contact with the surface, so that the sum of the adsorption energy gained from the adsorbed monomers is greater than the entropic loss.[4,215] This means it is favourable for the longer chains to maximise contact with the surface, despite the loss of entropy due to confinement.[244] However, for the lower molecular weight chains, it is less energetically favourable for them to adsorb to the surface, as the sum of the adsorption energy gained may not exceed the entropic loss. Consequently, the shorter chains will stay away from the surface in a more unperturbed state, meaning that larger features are more likely.[4] This is prevalent during the final stages of evaporation where the shorter chains can desorb more easily following the instabilities of the solvent and create larger features, whereas the longer chains are strongly bound to the surface. This behaviour explains why at higher concentrations, there was larger polymer features at lower molecular weights. However, at lower

concentrations, the size of the polymer features remained fairly constant with increasing molecular weight. This is because there were fewer chains present at the surface during solvent evaporation, which means the chains were likely to be adsorbed onto the graphite surface regardless of molecular weight.

The relationship between feature size and molecular weight on the graphite surface is very different to when the poly(styrene-co-butadiene) was deposited onto mica. On the mica substrate, the average size of the polymer features generally increased with increasing molecular weight at each concentration. This is because the poly(styrene-co-butadiene) weakly adsorbs onto the mica surface which means that the chains do not experience the same loss of entropy and gain in adsorption energy due to confinement effects. Instead, it is favourable for the chains to minimise surface energy and aggregate into spherical caps, regardless of molecular weight. This behaviour leads to fewer but larger aggregates on the mica surface at higher molecular weights.

5.3.3.2 Thin film morphology

The 355 kg/mol polymer films had greater thickness values than the 46 kg/mol films. Furthermore, the 355 kg/mol thin films appeared to be in a more advanced state of dewetting, exhibiting larger holes (diameters up to ~3 μm) with distinct raised rims around their circumferences. The 46 kg/mol films had smaller holes (diameters up to ~2 μm) and no raised rims. The apparent reason for this increased dewetting for the 355 kg/mol sample does not appear to be directly due to molecular weight effects. Previous investigations have demonstrated that the rate of dewetting for thin films with similar thicknesses did not change with variations in molecular weight.[49] The likely reason for this dewetting behaviour appears to be due to a greater initial film thickness for the 355 kg/mol sample. A greater amount of dewetting in polymer thin films with a larger thickness has been reported in the literature, as well as, in Chapter 4.[98,206] However, the reason why the 355 kg/mol sample had a greater film thickness could be due to a higher molecular weight. This allowed more polymeric material to remain on the graphite substrate during spin coating due to increased viscosity and entanglements. This

suggests that molecular weight effects did not directly cause an increase in dewetting. However, they were indirectly influencing this behaviour by creating films with larger thicknesses.[101]

5.3.4 Contact angle effects

5.3.4.1 Contact angle of nanostructures

Figure 5.22 compares the average contact angle values of the polymer features at varying concentrations at each molecular weight. For the 46 kg/mol and 86 kg/mol samples, similar trends are observed with minimum and maximum average contact angle values at 0.001c* and 0.01c*, respectively. For the 355 kg/mol sample, maximum values occur at 0.001c* and 1c*. This is the same trend which was observed on the mica surface in Chapter 4. At each molecular weight, the graphs show some similarities but there is not a clear trend that occurs in all graphs. This is likely because at each concentration, there was a wide variety of feature sizes.

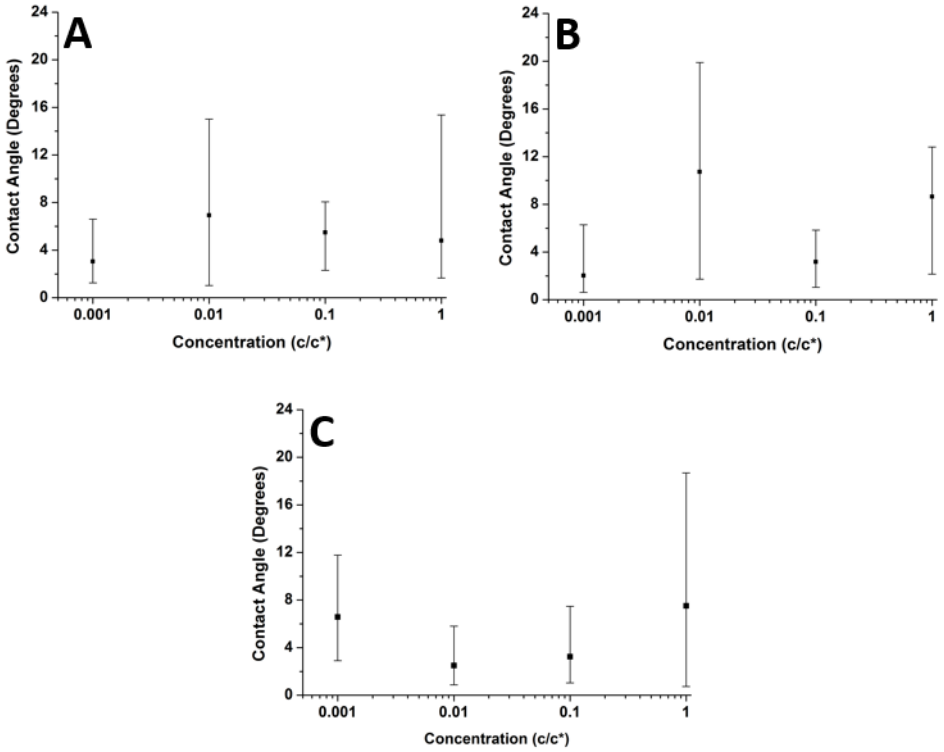

Figure 5.22: Graphs showing the relationship between contact angle and concentration at varying molecular weights. Each graph presents the average values and has bars which indicate the range of values. (A) M_n= 46 kg/mol, (B) M_n= 86 kg/mol, (C) M_n= 355 kg/mol.

Figure 5.23 shows how the contact angle of the polymer features varied with feature width at the nanoscale. There was no specific size dependence on the polymer contact angle and the average contact angle values were all small (<9˚). Across the nanoscale, the average contact angle values were fairly constant and only fluctuated by 4.2˚, 5.4˚, and 2.9˚ for the 46 kg/mol, 86 kg/mol, and the 355 kg/mol samples, respectively. This opposes the results observed when the polymer was deposited onto mica, where the contact angle of the nanodroplets were found to be extremely size dependent.

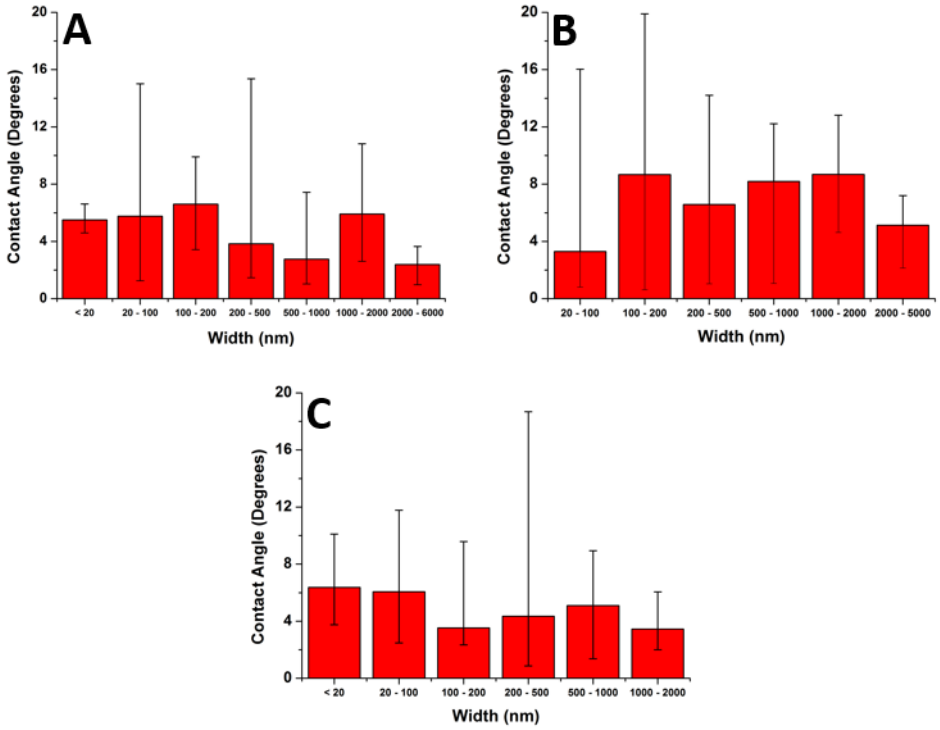

Figure 5.23: Graphs showing contact angle against width for the polymer features at varying molecular weights. Each graph presents the average values and has bars which indicate the range of values. (A) M_n= 46 kg/mol, (B) M_n= 86 kg/mol, (C) M_n= 355 kg/mol.

Milchev et al.[123] simulations study demonstrated that when polymer/substrate adhesion was strong, the contact angle of polymer droplets at a surface remained fairly constant as their size was reduced across the nanoscale. This behaviour was attributed to the droplets having no influence from line tension effects, due to strong polymer/substrate adhesion. Despite having a more variable polymer morphology, the current experimental results are in line with Milchev et al. simulations. There was strong polymer/substrate adhesion, and the polymer contact angle remained fairly constant across the nanoscale. This may provide experimental confirmation of Milchev et al. simulations study regarding the fairly controversial subject of line tension. Furthermore, any possible influence on the polymer contact angle caused by an increased effective elastic modulus due to confinement effects was also prevented by the strong polymer/substrate adhesion.[28]

Figure 5.24 shows the relationship between contact angle and feature height. The graphs demonstrate that the contact angle of the features did not stay constant with varying

height. However, there is not a consistent trend observed between the graphs, which shows that there is not a specific dependence between feature height and contact angle. For the 46 kg/mol sample, the general trend was fluctuating and the largest contact angle value was at a height of 5 - 10 nm, and the two lowest values were at >2 nm and 10 - 35 nm. For the 86 kg/mol sample, there was a generally increasing trend with the highest value at 10 - 35 nm and lowest value at >2 nm. For the 355 kg/mol sample, there was a generally increasing trend, and the highest value was at 10 - 35 nm and a lowest value of 2 - 5 nm.

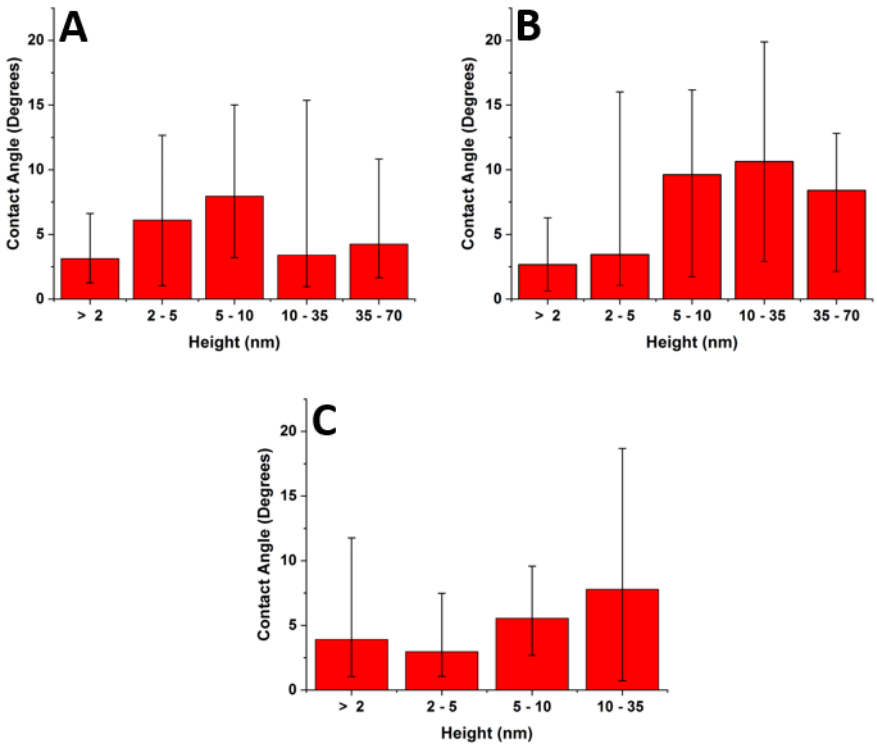

Figure 5.24: Graphs showing contact angle against feature height for the polymer features at varying molecular weights. Each graph presents the average values and has bars which indicate the range of values. (A) M_n= 46 kg/mol, (B) M_n= 86 kg/mol, (C) M_n= 355 kg/mol.

Figure 5.25 shows the relationship between contact angle and height normalised by R_g for the polymer features. Many of the polymer features had height values lower than the polymer's R_g values. If the height of the features was close to/lower than the R_g value of the polymer, this could have changed the polymer conformation and affect the contact

angles of the features. However, this should not have a very large impact as the polymers already strongly adsorbed to the graphite. Figure 5.25 shows that when height/R_g ~ 1, the contact angles values are at a maximum for the 46 kg/mol sample, close to a maximum for the 86 kg/mol sample, and at a midpoint for the 355 kg/mol sample. When height/R_g < 1, the contact angle of the polymer features are generally low. This suggests that as the heights of the features get to extremely low values, it is likely that the random coil conformation of the polymers is perturbed.

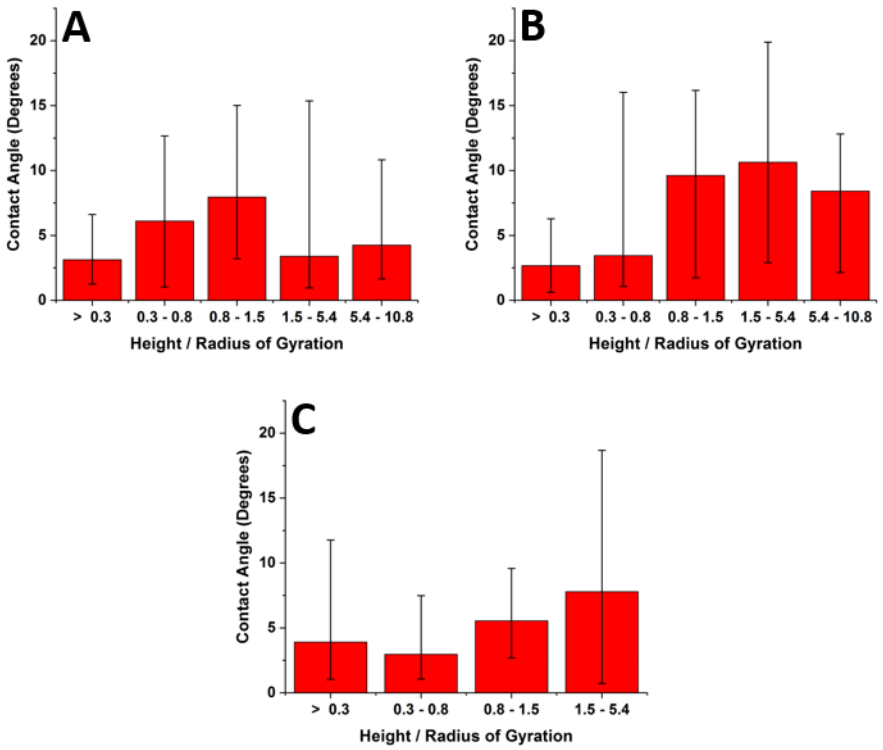

Figure 5.25: Graphs showing contact angle against feature height normalised by radius of gyration for the polymer features at varying molecular weights. Each graph presents the average values and has bars which indicate the range of values. (A) M_n= 46 kg/mol, (B) M_n= 86 kg/mol, (C) M_n= 355 kg/mol.

The results in Chapters 4 and 5 demonstrate that the substrate physicochemical properties and strength of adsorption between the polymer and the substrate are extremely influential in determining how the contact angle of polymer features varied with the lateral droplet size. Furthermore, the chapters also demonstrate that there is not a consistent relationship between feature height and contact angle.

Experiments were also carried out which investigated the contact angles of macroscopic poly(styrene-co-butadiene) droplets on graphite. However, it appeared that the annealing time was not sufficient to allow the polymer droplets to create equilibrium structures on the graphite, and the contact angle values appeared larger than expected. The experiments were repeated with longer annealing times, but only a small amount of data was obtained (see appendix for preliminary results). Therefore, this experiment remains an area for potential future work.

5.4 Conclusions

This chapter presented a comprehensive study on the fundamental behaviour of poly(styrene-co-butadiene) random copolymers on a graphite surface at the nanoscale. Above the overlap concentration, mostly continuous thin films formed which experienced partial dewetting. This is significant as the polymers had very low $T_g's$ and the films had thickness values greater than the polymer's R_g. Furthermore, the effective Hamaker constant for the system was negative. Therefore, it was expected that no dewetting would take place and equilibrium structures would form on the surface. However, this was not the case and dewetting occurred, demonstrating that the polymers were in a state of metastable equilibrium. This could be caused by interface and confinement effects.

For the 355 kg/mol sample, a linear relationship between the diameter of the dewetted holes and the height of their raised rims was observed, in addition to evidence of viscous fingering. This demonstrated that the thin films exhibited both viscous dewetting and plastic deformation. As concentration was reduced; networks, asymmetrical nanoislands, and nanoribbons formed on the graphite. There was variability in feature size at different concentrations which appeared to be due to the changes in polymer morphology from continuous networks to nanoislands and nanoribbons.

Precise ordering of the polymer chains was observed at the lowest concentration, creating epitaxy-like nanotrenches on the surface arranged at 60° intervals. This demonstrated that through π-π stacking interactions; poly(styrene-co-butadiene) can self-assemble via spin coating to reflect the crystalline structure of the graphite and

create ordered nanopatterns. Furthermore, at higher concentrations (up to 1c*), polymer morphology also experiences some degree of ordering in nanostructures with average heights up to 38 nm. This demonstrated that the π-π stacking interactions between the copolymer and the graphite are highly favourable. To further investigate the interactions between the random copolymer and the graphite, the experiments were repeated using polybutadiene and polystyrene homopolymers. Both homopolymers experienced significantly less ordering on the surface compared to poly(styrene-co-butadiene). This means that a high degree of ordering was observed in poly(styrene-co-butadiene) due to the aromatic rings being randomly spaced along a flexible chain which maximises π-π stacking interactions.

The 355 kg/mol thin film exhibited a greater amount of dewetting than the 46 kg/mol thin film. The likely reason for this is that the 355 kg/mol sample had a larger film thickness which increased the rate of dewetting. For the networks that formed at 1c* and 0.1c*, the size of the features were generally largest at the lowest molecular weight. This is because the shorter chains will be less likely to adsorb to the surface and remain in an unperturbed state, due to limited gains in adsorption energy from binding to the surface. However, at 0.01c* and 0.001c*, the size of the nanoislands and nanoribbons remained more constant with increasing molecular weight. This is because at lower concentrations, there were fewer chains at the surface during solvent evaporation. This means at every molecular weight, it is more probable for the individual chains to adsorb to the surface.

This chapter has demonstrated experimentally that the contact angle of the polymer features remained fairly constant with varying feature size. These results are in line with previous simulation experiments, and show that the strong polymer/graphite adhesion prevents any influence on contact angle from line tension or an increased effective elastic modulus.

This chapter provides a greater understanding of how polymers behave at a carbon surface at the nanoscale. This could prove beneficial in optimising the design and manufacturing processes of composite materials, and lead to improvements in their bulk physicochemical properties.

6 Investigating polymer/substrate adhesion with force spectroscopy techniques

Summary

This chapter presents two experimentally simple techniques which were developed to investigate the strength of interactions between polymers and various substrates at the nanoscale. Polymer chains were physically adhered to AFM tips and utilised in force spectroscopy experiments on silicon, mica, and graphite substrates. The results provided information regarding the strength of polymer/substrate interactions, but there was a significant influence from capillary forces on the more hydrophilic substrates. Furthermore, very few single chain desorption events were observed.

6.1 Introduction

The fundamental behaviour of polymers at surfaces is governed by intermolecular and surface forces.[150] These forces are dominant at the nanoscale and directly influence macroscopic behaviour.[81] Understanding the intermolecular and surfaces forces acting on polymers at the nanoscale is vitally important for many fields of research, including materials science, biology, and medicine[50,126].

Relatively recent technological advancements have led to the development of techniques which can accurately investigate forces at the nanoscale. These include AFM force spectroscopy, optical tweezers, and magnetic tweezers.[81] AFM force spectroscopy is the most commonly utilised technique for investigating the fundamental interactions between polymers and surfaces. It works by measuring the deflection of a cantilever through variations in laser alignment on a photosensitive diode, and then converting the deflection into a force. AFM force spectroscopy is extremely sensitive with a force resolution of approximately 10 pN.[245] Due to this high resolution, force spectroscopy experiments can accurately investigate the forces associated with single polymer chains at surfaces. This field of research is known as single-molecule force spectroscopy.

Many AFM force spectroscopy studies have investigated the molecular-scale forces which govern biological processes. These commonly include experiments using biopolymers, such as DNA, proteins, and polysaccharides.[50,246–248] There are also many force spectroscopy studies which have investigated synthetic polymers. These often include examinations into the stretching and rupturing of single polymer chains or measuring the force required to desorb single polymers chains from a surface.[85,128,129,249] There are no known AFM force spectroscopy studies which have investigated the interaction forces between poly(styrene-co-butadiene) random copolymers and various substrates.

It is very common for AFM force spectroscopy experiments to use complex and laborious experimental techniques when examining the interactions between polymers and surfaces. This commonly involves functionalising the surface of a substrate or an AFM tip which allows for polymers to be chemically bonded to them.[126,249] Furthermore, experiments can often be very time inefficient due to the very low probabilities of

observing single chain events and the process of carrying out the experiments in aqueous solutions.[85,128]

The following chapter presents an AFM force spectroscopy study which comprehensively investigated the interactions between poly(styrene-co-butadiene) random copolymer-coated AFM tips and silicon, mica, and graphite substrates in ambient conditions. Polymer chains were physically adhered to AFM tips using dip coating and force spectroscopy methods. The experimental system was uncomplicated and time efficient. Dip coating parameters were varied in order to create a wide range of polymer surface coverages on the AFM tips. Furthermore, different aspects of the experimental procedure were altered to investigate how this impacted adhesion results. This involved studying the difference between carrying out cycles at a fixed location compared to in an array, increasing tip/substrate contact time, and using a single tip to interact with numerous substrates. The results provided quantitative information regarding polymer/substrate interactions and some single chain desorption events were observed and analysed. However, there were two significant issues associated with the experimental system. These were increased adhesion on the more hydrophilic substrates due to capillary forces and the low probability of observing specific desorption events.

6.2 Materials and methods

Two poly(styrene-co-butadiene) random copolymer samples with molecular weights of 46 kg/mol and 355 kg/mol were used in the experiments presented in this chapter. The polymers were identical to the ones used in the experiments in Chapters 4 and 5, and were prepared in toluene solutions at three concentrations (1c*, 3c*, and 5c*). Dip coating was used to physically adhere polymer chains to the silicon AFM tips. Furthermore, polymer chains were also physically adhered to AFM tips using force spectroscopy techniques. In these instances, blank tips were used to interact with thin polymer films on silicon substrates which adhered a small amount of polymeric material to the very end of the tips.

6.2.1 Polymer morphology on silicon

It was important to analyse polymer morphology on the surface of the AFM tips after dip coating. This was because variations to dip coating parameters, such as concentration, molecular weight, and immersion time impacted polymer morphology on the tips, and therefore influenced polymer/substrate adhesion. However, to directly observe and analyse polymer nanostructures on the surface of an AFM tip is very challenging experimentally. SEM imaging was carried out on the tips, but the spatial resolution was insufficient to accurately image polymer morphology. Therefore, silicon substrates were purchased with surfaces which were nominally composed of a similar material to the AFM tips. As described in Chapter 3, the properties of silicon surfaces can depend on factors such as cleaning processes and native oxide growth due to exposure to ambient conditions.[174] This meant that the silicon tip and silicon substrates may have had some differences in surface properties. However, these differences should not have been large enough to significantly impact polymer morphology on each surface. Consequently, the silicon substrates were prepared using identical experimental methods, and the resulting polymer nanostructures were imaged using AFM. This allowed the polymer morphology on the silicon substrates to be thoroughly examined for each set of dip coating parameters. Therefore, an estimation of polymer morphology on the surface of the AFM tips was achieved without directly imaging the tips themselves.

6.2.2 Dip coating parameters

AFM tips were prepared with low and high polymer surface coverages using dip coating. The low surface coverage was classified as <20% polymer coverage, whilst the high surface coverage was classified as >90% polymer coverage. Two sets of experiments were carried out using AFM tips with low surface coverages. In the first, the tips were immersed in a 1c* solution of the 46 kg/mol sample for 10 minutes and were rinsed in toluene immediately after removal from the polymer solution. The corresponding silicon substrate had a polymer surface coverage of 16%. In the second experiment, the tips were immersed in a 3c* solution of the 355 kg/mol polymer for 10 minutes and were then rinsed with toluene. The corresponding silicon substrate had a polymer surface coverage of 9%. Although solution concentration and polymer molecular weight were

increased from the previous experiment, the polymer surface coverage decreased. As the dip coating immersion time was relatively short, this result could be due to the kinetics of the polymer chains within the solution. Higher molecular weight chains will generally move at a slower rate compared to lower molecular chains in a solution. Therefore, the immersion time may have been insufficient to allow a large amount of the higher molecular weight chains to move through the solution and adsorb to the silicon substrate.[250]

At low surface coverages, the polymers weakly adsorbed to the silicon substrates and self-assembled to create nanodroplets. For some samples, the polymer morphology was very consistent and the nanodroplets formed exact spherical caps of similar sizes (see Figure 6.1) However, for other samples, the polymer morphology (and surface coverage) was more variable and the shapes of the nanodroplets deviated from spherical caps (see Figure 6.2). This variable polymer morphology was not caused by altering dip coating parameters, but instead appeared to be due to the inherent inconsistencies associated with dip coating. It is very difficult to achieve a high degree of homogeneity in polymer nanostructures when using dip coating techniques.[185] Furthermore, variations in morphology could occur due to rinsing the samples in toluene. This inconsistency in polymer morphology at low surface coverages was a disadvantage of using dip coating, and may have impacted the force spectroscopy results. However, dip coating had a significant advantage as the polymer tips were not damaged during coating, which was vitally important for the success of the experiments.

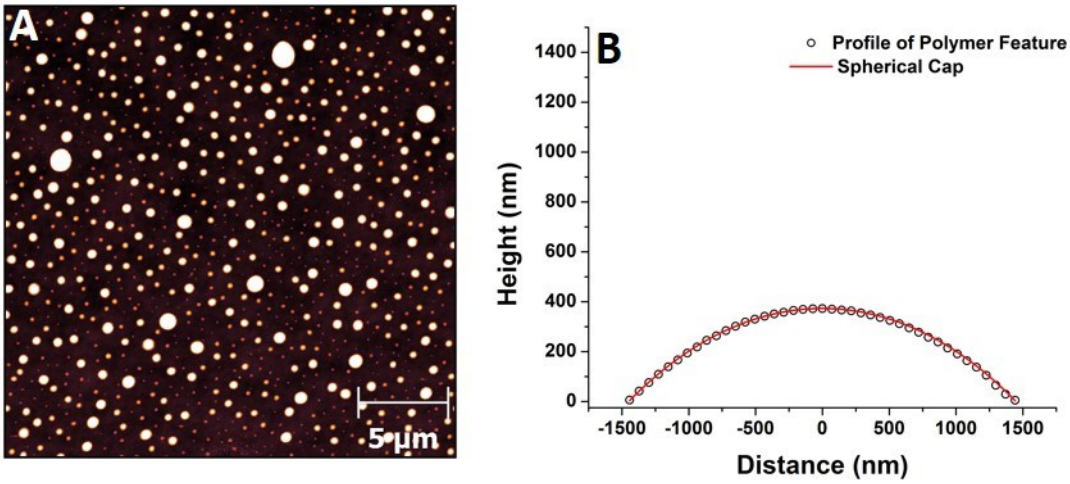

Figure 6.1: (A) AFM image of poly(styrene-co-butadiene) nanostructures on a silicon surface. The polymers were deposited onto the surface by dip coating in a 1c* solution of the 355 kg/mol sample for 10 minutes and were then rinsed with toluene. (B) A typical cross-sectional profile plot of a polymer nanodroplet in (A) fitted to a spherical cap.

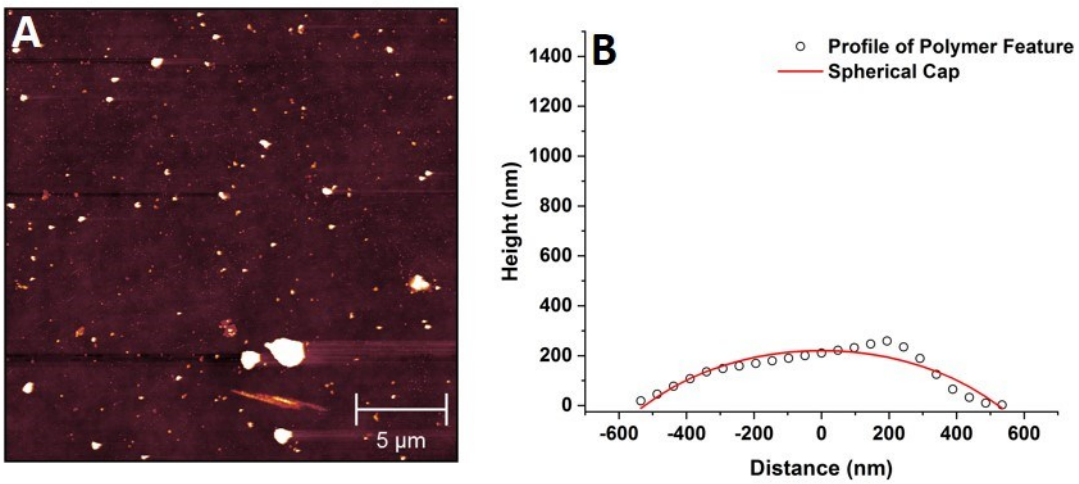

Figure 6.2: (A) AFM image of poly(styrene-co-butadiene) nanostructures on a silicon surface. The polymers were deposited onto the surface by dip coating in a 3c* solution of the 355 kg/mol sample for 10 minutes and were then rinsed with toluene. (B) A typical cross-sectional profile plot of a polymer nanodroplet in (A) fitted to a spherical cap.

The AFM tips with high polymer surface coverage were prepared by dip coating in a 5c* solution of the 355 kg/mol sample for 60 minutes. The tips were not rinsed with toluene after removal from the solution. This created a mostly continuous thin film on the corresponding silicon substrate with a thickness of 41 nm (see Figure 6.3). Some dewetting occurred which created circular holes in the films. However, this was fairly minimal and the polymer surface coverage was still very high (~95%). Therefore, heterogeneous polymer morphology should not have significantly impacted the adhesion results for the experiments which used tips with high surface coverages.

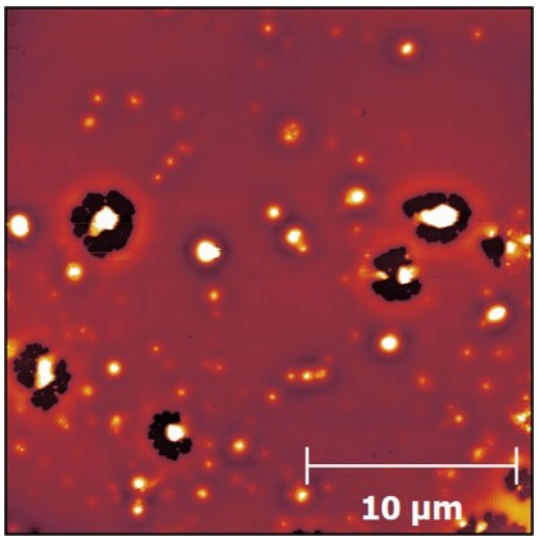

Figure 6.3: Typical AFM image showing a mostly continuous polymer film on a silicon surface. The film was created by dip coating in a 5c* solution of the 355 kg/mol sample for 60 minutes with no toluene rinsing.

6.2.3 AFM

All AFM experiments were performed using the Multimode/Nanoscope IIIa AFM as described in the previous chapters. AFM force spectroscopy was carried out in air under ambient conditions, using MSNL-10 probes with very low nominal spring constants of 0.01 N/m. The AFM tips were made of silicon with a nominal tip radius of 2 nm (see Chapter 3 for details). The three substrates used in the force spectroscopy experiments were silicon, mica, and graphite. The mica and graphite substrates were cleaved immediately before the experiments. Whereas, a new silicon substrate was used for each experiment, which was cleaned with acetone and ethanol before use. All AFM imaging was carried out using the same methods and probes as the experiments in Chapters 4 and 5.

6.2.4 Data analysis

All image analysis was performed using Gwyddion. Whilst all analysis of force-distance curves was carried out on Nanoscope Analysis and Origin software. This included calculating values of overall adhesive force and adhesive energy, as well as, analysis of

specific desorption events (see Chapter 3 for details). The adhesive force was taken from the value of the largest minimum in each force-distance graph. Whereas, the adhesive energy was calculated by integrating the complete area above each curve in the fourth quadrant of the force-separation graphs. The adhesive energy per Kuhn segment was calculated by integrating the specific area above the curves in the fourth quadrant only where force plateaus and steps occurred. This provided a value of the adhesive energy of the specific desorption events which could then be used in Equation 3.11 to calculate the adhesive energy per Kuhn segment. Due to the wide range of adhesive energy values, the overall adhesive energy was presented in eV, whereas the adhesive energy per segment was presented in kJ/mol. The arithmetic surface roughness (R_a) values of each substrate were calculated from AFM height images using Gwyddion. R_a is defined as the average value of deviations in surface roughness from the mean line over an evaluation length. The mathematical definition of R_a is represented by the following formula:[251]

$$R_a = \frac{1}{l}\int_0^l |y(x)|dx \tag{6.1}$$

Where l is the evaluation length and $y(x)$ is the profile height function.

6.3 Results and discussion

6.3.1 Surface roughness measurements

It has been reported that surface roughness can affect polymer/substrate adhesion at the nanoscale. If a substrate has a large surface roughness, this reduces the interfacial contact with the polymer chains which leads to a decrease in the overall strength of adhesion at the interface.[252] Therefore, analysis of AFM images was carried out in order to provide R_a values for each substrate. As the desorption events of single polymer chains occurred across very small length scales, the surface roughness measurements were carried out on AFM images with small areas ($2.5\ \mu m^2$). Figure 6.4 shows typical AFM images of each blank substrate. The mica was the smoothest of the substrates with a surface roughness value of 0.1 nm. This was expected as mica has perfect cleavage which means a completely flat top surface is exposed upon cleaving.[153,156] The silicon

surfaces were polished by the provider and had a roughness value of 0.4 nm. The graphite had the highest surface roughness value of 0.8 nm. Although graphite can be cleaved, it often exhibits a distinct terraced structure (see Figure 6.4C) which increases surface roughness. Despite the substrates having some variation in surface roughness values, each substrate is still relatively very smooth (<1 nm). This meant that the roughness of the substrates should have not significantly impacted polymer/substrate adhesion.

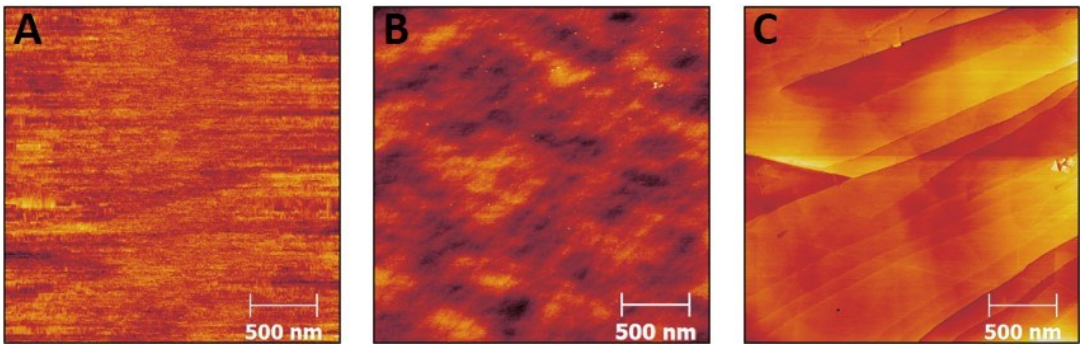

Figure 6.4: Typical AFM height images of each blank substrate with an area of 2.5 μm^2. (A) Mica, (B) silicon, (C) graphite.

6.3.2 Blank tip experiments

Experiments were carried out to investigate the strength of interactions between a blank AFM tip and each substrate. Figure 6.5 shows typical force-distance curves for the interactions between each substrate and the AFM tip. All of the force-distance curves for each substrate exhibited a simple snap-out shape, which is typically observed between two hard surfaces where short range interactions are dominant. Table 6.1 demonstrates that the tip/substrate adhesion was weakest on the graphite, and strongest by a significant margin on the mica. Specifically, the average adhesive force on the silicon substrate was 0.37 nN larger than the graphite, whilst the average adhesive force on the mica was 1.31 nN larger than the graphite. It appeared that capillary forces were influencing the results as there was a correlation between the measured adhesion values and the substrate hydrophilicity. In force spectroscopy experiments, capillary forces occur when a thin film of water condenses on the surface of the substrate or AFM tip. As

the tip approaches the substrate, a meniscus is formed between the substrate and tip, which creates surface tension and increases the measured adhesive force. The magnitude of capillary forces is influenced by the hydrophilicity of the substrate and the AFM tip.[159]

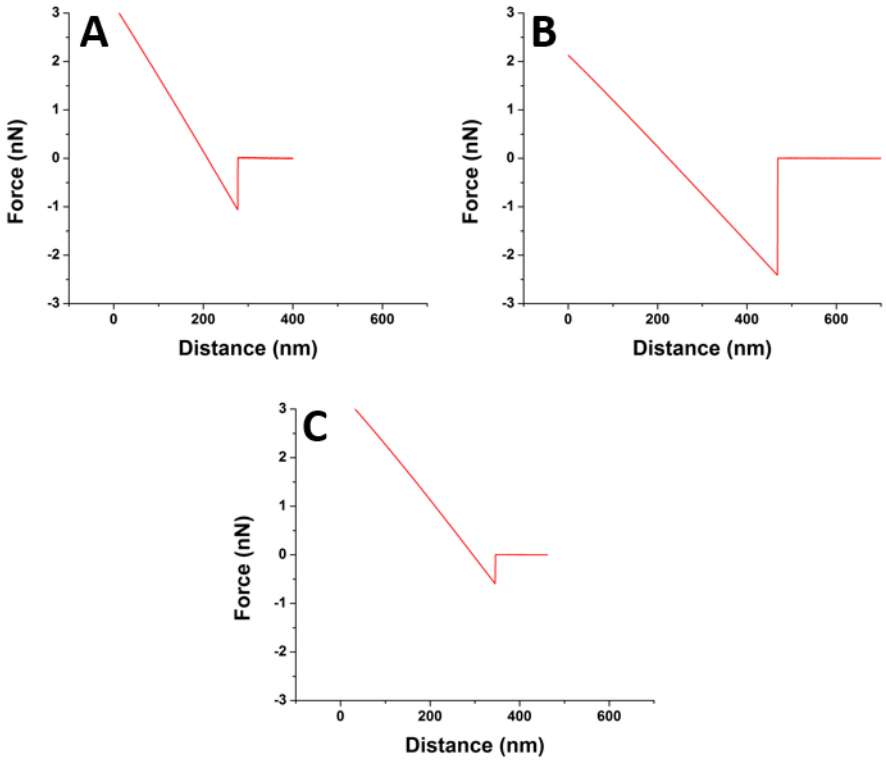

Figure 6.5: Typical force-distance curves showing the interactions between a blank AFM tip and each substrate. The approach/retract cycles were carried out in an array with a step size of 500 nm in the x and y directions. (A) Silicon, (B) mica, (C) graphite.

Table 6.1: Average adhesive force and energy between a blank AFM tip and each substrate. The approach/retract cycles were carried out in an array, with a step size of 500 nm in both the x and y directions.

Substrate	Average Adhesive Force (nN)	Average Adhesive Energy (eV)
Silicon	0.93 ± 0.06	173 ± 21
Mica	1.87 ± 0.82	1289 ± 1017
Graphite	0.56 ± 0.05	91 ± 20

Mica is extremely hydrophilic, with a water contact angle of <5° which means that a water layer forms on its surface under ambient conditions.[157,158,253] Consequently, the effects of capillary forces were significant on the mica, which increased the measured adhesion values in the force spectroscopy experiment. The degree of hydrophilicity of silicon substrates can be influenced by various factors, such as native oxide layer thickness and the cleaning process of the surface.[174,175] Therefore, contact angle goniometry was implemented to measure the water contact angle of the silicon substrates used in the experiments. The average water contact angle on the silicon substrates was 45.8°, which is less hydrophilic than mica. This meant that the effects of capillary forces on the silicon substrate were smaller than those on mica. The water contact angle of freshly cleaved graphite ranges from 84° to 86°.[164–166] Therefore, graphite is significantly less hydrophilic than both silicon and mica. Subsequently, capillary forces should not have impacted the force spectroscopy results on the graphite. The adhesive force and energy values in Table 6.1 directly relate to the hydrophobicity of each substrate. This confirmed that capillary forces were influencing the adhesion results.

Additionally, the results in Table 6.1 demonstrate that the standard deviation values for the mica substrate were significantly larger than those for the silicon and graphite. This meant that there were substantial variations in the tip/substrate adhesion for cycles on different areas of the mica substrate. This was likely due to well-documented water-layer variations on the mica surface.[125,218] Therefore, the magnitude of capillary forces varied in accordance with the water layer on the mica surface at the specific location of each cycle.

6.3.3 Dip coated tip experiments

The following force spectroscopy experiments investigated the adhesion between polymer-coated AFM tips (prepared using dip coating) and silicon, mica, and graphite substrates. The experiments were carried out using tips with low (<20%) and high (>90%) polymer surface coverages.

6.3.3.1 Low polymer surface coverage

In the first experiment, the AFM tips had an approximate polymer surface coverage of 16% (46 kg/mol). Figure 6.6 shows typical force-distance curves for the interactions between the polymer-coated AFM tips and each substrate. All of the graphs had simple snap-out shapes which did not exhibit any obvious signs of polymer bridging or individual desorption events.

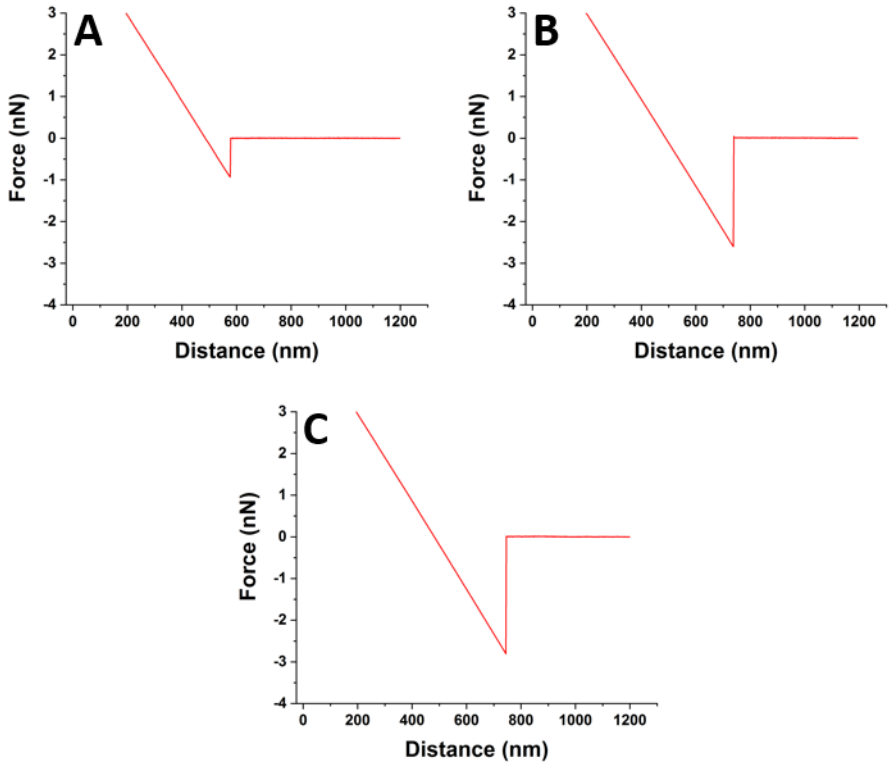

Figure 6.6: Typical force-distance curves showing the adhesion between a polymer-coated AFM tip (1c*, 46 kg/mol, 10 minutes, rinsed in toluene) with a surface coverage of 16% and each substrate. The approach/retract cycles were carried at a fixed location on the substrates. (A) Silicon, (B) mica, (C) graphite.

Despite the simple snap-out shapes of the curves, analysis of the overall adhesion in the graphs provided information regarding the polymer/substrate interactions. Table 6.2 shows that the measured adhesion was largest for the graphite substrate. This agrees with previous AFM observations (Chapter 5) where the hydrophobic poly(styrene-co-butadiene) strongly absorbed to the hydrophobic graphite surface, and created nanostructures with large surface coverages and low contact angles. Furthermore,

distinct ordering of the polymer nanostructures was observed on the graphite surface due to $\pi - \pi$ stacking interactions. In contrast, the polymer weakly adsorbed onto the silicon and mica substrates, and self-assembled into nanodroplets (Chapter 4). As mica is extremely hydrophilic, it was expected that the polymer/substrate adhesion would be the smallest for this substrate.[157,158] The silicon surface is less hydrophilic, so a marginally larger polymer/substrate adhesion was expected. However, this was not the case as the adhesion on the mica was considerably larger than on the silicon, and only slightly smaller than the results obtained using graphite. Therefore, this demonstrated that capillary forces were significantly increasing the measured adhesion on the hydrophilic mica surface. The average adhesive force on the silicon substrate was very similar to the value obtained for the experiments using the blank AFM tip. This suggested that capillary forces and heterogeneous positioning of polymeric material on the surface of AFM tip were influencing the adhesion results.

Table 6.2: Average adhesive force and energy between the polymer-coated AFM tips (46 kg/mol, 1c*, 10 minutes, rinsed with toluene) with ~16% coverage and each substrate. The approach/retract cycles were carried out at a fixed position on the substrates.

Substrate	Average Adhesive Force (nN)	Average Adhesive Energy (eV)
Silicon	0.93 ± 0.04	280 ± 10
Mica	2.45 ± 0.25	1690 ± 360
Graphite	3.64 ± 0.24	3610 ± 710

The force spectroscopy experiments were repeated using coated tips with a surface coverage of approximately 9% (355 kg/mol). A higher molecular weight polymer was used to attempt to increase the probability of observing specific desorption events. All of the force-distance curves for the mica and graphite substrates exhibited simple snap-out shapes and no obvious desorption events occurred. However, for the silicon substrate, there was a 10% probability of observing specific desorption events. Figure 6.7 is a force-separation graph which shows desorption events for the polymer-coated tip with a surface coverage of 9% and a silicon substrate. Force-separation graphs were more

suitable for presenting data where desorption events occurred. The graph exhibits force plateaus and steps, which can be characteristic of the desorption of individual polymer chains.[126] The final plateau where the adhesive force is equal to zero signifies that all of the bridged polymer chains have been completely desorbed from the tip or surface. The two plateaus which occur before the final force step are not completely horizontal. Instead, the lines have a very slight negative gradient. Therefore, this suggests that a very small amount of chain stretching may have occurred during the experiments.

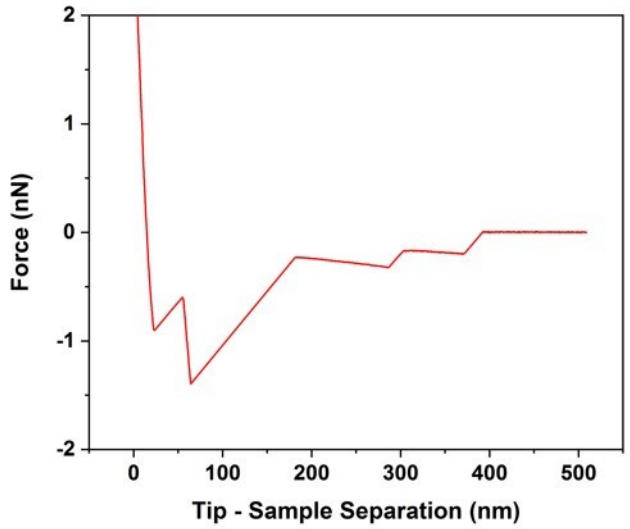

Figure 6.7: Force-separation graph for a polymer-coated AFM tip (355 kg/mol, 3c*, 10 minutes, rinsed with toluene) with a surface coverage of 9% and a silicon substrate. The approach/retract cycles were carried out at a fixed location on the silicon surface.

On the silicon substrate, the average force of each desorption event (step force) was 176 pN, and the average adhesive energy per segment was 105 kJ/mol (1.1 eV). Measuring the magnitude of desorption events can give insight into which intermolecular forces are dominant at the interface. In force spectroscopy investigations of polymers at surfaces, these commonly include van der Waals forces, $\pi - \pi$ stacking interactions, electrostatic interactions, and hydrophobic interactions.[87] In the current system, it was expected that weak van der Waals forces would be responsible for the polymer/silicon interactions. However, the average step force and adhesive energy per segment values were significantly larger than the typical magnitude of van der Waals forces ($\sim$1 kJ/mol per atom pair).[150] This confirmed that water associated forces were responsible for

increasing adhesion on the silicon surface, even at the single chain level. This was an interesting result as the effects of water associated forces on the desorption of single polymer chains does not appear to have been previously investigated within the literature.

To examine the degree of polymer bridging, the tip-sample separation at the final desorption event was compared to the length of a fully stretched 355 kg/mol polymer chain. The length of the chain was calculated using the following equation:

$$L = Nb \tag{6.2}$$

Where b is the Kuhn length,[4] N is the number of Kuhn monomers in the chain which was calculated using Equation 4.3, and L is the length of the stretched chain. The calculation was carried out according to the polymer's 25:75 styrene-butadiene ratio. Therefore, the calculated length of the fully stretched 355 kg/mol chain was ~2500 nm, which was considerably larger than the tip-sample separation at the final desorption event (391 nm). This demonstrated that a high degree of polymer adsorption was not achieved, and the chains were only partially adsorbed at a maximum of 16% of their total lengths. This result was consistent with the nature of the silicon substrate/tip.

Table 6.3 shows the average adhesive force and energy for the polymer-coated tips with a coverage of ~9% and each substrate. These results were obtained from all of the graphs generated in the force spectroscopy experiment (snap-out shapes and desorption events). Similarly to the results in Table 6.2, the average adhesive force and energy values were larger for the graphite than the silicon, which agreed with previous AFM observations. However, the adhesion on the mica was the largest of the three substrates, which did not agree with previous AFM observations. The average adhesive force on the mica was 0.18 nN larger than the value obtained on graphite. This difference in adhesion was considerably smaller than when the experiments were carried out using blank AFM tips (difference of 1.31 nN). This demonstrated that while polymer/substrate interactions were being measured in the experiments, the effects of capillary forces on the mica substrate were still large enough to significantly impact the adhesion results. The silicon substrate had an average adhesive force which was only marginally larger than the value obtained for the experiments using the blank AFM tip (0.93 nN). However,

specific desorption events were observed on the silicon, which confirmed that polymer/substrate interactions were taking place and capillary forces were impacting adhesion. It appeared that heterogeneous polymer morphology on the AFM tip also had a significant impact on the adhesion results. The adhesion on the graphite was considerably smaller than the result obtained in Table 6.2, which was consistent with the lower polymer surface coverage of the tips. However, for the mica substrate, the measured adhesion was very similar to the value obtained in Table 6.2 despite the lower surface coverage of the tip.

Table 6.3: Average adhesive force and energy between the polymer-coated AFM tips (355 kg/mol, 3c*, 10 minutes, rinsed with toluene) with a coverage of ~9% and each substrate. The approach/retract cycles were carried out at a fixed location on the substrates.

Substrate	Average Adhesive Force (nN)	Average Adhesive Energy (eV)
Silicon	0.96 ± 0.08	310 ± 50
Mica	2.38 ± 0.12	1780 ± 180
Graphite	2.20 ± 0.12	1610 ± 170

6.3.3.2 High polymer surface coverage

For the tips with a high polymer surface coverage (355 kg/mol), all of the graphs for each substrate exhibited simple snap-out shapes and no specific desorption events were observed. Table 6.4 shows the average adhesive force and energy values for the experiments using AFM tips with a coverage of ~95% and each substrate. The measured adhesion for each substrate was considerably larger than the results obtained when using tips with low surface coverages (Tables 6.2 and 6.3). Similarly to the previous results, the adhesion was smallest for the silicon and largest for the mica. In this instance, these results were not influenced by heterogeneous polymer morphology as there was an almost continuous thin polymer film on the surface of the tips. Therefore, it can be concluded that any inconsistencies in the adhesion results were solely due to capillary forces. The mica substrate had an average adhesive force which was 0.91 nN larger than

the average value on the graphite. This demonstrated the importance of water capillary forces on the measured adhesion.

Table 6.4: Average adhesive force and energy between the polymer-coated AFM tips (355 kg/mol, 5c*, 60 minutes, no rinse) with a coverage of ~95% and each substrate. The approach/retract cycles were carried out at a fixed position on the substrates.

Substrate	Average Adhesive Force (nN)	Average Adhesive Energy (eV)
Silicon	2.80 ± 0.08	3020 ± 170
Mica	6.67 ± 0.64	16180 ± 2310
Graphite	5.75 ± 0.18	13520 ± 990

The graphite substrate is hydrophobic, and therefore it did not appear that capillary forces influenced the adhesion results. This meant that the adhesion values obtained on graphite were predominantly due to polymer/substrate interactions. The results demonstrated that the measured adhesion was consistently larger on the graphite substrate compared to the silicon, despite the influence from capillary forces on the more hydrophilic silicon surface. This agreed with previous AFM observations, where the polymer weakly adsorbed onto the silicon and strongly adsorbed onto the graphite. On the silicon substrate, weak van der Waals forces are responsible for the polymer/substrate interactions. Whereas on the graphite, the van der Waals forces should be stronger between the hydrophobic polymer and substrate. Furthermore, it was previously demonstrated (Chapter 5) that π-π stacking interactions occurred between the aromatic rings in the styrene monomer units and the graphite surface, which created specific ordering of the nanostructures at 60° intervals. Therefore, it can be concluded that the fairly large polymer/substrate adhesion measured on the graphite substrate was due to strong van der Waals forces and π-π stacking interactions.

In conclusion, capillary forces significantly influenced the measured adhesion on the more hydrophilic substrates. The mica surface is extremely hydrophilic, and the adhesion results were significantly larger than expected for interactions with a hydrophobic polymer where weak van der Waals forces should be dominant. The silicon

surface is less hydrophilic than mica, but still had a water contact angle much smaller than 90°. Condensed water at the substrate surface also influenced adhesion results for the silicon, including the forces associated with the desorption of single chains. The graphite surface is hydrophobic and should have been mostly unaffected by capillary forces. The measured adhesion on the graphite was predominantly due to van der Waals forces and π-π stacking interactions.

6.3.4 Approach/retract cycles - fixed position vs array

Experiments were performed to investigate how polymer-coated tip/substrate adhesion varied over the course of many approach/retract cycles. If adhesion significantly reduced with the number of cycles, then this would suggest that many polymer chains were completely removed from the surface of the AFM tips during the experiments. The tips were prepared with high polymer surface coverage (5c*, 355 kg/mol, 60 mins, no rinse), and the experiments were carried out using two different modes of operation. In the first, the cycles were performed at a fixed location on the substrates for a total of 50 cycles. In the second, the cycles were carried out in an array with a step size of 500 nm, for a total of 49 (7x7) cycles.

Figure 6.8 shows the relationship between adhesion and the number of cycles at a fixed position on each substrate. All of the graphs exhibited a slightly negative gradient, which suggested that only a small amount of polymeric material was removed from the surface of the AFM tips during the 50 cycles. However, this result could also be influenced by the cycles being carried out at a fixed location on the substrate. This meant that any polymer chains which were removed from the tip were located in the same position where the additional cycles took place. Consequently, large amounts of polymeric material were not completely lost from the experimental system. Therefore, adhesion did not significantly decrease over the 50 cycles, although it deteriorated somewhat as the system was slightly altered.

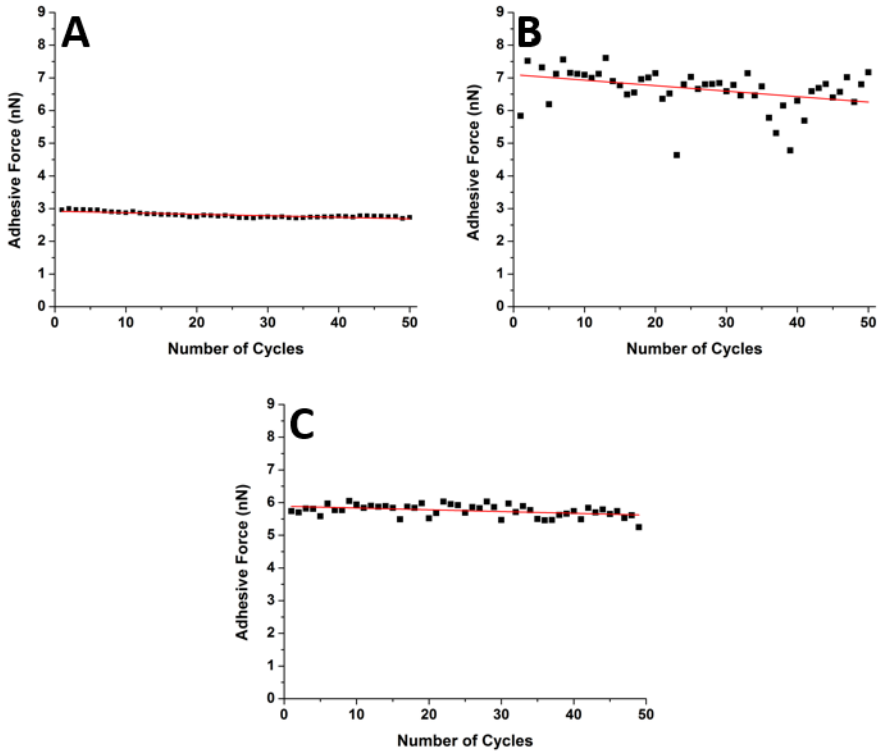

Figure 6.8: Graphs showing the relationship between polymer/substrate adhesion and the number of cycles at a fixed location on each substrate. The tips had a ~95% polymer surface coverage (355 kg/mol, 5c*, 60 minutes, no rinse). (A) Silicon, (B) mica, (C) graphite.

In Figure 6.8, the graphs for each substrate exhibited fluctuations in adhesion values. However, for the silicon and graphite substrates, the range of adhesion values were very small (0.3 nN and 0.8 nN, respectively). Whilst for the mica substrate, the fluctuations were much larger, with a range of 3.5 nN. This large range of adhesion values were likely caused by variations in the magnitude of capillary forces on the extremely hydrophilic mica surface. The cycles were carried out at a fixed location on the substrate. Therefore, any water which was located at this area was repeatedly interacted with by the AFM tip. Consequently, the water on the surface experienced a large amount of disruption and displacement, which impacted the magnitude of capillary forces for each cycle. This created large fluctuations in the measured adhesive force.

Figure 6.9 shows the relationship between polymer/substrate adhesion and the number of cycles in an array for each substrate. Similarly to Figure 6.8, each graph exhibited a negative gradient. However, the slope of the negative gradients were larger when the

cycles were carried out in an array, particularly on the strongly adsorbing graphite substrate (73% larger). The reason for this was that in an array, any polymer chains which were desorbed from the tip were located at an area of the substrate which was not in close proximity to any additional cycles. This meant that the polymer chains were completely removed from the system (unlike cycles in a fixed position), and therefore adhesion decreased more significantly. However, regardless of whether the cycles were carried out in an array or at a fixed positon, the adhesion did not drastically decrease with the increasing number of cycles. This demonstrated that there was only a limited amount of polymeric material which was actually desorbed from the surface of the tips during the experiments.

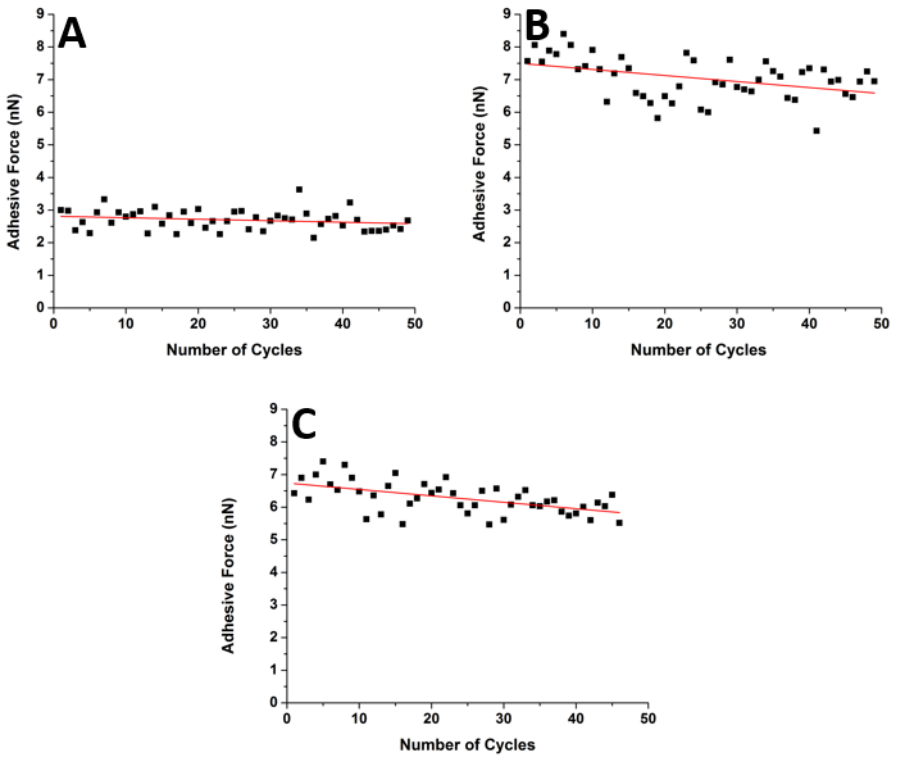

Figure 6.9: Graphs showing the relationship between polymer/substrate adhesion and the number of cycles in an array on each substrate. The tips had a ~95% polymer surface coverage (355 kg/mol, 5c*, 60 minutes, no rinse), and the cycles were carried out in a 7 x 7 array with a step size of 500 nm in the x and y directions. (A) Silicon, (B) mica, (C) graphite.

The range of adhesion value variations for the cycles in an array were 1.5 nN, 3.0 nN, and 1.9 nN for the silicon, mica, and graphite substrates, respectively. For the silicon and graphite substrates, these values were significantly larger than compared to when the cycles were carried out at a fixed location. However, the range of adhesion was still largest on the mica substrate. This was likely due to variations in the magnitude of capillary forces experienced by the cycles in an array caused by heterogeneities in the water layer on the mica surface. The graphs also exhibited distinct undulations, which in the case of the graphite, decreased in magnitude as the number of cycles increased. The likely reason for these undulations was due to the movement of polymer chains on the AFM tips over the course of many cycles. Polymer/substrate interactions caused the polymer chains to move and accumulate at the very end of the tip, which increased adhesion. However, as the cycles continued, some chains were removed from the end of the weakly adsorbing tip, which decreased adhesion. As the number of cycles increased further, the magnitude of the undulations decreased due to more polymeric material being removed from the tip.

6.3.5 Adhering polymers to AFM tips using force spectroscopy

An alternative technique was established to physically adhere polymer chains to AFM tips without using dip coating. Blank AFM tips were used in force spectroscopy experiments to interact with a thin polymer film on a silicon substrate. The film was prepared using dip coating (355 kg/mol, 5c*, 60 mins, no rinse), and had a thickness of 41 nm. The tips experienced 125 cycles on the polymer film in order to adhere a small amount of polymeric material to the end of the tips. The tips were then used in additional force spectroscopy experiments with blank silicon, mica, and graphite substrates to measure polymer-coated tip/substrate adhesion. This system did not remove any influence from capillary forces. However, any inconsistencies associated with dip coating should have been reduced. Furthermore, it is important to explore different methods of physically adhering polymer chains to AFM tips which are not commonly utilised within the literature.

The average adhesive force and energy values for the interactions between the tips prepared by force spectroscopy and each substrate are presented in Table 6.5. The

adhesion values were significantly larger than the results obtained for the experiments using blank tips (Table 6.1). This confirmed that polymer chains were physically adhered to the tips using the force spectroscopy technique. However, the adhesion values were considerably lower than when the tips had a high polymer surface coverage prepared by dip coating (Table 6.4). This demonstrated that only a small amount of polymeric material was adhered to the tips. Similarly to the previous results, the silicon had the smallest adhesion, whilst the mica and graphite had much larger values. This once again, demonstrated that the effects of capillary forces were significant on the hydrophilic surfaces. The chance of observing specific desorption events was 11% for the silicon substrate, which was marginally larger than any of the previous experiments. However, no events were observed on the mica or graphite. The average force of the desorption events on the silicon was 238 pN, which is considerably larger than forces associated with van der Waals interactions.[150] Two additional experiments were carried out using tips prepared by force spectroscopy. They investigated tip/substrate contact time, and examined whether the history of the tips influenced adhesion results.

Table 6.5: Average adhesive force and energy between AFM tips coated with polymer chains using force spectroscopy techniques and each blank substrate. During preparation, the tips experienced 125 cycles on a thin polymer film on a silicon substrate. The cycles were carried out at a fixed location on the substrates.

Substrate	Average Adhesive Force (nN)	Average Adhesive Energy (eV)
Silicon	1.24 ± 0.33	412 ± 119
Mica	2.68 ± 0.30	2334 ± 468
Graphite	2.89 ± 0.32	2534 ± 531

6.3.5.1 Contact time analysis

An experiment was designed to investigate how variations in the tip/sample contact time impacted the measured adhesion. This provided information into the time scale of the specific interactions within each system. It has been demonstrated that increasing contact time can increase adhesion when carrying out force spectroscopy experiments

using proteins.[254,255] However, it appears that there are no comprehensive investigations regarding how changes to contact time can impact adhesion using synthetic polymers at various surfaces. AFM tips were prepared using force spectroscopy techniques and were utilised in a series of experiments with each substrate. In each force spectroscopy experiment, the time which the AFM tip was in contact with the substrate was systematically increased from 1 to 200 seconds, in 40 second increments. All other aspects of the cycles (approaching and retracting) were identical to the previous experiments, only the tip/substrate contact time was altered for each array of cycles. Figure 6.10 shows the average adhesive force at varying contact times for each substrate. The graphs for each substrate exhibited mildly fluctuating trends with slightly negative gradients overall. The negative gradient can be accounted for by the removal of small amounts of polymeric material from the AFM tips over many cycles as previously described (see Figures 6.8 and 6.9). The results demonstrated that there was no evidence of any systematic relationship between contact time and adhesive force for any of the substrates. Therefore, the majority of polymer/substrate interactions must have taken place within 1 second of tip/substrate contact.

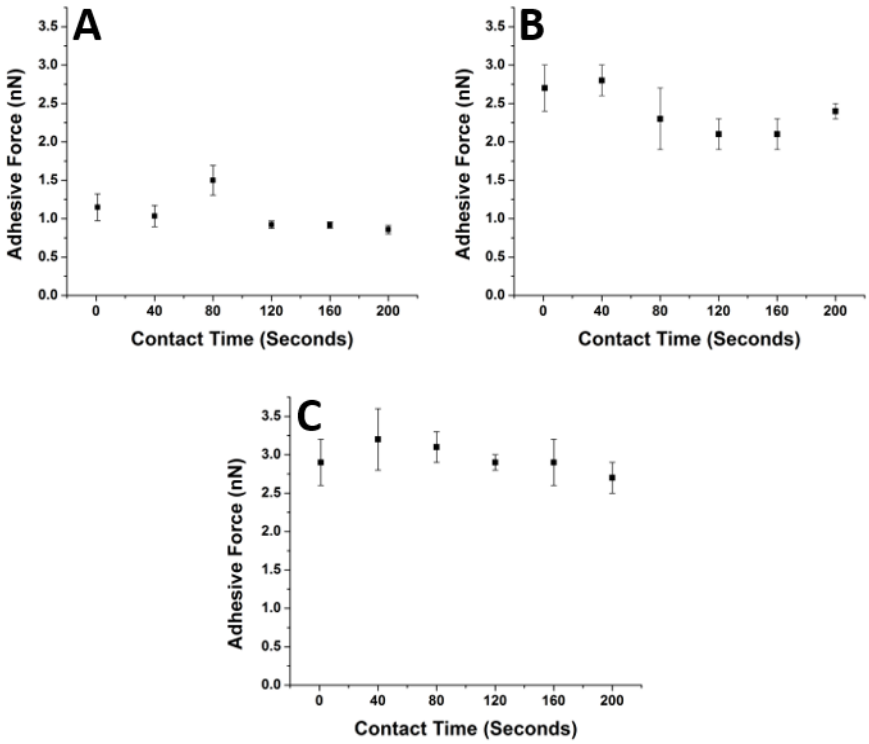

Figure 6.10: Graphs showing adhesion at varying tip/substrate contact times. Polymer chains were physically adhered to the tips using force spectroscopy, and the tip/substrate contact times ranged from 1 second to 200 seconds. The approach/retract cycles were carried out in an array (3 x 3). (A) Silicon, (B) mica, (C) graphite.

6.3.5.2 How tip history affects the measured adhesion

An experiment was designed to investigate whether the same tip could be used to interact with numerous substrates without generating inconsistencies in adhesion results, due to polymeric material moving on the tips or being completely desorbed. To examine this, three tips were prepared using force spectroscopy methods and were then used to interact with silicon, mica, and graphite substrates. Each tip interacted with all three substrates consecutively. However, the order of the substrates were different for each tip.

Figure 6.11 shows the polymer-coated tip/substrate adhesion for experiments using three different tips prepared by force spectroscopy, where the substrate order was altered for each experiment. The results showed that regardless of the substrate order, the observed trend was always the same. The silicon consistently had the lowest

adhesion with a value of ~0.7 nN in each experiment. Whilst the mica and graphite substrates had larger values which were similar to one another. This demonstrated that the measured adhesion was predominantly due to the surface properties of the substrates and not the history of the AFM tips. Previous results have demonstrated that adhesion can slightly decrease over many cycles due to chain desorption from the tip. However, this relatively minor effect was not significant enough to drastically alter the measured adhesion values, and the observed trend was the same in each experiment.

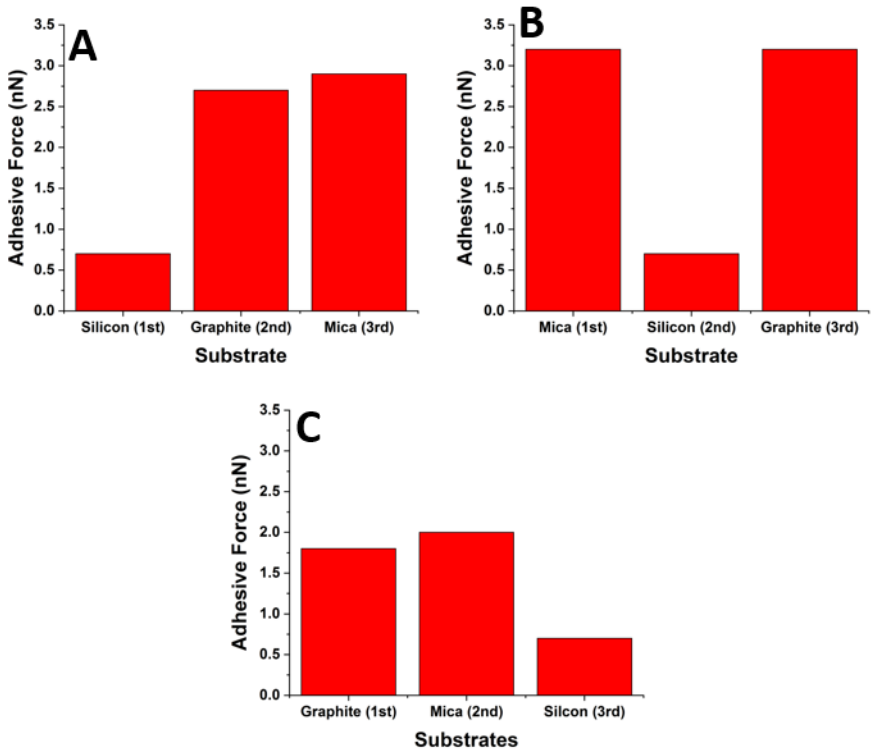

Figure 6.11: Graphs showing the adhesion between three polymer-coated AFM tips prepared using force spectroscopy and each substrate. For each tip, the substrate order was different. Each experiment was carried out at a fixed location for 50 cycles on each substrate. (A) Tip 1: Silicon - Graphite - Mica, (B) Tip 2: Mica - Silicon - Graphite, (C) Tip 3: Graphite - Mica - Silicon.

6.3.6 Review of experimental methods

Polymer chains were physically adhered to AFM tips in order to investigate polymer/substrate adhesion on various surfaces using force spectroscopy. Two methods

were presented to adhere polymer chains to the tips (dip coating and force spectroscopy) which were experimentally simple and time efficient. A large amount of information regarding the merits and drawbacks of the methods has been presented. This is very useful, as these methods are not commonly utilised within the literature. The experiments produced results regarding the strength of interactions between polymers and surfaces, including some direct evidence of single chain desorption events for the silicon substrate. On the hydrophobic graphite substrate, the technique appeared to accurately measure the strength of polymer/substrate interactions, which were due to van der Waals forces and π-π stacking interactions. However, some of the results were inconsistent with previous AFM observations, particularly on the mica substrate. This was primarily due to the presence of capillary forces, which increased adhesion on the more hydrophilic substrates (mica and silicon). In order to eliminate capillary forces, the experiments could have been carried out in a liquid medium. However, performing force spectroscopy experiments in aqueous solutions can introduce other problems, such as significantly increasing the duration and complexity of experiments, as well as, impacting polymer/substrate interactions. Therefore, other experimental avenues were investigated in Chapter 8, in an attempt to remove the influence of capillary forces whilst continuing to perform the experiments in air.

Across all of the experiments, specific desorption events were never observed on the mica or graphite substrates. For the silicon substrate, specific desorption events were observed, but they were very uncommon. It was likely that polymer bridging was only observed on the silicon substrates due to the experiments taking place in an approximately symmetrical system, where the polymer did not favour either the substrate or tip. However, this cannot be concluded unequivocally at this point. The low probability of observing polymer bridging was problematic. This was because studying desorption events provides information regarding specific polymer/substrate interactions which is of great fundamental interest and is useful for many fields of research.[50,126] Experiments from the literature have also discussed the low probability of observing single chain events using AFM force spectroscopy.[85,131] However, if a system was designed which increased the probability of observing desorption events on each substrate, it would provide a much greater breadth of information regarding polymer/substrate interactions and significantly reduce the duration of experiments. This issue was also addressed in Chapter 8.

6.4 Conclusions

Force spectroscopy experiments were carried out to investigate the interactions between poly(styrene-co-butadiene) random copolymer-coated AFM tips and silicon, mica, and graphite substrates in ambient conditions. Polymer chains were physically adhered to AFM tips using dip coating and force spectroscopy techniques, and polymer-coated tip/substrate adhesion was directly measured.

Initial experiments were performed which investigated the interactions between blank AFM tips and each substrate. The results demonstrated that capillary forces were influencing adhesion on the more hydrophilic surfaces as the measured tip/substrate adhesion was directly related to the water contact angle of each substrate.

Silicon AFM probes and substrates were dip coated in poly(styrene-co-butadiene) solutions at varying concentrations, molecular weights, and immersion times. The silicon substrates were imaged using AFM to provide a better understanding of polymer morphology on the corresponding AFM tips. At lower concentrations and shorter immersion times, the polymer formed nanodroplets on the silicon with low surface coverages. The droplets predominantly formed spherical cap shapes, although sometimes their morphology was more variable. Some results using tips with a low surface coverage appeared to be influenced by heterogeneous polymer morphology, which was due to the inconsistencies associated with dip coating. At higher concentrations and longer immersion times, the polymer formed mostly continuous thin films on the silicon with some dewetting. The very high surface coverage on the tips significantly reduced any influence from heterogeneous polymer morphology on the measured adhesion values.

On the extremely hydrophilic mica substrate (water contact angle of <5˚), the measured adhesion was consistently larger than expected. This was caused by capillary forces due to a condensed water layer which formed on the mica surface in ambient conditions. Weak van der Waals forces should be responsible for the polymer/mica interactions, and previous AFM results demonstrated that the polymer weakly adsorbed to the mica and formed spherical cap shaped nanodroplets. However, the measured adhesion on the mica was often the largest of the three substrates due to the influence from capillary

forces. This meant that the adhesion solely due to polymer/substrate interactions could not be accurately investigated.

The adhesion results on the silicon substrate were also influenced by capillary forces, and therefore were not completely consistent with previous AFM observations. However, the silicon was less hydrophilic than mica with a water contact angle of approximately 45.8˚. This meant that the effects of capillary forces were reduced on the silicon and the measured adhesion was consistently smallest on this substrate. The forces associated with the single chain desorption events on the silicon were much larger than expected for a typical system where weak van der Waals forces were responsible for the interactions. This confirmed that water associated forces were impacting the measured adhesion on the silicon, even at the single chain level.

The graphite substrate is hydrophobic, which meant that capillary forces should not have influenced the measured adhesion results, and therefore polymer/substrate interactions were accurately investigated. The measured adhesion on the graphite was consistently larger than the results on the silicon, despite the increased adhesion due to capillary forces on the more hydrophilic silicon substrate. The relatively large measured adhesion on the graphite was due to strong van der Waals forces, and π-π stacking interactions between the graphite and the aromatic rings in the polystyrene units.

An investigation was carried out which studied the polymer-coated tip/substrate adhesion (high surface coverage) over many cycles. The results showed that adhesion decreased more significantly when the cycles were carried out in an array compared to at a fixed position. This was because any chains which were desorbed from the tip when the cycles were carried out in a fixed position, continued to be interacted with in the following cycles. The range of adhesion values were always largest on the mica substrate due to increased capillary forces on the substrate.

A technique was established where AFM tips interacted with thin polymer films using force spectroscopy to physically adhere chains to the tips surface. The adhesion results confirmed that a small amount of polymeric material was adhered to the tips using this technique. The relationship between tip/substrate contact time was investigated with tips prepared by force spectroscopy. It was demonstrated that the majority of polymer/substrate interactions occurred within one second of tip/substrate contact.

Furthermore, it was shown that a single tip prepared using force spectroscopy could be used to interact with numerous substrates without significantly impacting adhesion results.

In Chapter 8, alternative methods were explored to create an experimental system in which capillary forces did not impact results, and the probability of observing specific desorption events was significantly increased.

7 Investigating single chain desorption events on various substrates

Summary

This chapter presents a force spectroscopy study which comprehensively investigated the specific interactions between poly(styrene-co-butadiene) random copolymers and mica, silicon, and graphite substrates. Blank AFM tips were used to interact with thin polymer films on each substrate, and the desorption forces and polymer behaviour were examined. The experimental system had no apparent influence from capillary forces and the probability of observing desorption events was high. The desorption forces and degree of bridging were largest on the graphite, due to stronger polymer/substrate interactions caused by van der Waals forces and π - π stacking interactions.

7.1 Introduction

As described in Chapter 6, AFM force spectroscopy can be utilised to investigate the interactions between polymers and surfaces.[81] The technique has a force resolution of approximately 10 pN, and therefore can accurately measure the interactions between single polymer chains and substrates at a molecular level.[126] This field of research is very important fundamentally, as well as, being useful to many applications.[50,126]

Force spectroscopy experiments often involve separating polymers from substrates and measuring the resulting adhesive force. In principle, these experiments are simple and the AFM has the capability to accurately measure any forces involved. However, in practice, the experiments can be very complex due to many interactions taking place at an incredibly small length scale.[245] It can be very difficult to create an experimental system which can effectively isolate and investigate single polymer chains. Consequently, there are many different experimental systems which are presented within the literature to investigate the behaviour of polymers at surfaces using AFM force spectroscopy methods.[81,82,85,127,142]

The experimental systems used to investigate the interactions between polymers and surfaces often have distinct advantages and disadvantages. For example, many experiments are carried out in an aqueous medium.[85,128,142] This eliminates any influence from capillary forces and allows investigations of polymer behaviour in different solvent conditions. However, it can increase the complexity and duration of experiments, as well as, having the potential to introduce hydrophobic effects which may be undesirable. In many experiments, AFM tips are functionalised and polymer chains are covalently bonded to the surfaces of the tips.[50,81,82,127] These experiments ensure that chains cannot be desorbed from the AFM tip, which increases consistency in the results. However, the procedures associated with these experiments can be laborious and complex. AFM probes have a relatively short working life, so the tip preparation methods have to be repeated many times. Finally, many experiments have very low probabilities of observing specific desorption events, and therefore it can be very time consuming to obtain suitable amounts of meaningful data.[85,131]

AFM force spectroscopy experiments using synthetic polymers can generally be separated into two main categories. The first is studying the specific desorption forces

associated with polymers at surfaces. These experiments generally produce force-separation graphs which exhibit plateaus and steps. The plateaus and steps can be analysed to provide valuable information regarding the nature of the intermolecular forces which are dominant in the system.[82,142] The second common area of investigation involves stretching polymer chains and examining the force response. These experiments produce force-separation graphs with spiked curves which can be fitted to statistical models such as the worm-like chain (WLC) or freely-joint chain (FJC) models.[85,145] This experimental analysis can be used to obtain values of relevant physical quantities (derived from theoretical concepts), such as the polymer Kuhn length. A force spectroscopy investigation which examines the forces associated with poly(styrene-co-butadiene) random copolymers on various substrates at the nanoscale has not yet been carried out within the literature.

This chapter presents a force spectroscopy study which comprehensively examined the interactions between poly(styrene-co-butadiene) random copolymers and mica, silicon, and graphite substrates. The experimental system was uncomplicated, time efficient, and produced significant amounts of meaningful data. The results provided information regarding the specific desorption forces between single polymer chains and each substrate/AFM tip, as well as, identifying the force associated with chain pull-out from the thin films and the globule-extended coil conformational transition.

7.2 Materials and methods

Dip coating was used to create polymer thin films on mica, silicon, and graphite substrates. Immediately before dip coating, the mica and graphite substrates were cleaved with scotch tape. The silicon could not be cleaved, therefore it was cleaned with acetone and ethanol before use. The mica, silicon, and graphite substrates were dip coated in 5c* solutions of the 355 kg/mol poly(styrene-co-butadiene) random copolymer for 60 minutes. The substrates were then dried with a gentle stream of nitrogen for 2 minutes, before being left in a fume hood overnight. The polymer thin films which formed on each substrate were characterised using AFM imaging. AFM imaging was carried out using the same machine, probes, and experimental procedures as the previous chapters. AFM force spectroscopy was carried out in ambient conditions on the

polymer films on each substrate. Blank silicon MSNL-10 tips with spring constants of 0.01 N/m and tip radii of 2 nm were used for each experiment (see Chapter 3 for details). However, in some instances, tips which had interacted with thin polymer films on each substrate were then used in force spectroscopy experiments with blank silicon substrates. This was to confirm whether the previous interactions with the polymer thin films had adhered polymer chains to the tips.

All analysis of the AFM images was carried out using Gwyddion. Whereas analysis of the force-separation curves was performed using Nanoscope Analysis and Origin. The overall adhesive force was taken as the value associated with the largest minimum in each graph. The overall adhesive energy was presented in eV and was measured by integrating the complete area above each curve in the fourth quadrant. The analysis of specific desorption events, such as calculating step force and plateau lengths, was carried out using an Origin measuring tool plugin. The step force was taken as the height of each individual step. The adhesive energy per segment was presented in kJ/mol and was calculated by first integrating the specific area above the curves in the fourth quadrant where force plateaus and steps occurred. This provided a value of the adhesive energy for the desorption events, which could then be used in accordance with Equation 3.11 to obtain a value for the adhesive energy per segment. Chapter 3 contains detailed descriptions of all the experimental methods and analysis used for AFM imaging and force spectroscopy.

7.3 Designing the experiments

Some of the results from the force spectroscopy experiments in Chapter 6 were ambiguous due to the presence of capillary forces, which increased adhesion on the more hydrophilic substrates. This was problematic as the adhesion forces solely associated with polymer/substrate interactions could not be accurately investigated on the hydrophilic substrates. Therefore, in the current chapter, an experimental system was designed where any apparent influence from capillary forces was eliminated. This was achieved by carrying out force spectroscopy experiments using a blank silicon tip which probed thin poly(styrene-co-butadiene) films on each substrate. This meant that the tip picked up polymer chains and pulled them from the films, which allowed the strength of

polymer/substrate interactions to be directly measured. Furthermore, both polystyrene and polybutadiene are hydrophobic with water contact angles of approximately 86° and 97°, respectively.[256,257] Therefore, using these values from the literature and the styrene-butadiene ratio of 25:75, it can be expected that the water contact angle of the 355 kg/mol poly(styrene-co-butadiene) polymer was approximately 94°. Consequently, any influence from capillary forces was drastically reduced as each substrate was now almost completely covered in a thin film of hydrophobic polymeric material. All experiments were carried out in air under ambient conditions. If the experiments were carried out in an aqueous solution, this would have created significant problems. For example, if a polymer-coated mica substrate was immersed in water, the favourable interactions between the water and mica would lead to the separation of the thin polymer film from the mica surface.[258] This would have made it impossible to obtain accurate results regarding polymer/substrate interactions.

Another disadvantage with the experimental system in Chapter 6 was that desorption events were never observed on the mica or graphite substrates, and had a very low probability of occurring on silicon. This was problematic as very little information was generated regarding the specific polymer/substrate interactions. For the current experimental system, the probability of observing desorption events was 98%, 94%, and 99% on the mica, silicon, and graphite substrates, respectively. This was far greater than the probabilities in the previous chapter, as well as, many similar experiments within the literature.[82,85,131] For example, a study by Grebíková et al.[131] which investigated the strength of interactions between polymer chains (PMMA and PHEMA), which were covalently attached to an AFM tip and mica, silicon, and graphite substrates. In this study, the probability of observing multiple desorption events (steps and plateaus) in each force-separation graph was reported as 1.2%, 7.0%, and 88.1% for mica, silicon, and graphite substrates, respectively. These probabilities were directly related to the strength of the polymer/substrate interactions. Despite the simplicity of the experimental system in the current chapter, the probability of observing specific desorption events was very high for each substrate.

The problems associated with the force spectroscopy experiments in Chapter 6 were eliminated by redesigning the experiments. The system presented in this chapter is time efficient and uncomplicated compared to many similar experiments within the

literature.[50,81,82,127] The process of physically adsorbing polymer chains to substrates for AFM force spectroscopy experiments has also been recommended for its simplicity in the recent study by Zhang et al.[127]

7.4 Results and discussion

7.4.1 Polymer thin films

Thin films of poly(styrene-co-butadiene) were prepared on each substrate using dip coating. The same parameters were used to create the thin films on the AFM tips in Chapter 6, and the substrates in the current chapter. This meant that direct comparisons could be made between the two experimental systems. Figure 7.1 shows typical AFM images of the mostly continuous thin films on each substrate. Each polymer film experienced a small amount of dewetting, which created circular holes in the films with some evidence of viscous fingering and raised rims. However, dewetting was very limited and the polymer surface coverage was large with average values of 99%, 95%, 99% for the mica, silicon, and graphite substrates, respectively. This meant that there was a very high probability that each cycle would interact with an area on the substrate which was covered by the polymer film.

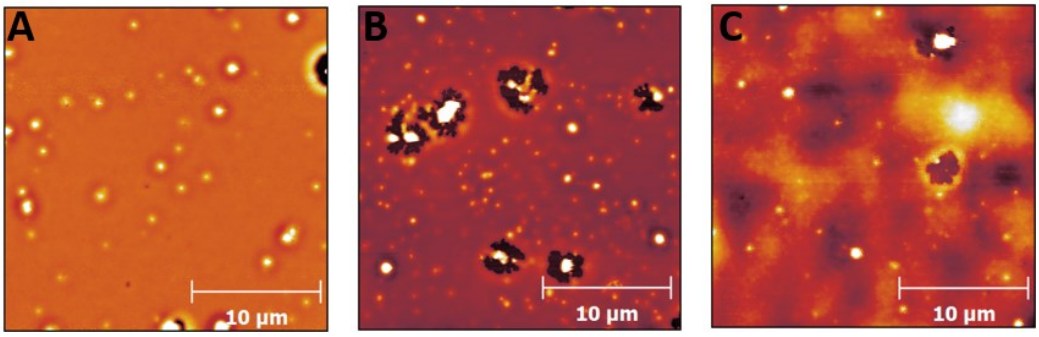

Figure 7.1: Typical AFM height images of mostly continuous polymer thin films on each substrate. The films were created by dip coating (355 kg/mol, 5c*, 60 minutes, no rinse). (A) Mica, (B) silicon, (C) graphite.

The film thickness values were calculated using the AFM techniques which are described in Chapter 4. The approximate thickness of the films were 31 nm, 41 nm, and 27 nm for the mica, silicon, and graphite substrates, respectively. The values of film thickness were similar on the mica and graphite, but slightly larger on the silicon. This was due to difficulties in repeatedly creating homogenous polymer nanostructures using dip coating. Furthermore, the magnitude of polymer/substrate interactions were different on each substrate, which can also lead to differences in film thickness. Despite this, the differences in film thickness on each substrate were relatively small and should not have significantly impacted the results.

7.4.2 Force-separation graphs

Force spectroscopy experiments were carried out at 5 different areas of the films on each substrate. At each area, the tips experienced 25 cycles at a fixed location. Figure 7.2 shows typical force-separation graphs for each substrate. The graphs all show an initial adhesion followed by a period of force plateaus and steps. The graphs for the silicon and mica substrates (Figures 7.2A and 7.2B) were similar and exhibited a smaller initial adhesion followed by a large period of force plateaus and steps. On the graphite substrate (Figure 7.2C), the overall adhesion was much larger and significant fluctuations were observed in the graphs at smaller tip-sample separations. At larger tip-sample separations, force steps and plateaus were observed but they occurred over much smaller length scales.

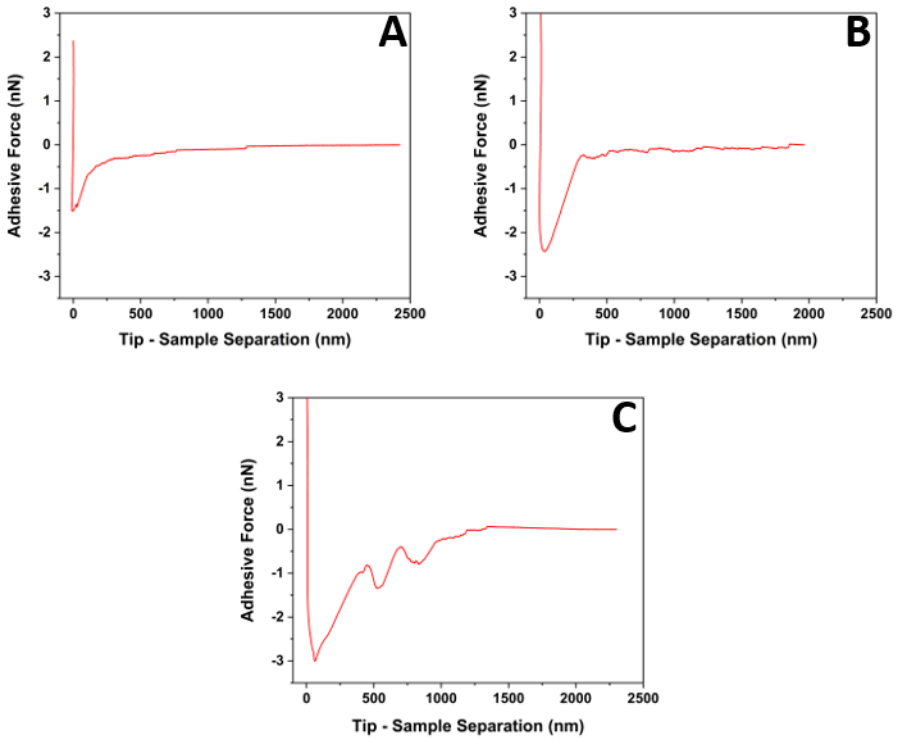

Figure 7.2: Typical force-separation graphs for interactions between a blank silicon AFM tip and a polymer thin film on each substrate. (A) Mica, (B) silicon, (C) graphite.

Before analysis of the specific polymer/substrate interactions was carried out, the overall adhesive force and energy for each substrate was investigated in Section 7.4.3. To simplify the analysis of the polymer/substrate interactions, the features on the graphs were separated into two categories which were called 'initial events' and 'force plateaus and steps'. The force plateaus and steps were analysed in Section 7.4.4, whilst analysis of the initial events can be found in Section 7.4.5.

7.4.3 Analysis of overall adhesion

Force-separation curves were analysed to confirm that the overall polymer/substrate adhesion was consistent with previous AFM observations, where the polymer was more weakly adsorbed onto the silicon and mica substrates, and strongly adsorbed onto the graphite. Table 7.1 shows the average adhesive force and energy for the interactions

between the AFM tips and the polymer films on each substrate. The results demonstrated that the polymer/substrate adhesion was smallest for the extremely hydrophilic mica substrate, and slightly larger for the less hydrophilic silicon substrate. Whilst the adhesion was the largest by a considerable margin on the hydrophobic graphite substrate. Therefore, the results agreed with previous AFM observations and demonstrated that polymer/substrate interactions were directly measured without any apparent influence from capillary forces.

Table 7.1: Average adhesive force and energy between the blank silicon AFM tips and the thin polymer films on each substrate.

Substrate	Average Adhesive Force (nN)	Average Adhesive Energy (eV)
Mica	1.62 ± 0.20	2060 ± 506
Silicon	1.80 ± 0.62	2628 ± 2186
Graphite	2.58 ± 0.47	5748 ± 1754

7.4.4 Force plateaus and steps analysis

7.4.4.1 Force at steps

The plateaus and steps in the force-separation graphs can be interpreted as the force required to desorb chain segments from the surface of the substrates or AFM tips. However, they can also represent the force associated with the globule-extended coil transition, chain pull-out from a film, and chain friction with the tip and/or substrate.[131,140,259–261] The overall graphs (see Figure 7.2) did not show the force plateaus and steps in great detail, therefore analysis was carried out on zoomed sections of the graphs (see Figure 7.3). On the zoomed graphs, the force steps and plateaus were clearly visible which allowed for the accurate analysis of the events.

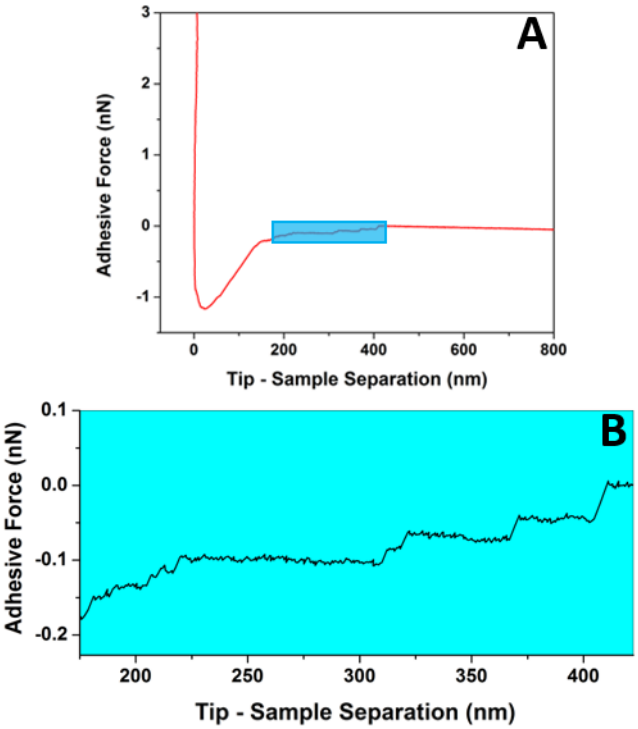

Figure 7.3: (A) Typical force-separation graph which shows the interactions between a blank silicon tip and a thin polymer film on a silicon substrate. (B) Zoomed section of the graph which clearly shows force steps and plateaus. The zoomed area is represented by the blue box in (A).

The force-separation graphs exhibited numerous plateaus and steps which were the product of the following phenomena. Several individual chains could desorb from the surface of the tip or substrate within a single cycle. Furthermore, each chain was not necessarily fully adsorbed to the substrate's surface. Adsorbed chains form loop, train, and tail conformations on surfaces (see Figure 7.3).[262] Trains are segments of the polymer chains which are fully adsorbed to a substrate at the monomer scale, loops are desorbed segments with trains at either end, and tails are desorbed segments located at either end of the chain.[263] The presence of multiple trains means that there can be many force steps and plateaus created by a single polymer chain. As the polymer was more weakly adsorbed onto the mica and silicon, it was expected that the polymer would form a greater number of loop and tail conformations on these surfaces. The polymer strongly adsorbed to the graphite, so a greater proportion of train conformations was expected. This was affirmed by examining the average number of force steps per graph which was 7, 6, and 5 for the mica, silicon, and graphite substrates, respectively. Therefore, more

desorption events were observed on the substrates where the polymer formed more loop conformations. The AFM tip could also come into contact with any point along the length of the polymer chains, which meant that both ends of the same chain could desorb individually. Furthermore, the plateaus and steps could also be created by the globule-extended coil transition, chain pull-out, and chain friction.[131,140,259–261] It is expected that the steps which represented the globule-extended coil transition and chain pull-out have a very similar magnitude. This is because for chains with the same composition, the force required to extend a polymer from its own globule should be the same as the force required to pull-out a chain from a film. Chain friction with a substrate should also generate similar forces to chain desorption; polymer chain friction with a solid substrate can be envisaged as a process of adsorption - desorption.

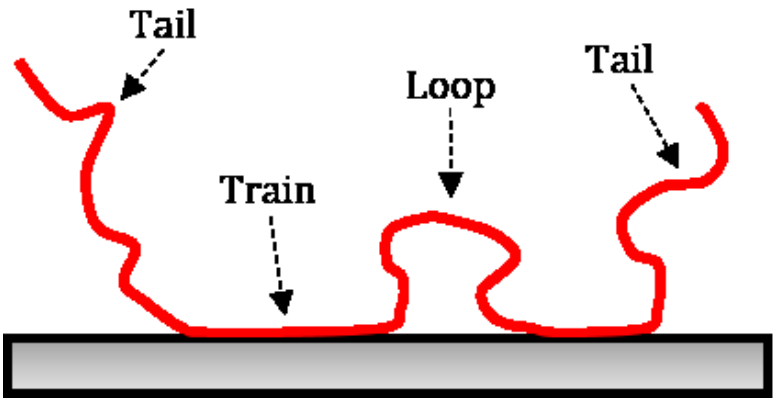

Figure 7.4: Illustration of an adsorbed polymer chain with loop, train, and tail conformations.

Figure 7.5 presents a series of histograms which show the distributions of step force values for each substrate. The histograms all have a number of peaks which represent the forces associated with specific phenomena to be discussed now. The histograms for each substrate have two distinctive common features: a main peak at 20 - 25 pN and a secondary peak at 55 - 60 pN. As these peaks are in the same position for each histogram, they cannot represent desorption from the three different substrates. Therefore, they must represent the forces associated with desorption from the AFM tip and polymer/polymer interactions as these phenomena will have the same step force values on each substrate.

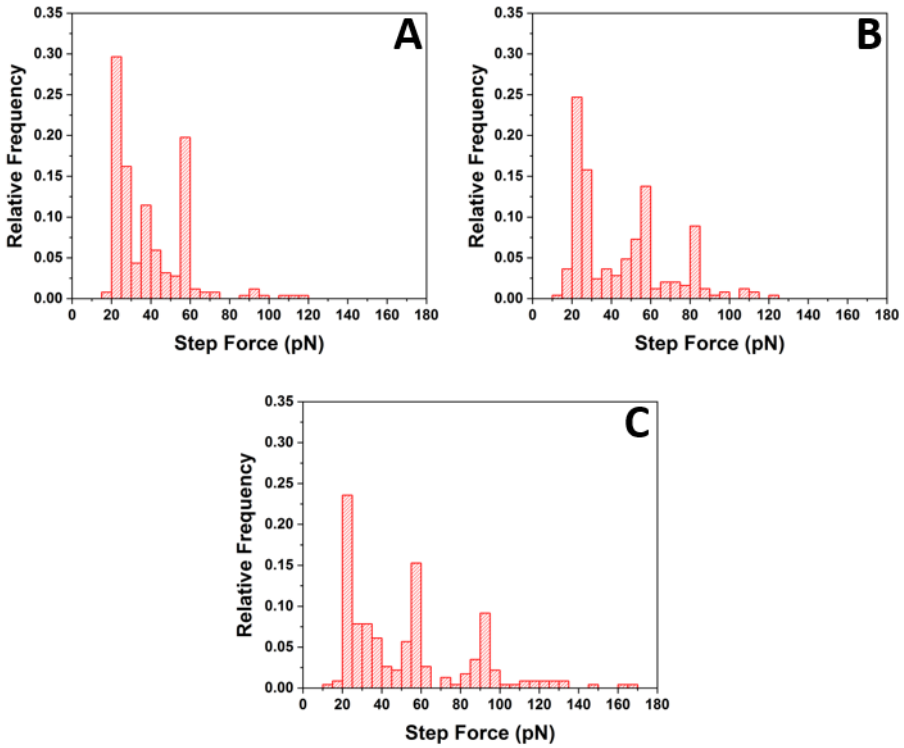

Figure 7.5: Histograms showing the step force distribution for each substrate. (A) Mica, (B) silicon, (C) graphite.

Forces associated with polymer/polymer interactions (chain pull-out from the thin films or globule-extended coil transitions) are expected to be prominent during the experiments on each substrate. On weakly adsorbing substrates and bad solvent conditions, polymers generally create globular conformations to minimise surface contact. Therefore, when polymer globules were picked up by the AFM tip in the force spectroscopy experiments, they may have experienced a transition from a globule to an extended coil.[264] The force associated with this conformational transition is a plateau and when it finishes a force step appears in the force-separation graphs.[141] Similarly, the force associated with chain pull-out from the films is also a plateau and when it finishes a step appears. The force associated with the globule-extended coil transition has been previously examined using AFM force spectroscopy, where Koutsos et al.[140] demonstrated that the force associated with extending a polydimethylsiloxane polymer globule in air was 25 ± 10 pN. Similarly, Haupt et al.[141] demonstrated that the force

associated with extending poly(N-isopropylacrylamide) from its globular conformation in a poor solvent had a peak value of 12 - 18 pN. Halperin et al.[264] presented an equation which can be utilised to estimate the force (F_{Step}) associated with the globule-extended coil transition for a specific polymer:

$$F_{Step} = 2\pi r\gamma \tag{7.1}$$

Where r is the radius of the coil, which was estimated at approximately 0.15 nm, and γ is the surface energy of the polymer.[140,264] The surface energy of polystyrene and polybutadiene are approximately 39 mJ/m^2 and 31 mJ/m^2, respectively.[26,265] Taking into account the polymer's 25:75 styrene-butadiene ratio, the force associated with the globule-extended coil transition was estimated at 31 pN. Similarly, the force associated with chain pull-out from the thin films could also be estimated at approximately 31 pN. This is because the mechanisms of both the globule-extended coil transition and chain pull-out are very similar, and the force of each phenomena is governed by polymer/polymer interactions. Therefore, it is highly plausible that the observed peaks at 20 - 25 pN represent the force associated with extending polymer chains from their globular conformations, and chain pull-out from the thin films. Consequently, this suggests that the peak at 55 - 60 pN on each substrate likely represented the force associated with polymer desorption from the silicon AFM tip.

The histograms for the silicon and graphite substrates (Figures 7.5B and 7.5C) also have distinct peaks with force values of 80 - 85 pN and 90 - 95 pN, respectively. As the peaks have different force values on the silicon and graphite, it can be assumed that they are influenced by desorption from each substrate. On the mica, it appears that the force associated with desorption from the substrate and desorption from the AFM tip both have values of 55 - 60 pN, and therefore are represented by a single peak with a larger relative frequency in the histogram (Figure 7.5A). However, these values do not accurately represent the true desorption forces of the polymer from each substrate. This is because when the chains are desorbed from each substrate, they are also pulled out of the polymer films. As these two phenomena occur simultaneously, they are represented by a single step in the force-separation profiles. Therefore, the final peaks in each histogram (values presented above) represent the force associated with

desorption from the substrate, in addition to, chain pull-out from the thin films. This means that in order to achieve an accurate force value for only substrate desorption, the force values at the final peaks must be subtracted by the force associated with chain pull-out. Therefore, the true desorption forces are approximately 35 - 40 pN, 60 - 65 pN, and 70 - 75 pN for the mica, silicon, and graphite substrates, respectively.

The results for the desorption force from each substrate agree with the AFM observations in Chapters 4 and 5. The polymer was very weakly adsorbed onto the mica which resulted in the formation of spherical cap shaped nanodroplets. Whilst on the graphite, the polymer was more strongly adsorbed and formed structures, such as networks and nanoribbons. The desorption force values correlate with the effective Hamaker constants (calculated using Equation 2.2) of each system (Table 7.2). The effective Hamaker constants provide information regarding the strength of the van der Waals interactions between the polymer films and each substrate.[266] The Hamaker constant for the graphite substrate has the largest (negative) value, and therefore the van der Waals interactions were strongest for this system, which agrees with the force spectroscopy results. The desorption force values also correlate with the water contact angle of each substrate (Table 7.2).

Table 7.2: The desorption force, effective Hamaker constant, and water contact angle of each substrate.

Substrate	Desorption Force (pN)	Effective Hamaker Constant ($10^{-20} J$)[150]	Water Contact Angle (°C)[157,164–166,267]
Mica	35 - 40	-1.1	<5
Silicon	60 - 65	-6.3	45.8
Graphite	70 - 75	-11.3	84 - 86

It is expected that the desorption force would be the smallest for the mica substrate. This is because weak van der Waals forces were solely responsible for the interactions between the highly polar mica and the apolar poly(styrene-co-butadiene). On the silicon substrate, van der Waals forces were also exclusively responsible for the polymer/substrate interactions. However, the van der Waals forces were stronger

between the polymer and the silicon substrate. This was because the silicon substrate only had a thin oxide layer, and therefore was less polar than the mica. Both van der Waals forces and π - π stacking interactions were responsible for the polymer/graphite interactions. The van der Waals forces were expected to be stronger for this system due to the polymer and substrate both being hydrophobic (apolar). Additionally, results in Chapter 5 demonstrate that π - π stacking interactions were responsible for creating ordered poly(styrene-co-butadiene) nanostructures on the graphite substrates. The π - π stacking interactions were optimal for the poly(styrene-co-butadiene) random copolymers due to the aromatic rings in the polystyrene monomer, but also the increased flexibility from the butadiene units. Table 7.3 shows the force values of each interaction which occurred during the force spectroscopy experiments.

Table 7.3: The force values of each interaction which occurred during the experiments.

Interaction	Force (pN)
Polymer - Polymer	20 - 25
Polymer - Mica Substrate	35 - 40
Polymer - Silicon AFM Tip	55 - 60
Polymer - Silicon Substrate	60 - 65
Polymer - Graphite Substrate	70 - 75

7.4.4.2 Adhesive energy per segment

To carry out further analysis on the force spectroscopy results, the adhesive energy per segment values were calculated from the force plateaus and steps. Figure 7.6 presents histograms showing the adhesive energy per segment distributions for each substrate. The mica and silicon substrates have peaks at similar positions (20 - 25 kJ/mol and 15 - 20 kJ/mol, respectively). Whereas, the histogram for the graphite substrate has no distinct peaks. It was likely that the main peaks at approximately 20 kJ/mol for the mica

and silicon substrates were influenced by the energy associated with the globule-extended coil transition and chain pull-out from the films. This was affirmed when the surface energy (γ) of poly(styrene-co-butadiene) was estimated using the following equation:

$$\gamma = \frac{E_S}{2\pi r b N_A} \tag{7.2}$$

Where E_S was the energy per segment (20 kJ/mol), and b was the length of the segment (1.19 nm). Using Equation 7.2, the surface energy of poly(styrene-co-butadiene) was calculated as 30 mJ/m^2. This was in good agreement with the calculated value of surface energy using values from the literature, which was 32 mJ/m^2.[26,265] Therefore, this demonstrated that an adhesive energy per segment of approximately 20 kJ/mol likely related to globule-extended coil transitions and chain pull-out from the films. However, unlike the distributions of step force in Figure 7.5, the histograms did not exhibit distinct secondary peaks. Therefore, accurate quantitative information regarding the specific polymer/substrate interactions cannot be extrapolated from these histograms. Despite this, the histogram for the mica substrate has the narrowest distribution and the histogram for the graphite has the widest distribution which extends to higher adhesive energy per segment values, and therefore shows the influence from the stronger polymer/graphite interactions.

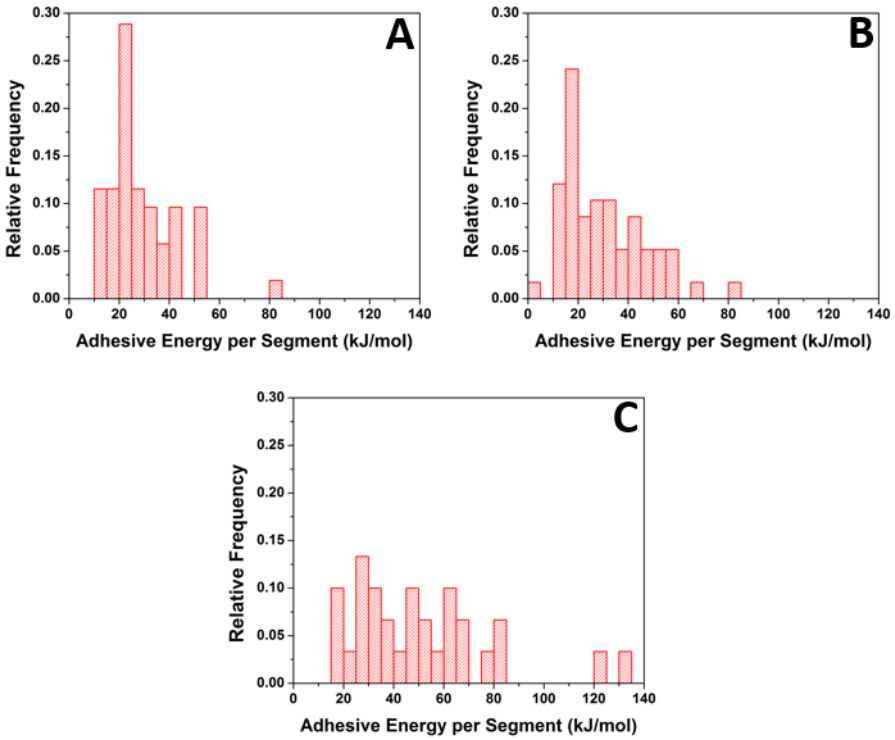

Figure 7.6: Histograms showing the adhesive energy per segment on each substrate. (A) Mica, (B) silicon, (C) graphite.

7.4.4.3 Length of polymer bridging

During the force spectroscopy experiments, there were significant amounts of polymer bridging between the tips and the substrates. The extent of bridging was characterised by investigating the tip-sample separation at the force steps. There were multiple steps in each graph which occurred across relatively large ranges of tip-sample separations. In previous experiments, similar results have been interpreted as picking up numerous chains with different lengths in polydisperse polymer samples.[86] However, for the current experiments, this was not the case as the polymer was monodisperse with a Đ of 1.02. Instead, there are a number of different factors which are responsible for the large variations in bridging length. The first was that the AFM tip could come into contact and pick up polymer chains at any point along their lengths. This effectively creates two individual chains of different lengths which can desorb at slightly different tip-sample

separations. The second reason is due to the adsorbed conformations of the polymer chains. The presence of multiple train conformations can create numerous desorption events for an individual chain, and tail conformations can reduce the adsorbed length of the polymer chains. Finally, the force plateaus and steps could be associated with globule-extended coil transitions, chain pull-out from the films, and chain friction. The last step in the graphs signifies the final desorption event has occurred, and presents the maximum amount of polymer bridging for that specific cycle.

Figure 7.7 presents histograms which show the values of tip-sample separation at the force steps. Each histogram has a wide and fairly asymmetric distribution, which demonstrated that desorption events occurred at a large range of tip-sample separations for each substrate. The main peaks on the histograms were located at 560 - 600 nm and 680 - 760 nm for the mica substrate, 320 - 360 nm and 600 - 640 nm for the silicon substrate, and 720 - 760 nm and 1040 - 1080 nm for the graphite substrate. The average values of tip-sample separation at the force steps were 740 nm, 610 nm, and 889 nm for the mica, silicon, and graphite substrates, respectively. Therefore, on average, the chains bridged to 30%, 24%, and 36% of their full lengths (~2500 nm) for the mica, silicon, and graphite substrates, respectively. This demonstrated that the polymer was more strongly adsorbed to the graphite, and there was a higher degree of loop and tail conformations on the more weakly adsorbing mica and silicon substrates. However, it was expected that the average value would be the smallest on the extremely hydrophilic mica substrate due to it having the weakest polymer adsorption. Although as aforementioned, these results were also influenced by several factors, such as where the AFM tip came into contact with each chain along its length, which was completely random.

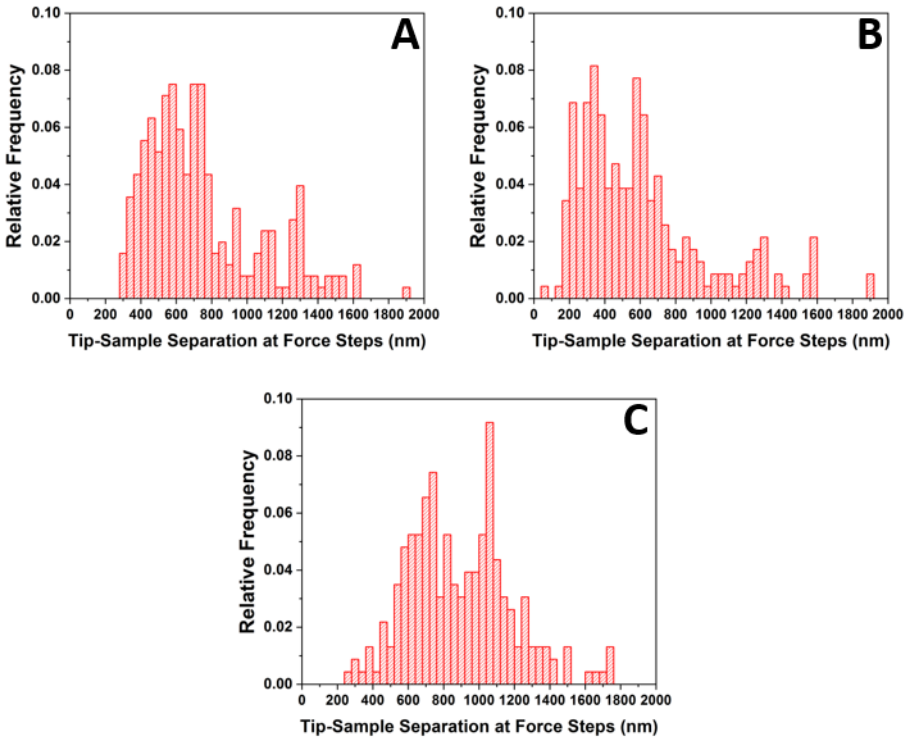

Figure 7.7: Histograms showing the tip-sample separations at force steps for each substrate. (A) Mica, (B) silicon, (C) graphite.

The analysis of polymer bridging demonstrated that for the mica and silicon substrates, there was a greater probability of single chain desorption events occurring at smaller tip-sample separations. Whilst for the graphite substrate, single chain desorption events generally began at larger tip-sample separations. This trend also became obvious when examining the force-separation graphs. The graphs for the graphite substrate (see Figure 7.2C for typical example), generally did not exhibit force plateaus and steps at small tip-sample separations, but instead much larger heterogeneous fluctuations in adhesion occurred. As aforementioned, these fluctuations were called initial events. For the mica and silicon substrates (Figures 7.2A and 7.2B), the initial events were generally more subtle due to weaker polymer/substrate interactions. Whereas, on the strongly adsorbing graphite, the initial events were more significant and generally continued until larger tip-sample separations. Detailed analysis of the initial events is included in Section 7.4.5.

7.4.4.4 Force plateau length

The length of the force plateaus generally represents the distance between individual desorption events. Figure 7.8 presents histograms which show the distribution of force plateau lengths for each substrate. The histograms all had right-skewed distributions with main peaks in the same position (20 - 40 nm) and extended tails. The average plateau length was 162 nm, 78 nm, and 112 nm for the mica, silicon, and graphite substrates, respectively. Therefore, the distance between the events was largest for the mica substrate. This was expected due to the weak polymer/substrate interactions on the mica, which caused larger periods of force plateaus and steps. Consequently, there was generally a larger window where individual desorption events could occur on the mica. On the graphite surface, the strong polymer/substrate interactions meant that the force plateaus and steps did not generally begin until larger tip-sample separations. This meant that there was a much smaller window where individual desorption events could occur. Furthermore, on the strongly adsorbing graphite, there was a higher probability that the chains which were picked up by the tip had final contact points which were in closer proximity to each other. On the silicon substrate, the average distance between events was the smallest of the three substrates by 34 nm. This was not in line with the strength of polymer/substrate interactions and demonstrated that many other factors, such as the position of where the AFM tip interacted with each chain, can significantly influence the results.

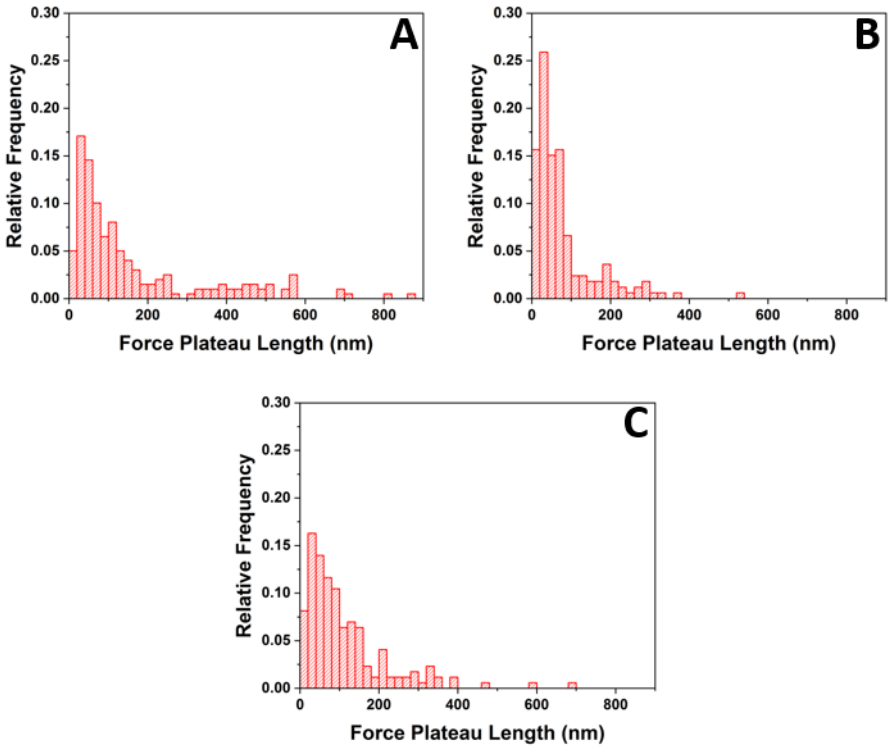

Figure 7.8: Histograms showing the length of force plateaus for each substrate. (A) Mica, (B) silicon, (C) graphite.

7.4.5 Initial event analysis

Many of the graphs for each substrate exhibited evidence of polymer/substrate interactions at smaller tip-sample separations. These were called initial events and provided information regarding the polymer/substrate interactions immediately after initial tip retraction. The initial events were defined as sudden changes in the slope of the curves or secondary minima, which were not characterised by force plateaus and steps. These events were most significant on the graphite due to stronger polymer/substrate interactions. However, they still occurred on the mica and silicon but were generally much more subtle. Interpretation of the initial events can be difficult as they are unspecified in their origin, and can be representative of numerous physical phenomena. However, detailed analysis could provide new information regarding polymer behaviour during initial tip retraction in the force spectroscopy experiments. Figure 7.9 shows a typical force-separation graph for the polymer thin film on the

graphite substrate, as well as, a zoomed section of the same graph. The zoomed sections of the curves were used for analysis as they showed the initial events in much greater detail.

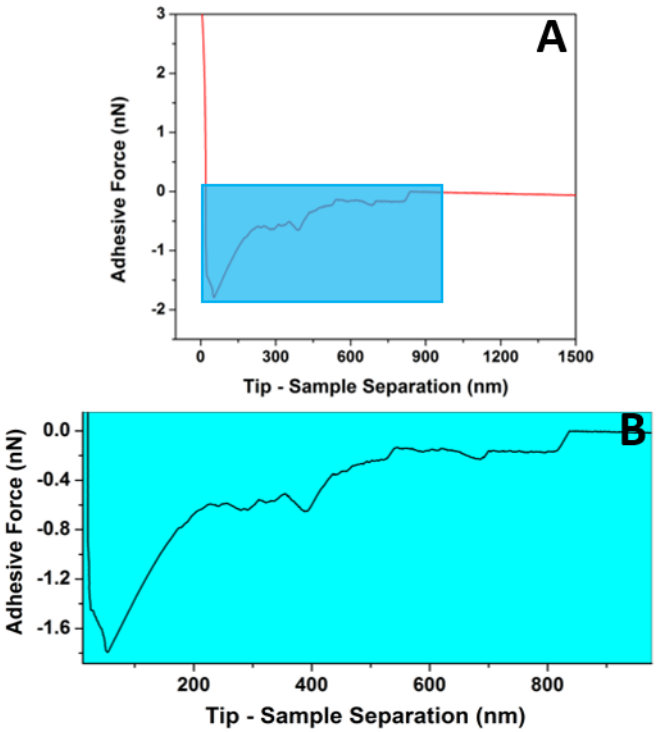

Figure 7.9: (A) Typical force-separation graph for the polymer thin film on the graphite substrate. (B) Zoomed section of the graph which shows the initial events in more detail. The zoomed area is represented by the blue box in (A).

7.4.5.1 Force at events

Similarly to the force plateaus and steps, the initial events can be associated with the desorption of single chains from the substrates or tips, globule-extended coil transitions, chain pull-out from the thin films, and chain friction with the tip and/or substrate.[131,140,259–261] However, as the number of chains involved in the initial events is high, the experimental conditions are very similar to a probe tack experiment and there are a number of other physical phenomena which can occur.[268–270] These include film cavitation, the desorption of many chains simultaneously from the tip or substrate, the formation of nanofibrils (reminiscent of crazing structures), and stick-slip phenomena

at the interfaces.[131,141,259,260,271] Many of the graphs, particularly for the graphite substrate, experienced large, fairly sharp fluctuations in adhesion (see Figure 7.10). Some of these were similar in appearance to saw-tooth patterns which are commonly associated with the stretching of polymer chains in a solvent (good - poor conditions).[143,144,245] The current experiment was carried out in bad solvent conditions (air), which is generally not a suitable environment to observe chain stretching. However, stretching may have been possible as the polymers formed densely packed thin films, which meant that some chains should have experienced melt (Θ-solvent) conditions. Furthermore, the polymer had a low T_g and fairly high flexibility which also promoted stretching. Although chain stretching may have been possible, there was a low probability of it occurring. This was because the chains were not permanently fixed to either to the tip or substrate.[86] It appeared that it was much more common for the initial events to represent the numerous other physical phenomena which were described above.

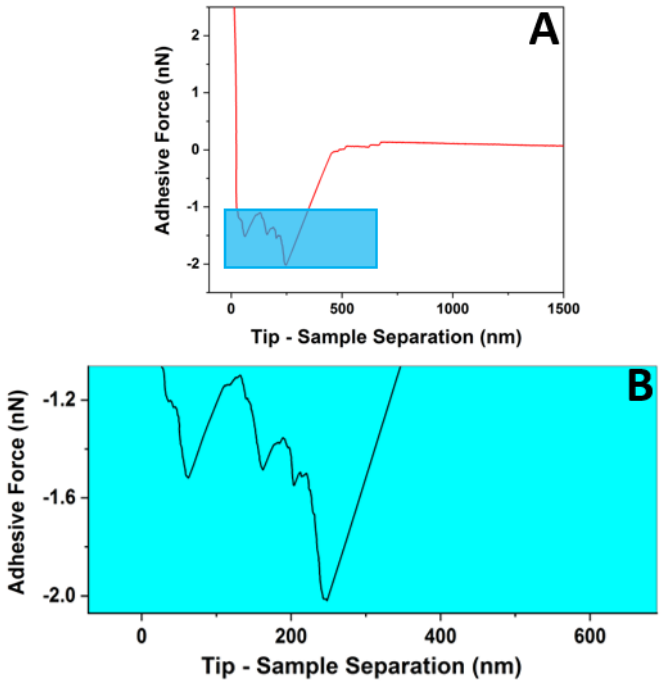

Figure 7.10: (A) Typical force-separation graph where sharp fluctuations in adhesion are observed for the polymer thin film on the graphite substrate. (B) Zoomed section of the graph which shows the fluctuations in greater detail. The zoomed area is represented by the blue box in (A).

Figure 7.11 presents histograms which show the force of the initial events for each substrate. In each histogram, the distributions were right-skewed with very long tails. Consequently, an inlay graph was included to show the events with larger forces (500 - 1500 pN). The wide distributions of each graph were due to the large array of physical phenomena which can occur during the initial events. Despite this, the histograms all had main peaks in very similar positions with values of 20 - 25 pN, 15 - 20 pN, and 15 - 20 pN for the mica, silicon, and graphite substrates, respectively. Therefore, the histograms which examined the force steps (Figure 7.5) and the force of initial events all had main peaks in very similar positions of 15 - 25 pN. It was expected that chain pull-out from the films and globule-extended coil transitions of polymer chains would be prevalent during the initial events, as well as, the force plateaus and steps. Therefore, this confirmed that a force of approximately 15 - 25 pN represented chain pull-out and the globule-extended coil transition. Similarly to the histograms in Figure 7.5, the main peak had the largest relative frequency on the mica substrate. This was because the polymer/substrate interactions were weakest on the mica, which meant that the chains were more likely to form globular conformations on the surface, and the probability of chain pull-out was higher. The average force of the initial events was 73 pN, 84 pN, and 151 pN for the mica, silicon, and graphite substrates, respectively. Therefore, the average values directly related to the strength of the polymer/substrate interactions on each surface. However, the average values of the initial events were significantly larger than the force associated with the desorption of single polymer chains from each substrate. Therefore, this demonstrated that generally the initial events represented phenomena involving numerous chains.

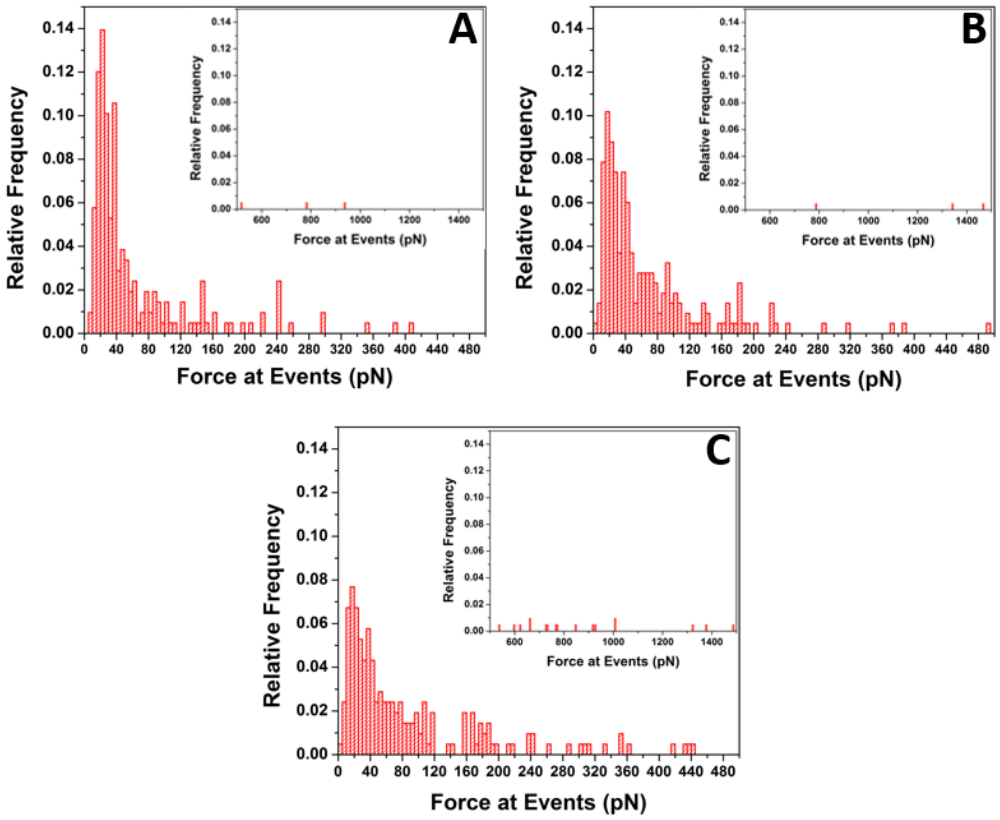

Figure 7.11: Histograms showing the force of the initial events on each substrate. The inlay graphs show the events which occurred at larger forces (500 - 1500 pN). (A) Mica, (B) silicon, (C) graphite.

7.4.5.2 Polymer bridging during initial events

Figure 7.12 shows the tip-sample separations at the initial events for each substrate. The histogram for the mica substrate had a very narrow distribution with a distinct peak at 240 - 320 nm. Whereas, the histograms for the silicon and graphite substrates had much wider distributions with long tails. The silicon substrate had a peak at 320 - 360 nm, and the graphite substrate had a very subtle peak at 400 - 440 nm. The average values of tip-sample separation at the initial events were 331 nm (13% of chain length), 556 nm (22% of chain length), and 616 nm (26% of chain length) for the mica, silicon, and graphite substrates, respectively. Therefore, this demonstrated that the initial events generally occurred at larger tip-sample separations for the graphite substrate. This was due to the strong polymer/substrate interactions on the graphite. The average number of initial

events per force-separation graph was 7, 9, and 11 for the mica, silicon, and graphite substrates, respectively. This trend was expected, as there was generally a larger window where the initial events could occur on the graphite substrate, and a much smaller window on the weakly adsorbing mica.

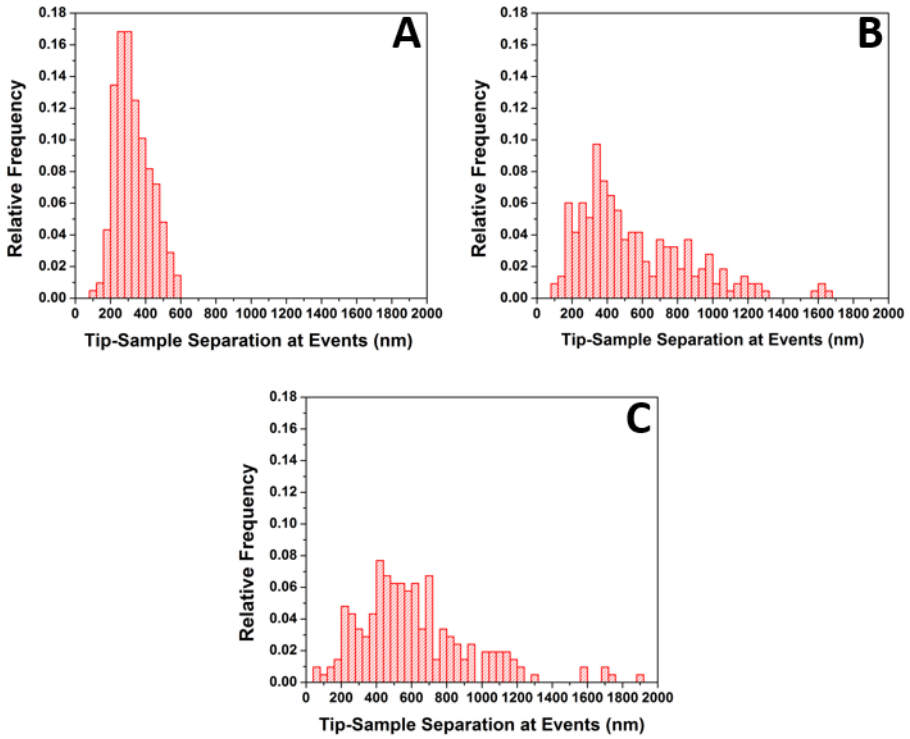

Figure 7.12: Histograms showing the tip-sample separations at initial events for each substrate. (A) Mica, (B) silicon, (C) graphite.

7.4.5.3 Distance between initial events

Figure 7.13 presents histograms which show the distance between the initial events for each substrate. The histograms all had right-skewed distributions and exhibited peaks at 20 - 40 nm. However, the relative frequency of the peak was largest for the mica (0.34), and smallest for the graphite (0.25). The average distance between the initial events was 37 nm, 49 nm, and 54 nm for the mica, silicon, and graphite substrates, respectively. The average distance was largest for the graphite substrate, as the initial events generally continued until larger tip-sample separations. All of the average values were

considerably smaller than the distances between force steps examined in Section 7.4.4.4. This demonstrated that many initial events occurred across relatively small length scales during the cycles.

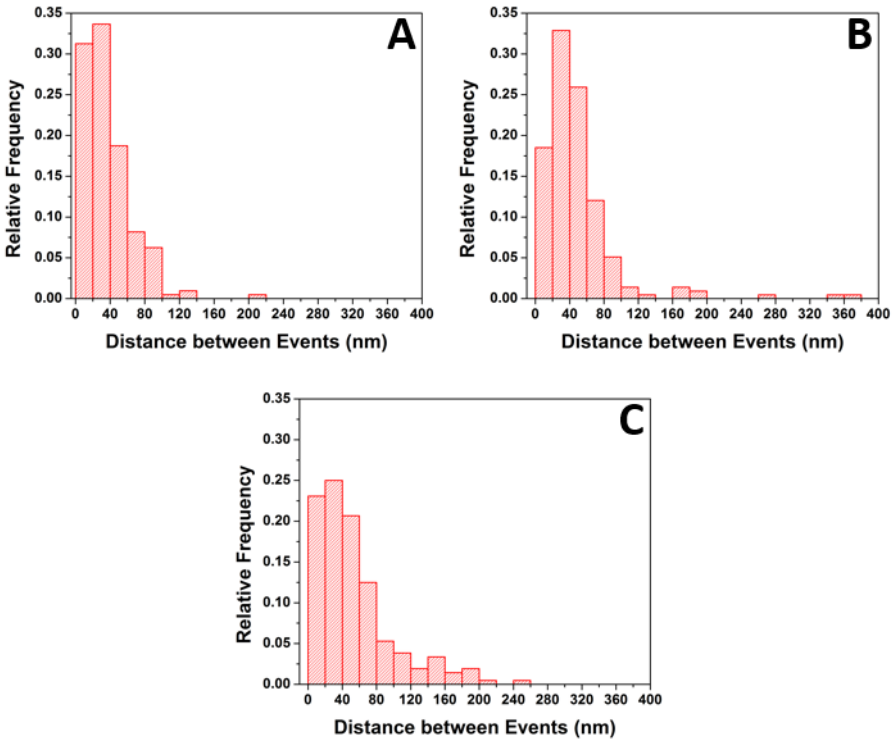

Figure 7.13: Histograms showing the distance between the initial events for each substrate. (A) Mica, (B) silicon, (C) graphite.

7.4.6 Confirmation of chain adsorption to AFM tips

An additional experiment was carried out to confirm whether polymer chains were completely desorbed from each substrate and fixed to the AFM tips during the force spectroscopy experiments. In the experiment, three AFM tips were used to interact with polymer thin films on either a mica, silicon, or graphite substrate for 125 cycles. The tips were then used to interact with a blank silicon substrate for an additional 50 cycles. The adhesion results from the tip/silicon interactions were compared to the average adhesive force and energy values for the interactions between a blank AFM tip and a

silicon substrate, which were obtained in Chapter 6 (0.93 nN and 170 eV, respectively). If the adhesion results for each tip in the current experiment were larger than the values obtained for the blank tip, it can be assumed that polymer/substrate interactions were being measured. Therefore, this demonstrates that polymer chains were desorbed from the thin films on each substrate and attached to the AFM tips during the force spectroscopy experiments. Table 7.4 shows the average adhesive force and energy between the tips prepared by force spectroscopy and the silicon substrates.

Table 7.4: Average adhesive force and energy between AFM tips prepared by force spectroscopy and a blank silicon substrate. Each tip experienced 125 cycles with a thin polymer film on either a mica, silicon, or graphite substrate prior to the experiments with the blank silicon substrate. In each experiment, the cycles were carried out at a fixed location.

Thin Film Substrate	Average Adhesive Force (nN)	Average Adhesive Energy (eV)
Mica	3.76 ± 0.03	4525 ± 62
Silicon	1.24 ± 0.33	412 ± 119
Graphite	1.02 ± 0.04	410 ± 12

For the tip which initially interacted with the polymer film on the mica substrate, all of the force-separation graphs exhibited simple snap-out shapes. However, the average adhesive force and energy were 2.83 nN and 4355 eV larger than the values obtained in the experiment using the blank tip/silicon substrate. This demonstrated that a large amount of polymeric material was desorbed from the mica surface and fixed to the AFM tip during the force spectroscopy experiments as expected. For the tip which had interacted with the polymer thin film on silicon, the average adhesive force and energy were 0.31 nN and 242 eV larger than the values obtained in the blank tip/silicon experiments. Furthermore, force plateaus and steps were observed in some of the graphs which provided direct evidence of polymer interactions. Therefore, this confirmed that polymer chains were completely desorbed from the silicon substrate during the force spectroscopy experiments. For the tip which initially interacted with the polymer film on the graphite, the graphs all exhibited simple snap-out shapes. However, the adhesive force and energy were 0.09 nN and 240 eV larger than the values obtained for the

experiments using the blank AFM tip, which suggested that a small amount of polymer/substrate interactions were being measured.

The results demonstrated that polymer chains were desorbed from the films on each substrate during the force spectroscopy experiments. This was essential in order to produce reliable results regarding polymer/substrate interactions. However, as expected, the amount of polymeric material which was desorbed from the substrate and fixed to the AFM tip appeared to be directly related to the strength of the polymer/substrate interactions.

7.5 Conclusions

A series of force spectroscopy experiments were carried out to investigate the specific interactions between polymers and various substrates in ambient conditions. Blank AFM tips were used to interact with thin poly(styrene-co-butadiene) random copolymer films on mica, silicon, and graphite substrates. The experimental system was vastly improved in comparison to the previous chapter, as there appeared to be no influence from capillary forces and the probability of observing desorption events was very high. Furthermore, the experimental procedure was uncomplicated and time efficient.

The force-separation graphs exhibited plateaus and steps, as well as, initial events. The plateaus and steps represented the desorption of single chains from the substrate or tip. However, they also represented the force associated with the globule-extended coil transition, chain pull-out from the thin films, and chain friction. Analysis of the steps demonstrated that the polymer desorption was largest for the graphite substrate and smallest for the mica. This trend agreed with previous AFM observations in Chapters 4 and 5, and directly correlated to the Hamaker constant and hydrophobicity of each substrate. The larger desorption force on the graphite substrate was due to stronger van der Waals interactions between the hydrophobic polymer and graphite surface, and π-π stacking interactions. The force and energy associated with chain pull-out from the thin films and the globule-extended coil transition was also identified. Significant amounts of polymer bridging were observed for each substrate. Generally, force plateaus and steps did not begin until larger tip-sample separations on the graphite. This was due to the

stronger polymer/substrate interactions, which meant that there were less loop conformations in the chains, and extended periods of initial events at smaller tip-sample separations. The distance between the steps was largest on the mica substrate. This was because the force plateaus and steps occurred over a larger length scale, generally beginning at fairly low tip-sample separations.

Initial events were observed in the force-separation graphs for each substrate, although they were most prominent on the graphite. The initial events were defined as sudden changes in the slope of the curves or secondary minima, and generally occurred at smaller tip-sample separations. The initial events could represent many different physical phenomena, including some which are associated with probe tack experiments such as film cavitation and the formation of nanofibrils. The average force of the initial events was largest for the strongly adsorbing graphite substrate and smallest for the weakly adsorbing mica. For each substrate, the average force of the initial events was considerably larger than the forces associated with the desorption of single chains. Furthermore, there was a relatively high probability of chain pull-out and globule-extended coil transitions occurring during the initial events. The tip-sample separation at the initial events was generally largest on the graphite and smallest on the mica. This was due to the strong polymer/substrate interactions on the graphite, which created extended periods of initial events up to much larger tip-sample separations. Similarly, the distance between the initial events was largest on the graphite, which was also due to the relatively large range of tip-sample separations where the events occurred.

Additional experiments were carried out which confirmed that polymer chains were desorbed from each substrate during the force spectroscopy experiments. The amount of polymeric material which was desorbed from each substrate was directly related to the strength of the polymer/substrate interactions. This confirmation provided validation of the experimental system.

A comprehensive force spectroscopy study was carried out which investigated the strength of interactions between poly(styrene-co-butadiene) and various substrates. The results provided detailed information regarding the strength of specific polymer/substrate interactions, as well as, identifying the force associated with the globule-extended coil conformational transition, chain pull-out from the thin films, and desorption from the AFM tip. These results are not only of fundamental interest, but are

also useful to many applications which rely on polymers functioning at surfaces, such as composite materials. Furthermore, the concept of the experimental system has many advantages and could be utilised for further experiments.

8 Conclusions

8.1 Conclusions

The aim of this thesis was to investigate the behaviour of adsorbed poly(styrene-co-butadiene) random copolymer nanostructures on various substrates. This was achieved by primarily using AFM imaging and force spectroscopy techniques. AFM imaging was utilised to investigate the morphology of poly(styrene-co-butadiene) on mica and graphite substrates at varying concentrations and molecular weights. Whilst AFM force spectroscopy was utilised to investigate the adhesion and specific interactions between poly(styrene-co-butadiene) and mica, silicon, and graphite substrates.

Key conclusions deduced from this work are as follows:

1. The adsorbed poly(styrene-co-butadiene) generally formed spherical cap shaped nanodroplets on the mica substrate to minimise surface contact. However, the size of the nanodroplets varied significantly, from single chains to aggregates containing many thousands of chains. As the molecular weight of the polymer increased, there were fewer but larger aggregates observed on the mica substrate. This was due to increased solution viscosity and chain entanglements at higher molecular weights.

2. On the mica substrate, a distinct minimum in contact angle was observed for nanodroplets of all molecular weights with radii ranging from 100 nm to 250 nm. As nanodroplet radius decreased from this range, the contact angle of the droplets increased dramatically. This appeared to be caused by an increase in the elastic modulus of the nanodroplets and/or a positive line tension effect. When the droplet radius was larger than 250 nm, the contact angle of the droplets also increased. This appeared to be due to surface heterogeneities which formed on the mica substrate over time. At the macroscale, there was no size dependence on the polymer droplet contact angle.

3. On the graphite substrate, the adsorbed poly(styrene-co-butadiene) formed various nanostructures depending on solution concentration. These included networks, asymmetrical nanoislands, and nanoribbons. For the networks that formed at higher concentrations, the size of the features were generally largest for the lowest molecular weight polymer. This is because the shorter chains

were more likely to remain in an unperturbed state due to limited gains in adsorption energy at the surface. However, at lower concentrations, the size of the nanoislands and nanoribbons were mostly unaffected by changes to molecular weight. This is because there were fewer chains at the surface during solvent evaporation, which meant that it was probable for chains of all lengths to adsorb to the surface.

4. The poly(styrene-co-butadiene) nanostructures exhibited distinct ordering at 60˚ intervals on the graphite substrate. This demonstrated that π-π stacking interactions caused the nanostructures to reflect the crystalline symmetry of the graphite. At the lowest concentration, the ordering was very precise. Whilst at higher concentrations, the ordering was less defined, but remained statistically significant. It was also demonstrated that the degree of ordering for poly(styrene-co-butadiene) on graphite was considerably greater compared to polybutadiene and polystyrene homopolymers. This was due to the aromatic rings in the styrene units being randomly positioned along a flexible chain in poly(styrene-co-butadiene) which maximises the possibility for π-π stacking interactions.

5. At the highest concentration investigated, the poly(styrene-co-butadiene) formed mostly continuous thin films on both the mica and graphite substrates. Dewetting occurred which created circular holes in the films with raised rims and some evidence of viscous fingering patterns. On both substrates, the rim height scaled linearly with the diameter of the dewetted holes. This suggested that the polymer films exhibited both viscous dewetting and plastic deformation, regardless of the substrate surface properties.

6. AFM force spectroscopy was utilised to investigate the adhesion between poly(styrene-co-butadiene)-coated AFM tips and mica, silicon, and graphite substrates. It was demonstrated that polymer/substrate adhesion could be investigated by preparing AFM tips using dip coating and force spectroscopy techniques. The experimental system was uncomplicated and appeared to accurately investigate polymer/substrate adhesion due to van der Waals forces and π-π stacking interactions on the hydrophobic graphite substrate. However,

on the more hydrophilic mica and silicon substrates, the measured adhesion was larger than expected. This was due to condensed water at the substrate surfaces, which created capillary forces. The influence from capillary forces was largest on the extremely hydrophilic mica substrate. The results also demonstrated that water associated forces influenced the measured adhesion at the single chain level on the silicon substrate.

7. AFM force spectroscopy experiments using poly(styrene-co-butadiene)-coated tips examined polymer/substrate adhesion over the course of many cycles. It was demonstrated that adhesion decreased more significantly when the cycles were carried out in an array compared to at a fixed location on the substrates. This was because when the cycles were carried out at a fixed location, any desorbed polymer chains continued to be interacted with in the additional cycles. Furthermore, it was demonstrated that variations to tip/substrate contact time and the history of the AFM tips did not significantly impact polymer/substrate adhesion.

8. AFM force spectroscopy experiments were carried out where blank AFM tips were used to interact with polymer thin films on mica, silicon, and graphite substrates. This experimental system was simple and appeared to eliminate any influence from capillary forces. Furthermore, the probability of observing desorption events was very high. The resulting force-separation graphs for each substrate exhibited initial events, as well as, force plateaus and steps. These represented a number of physical phenomena which occurred during the experiments including single chain desorption events, globule-extended coil conformational transitions, chain pull-out from the thin films, chain friction, film cavitation, and the formation of nanofibrils.

9. When blank AFM tips interacted with polymer films on each substrate, the desorption force and adhesive energy per segment values were largest on the graphite. This was due to strong van der Waals forces and π-π stacking interactions between the hydrophobic poly(styrene-co-butadiene) and graphite substrate. On the more hydrophilic silicon substrate/tip and mica substrate, the desorption forces and adhesive energy per segment values were smaller

because weak van der Waals forces were responsible for the polymer/substrate interactions. The degree of polymer bridging between the substrate and tip was largest on the graphite. This was due to stronger polymer/substrate interactions which meant that the adsorbed chains formed a smaller proportion of loop conformations, and there was an extended period of initial events at lower tip-sample separations.

10. In the force spectroscopy experiments, the force associated with the globule-extended coil transition and chain pull-out from the thin films was identified. The value obtained from the force spectroscopy experiments was in good agreement with theoretical predictions. On the mica substrate, there was the highest probability of globule-extended coil transitions and chain pull-out occurring due to the weaker polymer/substrate interactions.

8.2 Future work

Building on the work from this thesis, there are a number of potential areas for additional research using both AFM imaging and force spectroscopy to further investigate the behaviour of polymers at surfaces.

8.2.1 AFM imaging

This thesis has comprehensively investigated the morphology of poly(styrene-co-butadiene) nanostructures on a strongly adsorbing graphite substrate and a very weakly adsorbing mica substrate. However, polymer morphology on silicon was not systematically explored. Therefore, it would be interesting and useful to investigate polymer morphology on the moderately hydrophilic silicon substrate, and observe how the morphology is impacted with changes to concentration and molecular weight. This would provide a more complete understanding of how the morphology of poly(styrene-co-butadiene) varies across a spectrum of substrates with different surface properties. Another area for potential work would be to repeat the AFM imaging experiments using end-functionalised poly(styrene-co-butadiene) random copolymers. A direct

comparison could be made with the AFM results obtained using the non-functionalised polymers. This would demonstrate exactly how the end-functionalisation impacts polymer morphology on different substrates under various conditions.

In Chapter 4, it was demonstrated that the contact angle of nanodroplets on a mica substrate was size dependent by a distinct trend irrespective of molecular weight. The contact angle of polymer droplets at the macroscale was also investigated, and it appeared that there was no size dependence at this length scale. These experiments presented some interesting results regarding the complex dewetting behaviour of polymer droplets. Therefore, it would be worthwhile to continue this work and carry out a thorough investigation of the contact angles of polymer droplets at the microscale. This would allow the droplet size dependence on contact angle to be comprehensively investigated across all plausible length scales.

In Chapter 5, it was demonstrated that a high degree of ordering occurred in poly(styrene-co-butadiene) nanostructures on a graphite substrate due to π-π stacking interactions. Furthermore, the degree of ordering was significantly greater compared to when the experiments were repeated using polystyrene and polybutadiene homopolymers. This demonstrated that both the aromatic rings in the styrene units, and the flexibility of the butadiene units increased the amount of π-π stacking interactions for the random copolymer. This result suggests that there should be a specific styrene-butadiene ratio in the random copolymer chains which maximises the possible π-π stacking interactions with the graphite, and therefore creates the largest amount of ordering. Consequently, it would be very interesting to perform an AFM imaging experiment to identify this optimal styrene-butadiene ratio in the random copolymer chains, which maximises the degree of ordering on the graphite. Furthermore, examining the specific ordering of poly(styrene-co-butadiene) copolymers on graphite substrates with different compositions, such as block and alternating copolymers would be worthwhile.

8.2.2 AFM force spectroscopy

The AFM imaging results demonstrated that due to increased π-π stacking interactions, there was a higher degree of ordering for poly(styrene-co-butadiene) on graphite

compared to polybutadiene and polystyrene. Therefore, an interesting area for future research would be to repeat the AFM force spectroscopy experiments in Chapter 7 using polybutadiene and polystyrene homopolymers on graphite substrates. The desorption forces between each homopolymer and the graphite substrate could be directly compared to the results obtained using the poly(styrene-co-butadiene) random copolymer. This would allow the influence of π-π stacking interactions for each polymer to be quantitatively investigated using AFM force spectroscopy, in addition to being qualitatively investigated using AFM imaging.

Another potential area for future research would be to repeat the force spectroscopy experiments in Chapter 7 using polymer films with varying thicknesses on each substrate. The polymer/substrate interactions could be investigated at varying film thicknesses. Furthermore, it would be useful to identify if the probability of chain pull-out and globule-extended coil transitions occurring would decrease as film thickness reduced. However, it is worthwhile noting that polymer films with extremely small thicknesses could not be created on each substrate due to dewetting and instabilities.

9 Appendix

9.1 Supplementary data for Chapter 5

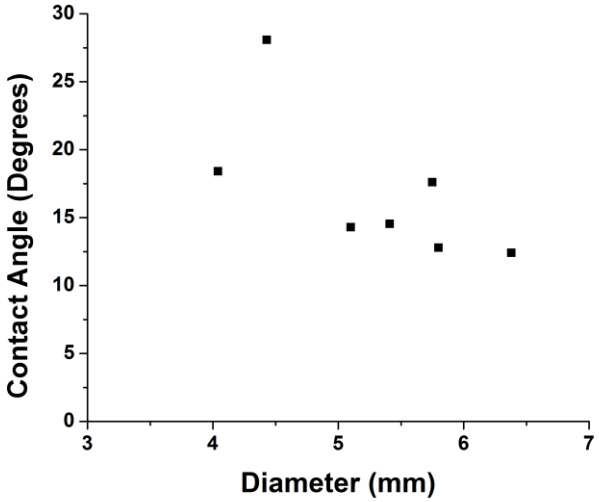

Figure A1: Graph showing the contact angle of various 46 kg/mol poly(styrene-co-butadiene) macroscopic droplets against droplet diameter on a graphite substrate. The droplets were annealed at 65˚C for 48 hours and were then left for 1 week at room temperature before contact angle measurements were carried out on the KRUSS DSA30.

10 Literature References

(1) Young, R. J.; Lovell, P. A. *Introduction to Polymers*, Third.; CRC Press: Boca Raton, 2011.

(2) Weinberg, R. A. The Molecules of Life. *Sci. Am.* **1985**, *253*, 48–57.

(3) Lewis, R. V. Spider Silk: Ancient Ideas for New Biomaterials. *Chem. Rev.* **2006**, *106*, 3762–3774.

(4) Rubinstein, M.; Colby, R. H. *Polymer Physics*; Oxford University Press: Oxford, 2003.

(5) Fisher, H. L. Vulcanization of Rubber. *Ind. Eng. Chem.* **1939**, *31*, 1381–1389.

(6) Crespy, D.; Bozonnet, M.; Meier, M. 100 Years of Bakelite, the Material of a 1000 Uses. *Angew. Chemie - Int. Ed.* **2008**, *47*, 3322–3328.

(7) Thompson, R. C.; Swan, S. H.; Moore, C. J.; Vom Saal, F. S. Our Plastic Age. *Philos. Trans. R. Soc. B Biol. Sci.* **2009**, *364*, 1973–1976.

(8) Mülhaupt, R. Hermann Staudinger and the Origin of Macromolecular Chemistry. *Angew. Chemie - Int. Ed.* **2004**, *43*, 1054–1063.

(9) Jensen, W. B. The Origin of the Polymer Concept. *J. Chem. Educ.* **2008**, *85*, 624–625.

(10) Paul, D. R.; Robeson, L. M. Polymer Nanotechnology: Nanocomposites. *Polymer* **2008**, *49*, 3187–3204.

(11) Roy, I.; Gupta, M. N. Smart Polymeric Materials: Emerging Biochemical Applications. *Chem. Biol.* **2003**, *10*, 1161–1171.

(12) Ferrari, M. Cancer Nanotechnology: Opportunities and Challenges. *Nat. Rev. Cancer* **2005**, *5*, 161–171.

(13) Andrady, A. L.; Neal, M. A. Applications and Societal Benefits of Plastics. *Philos. Trans. R. Soc. B Biol. Sci.* **2009**, *364*, 1977–1984.

(14) Tsao, C.-W.; DeVoe, D. L. Bonding of Thermoplastic Polymer Microfluidics. *Microfluid Nanofluid* **2009**, *6*, 1–16.

(15) Giboz, J.; Copponnex, T.; Mélé, P. Microinjection Molding of Thermoplastic Polymers: A

Review. *J. Micromechanics Microengineering* **2007**, *17*, R96–R109.

(16) Cox, A. P. D.; Fenner, R. T. Melting Performance in the Single Screw Extrusion of Thermoplastics. *Polym. Eng. Sci.* **1980**, *20*, 562–571.

(17) Kanaya, T.; Kawaguchi, T.; Kaji, K. Local Dynamics of Cis-1,4-Polybutadiene near the Glass Transition Temperature Tg. *Phys. B* **1992**, *182*, 403–408.

(18) Brinke, A. T. Silica Reinforced Tyre Rubbers, Univesity of Twente, 2002.

(19) Yousefi, A.; Lafleur, P. G.; Gauvin, R. Kinetic Studies of Thermoset Cure Reactions : A Review. *Polym. Compos.* **1997**, *18*, 157–168.

(20) Meier, U. Strengthening of Structures Using Carbon Fibre/Epoxy Composites. *Constr. Build. Mater.* **1995**, *9*, 341–351.

(21) Rijswijk, K. V. Thermoplastic Composite Wind Turbine Blades, Deflt University of Technology, 2007.

(22) Lattime, R. R. Styrene-Butadiene Rubber. In *Van Nostrand's Encyclopedia of Chemistry*; Considine, G. D., Ed.; Wiley: Hoboken, 2005.

(23) Byrdson, J. A. Styrene-Butadiene Rubber. In *Developments in Rubber Technology - 2*; Springer: Dordrecht, 1981.

(24) Heinrich, G.; Klüppel, M.; Vilgis, T. A. Reinforcement of Elastomers. *Curr. Opin. Solid State Mater. Sci.* **2002**, *6*, 195–203.

(25) Han, J.; Zhang, X.; Guo, W.; Wu, C. Effect of Modified Carbon Black on the Filler-Elastomer Interaction and Dynamic Mechanical Properties of SBR Vulcanizates. *J. Appl. Polym. Sci.* **2006**, *100*, 3707–3712.

(26) Jones, R. A. L.; Richards, R. W. *Polymers at Surfaces and Interfaces*; Cambridge University Press: Cambridge, 1999.

(27) Binder, K. Monte Carlo Simulation of Polymers at Interfaces. *Physica A* **1993**, *200*, 722–729.

(28) Evangelopoulos, A. E. A. S.; Glynos, E.; Madani-Grasset, F.; Koutsos, V. Elastic Modulus of a Polymer Nanodroplet: Theory and Experiment. *Langmuir* **2012**, *28*, 4754–4767.

(29) Keddie, J. L.; Jones, R. A. L.; Cory, R. A. Interface and Surface Effects on the Glass-Transition Temperature in Thin Polymer Films. *Faraday Discuss.* **1994**, *98*, 219–230.

(30) Vigneswaran, N.; Samsuri, F.; Ranganathan, B.; Padmapriya. Recent Advances in Nano Patterning and Nano Imprint Lithography for Biological Applications. *Procedia Eng.* **2014**, *97*, 1387–1398.

(31) Nie, Z.; Kumacheva, E. Patterning Surfaces with Functional Polymers. *Nat. Mater.* **2008**, *7*, 277–290.

(32) Acikgoz, C.; Hempenius, M. A.; Huskens, J.; Vancso, G. J. Polymers in Conventional and Alternative Lithography for the Fabrication of Nanostructures. *Eur. Polym. J.* **2011**, *47*, 2033–2052.

(33) Herr, D. J. C. Directed Block Copolymer Self-Assembly for Nanoelectronics Fabrication. *J. Mater. Res.* **2011**, *26*, 122–139.

(34) Behl, M.; Seekamp, J.; Zankovych, S.; Torres, C. M. S.; Zentel, R.; Ahopelto, J. Towards Plastic Electronics: Patterning Semiconducting Polymers by Nanoimprint Lithography.

Adv. Mater. **2002**, *14*, 588–591.

(35) Hollister, S. J. Porous Scaffold Design for Tissue Engineering. *Nat. Mater.* **2005**, *4*, 518–524.

(36) Schultz, M. P.; Bendick, J. A.; Holm, E. R.; Hertel, W. M. Economic Impact of Biofouling on a Naval Surface Ship. *Biofouling* **2011**, *27*, 87–98.

(37) McCoy, C. P.; Irwin, N. J.; Donnelly, L.; Jones, D. S.; Hardy, J. G.; Carson, L. Anti-Adherent Biomaterials for Prevention of Catheter Biofouling. *Int. J. Pharm.* **2018**, *535*, 420–427.

(38) Cho, W. K.; Kang, S. M.; Lee, J. K. Non-Biofouling Polymeric Thin Films on Solid Substrates. *J. Nanosci. Nanotechnol.* **2014**, *14*, 1231–1252.

(39) Moropoulou, A.; Bakolas, A.; Anagnostopoulou, S. Composite Materials in Ancient Structures. *Cem. Concr. Compos.* **2005**, *27*, 295–300.

(40) Breuer, O.; Sundararaj, U. Big Returns from Small Fibers: A Review of Polymer/Carbon Nanotube Composites. *Polym. Compos.* **2004**, *25*, 630–641.

(41) McCarthy, R. F. J.; Haines, G. H.; Newley, R. A. Polymer Composite Applications to Aerospace Equipment. *Compos. Manuf.* **1994**, *5*, 83–93.

(42) Thuau, D.; Koutsos, V.; Cheung, R. Electrical and Mechanical Properties of Carbon Nanotube-Polyimide Composites. *J. Vac. Sci. Technol. B* **2009**, *27*, 3139–3144.

(43) Gao, S.-L.; Mäder, E.; Zhandarov, S. F. Carbon Fibers and Composites with Epoxy Resins: Topography, Fractography and Interphases. *Carbon* **2004**, *42*, 515–529.

(44) Iijima, S. Helical Microtubules of Graphitic Carbon. *Nature* **1991**, *354*, 56–58.

(45) Novoselov, K. S.; Geim, A. K.; Morozov, S. V.; Jiang, D.; Zhang, Y.; Dubonos, S. V.; Grigorieva, I. V.; Firsov, A. A. Electric Field Effect in Atomically Thin Carbon Films. *Science* **2004**, *306*, 666–669.

(46) Berton, N.; Lemasson, F.; Poschlad, A.; Meded, V.; Tristram, F.; Wenzel, W.; Hennrich, F.; Kappes, M. M.; Mayor, M. Selective Dispersion of Large-Diameter Semiconducting Single-Walled Carbon Nanotubes with Pyridine-Containing Copolymers. *Small* **2014**, *10*, 360–367.

(47) Stankovich, S.; Dikin, D. A.; Dommett, G. H. B.; Kohlhaas, K. M.; Zimney, E. J.; Stach, E. A.; Piner, R. D.; Nguyen, S. T.; Ruoff, R. S. Graphene-Based Composite Materials. *Nature* **2006**, *442*, 282–286.

(48) Wesełucha-Birczyńska, A.; Frączek-Szczypta, A.; Długoń, E.; Paciorek, K.; Bajowska, A.; Kościelna, A.; Błazewicz, M. Application of Raman Spectroscopy to Study of the Polymer Foams Modified in the Volume and on the Surface by Carbon Nanotubes. *Vib. Spectrosc.* **2014**, *72*, 50–56.

(49) Reiter, G. Dewetting of Highly Elastic Thin Polymer Films. *Phys. Rev. Lett.* **2001**, *87*, 186101–1.

(50) Neuman, K. C.; Nagy, A. Single-Molecule Force Spectroscopy: Optical Tweezers, Magnetic Tweezers and Atomic Force Microscopy. *Nat. Methods* **2008**, *5*, 491–505.

(51) Bogner, A.; Jouneau, P.-H.; Thollet, G.; Basset, D.; Gauthier, C. A History of Scanning Electron Microscopy Developments: Towards "Wet-STEM" Imaging. *Micron* **2007**, *38*, 390–401.

(52) Im, S. H.; Jeong, U.; Xia, Y. Polymer Hollow Particles with Controllable Holes in Their

Surfaces. *Nat. Mater.* **2005**, *4*, 671–675.

(53) Gaillard, C.; Stadelmann, P. A.; Plummer, C. J. G.; Fuchs, G. Practical Method for High-Resolution Imaging of Polymers by Low-Voltage Scanning Electron Microscopy. *Scanning* **2004**, *26*, 122–130.

(54) Jagtap, R. N.; Ambre, A. H. Overview Literature on Atomic Force Microscopy (AFM): Basics and Its Important Applications for Polymer Characterization. *Indian J. Eng. Mater. Sci.* **2006**, *13*, 368–384.

(55) Williams, D. B.; Carter, C. B. *Transmission Electron Microscopy*; Springer: Berlin, 2009.

(56) Michler, G. H. *Electron Microscopy of Polymers*; Springer: Berlin, 2008.

(57) Gosse, C.; Croquette, V. Magnetic Tweezers: Micromanipulation and Force Measurement at the Molecular Level. *Biophys. J.* **2002**, *82*, 3314–3329.

(58) Strick, T. R.; Allemand, J.-F.; Bensimon, D.; Croquette, V. The Elasticity of a Single Supercoiled DNA Molecule. *Science* **1996**, *271*, 1835–1837.

(59) Bustamante, C.; Bryant, Z.; Smith, S. B. Ten Years of Tension: Single-Molecule DNA Mechanics. *Nature* **2003**, *421*, 423–427.

(60) Bustamante, C.; Smith, S. B.; Liphardt, J.; Smith, D. Single-Molecule Studies of DNA Mechanics. *Curr. Opin. Struct. Biol.* **2000**, *10*, 279–285.

(61) Wang, M. D.; Yin, H.; Landick, R.; Gelles, J.; Block, S. M. Stretching DNA with Optical Tweezers. *Biophys. J.* **1997**, *72*, 1335–1346.

(62) Smith, S. B.; Cui, Y.; Bustamante, C. Overstretching B-DNA: The Elastic Response of Individual Double-Stranded and Single-Stranded DNA Molecules. *Science* **1996**, *271*, 795–799.

(63) Mangeol, P.; Côte, D.; Bizebard, T.; Legrand, O.; Bockelmann, U. Probing DNA and RNA Single Molecules with a Double Optical Tweezer. *Eur. Phys. J. E* **2006**, *19*, 311–317.

(64) Yuan, Y.; Lee, T. R. Contact Angle and Wetting Properties. In *Surface Science Techniques*; Springer: Berlin, 2013; pp 3–34.

(65) Uyama, Y.; Inoue, H.; Ito, K.; Kishida, A.; Ikada, Y. Comparison of Different Methods for Contact Angle Measurement. *J. Colloid Interface Sci.* **1991**, *141*, 275–279.

(66) Kwok, D. Y.; Gietzelt, T.; Grundke, K.; Jacobasch, H.-J.; Neumann, A. W. Contact Angle Measurements and Contact Angle Interpretation. 1. Contact Angle Measurements by Axisymmetric Drop Shape Analysis and a Goniometer Sessile Drop Technique. *Langmuir* **1997**, *13*, 2880–2894.

(67) Tavana, H.; Petong, N.; Hennig, A.; Grundke, K.; Neumann, A. W. Contact Angles and Coating Film Thickness. *J. Adhes.* **2005**, *81*, 29–39.

(68) Binnig, G.; Rohrer, H.; Gerber, C.; Weibel, E. Surface Studies by Scanning Tunneling Microscopy. *Phys. Rev. Lett.* **1982**, *49*, 57–61.

(69) Binnig, G.; Rohrer, H.; Gerber, C.; Weibel, E. Tunneling through a Controllable Vacuum Gap. *Appl. Phys. Lett.* **1982**, *40*, 178–180.

(70) Eigler, D. M.; Schweizer, E. K. Positioning Single Atoms with a Scanning Tunneling Microscope. *Nature* **1990**, *344*, 524–526.

(71) Binnig, G.; Quate, C. F.; Gerber, C. Atomic Force Microscope. *Phys. Rev. Lett.* **1986**, *56*,

930–933.

(72) Giessibl, F. J. Advances in Atomic Force Microscopy. *Rev. Mod. Phys.* **2003**, *75*, 949–983.

(73) Kalloudis, M.; Glynos, E.; Pispas, S.; Walker, J.; Koutsos, V. Thin Films of Poly(Isoprene‐b‐ethylene Oxide) Diblock Copolymers on Mica: An Atomic Force Microscopy Study. *Langmuir* **2013**, *29*, 2339–2349.

(74) Adamcik, J.; Klinov, D. V.; Witz, G.; Sekatskii, S. K.; Dietler, G. Observation of Single-Stranded DNA on Mica and Highly Oriented Pyrolytic Graphite by Atomic Force Microscopy. *FEBS Lett.* **2006**, *580*, 5671–5675.

(75) Kumaki, J.; Hashimoto, T. Conformational Change in an Isolated Single Synthetic Polymer Chain on a Mica Surface Observed by Atomic Force Microscopy. *J. Am. Chem. Soc.* **2003**, *125*, 4907–4917.

(76) Gross, L.; Mohn, F.; Moll, N.; Liljeroth, P.; Meyer, G. The Chemical Structure of a Molecule Resolved by Atomic Force Microscopy. *Science* **2009**, *325*, 1110–1114.

(77) Pavliček, N.; Mistry, A.; Majzik, Z.; Moll, N.; Meyer, G.; Fox, D. J.; Gross, L. Synthesis and Characterization of Triangulene. *Nat. Nanotechnol.* **2017**, *12*, 308–311.

(78) Markiewicz, P.; Goh, M. C. Atomic Force Microscopy Probe Tip Visualization and Improvement of Images Using a Simple Deconvolution Procedure. *Langmuir* **1994**, *10*, 5–7.

(79) Burnham, N. A.; Colton, R. J. Measuring the Nanomechanical Properties and Surface Forces of Materials Using an Atomic Force Microscope. *J. Vac. Sci. Technol. A* **1989**, *7*, 2906–2913.

(80) Weisenhorn, A. L.; Hansma, P. K.; Albrecht, T. R.; Quate, C. F. Forces in Atomic Force Microscopy in Air and Water. *Appl. Phys. Lett.* **1989**, *54*, 2651–2653.

(81) Giannotti, M. I.; Vancso, G. J. Interrogation of Single Synthetic Polymer Chains and Polysaccharides by AFM-Based Force Spectroscopy. *ChemPhysChem* **2007**, *8*, 2290–2307.

(82) Balzer, B. N.; Micciulla, S.; Dodoo, S.; Zerball, M.; Gallei, M.; Rehahn, M.; Klitzing, R. V; Hugel, T. Adhesion Property Profiles of Supported Thin Polymer Films. *ACS Appl. Mater. Interfaces* **2013**, *5*, 6300–6306.

(83) Hugel, T.; Grosholz, M.; Clausen-Schaumann, H.; Pfau, A.; Gaub, H.; Seitz, M. Elasticity of Single Polyelectrolyte Chains and Their Desorption from Solid Supports Studied by AFM Based Single Molecule Force Spectroscopy. *Macromolecules* **2001**, *34*, 1039–1047.

(84) Zhang, W.; Zou, S.; Wang, C.; Zhang, X. Single Polymer Chain Elongation of Poly(N -Isopropylacrylamide) and Poly(Acrylamide) by Atomic Force Microscopy. *J. Phys. Chem. B* **2000**, *104*, 10258–10264.

(85) Radiom, M.; Maroni, P.; Borkovec, M. Influence of Solvent Quality on the Force Response of Individual Poly(Styrene) Polymer Chains. *ACS Macro Lett.* **2017**, *6*, 1052–1055.

(86) Kienle, S.; Gallei, M.; Yu, H.; Zhang, B.; Krysiak, S.; Balzer, B. N.; Rehahn, M.; Schlüter, A. D.; Hugel, T. Effect of Molecular Architecture on Single Polymer Adhesion. *Langmuir* **2014**, *30*, 4351–4357.

(87) Zhang, X.; Liu, C.; Wang, Z. Force Spectroscopy of Polymers: Studying on Intramolecular and Intermolecular Interactions in Single Molecular Level. *Polymer* **2008**, *49*, 3353–3361.

(88) Vendra, V. K.; Wu, L.; Krishnan, S. Polymer Thin Films for Biomedical Applications. In *Nanostructured thin films and surfaces*; Kumar, C. S. S., Ed.; Wiley: Baton Rouge, 2010; pp 1–54.

(89) Rodriquez, D.; Kim, J.; Root, S. E.; Fei, Z.; Boufflet, P.; Heeney, M.; Kim, T.; Lipomi, D. J. Comparison of Methods for Determining the Mechanical Properties of Semiconducting Polymer Films for Stretchable Electronics. *Appl. Mater. interfaces* **2017**, *9*, 8855–8862.

(90) Krebs, F. C. Fabrication and Processing of Polymer Solar Cells: A Review of Printing and Coating Techniques. *Sol. Energy Mater. Sol. Cells* **2009**, *93*, 394–412.

(91) Reiter, G. Probing Properties of Polymers in Thin Films Via Dewetting. In *Advances in Polymer Science*; Springer: Berlin, 2012; Vol. 252, pp 29–64.

(92) Seemann, R.; Jacobs, K.; Blossey, R. Polystyrene Nanodroplets. *J. Phys. Condens. Matter* **2001**, *13*, 4915–4923.

(93) Vilmin, T.; Raphaël, E. Dewetting of Thin Polymer Films. *Eur. Phys. J. E* **2006**, *21*, 161–174.

(94) Bal, J. K.; Beuvier, T.; Unni, A. B.; Panduro, E. A. C.; Vignaud, G.; Delorme, N.; Chebil, M. S.; Grohens, Y.; Gibaud, A. Stability of Polymer Ultrathin Films (<7nm) Made by a Top-Down Approach. *ACS Nano* **2015**, *9*, 8184–8193.

(95) Akhrass, S. A.; Vonna, L.; Reiter, G. From Holes to Drops to Toroids: Conditions for the Transcription of Surface Patterns into Three-Dimensional Morphologies via Rim Instabilities in the Course of Dewetting. In *Polymer Surfaces in Motion: Unconventional Patterning Methods*; Rodríquez-Hernández, J., Drummond, C., Eds.; Springer: Cham, 2015; pp 23–42.

(96) Gan, D.; Cao, W.; Puat, N. E. Thermal Induced Instability of Thin Polymer Films: A Study by Atomic Force Microscopy. *High Perform. Polym.* **2001**, *13*, 259–267.

(97) Macdonald, B. F.; Cole, R. J.; Koutsos, V. The Formation of Dewetting Structures after Evaporation of N-Dodecane on Graphite Studied by Atomic Force Microscopy. *Surf. Sci.* **2004**, *548*, 41–50.

(98) Reiter, G. Unstable Thin Polymer Films: Rupture and Dewetting Processes. *Langmuir* **1993**, *9*, 1344–1351.

(99) Cai, Y.; Newby, B. Z. Dewetting of Polystyrene Thin Films on Poly (Ethylene Glycol) - Modified Surfaces as a Simple Approach for Patterning Proteins. *Langmuir* **2008**, *24*, 5202–5208.

(100) Damman, P.; Baudelet, N.; Reiter, G. Dewetting near the Glass Transition: Transition from a Capillary Force Dominated to a Dissipation Dominated Regime. *Phys. Rev. Lett.* **2003**, *91*, 216101–1.

(101) Spangler, L. L.; Torkelson, J. M.; Royal, J. S. Influence of Solvent and Molecular Weight on Thickness and Surface Topography of Spin-Coated Polymer Films. *Polym. Eng. Sci.* **1990**, *30*, 644–653.

(102) Reiter, G.; Hamieh, M.; Damman, P.; Sclavons, S.; Gabriele, S.; Vilmin, T.; Raphaël, E. Residual Stresses in Thin Polymer Films Cause Rupture and Dominate Early Stages of Dewetting. *Nat. Mater.* **2005**, *4*, 754–758.

(103) Kumaki, J.; Kawauchi, T.; Yashima, E. " Reptational " Movements of Single Synthetic Polymer Chains on Substrate Observed by in-Situ Atomic Force Microscopy. *Macromolecules* **2006**, *39*, 1209–1215.

(104) Ouchi, M.; Badi, N.; Lutz, J.-F.; Sawamoto, M. Single-Chain Technology Using Discrete Synthetic Macromolecules. *Nat. Chem.* **2011**, *3*, 917–924.

(105) Schappacher, M.; Deffieux, A. Imaging of Catenated, Figure-of-Eight, and Trefoil Knot Polymer Rings. *Angew. Chemie - Int. Ed.* **2009**, *48*, 5930–5933.

(106) Zhang, B.; Wepf, R.; Fischer, K.; Schmidt, M.; Besse, S.; Lindner, P.; King, B. T.; Sigel, R.; Schurtenberger, P.; Talmon, Y.; et al. The Largest Synthetic Structure with Molecular Precision: Towards a Molecular Object. *Angew. Chemie - Int. Ed.* **2011**, *50*, 737–740.

(107) Kumaki, J.; Nishikawa, Y.; Hashimoto, T. Visualization of Single-Chain Conformations of a Synthetic Polymer with Atomic Force Microscopy. *J. Am. Chem. Soc.* **1996**, *118*, 3321–3322.

(108) Kumaki, J. Observation of Polymer Chain Structures in Two-Dimensional Films by Atomic Force Microscopy. *Polym. J.* **2016**, *48*, 3–14.

(109) Roiter, Y.; Minko, S. AFM Single Molecule Experiments at the Solid-Liquid Interface: In Situ Conformation of Adsorbed Flexible Polyelectrolyte Chains. *J. Am. Chem. Soc.* **2005**, *127*, 15688–15689.

(110) Chen, D.; Handa, H.; Wan, L.; Mao, G. Surface Morphological Evolution of Ultrathin P4VP Films and Generation of Ordered Patterns on Graphite. *Macromol. Rapid Commun.* **2007**, *28*, 1619–1623.

(111) Tuinstra, F.; Baer, E. Epitaxial Crystallization of Polyethylene on Graphite. *J. Polym. Sci. Part C Polym. Lett.* **1970**, *8*, 861–865.

(112) Prokhorov, V. V.; Nitta, K. The AFM Observation of Linear Chain and Crystalline Conformations of Ultrahigh Molecular Weight Polyethylene Molecules on Mica and Graphite. *J. Polym. Sci. Part B Polym. Phys.* **2010**, *48*, 766–777.

(113) Takenaka, Y.; Miyaji, H.; Hoshino, A.; Tracz, A.; Jeszka, J. K.; Kucinska, I. Interface Structure of Epitaxial Polyethylene Crystal Grown on HOPG and MoS2 Substrates. *Macromolecules* **2004**, *37*, 9667–9669.

(114) Tracz, A.; Jeszka, J.; Kucińska, I.; Chapel, J.; Boiteux, G. Nanoscale Morphology of Melt Crystallized Polyethylene/Graphite (HOPG) Interphase. *Macromol. Symp.* **2001**, *169*, 129–135.

(115) Rabe, J. P.; Buchholz, S. Direct Observation of Molecular Structure and Dynamics at the Interface between a Solid Wall and an Organic Solution by Scanning Tunneling Microscopy. *Phys. Rev. Lett.* **1991**, *66*, 2096–2099.

(116) Rabe, J. P.; Buchholz, S. Commensurability and Mobility in Two-Dimensional Molecular Patterns on Graphite. *Science.* **1991**, *253*, 424–427.

(117) Prokhorova, S. A.; Sheiko, S. S.; Mourran, A.; Azumi, R.; Beginn, U.; Zipp, G.; Ahn, C.-H.; Holerca, M. N.; Percec, V.; Möller, M. Epitaxial Adsorption of Monodendron-Jacketed Linear Polymers on Highly Oriented Pyrolytic Graphite. *Langmuir* **2000**, *16*, 6862–6867.

(118) Glynos, E.; Chremos, A.; Petekidis, G.; Camp, P. J.; Koutsos, V. Polymer-like to Soft Colloid-like Behavior of Regular Star Polymers Adsorbed on Surfaces. *Macromolecules* **2007**, *40*, 6947–6958.

(119) Lau, A. W. C.; Portigliatti, M.; Raphael, E.; Leger, L. Spreading of Latex Particles on a Substrate. *Europhys. Lett.* **2002**, *60*, 717–723.

(120) Amirfazli, A.; Neumann, A. W. Status of the Three-Phase Line Tension: A Review. *Adv.*

Colloid Interface Sci. **2004**, *110*, 121–141.

(121) Weijs, J. H.; Marchand, A.; Andreotti, B.; Lohse, D.; Snoeijer, J. H. Origin of Line Tension for a Lennard-Jones Nanodroplet. *Phys. Fluids* **2011**, *23*, 022001-1.

(122) Li, D. Drop Size Dependence of Contact Angles and Line Tensions of Solid-Liquid Systems. *Colloids Surfaces A Physicochem. Eng. Asp.* **1996**, *116*, 1–23.

(123) Milchev, A. I.; Milchev, A. A. Wetting Behavior of Nanodroplets: The Limits of Young's Rule Validity. *Europhys. Lett.* **2001**, *56*, 695–701.

(124) Peng, H.; Birkett, G. R.; Nguyen, A. V. The Impact of Line Tension on the Contact Angle of Nanodroplets. *Mol. Simul.* **2014**, *40*, 934–941.

(125) Glynos, E.; Pispas, S.; Koutsos, V. Amphiphilic Diblock Copolymers on Mica: Formation of Flat Polymer Nanoislands and Evolution to Protruding Surface Micelles. *Macromolecules* **2008**, *41*, 4313–4320.

(126) Seitz, M.; Friedsam, C.; Jöstl, W.; Hugel, T.; Gaub, H. E. Probing Solid Surfaces with Single Polymers. *ChemPhysChem* **2003**, *4*, 986–990.

(127) Zhang, B.; Shi, R.; Duan, W.; Luo, Z.; Lu, Z.-Y.; Cui, S. Direct Comparison between Chemisorption and Physisorption: A Study of Poly(Ethylene Glycol) by Means of Single-Molecule Force Spectroscopy. *RSC Adv.* **2017**, *7*, 33883–1.

(128) Braithwaite, G. J. C.; Howe, A.; Luckham, P. F. Interactions between Poly(Ethylene Oxide) Layers Adsorbed to Glass Surfaces Probed by Using a Modified Atomic Force Microscope. *Langmuir* **1996**, *12*, 4224–4237.

(129) Liu, K.; Song, Y.; Feng, W.; Liu, N.; Zhang, W.; Zhang, X. Extracting a Single Polyethylene Oxide Chain from a Single Crystal by a Combination of Atomic Force Microscopy Imaging and Single-Molecule Force Spectroscopy: Toward the Investigation of Molecular Interactions in Their Condensed States. *J. Am. Chem. Soc.* **2011**, *133*, 3326–3329.

(130) Walder, R.; Patten, W. J. V; Adhikari, A.; Perkins, T. T. Going Vertical To Improve the Accuracy of Atomic Force Microscopy Based Single- Molecule Force Spectroscopy. *ACS Nano* **2018**, *12*, 198–207.

(131) Grebíková, L.; Whittington, S. G.; Vancso, J. G. Angle-Dependent Atomic Force Microscopy Single-Chain Pulling of Adsorbed Macromolecules from Planar Surfaces Unveils the Signature of an Adsorption-Desorption Transition. *J. Am. Chem. Soc.* **2018**, *140*, 6408–6415.

(132) Barber, A. H.; Cohen, S. R.; Wagner, H. D. Measurement of Carbon Nanotube-Polymer Interfacial Strength. *Appl. Phys. Lett.* **2003**, *82*, 4140–4142.

(133) Tsuda, T.; Ogasawara, T.; Deng, F.; Takeda, N. Direct Measurements of Interfacial Shear Strength of Multi-Walled Carbon Nanotube/PEEK Composite Using a Nano-Pullout Method. *Compos. Sci. Technol.* **2011**, *71*, 1295–1300.

(134) Barber, A. H.; Cohen, S. R.; Kenig, S.; Wagner, H. D. Interfacial Fracture Energy Measurements for Multi-Walled Carbon Nanotubes Pulled from a Polymer Matrix. *Compos. Sci. Technol.* **2004**, *64*, 2283–2289.

(135) Strus, M. C.; Cano, C. I.; Pipes, R. B.; Nguyen, C. V.; Raman, A. Interfacial Energy between Carbon Nanotubes and Polymers Measured from Nanoscale Peel Tests in the Atomic Force Microscope. *Compos. Sci. Technol.* **2009**, *69*, 1580–1586.

(136) Nishijima, H.; Kamo, S.; Akita, S.; Nakayama, Y.; Hohmura, K. I.; Yoshimura, S. H.;

Takeyasu, K. Carbon-Nanotube Tips for Scanning Probe Microscopy: Preparation by a Controlled Process and Observation of Deoxyribonucleic Acid. *Appl. Phys. Lett.* **1999**, *74*, 4061–4063.

(137) Rahmat, M.; Hubert, P. Carbon Nanotube-Polymer Interactions in Nanocomposites: A Review. *Compos. Sci. Technol.* **2011**, *72*, 72–84.

(138) Strus, M. C.; Zalamea, L.; Raman, A.; Pipes, R. B.; Nguyen, C. V.; Stach, E. A. Peeling Force Spectroscopy: Exposing the Adhesive Nanomechanics of One-Dimensional Nanostructures. *Nano Lett.* **2008**, *8*, 544–550.

(139) Cooper, C. A.; Cohen, S. R.; Barber, A. H.; Wagner, H. D. Detachment of Nanotubes from a Polymer Matrix. *Appl. Phys. Lett.* **2002**, *81*, 3873–3875.

(140) Koutsos, V.; Haschke, H.; Miles, M. J.; Madani, F. Pulling Single Chains out of a Collapsed Polymer Monolayer in Bad-Solvent Conditions. *MRS Proc.* **2002**, *734*, B1.6.

(141) Haupt, B. J.; Senden, T. J.; Sevick, E. M. AFM Evidence of Rayleigh Instability in Single Polymer Chains. *Langmuir* **2002**, *18*, 2174–2182.

(142) Cui, S.; Liu, C.; Zhang, W.; Zhang, X.; Wu, C. Desorption Force per Polystyrene Segment in Water. *Macromolecules* **2003**, *36*, 3779–3782.

(143) Zou, S.; Schönherr, H.; Vancso, G. J. Stretching and Rupturing Individual Supramolecular Polymer-Chains by AFM. *Angew. Chemie* **2005**, *117*, 978–981.

(144) Kikuchi, H.; Yokoyama, N.; Kajiyama, T. Direct Measurements of Stretching Force-Chain Ends Elongation Relationships of a Single Polystyrene Chain in Dilute Solution. *Chem. Lett.* **1997**, 1107–1108.

(145) Ortiz, C.; Hadziioannou, G. Entropic Elasticity of Single Polymer Chains of Poly(Methacrylic Acid) Measured by Atomic Force Microscopy. *Macromolecules* **1999**, *32*, 780–787.

(146) Stuart, M. A. C.; Huck, W. T. S.; Genzer, J.; Müller, M.; Ober, C.; Stamm, M.; Sukhorukov, G. B.; Szleifer, I.; Tsukruk, V. V; Urban, M.; et al. Emerging Applications of Stimuli-Responsive Polymer Materials. *Nat. Mater.* **2010**, *9*, 101–113.

(147) Bhushan, B.; Palacio, M. L. B. Atomic Force Microscopy. In *Encyclopedia of Nanotechnology*; Bhushan, B., Ed.; Springer: New York City, 2012; pp 146–159.

(148) Sugihara, K.; Kumaki, J. Visualization of Two-Dimensional Single Chain Conformations Solubilized in a Miscible Polymer Blend Monolayer by Atomic Force Microscopy. *J. Phys. Chem. B* **2012**, *116*, 6561–6568.

(149) McLean, R. S.; Sauer, B. B. Tapping-Mode AFM Studies Using Phase Detection for Resolution of Nanophases in Segmented Polyurethanes and Other Block Copolymers. *Macromolecules* **1997**, *30*, 8314–8317.

(150) Isrelachvili, J. N. *Intermolecular and Surface Forces*, second ed.; Academic Press: New York City, 1992.

(151) Fetters, L. J.; Lohse, D. J.; Milner, S. T.; Graessley, W. W. Packing Length Influence in Linear Polymer Melts on the Entanglement, Critical, and Reptation Molecular Weights. *Macromolecules* **1999**, *32*, 6847–6851.

(152) Fetters, L. J.; Lohse, D. J.; Graessley, W. W. Chain Dimensions and Entanglement Spacings in Dense Macromolecular Systems. *J. Polym. Sci. Part B Polym. Phys.* **1999**, *37*, 1023–1033.

(153) Christenson, H. K.; Thomson, N. H. The Nature of the Air-Cleaved Mica Surface. *Surf. Sci. Rep.* **2016**, *71*, 367–390.

(154) Fukuma, T. Wideband Low-Noise Optical Beam Deflection Sensor with Photothermal Excitation for Liquid-Environment Atomic Force Microscopy. *Rev. Sci. Instrum.* **2009**, *80*, 023707.

(155) Sakuma, H. Adhesion Energy between Mica Surfaces: Implications for the Frictional Coefficient under Dry and Wet Conditions. *J. Geophys. Res. Solid Earth* **2013**, *118*, 6066–6075.

(156) Morris, V. J.; Kirby, A. R.; Gunning, A. P. *Atomic Force Microscopy for Biologists*; Imperial College Press: London, 2009.

(157) Falini, G.; Fermani, S.; Conforti, G.; Ripamonti, A. Protein Crystallisation on Chemically Modified Mica Surfaces. *Acta Crystallogr. Sect. D Biol. Crystallogr.* **2002**, *58*, 1649–1652.

(158) Yang, H.; Fung, S.-Y. u; Pritzker, M.; Chen, P. Modification of Hydrophilic and Hydrophobic Surfaces Using an Ionic-Complementary Peptide. *PLoS One* **2007**, *2*, e1325.

(159) Eastman, T.; Zhu, D. Adhesion Forces between Surface-Modified AFM Tips and a Mica Surface. *Langmuir* **1996**, *12*, 2859–2862.

(160) Kyotani, T.; Sonobe, N.; Tomita, A. Formation of Highly Orientated Graphite from Polyacrylonitrile by Using a Two-Dimensional Space between Montmorillonite Lamellae. *Nature* **1988**, *331*, 331–333.

(161) Pak, A.; Gregori, G.; Knight, J.; Campbell, K.; Price, D.; Hammel, B.; Landen, O. L.; Glenzer, S. H. X-Ray Line Measurements with High Efficiency Bragg Crystals. *Rev. Sci. Instrum.* **2004**, *75*, 3747–3749.

(162) Hembacher, S.; Giessibl, F. J.; Mannhart, J.; Quate, C. F. Revealing the Hidden Atom in Graphite by Low-Temperature Atomic Force Microscopy. *Proc. Natl. Acad. Sci.* **2003**, *100*, 12539–12542.

(163) Lee, H.; Lee, H.-B.-R.; Kwon, S.; Salmeron, M.; Park, J. Y. Internal and External Atomic Steps in Graphite Exhibit Dramatically Different Physical and Chemical Properties. *ACS Nano* **2015**, *9*, 3814–3819.

(164) Morcos, I. On Contact Angle and Dispersion Energy of the Cleavage Graphite/Water System. *J. Colloid Interface Sci.* **1970**, *34*, 469–471.

(165) Garcia, R.; Osborne, K.; Subashi, E. Validity of the "Sharp-Kink Approximation" for Water and Other Fluids. *J. Phys. Chem. B* **2009**, *113*, 8119.

(166) Fowkes, F. M.; Harkins, W. D. The State of Monolayers Adsorbed at the Interface Solid-Aqueous Solution. *J. Am. Chem. Soc.* **1940**, *62*, 3377–3386.

(167) Gong, Y.; Zhang, S.; Geng, Y.; Niu, C.; Yin, S.; Zeng, Q.; Li, M. Orthogonal Supramolecular Polymer Formation on Highly Oriented Pyrolytic Graphite (HOPG) Surfaces Characterized by Scanning Probe Microscopy. *Langmuir* **2015**, *31*, 11525–11531.

(168) Asthana, A.; Maitra, T.; Büchel, R.; Tiwari, M. K.; Poulikakos, D. Multifunctional Superhydrophobic Polymer/Carbon Nanocomposites: Graphene, Carbon Nanotube or Carbon Black? *Appl. Mater. interfaces* **2014**, *6*, 8859–8867.

(169) Balamane, H.; Halicioglu, T.; Tiller, W. A. Comparative Study of Silicon Empirical Interatomic Potentials. *Phys. Rev. B* **1992**, *46*, 2250–2276.

(170) Schriever, C.; Bohley, C.; Schilling, J.; Wehrspohn, R. B. Strained Silicon Photonics.

Materials **2012**, *5*, 889–908.

(171) Acharya, K. P.; Erlacher, A.; Ullrich, B. Optoelectronic Properties of ZnTe/Si Heterostructures Formed by Nanosecond Laser Deposition at Different Nd:YAG Laser Lines. *Thin Solid Films* **2007**, *515*, 4066–4069.

(172) Takayanagi, K.; Tanishiro, Y.; Takahashi, M.; Takahashi, S. Structural Analysis of Si(111)-7×7 by UHV-Transmission Electron Diffraction and Microscopy. *J. Vac. Sci. Technol. A* **1985**, *3*, 1502–1506.

(173) Nomura, K.; Ohta, H.; Takagi, A.; Kamiya, T.; Hirano, M.; Hosono, H. Room-Temperature Fabrication of Transparent Flexible Thin-Film Transistors Using Amorphous Oxide Semiconductors. *Nature* **2004**, *432*, 488–492.

(174) Williams, R.; Goodman, A. M. Wetting of Thin Layers of SiO2 by Water. *Appl. Phys. Lett.* **1974**, *25*, 531–532.

(175) Morita, M.; Ohmi, T.; Hasegawa, E.; Kawakami, M.; Ohwada, M. Growth of Native Oxide on a Silicon Surface. *J. Appl. Phys.* **1990**, *68*, 1272–1281.

(176) Norrman, K.; Ghanbari-Siahkali, A.; Larsen, N. B. 6 Studies of Spin-Coated Polymer Films. *Annu. Reports Sect. "C" (Physical Chem.* **2005**, *101*, 174–201.

(177) Gu, X.; Raghavan, D.; Douglas, J. F.; Karim, A. Hole-Growth Instability in the Dewetting of Evaporating Polymer Solution Films. *J. Polym. Sci. Part B Polym. Phys.* **2002**, *40*, 2825–2832.

(178) Banga, R.; Yarwood, J.; Morgan, A. M.; Evans, B.; Kells, J. FTIR and AFM Studies of the Kinetics and Self-Assembly of Alkyltrichlorosilanes and (Perfluoroalkyl)Trichlorosilanes onto Glass and Silicon. *Langmuir* **1995**, *11*, 4393–4399.

(179) Senden, T. J.; Drummond, C. J. Surface Chemistry and Tip-Sample Interactions in Atomic Force Microscopy. *Colloids Surfaces A Physicochem. Eng. Asp.* **1995**, *94*, 29–51.

(180) Ying, Q.; Chu, B. Overlap Concentration of Macromolecules in Solution. *Macromolecules* **1987**, *20*, 362–366.

(181) Grosberg, A. Y.; Khokhlov, A. R. *Giant Molecules*; Academic Press: San Diego, 1997.

(182) Hall, D. B.; Underhill, P.; Torkelson, J. M. Spin Coating of Thin and Ultrathin Polymer Films. *Polym. Eng. Sci.* **1998**, *38*, 2039–2045.

(183) Sahu, N.; Parija, B.; Panigrahi, S. Fundamental Understanding and Modeling of Spin Coating Process: A Review. *Indian J. Phys.* **2009**, *83*, 493–502.

(184) Brinker, C. J. Dip Coating. In *Chemical Solution Deposition of Functional Oxide Thin Films*; Schneller, T Waser, R Kosec, M., Ed.; Springer: Vienna, 2013; pp 233–261.

(185) Takahashi, Y.; Wada, Y. Dip-Coating of Sb-Doped Sn02 Films by Ethanolamine-Alkoxide Method. *J. Electrochem. Soc.* **1990**, *137*, 267–272.

(186) Zhong, J.; Yan, J. Seeing Is Believing: Atomic Force Microscopy Imaging for Nanomaterial Research. *RSC Adv.* **2016**, *6*, 1103–1121.

(187) Jalili, N.; Laxminarayana, K. A Review of Atomic Force Microscopy Imaging Systems: Application to Molecular Metrology and Biological Sciences. *Mechatronics* **2004**, *14*, 907–945.

(188) Nečas, D.; Klapetek, P. Gwyddion: An Open-Source Software for SPM Data Analysis. *Cent. Eur. J. Phys.* **2012**, *10*, 181–188.

(189) Fung, S. Y.; Keyes, C.; Duhamel, J.; Chen, P. Concentration Effect on the Aggregation of a Self-Assembling Oligopeptide. *Biophys. J.* **2003**, *85*, 537–548.

(190) Butt, H.-J.; Jaschke, M. Calculation of Thermal Noise in Atomic Force Microscopy. *Nanotechnology* **1995**, *6*, 1–7.

(191) Li, Y.; Hu, K.; Han, X.; Yang, Q.; Xiong, Y.; Bai, Y.; Guo, X.; Cui, Y.; Yuan, C.; Ge, H.; et al. Phase Separation of Silicon-Containing Polymer/Polystyrene Blends in Spin-Coated Films. *Langmuir* **2016**, *32*, 3670–3678.

(192) Mortazavian, H.; Fennell, C. J.; Blum, F. D. Surface Bonding Is Stronger for Poly(Methyl Methacrylate) than for Poly(Vinyl Acetate). *Macromolecules* **2016**, *49*, 4211–4219.

(193) Maddumaarachchi, M.; Blum, F. D. Thermal Analysis and FT-IR Studies of Adsorbed Poly(Ethylene-Stat-Vinyl Acetate) on Silica. *J. Polym. Sci. Part B Polym. Phys.* **2014**, *52*, 727–736.

(194) Koutsos, V.; van der Vegte, E. W.; Pelletier, E.; Stamouli, A.; Hadziioannou, G. Structure of Chemically End-Grafted Polymer Chains Studied by Scanning Force Microscopy in Bad-Solvent Conditions. *Macromolecules* **1997**, *30*, 4719–4726.

(195) Koutsos, V.; van der Vegte, E. W.; Hadziioannou, G. Direct View of Structural Regimes of End-Grafted Polymer Monolayers: A Scanning Force Microscopy Study. *Macromolecules* **1999**, *32*, 1233–1236.

(196) Jang, J.; Kawazoe, M.; Yoshida, H. Characterization of Phase Separated Structure and Interface. *Japan Soc. Calorim. Therm. Anal.* **2012**, *39*, 33–37.

(197) Sato, G.; Nishitsuji, S.; Kumaki, J. Two-Dimensional Phase Separation of a Poly(Methyl Methacrylate)/Poly(l -Lactide) Mixed Langmuir Monolayer via a Spinodal Decomposition Mechanism. *J. Phys. Chem. B* **2013**, *117*, 9067–9072.

(198) Zhao, J.; Tian, S.; Wang, Q.; Liu, X.; Jiang, S.; Ji, X.; An, L.; Jiang, B. Nanoscopic Surface Patterns of Diblock Copolymer Thin Films. *Eur. Phys. J. E* **2005**, *16*, 49–56.

(199) Checco, A.; Guenoun, P.; Daillant, J. Nonlinear Dependence of the Contact Angle of Nanodroplets on Contact Line Curvature. *Phys. Rev. Lett.* **2003**, *91*, 186101–1.

(200) Arinstein, A.; Burman, M.; Gendelman, O.; Zussman, E. Effect of Supramolecular Structure on Polymer Nanofibre Elasticity. *Nat. Nanotechnol.* **2007**, *2*, 59–62.

(201) Johner, A.; Joanny, J. F. Polymer Adsorption in a Poor Solvent. *J. Phys. II* **1991**, *1*, 181–194.

(202) Wei, B.; Lam, P. G.; Braunfeld, M. B.; Agard, D. A.; Genzer, J.; Spontak, R. J. Tunable Instability Mechanisms of Polymer Thin Films by Molecular Self-Assembly. *Langmuir* **2006**, *22*, 8642–8645.

(203) Masson, J.-L.; Olufokunbi, O.; Green, P. F. Flow Instabilities in Entangled Polymer Thin Films. *Macromolecules* **2002**, *35*, 6992–6996.

(204) Ashley, K. M.; Raghavan, D.; Douglas, J. F.; Karim, A. Wetting-Dewetting Transition Line in Thin Polymer Films. *Langmuir* **2008**, *21*, 9518–9523.

(205) Xie, R.; Karim, A.; Douglas, J. F.; Han, C. C.; Weiss, R. A. Spinodal Dewetting of Thin Polymer Films. *Phys. Rev. Lett.* **1998**, *81*, 1251–1254.

(206) Vilmin, T.; Raphaël, E. Dewetting of Thin Polymer Films. *Phys. Rev. Lett.* **1992**, *68*, 75–78.

(207) Rittigstein, P.; Priestley, R. D.; Broadbelt, L. J.; Torkelson, J. M. Model Polymer Nanocomposites Provide an Understanding of Confinement Effects in Real

Nanocomposites. *Nat. Mater.* **2007**, *6*, 278–282.

(208) Liu, D.; Wang, T. Instability of Hydrophobic and Viscoelastic Polymer Thin Films in Water at Room Temperature. *J. Phys. Condens. Matter* **2013**, *25*, 415101.

(209) Al-Shammari, B.; Al-Fariss, T.; Al-Sewailm, F.; Elleithy, R. The Effect of Polymer Concentration and Temperature on the Rheological Behavior of Metallocene Linear Low Density Polyethylene (MLLDPE) Solutions. *J. King Saud Univ. - Eng. Sci.* **2011**, *23*, 9–14.

(210) Assael, M. J.; Dalaouti, N. K.; Dymond, J. H. Viscosity of Toluene in the Temperature Range 210 to 370 K. *Int. J. Thermophys.* **2000**, *21*, 291–299.

(211) Balazs, A. C.; Emrick, T.; Russell, T. P. Nanoparticle Polymer Composites: Where Two Small Worlds Meet. *Science* **2006**, *314*, 1107–1110.

(212) Miyake, K.; Satomi, N.; Sasaki, S. Elastic Modulus of Polystyrene Film from near Surface to Bulk Measured by Nanoindentation Using Atomic Force Microscopy. *Appl. Phys. Lett.* **2006**, *89*, 031925.

(213) Tweedie, C. A.; Constantinides, G.; Lehman, K. E.; Brill, D. J.; Blackman, G. S.; Van Vliet, K. J. Enhanced Stiffness of Amorphous Polymer Surfaces under Confinement of Localized Contact Loads. *Adv. Mater.* **2007**, *19*, 2540–2546.

(214) Glynos, E.; Frieberg, B.; Green, P. F. Wetting of a Multiarm Star-Shaped Molecule. *Phys. Rev. Lett.* **2011**, *107*, 118303.

(215) Glynos, E.; Chremos, A.; Frieberg, B.; Sakellariou, G.; Green, P. F. Wetting of Macromolecules: From Linear Chain to Soft Colloid-like Behavior. *Macromolecules* **2014**, *47*, 1137–1143.

(216) Burman, M.; Arinstein, A.; Zussman, E. Free Flight of an Oscillated String Pendulum as a Tool for the Mechanical Characterization of an Individual Polymer Nanofiber. *Appl. Phys. Lett.* **2008**, *93*, 193118.

(217) Shin, M. K.; Kim, S. I.; Kim, S. J.; Kim, S.-K.; Lee, H.; Spinks, G. M. Size-Dependent Elastic Modulus of Single Electroactive Polymer Nanofibers. *Appl. Phys. Lett.* **2006**, *89*, 231929.

(218) Spagnoli, C.; Loos, K.; Ulman, A.; Cowman, M. K. Imaging Structured Water and Bound Polysaccharide on Mica Surface at Ambient Temperature. *J. Am. Chem. Soc.* **2003**, *125*, 7124–7128.

(219) Holbery, J.; Houston, D. Natural-Fibre-Reinforced Polymer Composites in Automotive Applications. *J. Miner. Met. Mater. Soc.* **2006**, *58*, 80–86.

(220) Mallick, P. K. Fiber-Reinforced Composites: Materials, Manufacuring, and Design; CRC Press: Boca Raton, 2007; pp 6–12.

(221) Fu, S.-Y.; Feng, X.-Q.; Lauke, B.; Mai, Y.-W. Effects of Particle Size, Particle/Matrix Interface Adhesion and Particle Loading on Mechanical Properties of Particulate-Polymer Composites. *Compos. Part B Eng.* **2008**, *39*, 933–961.

(222) Fröhlich, J.; Niedermeier, W.; Luginsland, H.-D. The Effect of Filler-Filler and Filler-Elastomer Interaction on Rubber Reinforcement. *Compos. Part A Appl. Sci. Manuf.* **2005**, *36*, 449–460.

(223) Chung, D. D. L. Carbon Fiber Composites; Butterworth-Heinemann: Oxford, 1994; pp 49–51.

(224) Shalin, R. E. Polymer Matrix Composites; Chapman and Hall: London, 1995; pp 132–149.

(225) Li, Q.; Zaiser, M.; Blackford, J. R.; Jeffree, C.; He, Y.; Koutsos, V. Mechanical Properties and Microstructure of Single-Wall Carbon Nanotube/Elastomeric Epoxy Composites with Block Copolymers. *Mater. Lett.* **2014**, *125*, 116–119.

(226) Li, Q.; Zaiser, M.; Koutsos, V. Carbon Nanotube/Epoxy Resin Composites Using a Block Copolymer as a Dispersing Agent. *Phys. Status Solidi A* **2004**, *201*, R89–R91.

(227) Arash, B.; Wang, Q.; Varadan, V. K. Mechanical Properties of Carbon Nanotube/Polymer Composites. *Sci. Rep.* **2014**, *4*, 1–8.

(228) Coleman, J. N.; Khan, U.; Blau, W. J.; Gun'ko, Y. K. Small but Strong: A Review of the Mechanical Properties of Carbon Nanotube-Polymer Composites. *Carbon.* **2006**, *44*, 1624–1652.

(229) Nagata, K.; Iwabuki, H.; Nigo, H. Effect of Particle Size of Graphites on Electrical Conductivity of Graphite/Polymer Composite. *Compos. Interfaces* **1999**, *6*, 483–495.

(230) Kim, J. Y.; Kim, B. H.; Hwang, J. O.; Jeong, S.-J.; Shin, D. O.; Mun, J. H.; Choi, Y. J.; Jin, H. M.; Kim, S. O. Flexible and Transferrable Self-Assembled Nanopatterning on Chemically Modified Graphene. *Adv. Mater.* **2013**, *25*, 1331–1335.

(231) Kim, B. H.; Kim, J. Y.; Jeong, S.-J.; Hwang, J. O.; Lee, D. H.; Shin, D. O.; Choi, S.; Kim, S. O. Surface Energy Modification by Spin-Cast, Large-Area Graphene Film for Block Copolymer Lithography. *ACS Nano* **2010**, *4*, 5464–5470.

(232) Kim, J. Y.; Lim, J.; Jin, H. M.; Kim, B. H.; Jeong, S.-J.; Choi, D. S.; Li, D. J.; Kim, S. O. 3D Tailored Crumpling of Block-Copolymer Lithography on Chemically Modified Graphene. *Adv. Mater.* **2016**, *28*, 1591–1596.

(233) Jin, H. M.; Park, D. Y.; Jeong, S.-J.; Lee, G. Y.; Kim, J. Y.; Mun, J. H.; Cha, S. K.; Lim, J.; Kim, J. S.; Kim, K. H.; et al. Flash Light Millisecond Self-Assembly of High χ Block Copolymers for Wafer-Scale Sub-10 Nm Nanopatterning. *Adv. Mater.* **2017**, *29*, 1700595.

(234) Severin, N.; Rabe, J. P.; Kurth, D. G. Fully Extended Polyelectrolyte-Amphiphile Complexes Adsorbed on Graphite. *J. Am. Chem. Soc.* **2004**, *126*, 3696–3697.

(235) Schlüter, A. D.; Rabe, J. P. Dendronized Polymers: Synthesis, Characterization, Assembly at Interfaces, and Manipulation. *Angew. Chemie - Int. Ed.* **2000**, *39*, 864–883.

(236) Rabe, J. P.; Buchholz, S. Commensurability and Mobility in 2-Dimensional Molecular-Patterns on Graphite. *Science* **1991**, *253*, 424–427.

(237) Zhao, W.; Rafailovich, M. H.; Sokolov, J.; Fetters, L. J.; Plano, R.; Sanyal, M. K.; Sinha, S. K.; Sauer, B. B. Wetting Properties of Thin Liquid Polyethylene Propylene Films. *Phys. Rev. Lett.* **1993**, *70*, 1453–1456.

(238) Wheeler, S. E. Understanding Substituent Effects in Noncovalent Interactions Involving Aromatic Rings. *Acc. Chem. Res.* **2013**, *46*, 1029–1038.

(239) Vollhardt, P.; Schore, N. *Organic Chemistry Structure and Function*, 7th ed.; W.H Freeman and Company: New York City, 2014.

(240) Sci, C.; Martinez, C. R.; Iverson, B. L. Rethinking the Term '"Pi-Stacking."' *Chem. Sci.* **2012**, *3*, 2191–2201.

(241) Yang, M.; Koutsos, V.; Zaiser, M. Interactions between Polymers and Carbon Nanotubes: A Molecular Dynamics Study. *J. Phys. Chem. B* **2005**, *109*, 10009–10014.

(242) Lambert, A. Glass Transition Measurements on Polystyrene by Differential Scanning Calorimetry. *Polymer* **1969**, *10*, 319–326.

(243) Makhiyanov, N.; Temnikova, E. V. Glass-Transition Temperature and Microstructure of Polybutadienes. *Polym. Sci. Ser. A* **2010**, *52*, 1292–1300.

(244) Chremos, A.; Glynos, E.; Koutsos, V.; Camp, P. J. Adsorption and Self-Assembly of Linear Polymers on Surfaces: A Computer Simulation Study. *Soft Matter* **2009**, *5*, 637–645.

(245) Friedsam, C.; Gaub, H. E.; Netz, R. R. Probing Surfaces with Single-Polymer Atomic Force Microscope Experiments. *Biointerphases* **2006**, *1*, MR1.

(246) Rief, M.; Oesterhelt, F.; Heymann, B.; Gaub, H. E. Single Molecule Force Spectroscopy on Polysaccharides by Atomic Force Microscopy. *Science* **1997**, *275*, 1295–1297.

(247) Li, H.; Linke, W. A.; Oberhauser, A. F.; Carrion-Vazquez, M.; Kerkvliet, J. G.; Lu, H.; Marszalek, P. E.; Fernandez, J. M. Reverse Engineering of the Giant Muscle Protein Titin. *Nature* **2002**, *418*, 998–1002.

(248) Rief, M.; Clausen-Schaumann, H.; Gaub, H. E. Sequence Dependent Mechanics of Single DNA Molecules. *Nat. Struct. Biol.* **1999**, *6*, 346–349.

(249) Stetter, F. W. S.; Kienle, S.; Krysiak, S.; Hugel, T. Investigating Single Molecule Adhesion by Atomic Force Spectroscopy. *J. Vis. Exp.* **2015**, *96*, e52456.

(250) Jacob Cornells Dijt. Kinetics of Polymer Adsorption, Desorption and Exchange, Wageningen University, 1993.

(251) Gadelmawla, E. S.; Koura, M. M.; Maksoud, T. M. A.; Elewa, I. M.; Soliman, H. H. Roughness Parameters. *J. Mater. Process. Technol.* **2002**, *123*, 133–145.

(252) Balzer, B. N. A. Single Polymer Friction, Technical University of Munich, 2013.

(253) Israelachvili, J. N.; Pashley, R. M. Molecular Layering of Water at Surfaces and Origin of Repulsive Hydration Forces. *Nature* **1983**, *306*, 249–250.

(254) Celik, E.; Moy, V. T. Nonspecific Interactions in AFM Force Spectroscopy Measurements. *J. Mol. Recognit.* **2012**, *25*, 53–56.

(255) Xu, L.-C.; Siedlecki, C. A. Effects of Surface Wettability and Contact Time on Protein Adhesion to Biomaterial Surfaces. *Biomaterials* **2007**, *28*, 3273–3283.

(256) Li, Y.; Pham, J. Q.; Johnston, K. P.; Green, P. F. Contact Angle of Water on Polystyrene Thin Films: Effects of CO2 Environment and Film Thickness. *Langmuir* **2007**, *23*, 9785–9793.

(257) Carey, D. H.; Ferguson, G. S. Synthesis and Characterization of Surface-Functionalized 1,2-Polybutadiene Bearing Hydroxyl or Carboxylic Acid Groups. *Macromolecules* **1994**, *27*, 7254–7266.

(258) Liu, Y.; Chen, Y.-C.; Hutchens, S.; Lawrence, J.; Emrick, T.; Crosby, A. J. Directly Measuring the Complete Stress-Strain Response of Ultrathin Polymer Films. *Macromolecules* **2015**, *48*, 6534–6540.

(259) Serr, A.; Netz, R. R. Pulling Adsorbed Polymers from Surfaces with the AFM: Stick vs. Slip, Peeling vs. Gliding. *Europhys. Lett.* **2006**, *73*, 292–298.

(260) Washiyama, J.; Kramer, E. J.; Hui, C.-Y. Fracture Mechanisms of Polymer Interfaces Reinforced with Block Copolymers: Transition from Chain Pullout to Crazing. *Macromolecules* **1993**, *26*, 2928–2934.

(261) Washiyama, J.; Kramer, E. J.; Creton, C. F.; Hui, C.-Y. Chain Pullout Fracture of Polymer Interfaces. *Macromolecules* **1994**, *27*, 2019–2024.

(262) Semenov, A. N.; Bonet-Avalos, J.; Johner, A.; Joanny, J. F. Adsorption of Polymer Solutions onto a Flat Surface. *Macromolecules* **1996**, *29*, 2179–2196.

(263) Welch, D.; Lettinga, M. P.; Ripoll, M.; Dogic, Z.; Vliegenthart, G. A. Trains, Tails and Loops of Partially Adsorbed Semi-Flexible Filaments. *Soft Matter* **2015**, *11*, 7507–7514.

(264) Halperin, A.; Zhulina, E. B. On the Deformation Behavior of Collapsed Polymers. *Europhys. Lett.* **1991**, *15*, 417–421.

(265) Misra, S.; Fleming, P. D.; Mattice, W. L. Structure and Energy of Thin Films of Poly-(1,4-Cis-Butadiene): A New Atomistic Approach. *J. Comput. Mater. Des.* **1995**, *2*, 101–112.

(266) Feldman, K.; Tervoort, T.; Smith, P.; Spencer, N. D. Toward a Force Spectroscopy of Polymer Surfaces. *Langmuir* **1998**, *14*, 372–378.

(267) Li, Z.; Wang, Y.; Kozbial, A.; Shenoy, G.; Zhou, F.; McGinley, R.; Ireland, P.; Morganstein, B.; Kunkel, A.; Surwade, S. P.; et al. Effect of Airborne Contaminants on the Wettability of Supported Graphene and Graphite. *Nat. Mater.* **2013**, *12*, 925–931.

(268) Portigliatti, M.; Hervet, H.; Léger, L. Nanotack Test: Adhesive Behavior of Single Latex Particles. *Comptes Rendus l'Academie des Sci. - Ser. IV Physics, Astrophys.* **2000**, *1*, 1187–1196.

(269) Creton, C. Pressure-Sensitive Adhesives: An Introductory Course. *MRS Bull.* **2003**, *28*, 434–439.

(270) Lakrout, H.; Sergot, P.; Creton, C. Direct Observation of Cavitation and Fibrillation in a Probe Tack Experiment on Model Acrylic Pressure-Sensitive-Adhesives. *J. Adhes.* **1999**, *69*, 307–359.

(271) Ondarçuhu, T. Tack of a Polymer Melt: Adhesion Measurements and Fracture Profile Observations. *J. Phys. II* **1997**, *7*, 1893–1916.